International Workshop of Energy Conversion 2023
(IWEC 2023)

March 15-17, 2023

Kyoto, Japan

Proceedings

Venue: Kambaikan Building, Muromachi Campus,
Doshisha University, Kyoto, Japan

Sponsor: Energy Conversion Research Center,
Doshisha University, Kyoto, Japan

Co-sponsor: Nantong Institute of Technology, Nantong, China

International Workshop of Energy Conversion 2023

March 15-17, 2023
Kyoto, Japan

Welcome to IWEC 2023

The **International Workshop of Energy Conversion 2023 (IWEC 2023)** is organized by Energy Conversion Research Center, Doshisha University, Japan. For promoting and exchanging the knowledge of the energy conversion, the seven workshops (following up a series of meeting that first, third, fourth and sixth held in Doshisha University in Japan, and second in Beijing University, fifth in Shantou University, seventh in Nantong University and eighth in Jiangsu University in China) are held so far. This time is the ninth, and the conference on March, 2023 will be held in Doshisha University, Japan.

Topics

The situation of world energy has become critical and new issues are arising in the sector of energy conversion. Many of these issues are strictly related to efficient use or conversion of energies, and the possibility to solve these problems strongly depends on the new developments of science and engineering. Those problems are often rising in new areas of research, such as energy transport caused by flow of mass or electromagnetism and chemical reaction, where new techniques, numerical methods and solution methods need to be developed. The aims of the IWEC 2023 are to bring together researchers, scientists, practitioners from academia, research institutions and industries in Japan and the world to Doshisha University to exchange experiences, disseminate up-to-date information, and explore new opportunities in energy conversion. The topics on the IWEC 2023 could cover various aspects of theories, analyses, technologies and applications of energy conversion in experimental, theoretical and engineering science.

The conference language will be English.
(1) Energy Storage and Transportation of Renewable Energies
(2) Optimizing Energy System based on Hydrogen
(3) High Efficiency Energy Conversion Systems
(4) Proposal of Minimized Emission Energy Grid based on Holonic Path
(5) General: Energy Conversion and Related Research Topics

Venue

Kambaikan Building, **Muromachi Campus**, **Doshisha University**, Kyoto

<Address:>
103 Gosho Yahata-cho, Kamidachiuri-sagaru, Karasuma-dori, Kamigyo-ku, Kyoto-shi, Japan
(Nearest station: "**Imadegawa Station**" of Kyoto Municipal Subway)

Important dates

- First announcement: April 30, 2022
- Second announcement: August 1, 2022
- Third announcement: August 20, 2022
- Registration (deadline**):** September 16 *by E-mail
- Paper submission (deadline): December 16, 2022 *by E-mail
- Payment: On-site *Cash only (Credit card and electronic money cannot be accepted)

*The details of the paper submission will be informed by E-mail after the registration.

Conference fee (On-site payment only)

- Regular: 35 000 (JPY)
- Student/Accompany person: 15 000 (JPY)

Conference schedule

- March 15, 2023: Reception and Welcome party
- March 16, 2023: Opening, Oral presentations and Banquet
- March 17, 2023: Oral presentations and Closing

Organizing committee

Hiroshi Yamaguchi (Doshisha University, Japan)
Takuya Kuwahara (Nippon Institute of Technology, Japan)
Shigemitsu Shuchi (Akita Prefectural University, Japan)
Yuhiro Iwamoto (Nagoya Institute of Technology, Japan)
Haruhiko Yamasaki (Osaka Metropolitan University, Japan)
Guannan Xi (Nantong Institute of Technology)

Contact (Registration and Paper Submission)

E-mail: iwec@mail.doshisha.ac.jp

Access

About 10 min from "**Kyoto Station**" to "**Imadegawa Station**" on the Kyoto Municipal Subway, and about 1 min by walk from "**Imadegawa Station**" to the "**Conference Place**". (https://www.doshisha.ac.jp/en/information/campus/access/muromachi.html)

International Workshop of Energy Conversion 2023

IWEC2023 Program

Kambaikan Building, **Muromachi Campus**,
Doshisha University, Kyoto

＜March 15, Wednesday＞

Reception and Welcome party

13:00-18:30 **Reception** at reception desk

19:00-20:30 **Welcome party**
Kambaikan Building, Muromachi Campus,
Doshisha University

＜March 16, Thursday＞

Opening ceremony (Chair: Prof. T. Kuwahara)

09:30-09:40 **Opening**

09:40-09:50 **Opening speech**
Prof. Minoru Inaba
Director of Energy Conversion Research Center, Doshisha University

Session 1: Transportation of Energies and Energy Conversion Systems (Chair: Prof. Y. Iwamoto)

09:50-10:10 **A fractional step lattice Boltzmann method for interfacial behaviors of magnetic multiphase flows**
X. Li[1], Z.-Q. Dong[1], X.-R. Zhuang[2], L.-P. Wang[1], X.-D. Niu[3], H. Yamaguchi[4], P. Yu[1]*
[1]Department of Mechanics and Aerospace Engineering, Southern University of Science and Technology, Shenzhen, China
[2]School of Mechanical and Electrical Engineering, Shenzhen Polytechnic, Shenzhen
[3]College of Engineering, Shantou University, Shantou, China
[4]Energy Conversion Research Center, Doshisha University, Kyoto, Japan

10:10-10:30 **Development of La0.6Sr0.4CoO3-δ anode for oxygen generation by molten salt electrolysis**

S. Tanaka[1], Y. Suzuki[1], T. Fukumoto[2], T. Goto[2]

[1]Office for Research Initiatives and Development, Doshisha University, Kyoto, Japan

[2]Faculty of Science and Engineering, Doshisha University, Kyoto, Japan

10:30-10:50 **Experiment study on the exhaust-gas heat exchanger for small and medium-sized fishing marine diesel engine**

G. Xi, X. Wang

Nantong Institute of Technology, Nantong, China

10:50-11:10 **Adsorbed CO_2 reduction technique using nonthermal plasma flows**

H. Yamasaki[1,2]* H. Wakimoto[2], T. Kuroki[1,2], M. Okubo[1,2]

[1]Department of Mechanical Engineering, Osaka Metropolitan University, Sakai, Japan

[2]Department of Mechanical Engineering, Osaka Prefecture University, Sakai, Japan

11:10-11:30 Coffee break

Session 2: Keynote lecture (Chair: Prof. H. Yamaguchi)

11:30-12:00 **Numerical simulations of ferrofluid droplets and surface instabilities in ferrofluid layers**

X.-D. Niu[1,2], J.-X. Zhou[1,2], H.-W. Xiao[1,2], A. Khan[1,2], M.-F. Chen[3], D.-C. Li[4], H. Yamaguchi[5]

[1]Key Laboratory of Intelligent Manufacturing Technology, Shantou University, Guangdong, China

[2]College of Engineering, Shantou University, Guangdong, China

[3]College of Physics and Electromechanics Engineering, Longyan University, Longyan, China

[4]Department of Mechanical Engineering, Tsinghua University, Beijing, China

[5]Energy Conversion Research Center, Doshisha University, Kyoto, Japan

12:00-13:30 Lunch

Session 3: Energy Conversion and Related Research Topics 1 (Chair: Prof. G. Xi)

13:30-13:50 **Medium scale distribution chains for hydrogen**

P. Nekså[1,2], M. Z. Saeed[2], S. Trædal[1], I. Snustad[1], I. Koshelkov[2] ,L. D. Jacobsen [2]

[1]SINTEF Energy Research, Trondheim, Norway

[2]NTNU, Department of Energy and process engineering, Trondheim, Norway

13:50-14:10 **Recycling of fisheries waste**

H. Kobatake, S. Tanaka, Y. Suzuki, T. Goto

Doshisha University, Kyotanabe, Japan

14:10-14:30 **Reduction in energy consumption in water purification technology with water**

T. Kuwahara

Department of Mechanical Engineering, Nippon Institute of Techinology, Saitama, Japan

14:30-14:50 **Heat transport characteristics of a closed two phase thermosyphon by water with air mixed (effect of the internal structure)**

T. Kitamura, T. Kubota, S. Shuchi

Department of Mechanical Engineering, Akita Prefectural University, Akita, Japan

14:50-15:10 Coffee break

Session 4: Keynote lecture (Chair: Prof. X.-D. Niu)

15:10-15:40 **Centrifugal convection in a bidisperse medium with chemical reaction**

S. Saravanan*, S. Vigneshwaran

Centre for Differential Equations and Fluid Dynamics, Department of Mathematics, Bharathiar University, Coimbatore, India

15:40-15:50 Announcement

18:00-20:30 **Banquet**

Kiyomizu Kyoto Higashiyama

(Shuttle bus from Kambaikan Building)

＜March 17, Friday＞

Session 5: Energy Storage and Transportation of CO_2 (Chair: Prof. P. Neksa)

09:30-09:50 **CERN CO_2 primary cooling – Project roadmap and first operational units**

P. Barroca[1], A. Hafner[1], B. Verlaat[2], P. Hanf[2]

[1]Norwegian University of Science and Technology (NTNU), Trondheim, Norway

[2]European Organization for Nuclear Research (CERN), Geneva, Switzerland

09:50-10:10 **Performance improvement strategies for CO_2 based experimental Rankine cycle for better sustainability**

S. Celik-Toker[1]*, O. Kizilkan[1], H. Yamaguchi[2]

[1]Department of Mechanical Engineering, Isparta University of Applied Sciences, Faculty of Technology, Isparta, Turkey

[2]Department of Mechanical Engineering, Doshisha University, Kyoto, Japan

10:10-10:30 **Transient boundary heat transfer analysis of a near-critical experimental chamber realized by pixelated phase-shifting interferometry**

Y.Z. Zhang[1,2], L. Chen[1,2,3]*, Q.X. Wu[1,2], Y. Kanda[4], A. Komiya[4], J.G. Zang[5], Y.P. Huang[5]

[1]*Institute of Engineering Thermophysics, Chinese Academy of Sciences, Beijing, China*

[2]*University of Chinese Academy of Sciences, Beijing, China*

[3]*Innovation Academy for Light-Duty Gas Turbine, Chinese Academy of Sciences, Beijing, China*

[4]*Institute of Fluid Science, Tohoku University, Sendai, Japan*

[5]*CNNC Key Laboratory on Nuclear Reactor Thermal Hydraulics, Nuclear Power Institute of China, Chengdu, China*

10:30-10:50 Coffee break

Session 6: Energy Conversion and Related Research Topics 2 (Chair: Prof. O. Kizilkan)

10:50-11:10 **One-step reduction process of silica to silicon by molten salt electrolysis**

Y. Suzuki[1], S. Tanaka[1], T. Goto[2]

[1]*Organization for Research Initiatives and Development, Doshisha University, Kyoto, Japan*

[2]*Department of Science of Environment and Mathematical Modeling Graduate School of Science and Engineering, Kyoto, Japan*

11:10-11:30 **PM removal characteristics in magnetic fluid filter with dielectric barrier discharge**

Y. Asaka, T. Kuwahara

Department of Mechanical Engineering, Nippon Institute of Technology, Saitama, Japan

11:30-11:50 **Energy harvesting using magnetorheological elastomer dispersing magnetically-hard magnetic particles**

Y. Iwamoto[1]*, T. Saiki[1], Y. Ido[1], T. Deguchi[2], T. Tazawa[2], H. Yamamoto[2]

[1]*Department of Electrical and Mechanical Engineering, Nagoya Institute of Technology, Nagoya, Japan*

[2]*KRI Inc., Kyoto, Japan*

11:50-12:10 **Status of clean cooling systems**

A. Hafner

Norwegian University of Science and Technology, Trondheim, Norway

12:10-13:30 Lunch

Session 7: Keynote lecture (Chair: Prof. T. Kuwahara)

13:30-14:00 **Research history for magnetic fluid and CO_2 heat pump system**

H. Yamaguchi

Energy Research Center, Department of Mechanical Engineering, Doshisha University, Kyoto, Japan

14:00-14:10 Short break

Closing ceremony (Chair: Prof. S. Shuchi)

14:10-14:20 **Closing speech**

Prof. Hiroshi Yamaguchi

Organizer of IWEC 2023, Doshisha University

14:20-14:30 **Closing**

General presentation

Presentation 15 min and Discussion 5 min

Keynote lecture

Presentation 25 min and Discussion 5 min

Please note:

- Eating and drinking inside the building is NOT allowed.

Proceedings of IWEC2023
The International Workshop of Energy Conversion
March 15-17, 2023, Kyoto, Japan

Paper No. IWEC2023-01

A fractional step lattice Boltzmann method for interfacial behaviors of magnetic multiphase flows

Xiang Li[1], Zhi-Qiang Dong[1], Xiao-Ru Zhuang[2], Lian-Ping Wang[1], Xiao-Dong Niu[3], Hiroshi Yamaguchi[4], Peng Yu[1,*]

[1]Department of Mechanics and Aerospace Engineering, Southern University of Science and Technology, Shenzhen 518055, China

[2]School of Mechanical and Electrical Engineering, Shenzhen Polytechnic, 518055, Shenzhen

[3]College of Engineering, Shantou University, 243 Daxue Road, Shantou 515063, China

[4]Energy Conversion Research Center, Doshisha University, Kyoto 630-0321, Japan

[*]E-mail: yup6@sustech.edu.cn (Peng Yu)

Keywords: lattice Boltzmann method, diffuse interface method, fractional step method, multiphase flows, ferrofluid

Abstract

In the present study, a robust fractional-step lattice Boltzmann (FSLB) method is proposed to simulate mass transfer phenomena in incompressible multiphase flows with complex interfacial behavior and large density contrast. The previous simplified lattice Boltzmann method recovers the continuity equation in first-order accuracy and reconstructs the corrector step by directly applying the complex central difference scheme on the macroscopic variables. However, the present FSLB method employs the Chapman-Enskog expansion analysis to reconstruct the convection and diffusion terms of the macroscopic governing equations, and uses the equilibrium and non-equilibrium distribution functions to establish the predictor-corrector step. The intermediate variables are predicted by the equilibrium distribution functions without the consideration of the source terms, and then the physical variables are corrected by the non-equilibrium distribution functions and the source terms without the evolution of the distribution functions. The reconstructed governing equations with fully second-order accuracy in both the predictor and corrector steps can be recovered through the C-E expansion analysis and the Taylor

series expansion analysis. The present FSLB method inherits the excellent performance of kinetic theory from the conventional LB method and the good numerical stability from the matured fractional-step method, which is validated by several benchmark problems, such as Laplace law, bubble merging, interfacial deformation under a magnetic field, Rayleigh-Taylor instability at Reynolds number of 3000, Kelvin-Helmholtz instability at Reynolds number of 5000, and bubble rising at density ratio of 1000. A good agreement between the present numerical results with the published numerical data verifies the capability and reliability of the present FSLB method to handle the multiphase problems with severe interfacial deformation and large density contrast. To further validate the capability of present numerical method, a magnetic field coupling fractional step lattice Boltzmann (FSLB) method is proposed to simulate the interfacial behaviors of magnetic multiphase flows under a uniform magnetic field. This work successfully performs the first rigorous numerical simulation on the Rosensweig instability, which accurately captures the spikes forming at the surface of a ferrofluid under an applied magnetic field. Moreover, for the first time we numerically reproduce the falling ferrofluid droplet impacted on the solid surface. Intriguingly, our simulation results reveal that the falling velocity of the ferrofluid droplet is slightly accelerated by the elongation, although the direction of the magnetic field is opposite to that of the gravity. All the results for the interfacial behavior and the magnetic interaction highlight the comparative stability, accuracy, and capability of the present magnetic field coupling FSLB method for simulating the problems of complex fluid dynamics associated with a severe interface deformation in magnetic multiphase flows.

Proceedings of IWEC2023
The International Workshop of Energy Conversion
March 15-17, 2023, Kyoto, Japan

Paper No. IWEC2023-02

Development of $La_{0.6}Sr_{0.4}CoO_{3-\delta}$ Anode for Oxygen Generation by Molten Salt Electrolysis

S. Tanaka,* and Y. Suzuki
Office for Research Initiatives and Development, Doshisha University, Kyoto, Japan
*corresponding author, E-mail: stanaka@mail.doshisha.ac.jp

T. Fukumoto and T. Goto
Faculty of Science and Engineering, Doshisha University, Kyoto, Japan

ABSTRACT

For realizing carbon-free electrolysis method, the development of inert anodes, which have good resistance to oxidation and high conductivity. In this research, a perovskite oxide of $La_{0.6}Sr_{0.4}CoO_{3-\delta}$ was applied to the oxygen evolution anodes in molten salt electrolysis. As results of electrochemical experiments with chemical analysis, oxygen evolution from the $La_{0.6}Sr_{0.4}CoO_{3-\delta}$ anodes. Moreover, the corrosion and chemical structure change of anodes were small enough to be used as an inert anode.

INTRODUCTION

Carbon dioxide gas (COx) is generated on the graphite anode in electrowinning of metals in molten salt using metal oxides as raw materials, such as the Hall–Héroult process, the practical method of aluminum smelting. Emission of carbon dioxide causes enormous effects on the environment. For realizing carbon-free molten salt electrolysis process, inert anodes have been researched [1-4]. The inert anodes are undissolvable in molten salt and unreactable in the electrolysis process. Therefore, instead of using the chemical energy of carbon, only electricity is consumed in this process by applying the inert anodes. The difficulty of inert anodes development is the multiple requirements for its material as below[5].

- a low corrosion rate
- good resistance to fluorination and produced oxygen
- high conductivity for low current efficiency

In the previous research, many metals have been tested for the inert anode material: Pt, Ni, Cu–Al–Ni–Fe alloy and Cu-Ni-Fe-O alloy. However, the resistance to fluorination and produced oxygen was not enough low for usage as inert anodes. The development of inert anode material should be conducted for realizing the carbon-free electrolysis.

We have been researching perovskite oxides for the development of inert anodes. These oxides have unique characteristics: relatively high conductivity similar to metals and good oxidation resistance because the material is made from metal oxides. Therefore, the perovskite oxides should be suitable to the inert anode materials. In this research, $La_{0.6}Sr_{0.4}CoO_{3-\delta}$ was applied to the material of oxygen evolution inert anodes. The $La_{0.6}Sr_{0.4}CoO_{3-\delta}$ has high conductivity similar to metals to increase current density of oxygen evolution in the molten salt electrolysis [6]. The results of $La_{0.6}Sr_{0.4}CoO_{3-\delta}$ anodes production and electrolysis experiments in molten salts with CaO for resources of oxide ion would be presented, and the propriety of applying $La_{0.6}Sr_{0.4}CoO_{3-\delta}$ to inert anodes material would be discussed.

EXPERIMENTAL METHODS

Production process of $La_{0.6}Sr_{0.4}CoO_{3-\delta}$ anodes

The $La_{0.6}Sr_{0.4}CoO_{3-\delta}$ anodes were prepared by a solid-state reaction method. Raw powders of La_2O_3, SrO, and Co_3O_4 were mixed and pressed into pellets. These produced pellets were heated to synthesize $La_{0.6}Sr_{0.4}CoO_{3-\delta}$. The synthesized samples were ground and pressed into pellets again. The $La_{0.6}Sr_{0.4}CoO_{3-\delta}$ pellets were sintered in an electric furnace. After the production process, X-ray diffraction (XRD) analysis of samples was conducted for evaluation of adequacy of the production method. Moreover, the conductivities produced $La_{0.6}Sr_{0.4}CoO_{3-\delta}$ anodes were measured by a four-terminal method.

Process of molten salt electrolysis

The molten salt electrolysis with molten salts of LiCl-$CaCl_2$ was conducted at a temperature of 600°C. The percentage of CaO in the molten salt was 8mol%, which was over the CaO solubility into LiCl-$CaCl_2$ melts: 7mol%. For evaluating the anode characteristics, cyclic voltammetry (CV) and chronopotentiometry were conducted by using a potentiostat/galvanostat. All measurements were performed using the three-electrode method under a dry Ar atmosphere. The working electrode was the produced $La_{0.6}Sr_{0.4}CoO_{3-\delta}$ anode. The counter electrode was a nickel plate, and reference electrode was Ag/AgCl in an alumina tube. The corrosion rate

of the $La_{0.6}Sr_{0.4}CoO_{3-\delta}$ anode was calculated from the mass measurement results before and after the chronopotentiometry. For evaluating the resistance to fluorination and produced oxygen of anodes, ICP-AES analysis of molten salts and XRD analysis of $La_{0.6}Sr_{0.4}CoO_{3-\delta}$ anodes were conducted. The chemical composition of produced gas in the molten salt electrolysis was analyzed by gas chromatography (GC).

RESULTS AND DISCUSSION

Measured characteristics of $La_{0.6}Sr_{0.4}CoO_{3-\delta}$ anodes

The XRD analysis was conducted before and after the sintering process. The analysis results showed the produced material was single-phase of $La_{0.6}Sr_{0.4}CoO_{3-\delta}$, which demonstrated the production process of a solid-state reaction method was successfully conducted.

The measurement results show that the conductivity of $La_{0.6}Sr_{0.4}CoO_{3-\delta}$ anode decreased with temperature, which was consistent with previous research of $La_{0.6}Sr_{0.4}CoO_{3-\delta}$ production [6]. The obtained conductivity of $La_{0.6}Sr_{0.4}CoO_{3-\delta}$ at 600 °C was 1.0×10^5 S/m, which was comparable with that of carbon: 2.0×10^5 S/m [7]. Therefore, the characteristic measurements demonstrate that the produced $La_{0.6}Sr_{0.4}CoO_{3-\delta}$ anode had high conductivity.

Oxygen evolution performance of $La_{0.6}Sr_{0.4}CoO_{3-\delta}$ anodes in molten salt electrolysis

Figure 1 presents the results of CV measurements with a working electrode of the $La_{0.6}Sr_{0.4}CoO_{3-\delta}$ anode. The current density increased drastically at a potential of 2.9 V (vs. Ca(II)/Ca). The current density at the peak increased with the amount of added CaO. These results suggest that the increase of current density means the oxygen evolution was occurred at the $La_{0.6}Sr_{0.4}CoO_{3-\delta}$ anode by the electrolysis.

Secondly, the chronopotentiometry measurement was conducted at a current density of 120 mA/cm^2. Figure 2 shows the result of chronopotentiometry with a working electrode of the $La_{0.6}Sr_{0.4}CoO_{3-\delta}$ anode. The potential was maintained at 3.0–3.1 V during the electrolysis in 15 h. The amount increase of oxygen in the electrolysis was detected by GC of the produced gas. This result indicates that oxygen evolution was occurred at a potential range of 3.0–3.1 V, which was consistent with the range of current density increase in the CV in Fig. 1. Therefore, the measurement results demonstrate that the oxygen evolution could be conducted by using the $La_{0.6}Sr_{0.4}CoO_{3-\delta}$ anode.

The corrosion rate of the $La_{0.6}Sr_{0.4}CoO_{3-\delta}$ anode was 1.3×10^3 g/cm^2 h. This result means that the $La_{0.6}Sr_{0.4}CoO_{3-\delta}$ anode was inert because the value of corrosion rate was less than the standard value of inert anodes: 1.5×10^3 g/cm^2 h. The structure condition of the $La_{0.6}Sr_{0.4}CoO_{3-\delta}$ anode was measured by the XRD analysis. The analysis results show that the surface kept the state of $La_{0.6}Sr_{0.4}CoO_{3-\delta}$, which indicates the anode was not damaged drastically in the molten salt electrolysis. Moreover, the change of chemical composition of molten salts in the electrolysis was measured by the ICP-AES. The results show that small amounts of anode composition material were dissolved into the molten salts: La: 9.1 mg, Sr: 3.9 mg, Co: 2.5 mg. These results of chemical analysis demonstrate that the $La_{0.6}Sr_{0.4}CoO_{3-\delta}$ anode was inert in the molten salt electrolysis for oxygen evolution.

For further improvement of inert anodes, the ratio of Sr in anodes should be optimized. The doped Sr atoms in the $La_{0.6}Sr_{0.4}CoO_{3-\delta}$ anode could be unstable, which could be one cause of the dissolution of $La_{0.6}Sr_{0.4}CoO_{3-\delta}$ anodes into molten salts in the electrolysis process.

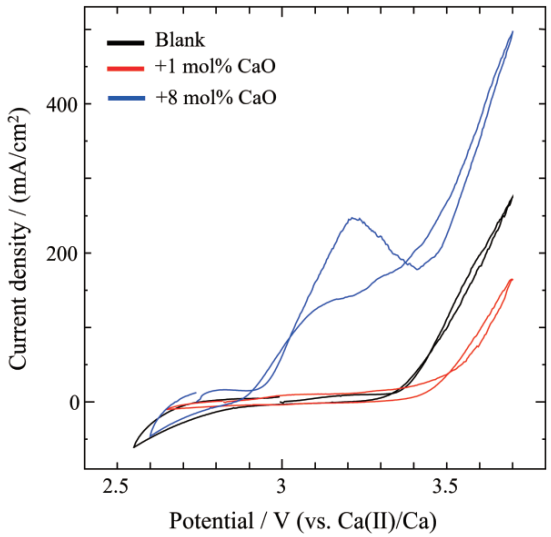

Fig. 1 Cyclic voltammograms recorded from a $La_{0.6}Sr_{0.4}CoO_{3-\delta}$ anode in the molten LiCl-$CaCl_2$-CaO at 600 °C.

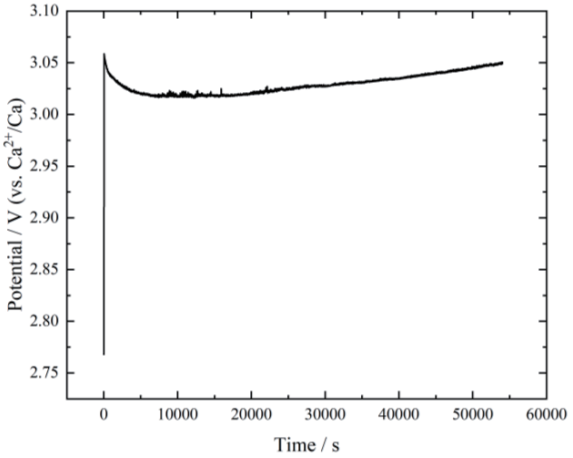

Fig. 2 Potential-time plots of the electrolysis at a current density of 120 mA/cm^2.

CONCLUSIONS

We applied $La_{0.6}Sr_{0.4}CoO_{3-\delta}$ to the oxygen evolution anodes in the molten salt electrolysis with salts of LiCl-$CaCl_2$-CaO at 600 °C. The oxygen evolution at the $La_{0.6}Sr_{0.4}CoO_{3-\delta}$ anodes in the electrolysis was demonstrated from the experimental results of cyclic voltammogram and chronopotentiometry with chemical analysis of produced gas by

gas chromatography. The corrosion rate was small enough to be used as an inert anode, and the drastic structure change of anodes was not detected. The $La_{0.6}Sr_{0.4}CoO_{3-\delta}$ anode is highly anticipated as inert anodes for oxygen evolution in the molten salt electrolysis.

REFERENCES

[1] N. Masuko, K Masio, 2015, Present aluminum smelting technology, Journal of the Japan Institute of Light Metals, Vol. 65-2, pp. 66–71.

[2] K. Xie, Z Shi, J Xu, X Hu, B Gao, Z. Wang, 2017, Aluminothermic Reduction-Molten Salt Electrolysis Using Inert Anode for Oxygen and Al-Base Alloy Extraction from Lunar Soil Simulant, Journal of Metals, Vol. 89-10, pp. 1963–1969.

[3] W. Wei, S. Geng, D. Xie, F. Wang, 2019, High temperature oxidation and corrosion behaviours of Ni–Fe–Cr alloys as inert anode for aluminum electrolysis, Corrosion Science, Vol. 157, 2019, pp. 382–391.

[4] S. Helle, B. Davis, D. Guay, L. Roue, 2013, Ball-Milled (Cu-Ni-Fe + Fe2O3) Composite as Inert Anode for Aluminum Electrolysis, Journal of the Electrochemical Society, Vol. 160-6, pp. 55–59.

[5] S. Helle, B. Davis, D. Guay, L. Roué, 2010, Electrolytic Production of Aluminum Using Mechanically Alloyed Cu–Al–Ni–Fe-Based Materials as Inert Anodes, Journal of The Electrochemical Society, Vol. 157-11, pp. 173–179.

[6] O. Gwon, S. Yoo, J. Shin, G. Kim, 2014, Optimization of LaSrCoO3 perovskite cathodes for intermediate temperature solid oxide fuel cells through the analysis of crystal structure and electrical properties, International journal of hydrogen energy, Vol. 39, pp. 20806–20811.

Proceedings of IWEC2023
The International Workshop of Energy Conversion
March 15-17, 2023, Kyoto, Japan

Paper No. IWEC2023-03

EXPERIMENT STUDY ON THE EXHAUST-GAS HEAT EXCHANGER FOR SMALL AND MEDIUM-SIZED FISHING MARINE DIESEL ENGINE

Guannan XI and Xiaomei Wang
Nantong Institute of Technology, Nantong, 226019, China
Email Address: guannanxi@ntit.edu.ccn

ABSTRACT

This paper aims to design a special exchanger to recover the exhaust gas heat of marine diesel engines used in small and medium-sized fishing vessels. A new exhaust-gas heat exchanger of fins and tube, with a reinforced heat transfer tube section, unequal spacing fins, a mixing zone between the fin groups and four routes tube bundle, was designed. Numerical simulations were also used to provide reference information for structural design. Experiments were carried out for exhaust gas waste heat recovery from a marine diesel engine in an engine test bench utilizing the heat exchanger. The experimental results show that the difference between heat absorption by water and heat reduction of exhaust gas is less than 6.5%. After the water flow rate was adjusted, the exhaust gas waste heat recovery efficiency was higher than 70%, and the exhaust-gas heat exchanger's outlet water temperature was 55°C–85°C at different engine loads. The heat recovery from the exhaust gas of a marine diesel engine meets the requirement to drive a membrane desalination device to produce fresh water in small and medium-sized fishing vessels.

INTRODUCTION

As the main power source of the ships, marine diesel engines have a thermal efficiency of 40% to 45% [1], exhaust gas heat accounts for 20%–35% of the total calorific value of diesel, and the exhaust gas temperature is 200°C–400°C under full working condition [2]. On the other hand, the offshore fishing cycle of fishers driving small and medium-sized fishing vessels to sea is about 7–10 days. Sometimes, fishing will take another several days if the vessel's cabin is not fully loaded with fish. When the ship is going out to the sea, a lot of freshwater is carried for fishers living on the sea to drink. However, the fresh water easily deteriorates over longer term storage, especially during the summer, and the metamorphic water as a drink is harmful to the fishers' health. To solve this problem then, seawater desalination devices need to be installed in small and medium-sized fishing vessels. Membrane distillation is such a type of device. It needs only 55°C–85°C hot water as a heat source to drive its water production parts [3] and produces 10L/h fresh water. Many types of research have previously been carried out on the use of waste heat from diesel engines. Lu et al. [4] improved the Coefficient of Performance (COP) of three sorption refrigerators driven by diesel exhaust gas with a pressurized thermal and multi-step recovery process. Hou et al. [5] proposed technology of a combined supercritical CO_2 recompression and heat recovery cycle. This technology applied to the waste heat recovery of marine gas turbines and has the advantages of high waste heat utilization, compactness, and low cost. Shafieian et al. [6] presented a new multifunctional desalination, cooling and air conditioning recovery system to recover the exhaust gas from a submarine engine and the waste heat from the cooling water. The system was mathematically modeled based on the actual thermophysical parameters and the engine's exhaust gas.

There were few studies on producing fresh water by using the waste heat of small and medium-sized fishing vessels. Large vessels usually use a Waste Heat Recovery (WHR) steam plant to recover heat from the exhaust gas, characterized mainly by a Heat Recovery Steam Generator (HRSG). This paper aims to obtain the outlet water of the exhaust-gas heat exchanger with a temperature of 55°C–85°C, and a heat larger than 38kW [7]. The heat of 38kW is a minimum heat source to drive a membrane distillation producing 10L/h fresh water. As for heat recovery efficiency of the exhaust gas, it is about 70%. In this way, the waste heat recovery of small and medium-sized fishing vessel exhaust gas becomes high practical application values.

EXHAUST GAS WASTE HEAT FROM MARINE DIESEL ENGINE

Test Device and Method

Fig. 1 shows a marine diesel engine test device used in the experiment. With the exhaust gas temperature monitoring point E, as shown in Fig. 1, at the rear of the turbine, can provide real-time monitoring of the exhaust gas outlet temperature of the marine diesel engine under different loads. If the internal circulating water temperature is too high, the volume flow rate of the external circulating water can be increased to take away more heat from the engine. Water temperature monitoring points are set up at four points, that is, a point, the inlet of the external circulating circuit, b point, the outlet of the external circulating circuit, c point, the inlet of the internal plate heat exchanger, and d point, the outlet of internal plate heat exchanger with the internal circulating water circuit. Table 1 shows the marine diesel engine-specific operating parameters. The marine diesel engine to be tested is four-strokes, and 6-cylinders and the rated power and speed are 295kW and 1500rpm, respectively.

The marine diesel engine rotation speed and load are controlled by an NCK2000 cabinet. One PT-1000 sensor is used to measure the exhaust gas temperature at point E, and four PT-100 sensors are used to measure the water temperatures at points a, b, c to d. A CKLWGYC-D40 turbine flowmeter and DN50-200 insertion exhaust gas flowmeter are used to measure the external circulating water flow rate and exhaust gas mass flow rate, respectively. The specific parameters of the experimental equipment are shown in Table 2.

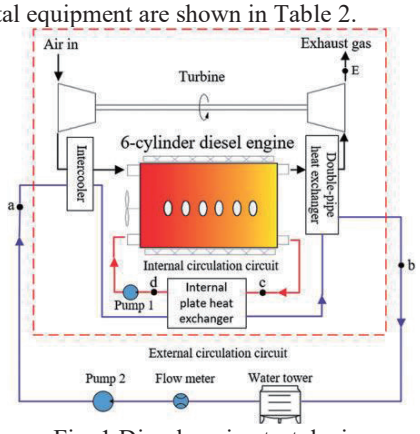

Fig. 1 Diesel engine test device

Table 1 Main technical parameters of marine diesel engine.

Parameters	Numerical values
Engine type	Inline, water-cooled, four-stroke, supercharged intercooled, 6-cylinder
Bore × Stroke (mm)	138×168
Total stroke volume (L)	15
Compression ratio	17
Rated speed (rpm)	1500
Rated power (kW)	295
Maximum power (kW)	324.5
Fuel consumption rate (g/kW·h)	≤232

Table 2 Main parameters of the equipment.

Parameters	Range	Accuracy
NCK2000 cabinet	500-7500rpm	±10rpm
PT-100 sensor	-50-200°C	±0.1°C
PT-1000 sensor	0-1300°C	±0.5°C
CKLWGYC-D40 flowmeter	0-20m³/h	±0.5%
DN50-200 flowmeter	11-11310m³/h	±1.5%

Test result and discussion

As shown in Table 3, when the external circulating water flow rate is 10m³/h and the marine diesel engine load is from 60% to 100%, the internal circulating water temperature at point c is higher than 80°C, which is not conducive to the long-term operation of marine diesel engine [8]. When the external circulating water flow rate is 13m³/h and 18m³/h, the internal circulating water temperature at point c under different loads is lower than the limit temperature of stable operation 85°C. Compared with 18m³/h, external circulating water carries less exhaust gas heat at the flow rate of 13m³/h through a double-pipe heat exchanger, and this leads to a higher exhaust gas outlet temperature of marine diesel engines, which is conducive to recovering more exhaust gas heat.

Table 3 Test temperatures of exhaust gas and cooling water.

Load (%)	External circulation water (m³/h)					
	10	13	18	10	13	18
	Turbine outlet temperature at E point (°C)			Water temperature at c point (°C)		
100	374	337	330	83	75	72
90	354	322	320	82	75	71
80	336	309	303	82	74	70
70	318	294	284	81	74	70
60	297	275	268	81	73	69
50	276	257	247	80	72	68
25	211	201	184	76	70	65

(External circulation water flow rate is 10m³/h, 13m³/h, 18m³/h; turbine outlet temperature at point E; water temperature at point c, which is the inlet of internal plate heat exchanger in internal water circuit)

Fig. 2 depicts the mass flow rate and volume flow rate of exhaust gas under 25-100% load of diesel engine, and the velocity of exhaust gas in the exhaust gas outlet pipe. As a load of marine diesel engine increases, exhaust gas flow rate and its velocity increases linearly. The pipe's mass flow rate, volume flow rate, and velocity are about 1030-1750kg/h, 825-1365m³/h, and 28-50m/s. Typically, the exhaust temperature is between 200°C and 400°C, and the exhaust gas pressure is slightly higher than atmospheric pressure. Therefore, the exhaust gas can be treated as a mixture of an ideal gas [9]. According to the formula (1), the recoverable heat of exhaust gas can be calculated:

$$Q = C_{p1}\rho_1 V_1(T_1 - T_2) = q_{m1}C_{p1}(T_1 - T_2) \quad (1)$$

where Q is the recovery heat of exhaust gas, C_{p1} for the average specific heat capacity of the exhaust gas when the exhaust gas temperature is 200°C to 400°C, ρ_1 for the exhaust gas density, V_1 and q_{m1} for the exhaust gas volume flow rate and mass flow rate, T_1 and T_2 for the exhaust gas temperature and lab room air temperature, respectively (The lab room air temperature T_2 is 15°C).

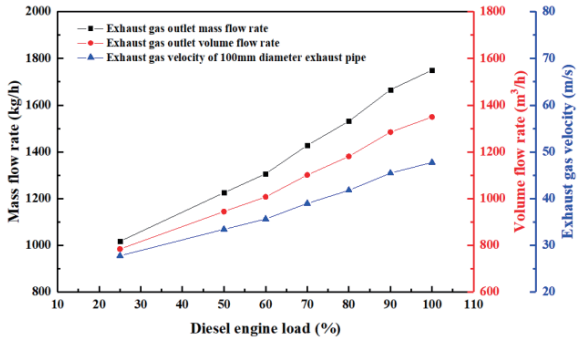

Fig. 2 Exhaust gas mass flow, volume flow, and flow rate

In Fig. 2, the external circulating water flow rate of the marine diesel engine is 13m³/h. As the load of the marine diesel engine increases, the minimum recoverable heat of exhaust gas is calculated at about 58kW, and the maximum recoverable heat of exhaust gas is calculated at about 172kW, based on the exhaust gas temperature at the outlet of the turbine measuring at point E, the exhaust gas mass flow rate and volume flow rate.

An additional seawater heat exchanger is added to transfer heat to the membrane desalination device from the hot water of the exhaust-gas heat exchanger. The membrane desalination device to be driven requires 30kW of heat. The seawater heat exchanger's heat exchange efficiency is about 80% [10], indicating that the heat recovery from exhaust gas needs to be greater than 38kW. The inlet water temperature of the exhaust-gas heat exchanger is 20°C, and the outlet water temperature needs to reach 55-85°C Therefore, the water temperature of the seawater desalination membrane module circuit can be 50-80°C by the seawater heat exchanger. The inlet and outlet water temperatures of the seawater heat exchanger are shown in Fig. 3.

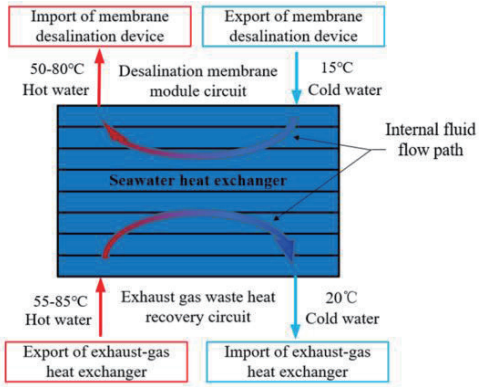

Fig. 3 The inlet and outlet water temperature of the seawater heat exchanger

DESIGN OF EXHAUST-GAS HEAT EXCHANGER

Heat transfer area calculation

The method of the exhaust gas heat recovery begins with the transferring of exhaust gas heat to the circulating water in the heat exchanger. The fin and tube structure heat exchanger is suitable for gas-liquid heat transfer [11] and has a large heat transfer area in a compact space. The windward surface of the exhaust gas entering the heat exchanger is small, and the exhaust gas flow rate is high. The exhaust gas enters the heat exchanger unevenly, which reduces the recovery rate of exhaust gas heat. The 2D model of the exhaust-gas heat exchanger is shown in Fig. 4. A reinforced heat transfer tube section is placed before the heat exchanger to disturb the exhaust gas. The fin part adopts an unequal spacing arrangement with a dense middle and sparse sides, which can improve exhaust gas resistance in the heat exchanger's middle. There is a mixing zone between the two fins group with an interval of 100 mm so that the exhaust gas is evenly mixed when passing through this particular zone.

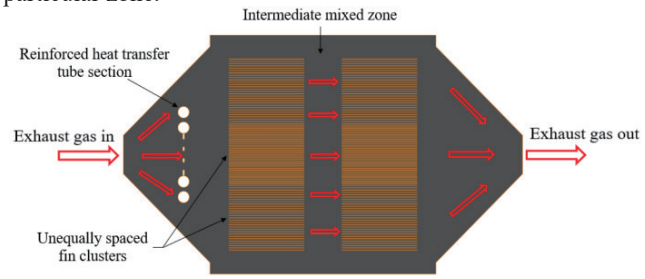

Fig. 4 2D model of exhaust-gas heat exchanger

The flow medium in heat exchanger consists of hot fluid and cold fluid. The hot fluid is high-temperature exhaust gas, and the cold fluid is liquid water. The maximum recoverable heat Q from the exhaust gas of this marine diesel engine is approximately 172kW. This paper calculates the heat transfer area by the logarithmic temperature difference method [12].

Logarithmic temperature difference of counter-flow heat exchanger:

$$\Delta Tm = \frac{[(T_{Air,in}-T_{W,out})-(T_{Air,out}-T_{W,in})]}{ln\frac{(T_{Air,in}-T_{W,out})}{(T_{Air,out}-T_{W,in})}} \quad (2)$$

The overall heat transfer coefficient of the heat exchanger can be calculated as follow:

$$K = [\frac{1}{h_o} + r_0 + \left(r_i + \frac{1}{h_i}\right)\frac{A_0}{A_i}]^{-1} \quad (3)$$

Heat transfer area:

$$A = \frac{Q}{K\Delta Tm} \quad (4)$$

where ΔTm is the logarithmic temperature difference, $T_{Air,in}$ and $T_{Air,out}$ are the inlet and outlet exhaust gas temperature, $T_{W,in}$ and $T_{W,out}$ are the inlet and outlet water temperature of the heat exchanger, and K is the heat transfer coefficient, h_0 is the heat transfer coefficient on the outside of the tube (85.5W/m²·K), h_i is the heat transfer coefficient on the inside of the tube (7353W/m²·K), r_0 is the fouling factor on the outside of the tube (0-0.000172m²·K/W), r_i is the fouling factor on the inside of the tube (0-0.0004m²·K/W), A_0 is the outside surface area, A_i is the inside surface area. K is about 60-80W/m²K; according to the equations, the heat transfer area is 15.5-20.7m². Considering 10% margin for the actual design area then, the final heat transfer area A is approximately equal to 23m².

Analysis of internal flow field in heat exchanger

Control equation

In order to verify the rationality of the 2D model structure and provide reference information for the structural design of

the exhaust-gas heat exchanger, this paper uses CFD (fluent) software to analyze the internal flow field of the heat exchanger model. Due to the symmetry inside the heat exchanger, half of the heat exchanger is taken for flow field simulation analysis. The numerical calculations for this study will use $k-\varepsilon$ turbulence model: the fluid is incompressible Newtonian fluid; the fluid flow is two-dimensional. The control equations are as follows:

Continuity equation:

$$\frac{\partial u_i}{\partial x_i} = 0 \quad (5)$$

Momentum equation:

$$u_j \frac{\partial u_i}{\partial x_i} = f_i - \frac{l}{\rho}\frac{\partial p}{\partial x_i} + \frac{\partial}{\partial x_j}\left[(v + v_t)\left(\frac{\partial u_i}{\partial x_j} + \frac{\partial u_j}{\partial x_i}\right)\right] \quad (6)$$

Turbulent kinetic energy k equation:

$$\frac{\partial u_i k}{\partial x_i} - \frac{\partial}{\partial x_i}\left[\left(v + \frac{v_t}{\sigma_k}\right)\frac{\partial k}{\partial x_i}\right] = P_r - \varepsilon \quad (7)$$

Turbulent kinetic energy dissipation rate ε equation:

$$\frac{\partial u_i \varepsilon}{\partial x_i} - \frac{\partial}{\partial x_i}\left[\left(v + \frac{v_t}{\sigma_\varepsilon}\right)\frac{\partial \varepsilon}{\partial x_i}\right] = \frac{C_{\varepsilon 1}\cdot\varepsilon\cdot P_r - C_{\varepsilon 2}\cdot\varepsilon^2}{k} \quad (8)$$

$C_{\varepsilon 1}$=1.44, $C_{\varepsilon 2}$=1.92, σ_k=1.0, σ_ε=1.3, P_r is a turbulent kinetic energy generation term, v_t is turbulent viscosity coefficient.

Calculation area and boundary conditions

The inlet condition of the heat exchanger model adopts velocity inlet condition, that is, given velocity, turbulent kinetic energy, and dissipation rate. The heat exchanger inlet exhaust gas velocity is set to 50m/s, and the temperature is set to 350°C. In addition, due to the range of exhaust gas Reynolds number between the simulated fin and tube is 2.8×10^4-5×10^4, which belongs to high Reynolds number turbulence, and the $k-\varepsilon$ model is selected. Since a heat transfer process accompanies the exhaust gas between the fin and tube during the flow process, the energy equation should be turned on in CFD (fluent) software during the simulation.

Mesh division and flow field

The mesh between the exhaust-gas heat exchanger with reinforced heat transfer tube section and the without is shown in Fig. 5. The round hole at the front of the mesh is the reinforced heat transfer tube section. The mesh numbers of the exhaust-gas heat exchanger with and the without reinforced heat transfer tube section taken into simulation are 541,659 and 534,670.

(a) Without reinforced heat transfer tube section

(b) Equipped with reinforced heat transfer tube section

Fig. 5 The mesh of the heat exchanger

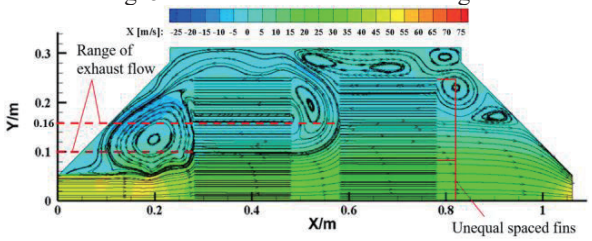

(a) Without reinforced heat transfer tube section

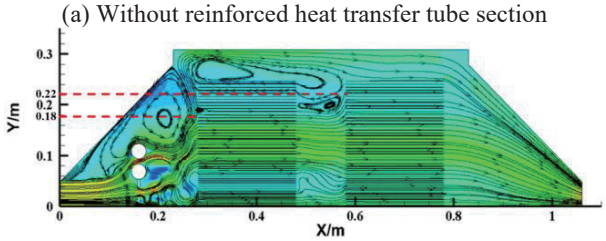

(b) Equipped with reinforced heat transfer tube section

Fig. 6 Distribution of internal flow field of the heat exchanger

Fig. 6 shows that distribution of internal flow field of the heat exchanger. From Fig. 6 (a) we can see that some of the exhaust gas is diffused to flow into the outer fins due to the resistance of the unequal-spaced fins, but the range of exhaust flow is small. Fig. 6 (b) depicts that the exhaust gas is disturbed by the reinforced heat transfer tube section, and exhaust gas velocity is slowed down. Due to the resistance of the first set of unequal-spaced fins, some of the exhaust gas is diffused to flow into the outer fins and enters the fin and tube section more evenly. A large number of fins are involved in heat transfer, and the dead zone vortex area between fins is small. Then the exhaust gas is thoroughly mixed in the mixing zone between the two sets of fins, which improves the uniformity of the flow field distribution. The exhaust gas is further diffused by the second set of unequal-spaced fins after passing through the mixing zone, which will lead to the heat transfer of the second set of fins as more uniform, and more fins will participate in the heat transfer. In summary, the exhaust gas flow field at the middle and outer fins of the heat exchanger is more evenly distributed, and the heat exchanger structure is reasonable.

Structure design of heat exchanger

The 3D structure of the heat exchanger is shown in Fig. 7. The inlet area and the windward area of the exhaust-gas heat exchanger are small, and the structure of the heat exchanger is reformed to make the exhaust gas diffusion more evenly. The exhaust gas first passes through the reinforced heat transfer tube section for scrambling, then sweeps through the first row of unequally spaced fins, enhancing the heat transfer due to the resistance effect on the exhaust gas. The exhaust gas then enters the intermediate mixing zone for fluid heat mixing, enhancing the heat transfer in the rear part of the fins as well. These are four characters in the exhaust-gas heat exchanger:

(1) A reinforced tube unit with a 225mm peripheral dimension is added at 115mm in front of the fin and tube heat exchanger unit, which can disturb the flow of exhaust gas and heat the water from four distributors uniformly.

(2) The fin part adopts an unequal spacing arrangement to increase the resistance of the middle fins to the exhaust gas.

(3) A mixing zone is set up between the fin groups to enhance the heat transfer effect of the rear half of the fins.

(4) The cold fluid in the tube bundle is divided into four routes, which can enhance the uniformity of heat transfer.

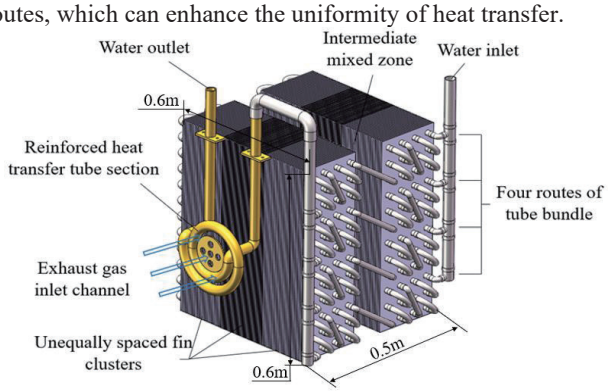

Fig. 7 3D structure of the heat exchanger

BUILDING THE EXPERIMENTAL SYSTEM BENCH AND ANALYSIS OF EXPERIMENTAL RESULTS

Systematic experimental loop construction

Fig. 8 depicts the flow direction of exhaust gas as well as that of water of the exhaust-gas heat exchanger at the experimental site. Fig. 9 shows an exhaust gas heat recovery system and seawater desalination system, which are added to the marine diesel engine test device. The circulating water flow rate of the exhaust gas heat recovery system can be controlled by the electric butterfly valve, which is from 1m³/h to 3m³/h. The exhaust gas heat is transferred to the exhaust gas heat recovery system's circulating water by the exhaust-gas heat exchanger. When the circulating water temperature of the exhaust gas heat recovery system meets the requirements of the seawater desalination membrane module, the seawater desalination circulating water loop starts to operate. The heat is transferred to the seawater desalination membrane device through a seawater heat exchanger, and then the freshwater is produced and stored in the tank. The temperature measuring points are set up at F point, the exhaust gas after heat recovery, at g and h points, and the inlet and outlet water temperature of the exhaust-gas heat exchanger, respectively.

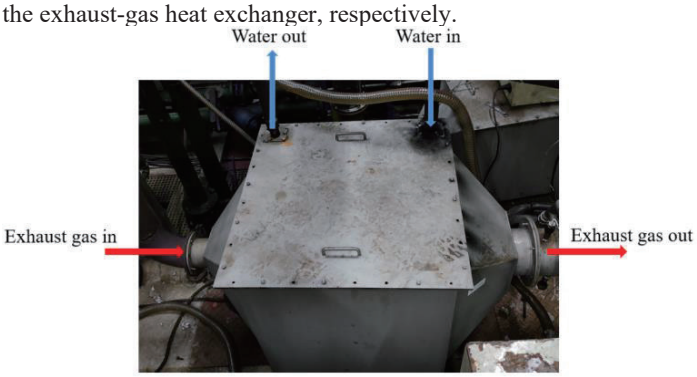

Fig. 8 Exhaust-gas heat exchanger at the experimental site

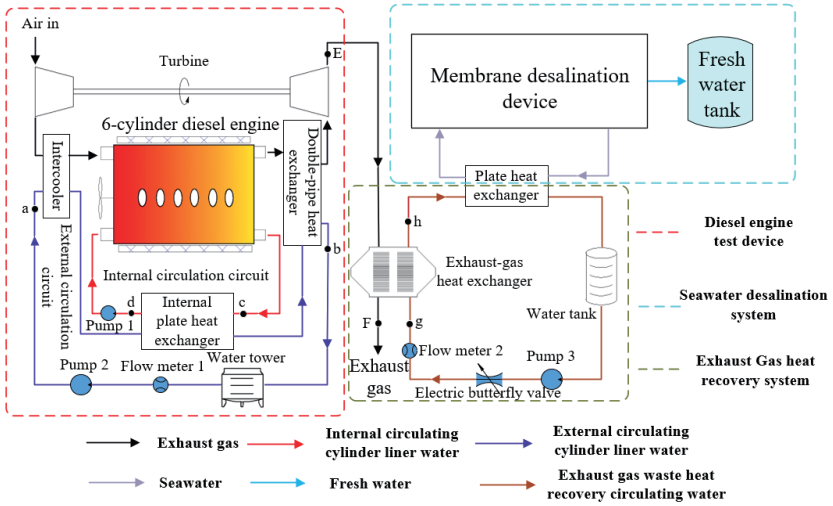

Fig. 9 Circulation loop diagram of the improved experimental bench system

Experimental results and discussion

Exhaust gas temperature and water temperature in the exchanger at different loads

The temperature difference between exhaust gas and that of circulating water through the exhaust-gas heat exchanger are shown in Fig. 10. As the marine diesel engine load increases, the temperature difference between the inlet and outlet circulating water and exhaust gas through the exhaust-gas heat exchanger increase linearly. With the circulating water flow rate reducing and the marine diesel engine load ranging from 60% to 100%, the increase of the exhaust gas temperature difference becomes smaller. This indicates that the waste heat recovery efficiency will be reduced at high diesel engine load, which will be more obvious as the circulating water flow rate is reduced. When the circulating water flow rate of the heat exchanger is 1m³/h and the marine diesel engine load is at 100%, the maximum water temperature difference is about 75°C, and the exhaust gas temperature difference is about

196°C. When the circulating water flow rate of the heat exchanger is 3m³/h, the water temperature difference is about 35°C, and the exhaust gas temperature difference is about 247°C. If the circulating water flow rate of the exhaust-gas heat exchanger increases more, the exhaust gas temperature difference becomes more significant, and the water temperature difference becomes smaller.

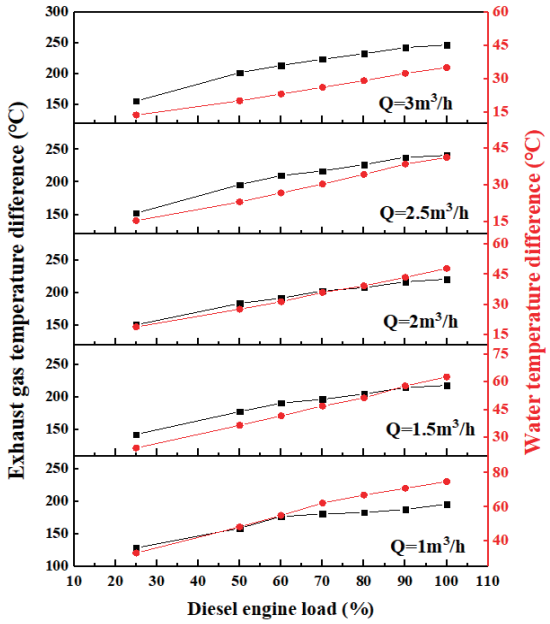

Fig. 10 Temperature difference of exhaust gas and water in heat exchanger

Heat difference between the exhaust gas side and water side

According to the average specific heat capacity of the exhaust gas, the recovered heat of the exhaust gas, Q_{gas}, can be calculated. The specific heat capacity of circulating water is 4.2kJ/kg·K, and the heat recovery, Q_{water}, from the exhaust gas can be calculated. The equations are as follows：

$$Q_{gas} = C_{p1}\rho_1 V_1 (T_1 - T_5) = q_{m1} C_{p1} (T_1 - T_5) \quad (9)$$

$$Q_{water} = C_{p2}\rho_2 V_2 (T_3 - T_4) \quad (10)$$

where C_{p2} for the specific heat capacity of circulating water, ρ_2 for the circulating water density, V_2 for the circulating water flow rate, T_3 and T_4 for the inlet and outlet circulating water temperature of the exhaust-gas heat exchanger, T_5 for the outlet exhaust gas temperature of exhaust-gas heat exchangers.

Fig. 11 depicts the comparison of heat difference between Q_{water} and Q_{gas} in the exhaust-gas heat exchanger. The formula is as follow:

$$\delta = \left(1 - \frac{Q_{water}}{Q_{gas}}\right) 100\% \quad (11)$$

As a load of the marine diesel engine increases, the heat of the circulating water and the exhaust gas increases, and the heat of the circulating water side is a little bit less than the exhaust gas side. This means there is a heat loss in the exhaust-gas heat exchanger.

When the circulating water flow rate is 1m³/h, the proportion of heat difference between the circulating water side and exhaust gas side is large. This means that the heat loss of the exhaust gas side is higher when the circulating water flow rate is small. When the circulating water flow rate is 3m³/h, the proportion of heat difference between the circulating water side and exhaust gas side becomes small. This means that the heat loss rate of the exhaust gas side is low when the circulating water flow rate is high. Based on the study of these contents, it can provide a reference for improving the heat recovery rate of the exhaust-gas heat exchanger.

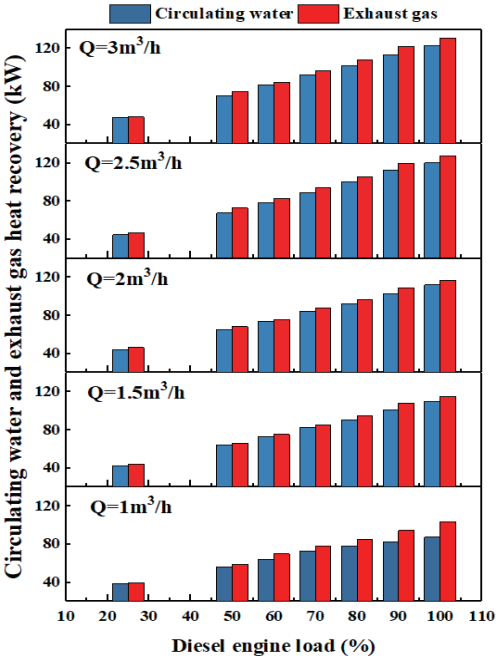

Fig. 11 Comparison of heat difference between the exhaust gas and water sides

The relationship between the heat difference rate δ and the circulating water flow rate is shown in Fig. 12. With the diesel engine load increasing, the value of δ increases. When the diesel engine load ranges from 50% to 100%, the value of δ increases faster, which indicates that the recovered heat of the exhaust gas increases faster than the increased heat in circulating water at a high diesel engine load. At the same time, with the diesel engine's load and exhaust gas flow rate increasing, the heat transfer between the shell of the exhaust-gas heat exchanger and the indoor air will be enhanced, and then more heat of exhaust gas will be lost. Therefore, the heat loss of the exhaust-gas heat exchanger increases rapidly at a high diesel engine load, which will also increase the heat difference between the exhaust gas and water sides, and the variation range of δ value will become larger. Under the same diesel engine load, the value of δ will be reduced with the flow rate of circulating water increasing, which shows that the increased heat in circulating water is closer to the recovered heat of the exhaust gas at a high water flow rate. The comparison of the heat difference δ is controlled within 6.5%, and this ensures the accuracy of the experiments.

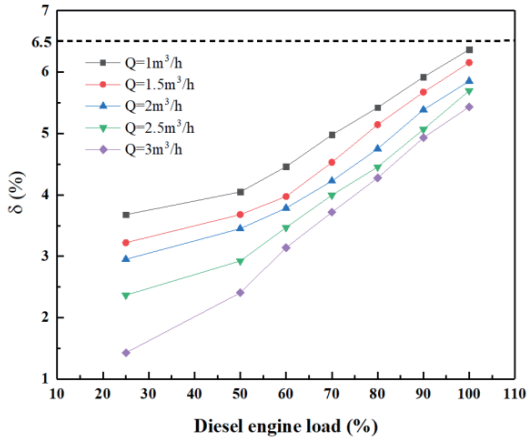

Fig. 12 Comparison of the heat difference and the circulating water flow rate

Heat recovery efficiency of the exhaust-gas heat exchanger

The heat recovery efficiency, η, of the exhaust-gas heat exchanger can be obtained by considering the heat recovered from the water to the recoverable heat from the exhaust gas, and can be written as:

$$\eta = \frac{Q_{water}\ (Recovery\ heat\ by\ heat\ exchanger)}{Q\ (Exhaust\ gas\ heat)} \quad (12)$$

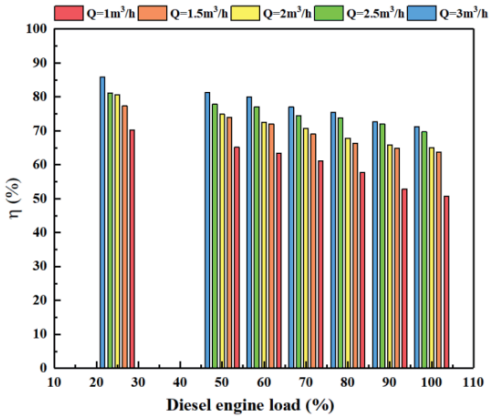

Fig. 13 Heat recovery efficiency of the exhaust-gas heat exchanger

The heat recovery efficiency of the exhaust-gas heat exchanger is shown in Fig. 13. Due to the increase in the water flow rates, the heat recovery efficiency increases at the same operating condition. As the diesel engine load increases, the heat recovery efficiency decreases at the same water flow rate. The heat recovery efficiency is low as the circulating water flow rate is 1m³/h, and there is a big difference when the water flow rate is 1.5-3m³/h, which shows that the heat recovery efficiency decreases obviously under low water flow rate. Therefore, the low water flow rate for heat recovery should be avoided at a high diesel engine load. When the engine load is constant and the circulating water flow rate is 1.5-3m³/h, the heat recovery efficiency is high and increases slowly, which indicates that the heat recovery efficiency is efficient and stable at a high water flow rate. The highest heat recovery efficiency can reach 85.9% at 25% load, and the water flow rate of 3m³/h, and the lowest heat recovery efficiency is 50.8% at 100% load and the water flow rate of 1m³/h, respectively. The analysis results indicate that a smaller volume flow rate and higher diesel engine load have a detrimental effect on the heat recovery efficiency.

Thermal coupling analysis

To meet the requirements of seawater desalination, the outlet water temperature of the exhaust-gas heat exchanger needs to be higher than 55°C and lower than 85°C. In all experimental cases, the inlet water temperature of the exhaust-gas heat exchanger is 20°C.

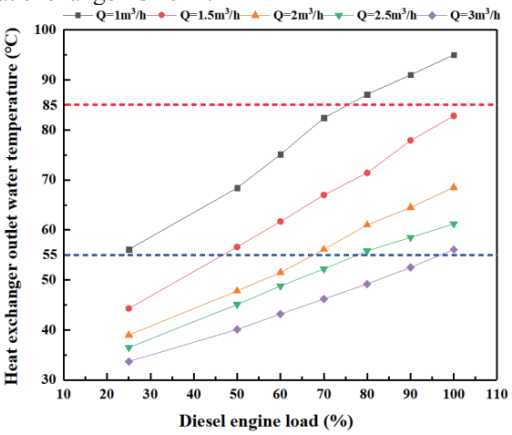

Fig. 14 Outlet water temperature at different loads

Fig. 14 depicts that the outlet water temperature decreases with the increase of the water flow rate at the same load. As the diesel engine load increases, the outlet water temperature increases at the same water flow rate. By changing the water flow rate of the exhaust-gas heat exchanger, the outlet water temperature can reach 55-85°C at different engine loads. The blue and red dotted lines represent the lower and upper limits of the water temperature required by the membrane desalination device: 55°C, and 85°C, respectively. In the region between the blue and red dotted lines, the exhaust-gas heat exchanger's outlet water temperature can meet the seawater desalination device requirements and the heat recovery is higher than 38kW. The details are as follows: when the marine diesel engine runs at 25% load, and the water flow rate is 1m³/h, the heat exchanger's outlet water temperature and heat recovery efficiency are 56°C and 70.2%. As the marine diesel engine runs at 50% and 60% loads and the water flow rate is 1.5m³/h, the heat exchanger's outlet water temperature and heat recovery efficiency are 57°C, 62°C, and 73.9%, 72%, respectively. When the marine diesel engine runs at 70% load and the water flow rate is 2m³/h, the heat exchanger's outlet water temperature and heat recovery efficiency are 56°C and 71%. As the marine diesel engine runs at 80% and 90% loads and the water flow rate of the heat exchanger is 2.5m³/h, the heat exchanger's outlet water temperature and heat recovery efficiency are 56°C, 59°C, and 73.8%, 72%, respectively. When the marine diesel engine runs at 100% load and the water flow rate of the heat exchanger is 3m³/h, the heat exchanger's outlet water temperature, and heat recovery efficiency are 57°C and 71.3%. With the diesel engine load increasing, the exhaust gas's heat recovery ranges from 38.6kW to 122.9kW. The water flow rate can be reduced in the regions between the blue and red dotted lines to obtain a higher outlet water temperature. Thus, by changing the water flow rate of the exhaust-gas heat

exchanger, the outlet water temperature of 55-85°C can be obtained, and the heat recovery from exhaust gas in all cases is greater than 38kW. This study can meet the requirements of the seawater desalination membrane module, and the heat recovery efficiency of the exhaust-gas heat exchanger is greater than 70%.

CONCLUSIONS

In this paper, a new heat exchanger was designed for the exhaust gas heat recovery of small and medium-sized marine diesel engines. The exhaust gas heat recovery experiments for the marine diesel engine at 25-100% load and rated speed were conducted to verify the heat transfer effect. The following conclusions are drawn.

(1) From the gas flow simulation, the exhaust gas is disturbed by the reinforced heat transfer tube section, and exhaust gas velocity is slowed down. Due to the resistance of the unequal spaced fins, some of the exhaust gas is diffused to flow into the outer fins and enters the fin and tube section more evenly. The exhaust gas is fully mixed in the mixing zone between the two sets of fins, and the dead zone vortex area between fins is small.

(2) The difference between the heat absorption by the water in the exhaust-gas heat exchanger and the heat reduction of exhaust gas is within 6.5%, which ensures the accuracy of the experiment.

(3) The outlet water temperature of the exhaust-gas heat exchanger can meet the requirements of the membrane desalination device, and the heat recovered from the exhaust gas ranges from 38.6kW to 122.9kW. With the cooling water flow rate adjusted, the heat recovery efficiency of the exhaust-gas heat exchanger is greater than 70%.

ACKNOWLEDGMENTS

The author sincerely thanked the National Key Research and Development Program of China, 2017YFE0116100, and NanTong People's Livelihood Science and Technology Plan Project (MSZ2022186), Jiangsu Province, China.

.

REFERENCES

[1] Badami, M., Mura, M., Campanile, P., Anzioso, F., 2008, “Design and performance evaluation of an innovative small-scale combined cycle cogeneration system,” Energy, 33, 1264-1276.

[2] Yu, C., Chau, K. T., 2009. “Thermoelectric automotive waste heat energy recovery using maximum power point tracking,” Energy Conversion and Management, 50(6), 1506-1512.

[3] Chung, S., Seo, C. D., Choi, J. H., Chung, J., 2014, “Evaluation method of membrane performance in membrane distillation process for seawater desalination,” Environmental Technology, 35(17), 2147-2152.

[4] Lu, Z. S., Wang, R. Z., 2016, “Experimental performance study of sorption refrigerators driven by waste gases from fishing vessels diesel engine,” Applied Energy, 174, 224-231.

[5] Hou, S. Y., Wu, Y. D., Zhou, Y. D., Yu, L. J., 2017, “Performance analysis of the combined supercritical CO_2 recompression and regenerative cycle used in waste heat recovery of marine gas turbine,” Energy Conversion and Management, 151. 73-85.

[6] Shafieian, A., Khiadani, M., 2020, “A multipurpose desalination, cooling, and air-conditioning system powered by waste heat recovery from diesel exhaust fumes and cooling water,” Case Studies in Thermal Engineering, 21, 100702.

[7] Li, K. L., Hou, D. Y., Fu, C. C., Wang, K., Wang, J., 2019, “Fabrication of PVDF nanofibrous hydrophobic composite membranes reinforced with fabric substrates via electrospinning for membrane distillation desalination,” Journal of Environmental Sciences, 75, 277-288.

[8] Lim, T., Lee, C. K., 2018, “Thermodynamic analysis of ORC to recover waste heat of jacket cooling water in diesel engine,” Journal of Fisheries and Marine Sciences Education, 30(3), 1032-1039.

[9] Zhang, H. G., Wang, E. H., Fan, B. Y., 2013, “Heat transfer analysis of a finned-tube evaporator for engine exhaust heat recovery,” Energy Conversion and Management, 65, 438-447.

[10] Saman, W. Y., Alizadeh, S., 2002, “An experimental study of a cross-flow type plate heat exchanger for dehumidification/cooling,” Solar Energy, 73(1), 59-71.

[11] Choi, J. M., Kim, Y., Lee, M., Kim, Y., 2009, “Air side heat transfer coefficients of discrete plate finned-tube heat exchangers with large fin pitch,” Applied Thermal Engineering, 30(2), 174-180.

[12] Shakir, A. M., Mohammed, A. K., Hasan, M. I., 2011, “Numerical investigation of counter flow microchannel heat exchanger with slip flow heat transfer,” International Journal of Thermal Sciences, 50(11), 2132-2140.

Proceedings of IWEC2023
The International Workshop of Energy Conversion
March 15-17, 2023, Kyoto, Japan

Paper No. IWEC2023-04

ADSORBED CO_2 REDUCTION TECHNIQUE USING NONTHERMAL PLASMA FLOWS

H. Yamsaki[1,2],* H. Wakimoto[2], T. Kuroki[1,2] and M. Okubo[1,2]
[1]Department of Mechanical Engineering, Osaka Metropolitan University, Sakai, Japan
[1]Department of Mechanical Engineering, Osaka Prefecture University, Sakai, Japan
*corresponding author, E-mail: hyamasaki@omu.ac.jp

ABSTRACT

To reduce carbon dioxide (CO_2) emission by self-consistent way at room temperature and atmospheric pressure, CO_2 reduction to CO by nonthermal plasma (NTP) is performed. In this study, in order to evaluate the CO_2 reduction performance using various mixture gas, the reduction is performed through two processes: the process that CO_2 is adsorbed from mixed gas flow of argon (Ar) or helium (He), nitrogen (N_2), and CO_2 (~10% concentration) onto the adsorbent, and the process that CO_2 is desorbed and reduced by Ar or He NTP flow. As a result, CO_2 adsorbed by the adsorbent is desorbed with higher concentration (10–22%) in all experimental conditions. The energy efficiencies increase with the elapsed time and reach 8–14%, and tend to be higher as Ar / (Ar + N_2) × 100 takes further away from 50%, and they tend to be higher as He / (He + N_2) × 100 take lower value. In all conditions, a part of the CO obtained by reduction is further reduced to atomic C. If reduction to atomic C is taken into account, the energy efficiencies increase significantly from 8–14% to 16–22%, and they increase with higher Ar concentration, and with lower He concentration.

INTRODUCTION

Since carbon dioxide (CO_2), which has the effect of absorbing heat emitted out of the atmosphere and keeping it in the atmosphere, i.e., the greenhouse effect, and is a major causative agent of global warming, so its emission should be reduced self-consistent way. Because of its immediate effectiveness, carbon capture and storage (CCS) is attracting attention as a medium-term countermeasure to global warming. However, since CCS only stores CO_2, it does not essentially reduce it from the earth. Also, if the downward leakage of the gas from the CCS transportation facility occurs, CO_2 turn into dry ice by Joule-Thomson effect, accumulates on the ground surface, sublimates, and then stays near the surface at high density, which may cause asphyxiation, cerebral vasodilation, and other effects on the human body [1].

In addition to CCS, another technology of CO_2 reduction to CO is being developed. Compared with the low energy efficiency of coal-fired power plants, which is about 35%, the conversion efficiency of liquefied natural gas (LNG) gas-turbine combined cycle (GTCC) power plants is as high as 60%, so it is possible to construct a self-consistent CO_2 treatment system by part of generated electricity and converting CO_2 to CO [2]. In addition, the power generation efficiency of the latest GTCC has been further improved to more than 64% [3], so the energy efficiency of CO_2 reduction must be more than 49% to achieve a self-consistent one.

Present mainstream reduction method is by using metal catalysts, but this method generally requires CO_2 to be high temperature and pressure [4]. Recently, CO_2 reduction at relatively low temperatures was achieved by applying an electric field to a 5 mass% Ru/CeO_2 catalyst [5]. Also, the photocatalytic method with an Ag@Cr mixture of $CaGa_4O_7$-loaded Ga_2O_3 and CaO photocatalyst leads with Ag@Cr resulted in CO_2 reduction with excellent selectivity under ambient temperature and pressure [6]. Thus, although catalysts have been studied, these technologies are still in the developmental stage due to problems such as deactivation of the catalyst and low efficiency.

On the other hand, the same reduction can be easily occurred by nonthermal plasma (NTP) at atmospheric pressure and ambient temperature [7], and in a smaller system than by catalyst. In any case, however, present reduction technology is not at the practical level of performance because of the low energy efficiency. To improve the energy efficiency, various study had been performed [8–16]. Ozkan et al. reported the CO_2 reduction performance in dielectric barrier discharges (DBD) and found that the CO_2 concentration increases with decreasing discharge frequency, especially when the discharge power is 16 kHz, 22% conversion efficiency and 15% energy efficiency are achieved [16]. Moreover, in some studies, experiments have been performed with the mixture of CO_2 and Ar or He [17–19]. Ramakers et al. reported that the CO_2 conversion during DBD discharge was higher for a mixture of CO_2 and Ar than for a mixture of CO_2 and He when the CO_2

concentration was less than 30% [17]. Also, Xu et al. achieved high energy efficiency by diluting CO_2 with Ar and N_2 and performing the reduction in a barium titanate packed bed NTP flow reactor at atmospheric pressure [18].

Under these study situations, we have conducted new laboratory-scale experiments with the CO_2 reduction treatment system using NTP flow. In our previous study, the experiment with a CO_2 reduction system using N_2 NTP flow and adsorbent was conducted, and the effect of the volume of adsorbent and the circulating flow rate in the system on the energy efficiency was reported [20]. The objective of this study is to improve the energy efficiency of reduction of CO_2 by using NTP flow with different mixing ratios of Ar or He, N_2, and CO_2.

EXPERIMENTAL SETUP AND METHODS

A schematic of the experimental setup is shown in **Fig. 1**. The experiment consists of two processes: an adsorption process with the adsorbent and a desorption and reduction process using NTP flow. In the adsorption process, valves I, K, L, O, and P are closed, valves A, B, C, D, E, F, G, H, J, and M are opened, and three-way valve N is turned to the exhaust side. Considering that the CO_2 concentration of combustion fuel gas generated from boilers and internal engines is almost 10%, Ar gas (purity = 99.995%) or He gas (purity = 99.995%), N_2 gas (purity = 99.995%), and CO_2 gas (purity = 99.5%) in cylinders are introduced and mixed inside the setup to prepare CO_2 gas at a concentration of 10% with a total flow rate of 10 L/min. Experiments are conducted by changing the flow rates of Ar or He, N_2, and CO_2 as shown in **Table 1**, and the results are compared with those of previous studies [20] to identify the optimal gas concentration ratio for CO_2 conversion. The flow rate and concentration are regulated by a mass flow controller (SFC-281E, Hitachi Metals, Ltd.). The mixed gas flow passes through the adsorbent packed in the adsorption chamber (1.8 L) located downstream of the plasma reactor. The CO_2 concentration upstream of the adsorption chamber is measured every 10 minutes using a gas detector tube (2H and 2HH, Gastec Co.) with a glass syringe at MP1 after the valve L is opened. The CO_2 concentration downstream of the adsorption chamber is measured every 10 minutes using a gas detector tube (2H, Gastec Co.) with a glass syringe at MP2 and a CO_2 analyzer (COZY-1; nondispersive infrared absorption method,

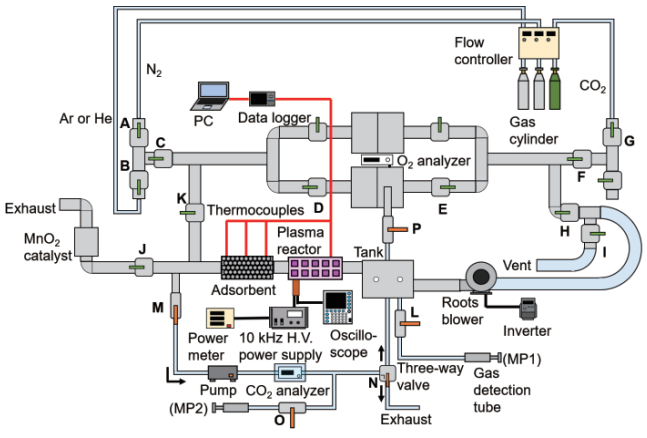

Fig. 1 Schematics of experimental setup [21].

accuracy = ±0.25%, Ichinen Jiko Co., Ltd.) from the gas suctioned by the pump after the valve O is opened. The concentration of O_2 is measured using an oxygen analyzer (OXY-1S; galvanic cell method; accuracy = 0.1%; Ichinen Jiko Co., Ltd.).

Molecular sieve zeolite 13X (APG-III, Union Syowa K. K.) is used as the adsorbent. The main components of the adsorbent are Na^+, Al_2O_3, and SiO_2. In order to evaluate the adsorption and desorption performance of the adsorbent, the gas temperature is measured every second at three points in the adsorption chamber (upstream, midstream, and downstream) using thermocouples connected to a data logger (Model 8430, Hioki Electric Co., Ltd.).

In the plasma reduction process, valves D, E, H, K, M, and P are opened, three-way valve N is turned to the side of valve P, and the other valves are closed. The flow channel becomes a circulation channel with a total channel volume of 86.7 L. NTP flow is generated by a plasma reactor and a blower (root type blower; BSS25Gz; maximum flow rate 540 L/min at 10 kPa gauge pressure; Anlet Co., Ltd.). The direction of the circulation flow is represented as clockwise in the figure. The NTP is induced with a plasma reactor energized by a high AC voltage power supply (input power = 300 W, frequency = 10 kHz). The power applied to the plasma reactor is measured by a power meter (POWER HiTESTER 3333, accuracy = ± 0.1%, Hioki E.E. Co.). Owing to the NTP flow, the CO_2 adsorbed on the adsorbent is desorbed by heat and reduced to mainly CO with plasma chemical reaction [2], as shown in reaction (1):

$$CO_2 \rightarrow CO + \frac{1}{2}O_2 \quad (1)$$

Reaction (1) requires the energy higher than ΔH = 2.9 eV/molecule, which is the negative value of standard enthalpy of the reaction. The CO concentration is measured every 10 minutes using a gas detector tube (1H, Gastec Co.) with a glass syringe from the gas suctioned by the pump after the valve O is opened.

The plasma reactor consists of 12 surface-discharge elements, 6 each on the left and right. The height, width, and length of the reactor are 100, 90, and 200 mm, respectively. The element comprises an alumina-ceramic tube with a discharge electrode made of tungsten on its surface, and a counter electrode is embedded inside the ceramic tube wall [20]. NTP is generated by surface discharge at the surface discharge elements. The plasma reactor is energized by the high AC voltage power supply at an input power of 300 W and a frequency of 10 kHz.

Table 1 Experimental conditions for flow rate during the adsorption process [21].

Condition	Flow rate L/min			
	Ar	He	N_2	CO_2
(a)	8.0	0	1.0	1.0
(b)	4.5	0	4.5	1.0
(c)	1.0	0	8.0	1.0
(d)	0	9.0	0	1.0
(e)	0	8.0	1.0	1.0
Previous study [20]	0	0	9.0	1.0

The experiment that combines both the adsorption process and the desorption process is performed for four cycles. For each cycle, both the adsorption and desorption processes are performed for 140 min each, i.e., a total 280 min.

The conversion efficiency α by NTP flow is defined by the following equation (2):

$$\alpha = \frac{\mathrm{CO}}{\mathrm{CO_2} + \mathrm{CO}} \times 100 . \quad (2)$$

The energy efficiency η based on the NTP flow is defined by the following equation (3):

$$\eta = \alpha \times \frac{\Delta H}{E_\mathrm{v}} \quad (3)$$

where E_v is the specific energy of the plasma (eV/molecule) [2]. In this study, the specific energy based on the input power is 4.48 eV/molecule (at a gas temperature of 20˚C).

To evaluate the performance of the adsorbent after each experiment, crystallinity and mass of attached carbon to the adsorbent are measured. The analysis is conducted on 100 g of the adsorbent after the four-cycle experiments. The measurement of the crystallinity is performed using X-ray diffraction. Crystallinity is the ratio of the intensity of used adsorbent to that of the unused product at a characteristic diffraction angle; the lower the value means the adsorbent is degraded. As for the attached carbon, because CO_2 can be reduced not only to CO but also atomic C as shown in the following reaction,

$$\mathrm{CO} \rightarrow \mathrm{C} + \frac{1}{2}\mathrm{O_2} \quad (4)$$

the mass of atomic carbon is measured. Atomic C is quantified by burning the 100 g of the used adsorbent in an O_2 environment after purging it with 60 L/min of N_2 gas flow, and measuring CO and CO_2 generated. These analyses are performed by an analysis company (Union Showa K.K.).

While performing this experiment, it is necessary to carefully observe that the concentration of CO does not exceed the lower explosion limit of CO, i.e., 12.5%.

EXPERIMENTAL RESULTS AND DISCUSSION

Adsorption Process

For each experimental condition, the upstream CO_2 concentration is approximately 10%. The reason is evident from the fact that the flow rate of CO_2 is 1.0 L/min while the total flow rate is 10 L/min.

In the first cycle, the downstream CO_2 concentration gradually increases with time and approaches 10%. For the other experimental conditions, similar results are obtained. The reason for this is that the adsorbent is fresh, and the CO_2 adsorption capacity of the adsorbent is sufficient. The total volumes of adsorbed CO_2 in the first cycle in the experimental condition (a)–(e) are 46 L, 47 L, 46 L, 40 L, and 58 L, respectively. In the first cycle, the volume of adsorbed CO_2 is about the same regardless of the flow rate of Ar and N_2 when using Ar gas flow, and it is higher as the flow rate of He is higher than that of N_2 when using He gas flow.

After the second cycle, the downstream CO_2 concentration suddenly increases after the elapsed time of 20–30 min and becomes saturated when the adsorbent is saturated. For the other experimental conditions, similar results are obtained. In condition (a), the total volumes of adsorbed CO_2 in the second, third, and fourth cycles are 8.9 L, 8.4 L, and 8.1 L, respectively. In condition (b), they are 11 L, 15 L, and 5.2 L, respectively. In condition (c), they are 10 L, 7.6 L, and 18 L, respectively. In condition (d), they are 16 L, 11 L, and 8.4 L, respectively. In condition (e), they are 10 L, 7.2 L, and 14 L, respectively. After the second cycle, the volume of CO_2 adsorbed decreases.

In the second cycle of condition (a), the temperature increases and then decreases in the order of upstream, midstream, and downstream as in the first cycle, but the maximum temperature reached is very low, 30.9°C in upstream, 30.2°C in midstream, and 33.1°C in midstream, and the temperature changes almost simultaneously at each position. For the other experimental conditions (b)–(e), similar results are obtained. After the second cycle, since a large amount of CO_2 is already adsorbed on the adsorbent, the amount of adsorbed CO_2 and the temperature change due to adsorption decreases.

Desorption Process

In the first cycle, as the elapsed time increases, the CO_2 concentration also increases, and after 60 min, the CO_2 concentration reaches about 12%. After the second cycle, the CO_2 concentration increases from the initial value rapidly and then reaches 17–20%. For the other experimental conditions (b)–(e), similar trends of low CO_2 concentration in the first cycle and increasing CO_2 concentration in the second to fourth cycles are obtained. The maximum CO_2 concentration during desorption is 20, 18, 19, 22, and 20% for experimental conditions (a)–(e), respectively. The CO concentrations increase with the elapsed time and reach 4.2, 2.5, 3.0, 2.6, and 3.5% for experimental conditions (a)–(e), respectively. The O_2 concentration increases monotonically and reaches 3.1, 5.4, 4.3, 5.2, and 3.5% for experimental conditions (a)–(e), respectively. The first and second cycles in the experimental condition (b) are excluded from the discussion because they result in a significant increase in O_2 concentration as a result of outside air contamination due to a malfunction in the experimental setup. As shown in reaction (1), in the process of CO_2 reduction, O_2 is generated along with CO. The reaction rate of the chemical reaction is faster for higher concentrations of the reactants and slower for higher concentrations of the products. Therefore, the higher the O_2 concentration is, the more forward reaction is suppressed, resulting in a lower CO concentration.

In the first cycle of condition (a), the temperature in the adsorption chamber increases from about 20°C in the order of upstream, midstream, and downstream almost simultaneously within 10 minutes, and then becomes almost constant at 50.7°C in upstream, 51.2°C in midstream, and 52.8°C in downstream of adsorption chamber. Also, no clear difference in the adsorption chamber temperature is observed in all conditions. For the other experimental conditions, similar results are obtained. Note that the results are similar for the second, third, and fourth cycles in all conditions. In this experiment, since the circulation flow rate is large (540 L/min) compared to the size of the adsorption chamber, the hot gas passes through the

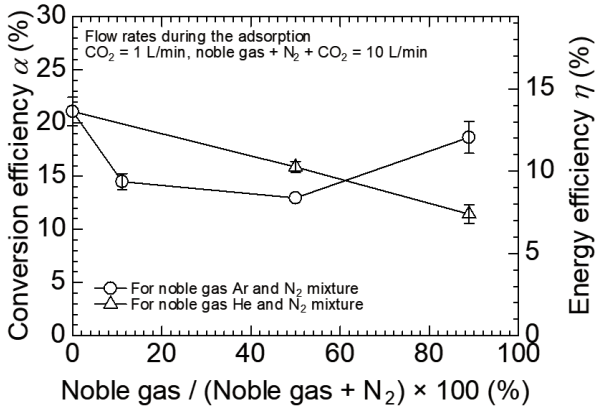

Fig. 2 Relationship between Ar/(Ar+N_2)×100 or He/(He+N_2)×100, conversion, and energy efficiency [21].

adsorption chamber at high velocity before the heat of gas is sufficiently transferred to the adsorbent, resulting in a small and almost of same time of increase for the adsorbent temperature at each position of the adsorption chamber. This resulted in no significant temperature differences being measured when the gas type and concentration ratio are changed. Therefore, the difference in CO_2 concentration under each condition is largely due to factors other than gas temperature.

Energy Efficiency of the Conversion of CO_2

Fig. 2 shows the relationship between the ratio of Ar / (Ar + N_2) × 100 or He / (He + N_2) × 100 and the efficiencies. Each plot is the average value of four cycles of conversion efficiency and energy efficiency at 140 min, and the error bars in the figures correspond to ±σ, where σ is the standard deviation of the 4 cycles. When using Ar NTP flow, the efficiencies are higher as Ar / (Ar + N_2) × 100 takes away from 50%. On the other hand, when using He NTP flow, the efficiencies are higher as He / (He + N_2) × 100 takes a lower value. This means that CO_2 can be reduced to CO with higher energy efficiency by using N_2 NTP flow than by using He NTP flow.

When using N_2 NTP flow, filament discharge is generated in the plasma reactor [22, 23]. Since filament discharge occurs ununiformly, the number of CO_2 molecules irradiated by NTP flow is reduced, but electrons are concentrated, and CO_2 molecules are strongly reduced in each streamer. The CO_2 reduction is usually caused by the electron collision on the CO_2 molecule and is expressed as

$$e^- + CO_2 \rightarrow e^- + CO_2^* \rightarrow CO + O \quad (6)$$

where CO_2^* indicates a CO_2 radical and e^- indicates an electron. On the other hand, when using Ar NTP flow, the Penning effect, which is expressed as

$$Ar^+ + CO_2 \rightarrow Ar + CO_2^+, \quad CO_2^+ + e^- \rightarrow CO + O \quad (7)$$

where charge transfer from Ar to CO_2 occurs, generate glow discharge in the plasma reactor [24]. Since glow discharge occurs uniformly, the number of CO_2 molecules irradiated by NTP flow increases, there are no regions of extremely high electron density. When Ar / (Ar + N_2) × 100 is 50%, the advantages of filamentary discharge cannot be utilized because some electrons are dispersed, and the number of streamers decreases, and the advantages of glow discharge cannot be utilized because the density of electrons dispersed throughout is insufficient to affect the CO_2 molecules much. When using He NTP flow, the Penning effect, which is expressed as

$$He^+ + CO_2 \rightarrow He + CO_2^+, \quad CO_2^+ + e^- \rightarrow CO + O \quad (8)$$

where charge transfer from He to CO_2 occurs, generate glow discharge in the plasma reactor [24, 25]. Because He has higher metastable excitation energy and is more prone to the Penning effect compared to Ar, He NTP flow is a stronger glow discharge than Ar NTP flow. Therefore, the efficiencies in the case where He / (He + N_2) × 100 is 50% increase compared to the case where Ar / (Ar + N_2) × 100 is 50%. However, He has high ionization energy and generates fewer electrons than that of Ar and N_2. Therefore, when He / (He + N_2) is high, the glow discharge is very weak, and the efficiencies decrease.

Analyses of the Adsorbent Deterioration and Atomic Carbon Generation

To confirm the adsorbent deterioration and atomic carbon (C) generation caused by the Ar and He NTP flows, the components of the used adsorbent have been analyzed by an analysis company (Union Showa K. K.). The crystallinity of 96, 93, 97, 99, and 98% are observed in the experimental condition (a)–(e), respectively. During the experiment, slight decrease in crystallinity of the adsorbent is observed, so the adsorption performance of the adsorbent is little degraded.

To measure carbon concentration CO and CO_2 generated by heating and burning the used adsorbent in an oxygen environment are quantified. The result of quantifying atomic C concentration is shown in **Fig. 3**. As a result, the amount of atomic C attached to the adsorbent is determined. When Ar / (Ar + N_2) is 89%, the part of CO is further reduced to atomic C, so the conversion efficiency to CO decreases compared with that using the N_2 NTP flow. In this study, it can be regarded that 0.20, 0.15, 0.13, 0.15, and 0.18 mol of atomic C can be generated per cycle in the condition (a)–(e), respectively. Therefore, the possible CO concentration, which takes into account the reduction of CO to atomic C, are 9.0, 5.8, 5.9, 6.2, and 7.8% in condition (a)–(e), respectively. In addition, the possible conversion efficiencies α are 34, 27, 26, 25, and 30%,

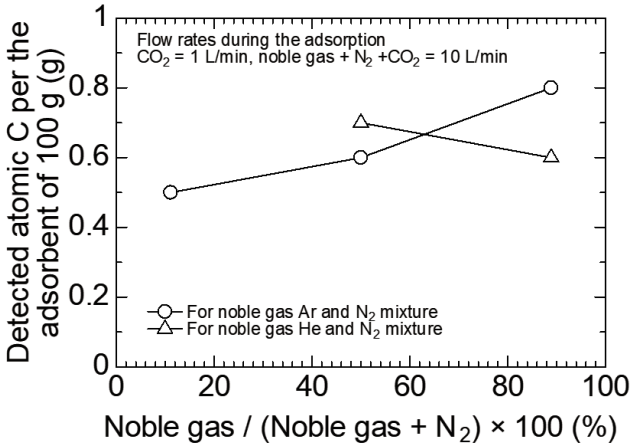

Fig. 3 Detected atomic carbon per 100 g of the adsorbent after the four-cycle adsorption-desorption experiments [21].

and the possible energy efficiencies η are to 22, 17, 17, 16, and 19% in condition (a)–(e), respectively. Therefore, the possible energy efficiency is found to be very high, considering the reduction to both CO and atomic C. The reason for the highest detection of atomic C in the experimental condition (a), where the Ar flow rate is the highest, is that uniform glow discharge is generated in the plasma reactor, so there is a high probability that the CO molecules obtained by reduction are irradiated with NTP flow again before leaving the plasma reactor. On the other hand, when using He NTP flow, glow discharge is generated in the plasma reactor, but that discharge is weak, so there is a low probability that the CO molecules are irradiated with NTP flow again.

Fig. 4 shows the relationship between the conversion efficiency and energy efficiency obtained from previous studies [20, 26] and this study. The maximum conversion and the maximum energy efficiencies are 19 and 12% in condition (a), which are similar in efficiency to previous studies of DBD, thermal plasma, and gliding arc. On the other hand, the maximum conversion efficiency and the maximum energy efficiency when considering the reduction to both CO and atomic C are 34 and 22% for condition (a), which are superior to the results used DBD, thermal plasma and, gliding arc.

The CO_2 reduction energy efficiency is a maximum of 9.4, 6.0, 6.4, 5.7, and 8.0 g(CO_2)/kWh for the condition (a)–(e), respectively. In this study, the initial CO_2 concentration of 10%, but if 100%-concentration CO_2 were treated, the values could increase to 47, 30, 32, 28, and 40 g(CO_2)/kWh for conditions (a)–(e), respectively. Assuming the treatment of 100% CO_2 concentration, an CO_2 reduction energy efficiency of 18 g(CO_2)/kWh needs to be achieved to achieve the energy efficiency η = 49% required for self-consistent CO_2 zero emission in GTCC. In this study, the reduction energy efficiency at η = 49% is achieved assuming a CO_2 concentration of 100%, so if the concentration of adsorbed and desorbed CO_2 can be further increased, a self-consistent CO_2 reduction cycle system will be closer to realization.

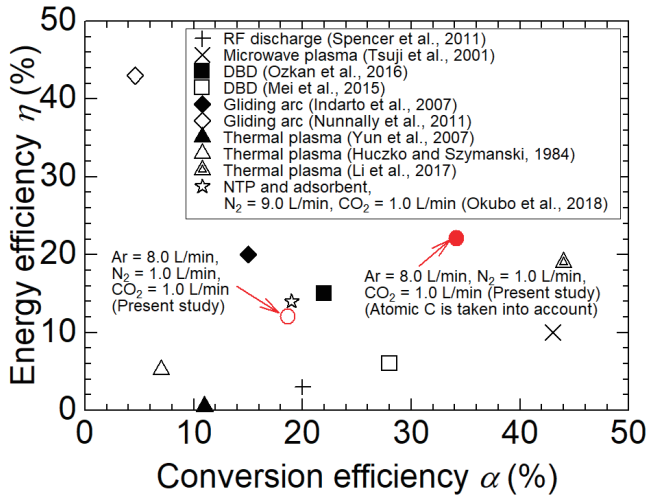

Fig.4 Relationship between the conversion efficiency and energy efficiency obtained from previous studies [20, 26] and this study [21].

CONCLUSIONS

To reduce CO_2 emission by self-consistent way at room temperature and atmospheric pressure, CO_2 reduction to CO by nonthermal plasma (NTP) flow was performed. The results are as summarized as follows.

1. In the desorption process, the CO_2 concentration downstream of the adsorbent gradually increases with elapsed time and approaches 10% in the first cycle. On the other hand, the CO_2 concentration downstream increases rapidly and becomes saturated at 10% after the second cycle. When Ar and N_2 mixed gas is used, there is no difference in the total volumes of adsorbed CO_2, but when He and N_2 mixed gas is used, the total volumes of adsorbed CO_2 increase as the N_2 mixing ratio increases.
2. In the desorption process, the maximum CO concentration of 4.2% is achieved when the ratio of Ar / (Ar + N_2) × 100 is 89%. The O_2 concentration produced during desorption is lower, and the decomposed CO concentration increases.
3. The maximum CO_2 conversion and energy efficiencies are achieved 21% and 14%. When using Ar NTP flow, the efficiencies tend to be higher as Ar / (Ar + N_2) × 100 takes away from 50%. On the other hand, when using He NTP flow, the efficiencies tend to be higher as He / (He + N_2) takes a lower value.
4. In all conditions, a part of the CO obtained by reduction is further reduced to atomic C. The possible efficiencies, the possible CO concentration, which takes into account the reduction of CO to atomic C, increase significantly from 8–14% of the actual efficiencies to 16–22%, and the possible efficiency increase with higher Ar concentration when using Ar NTP flow, and with lower He concentration when using He NTP flow. Particularly, higher possible conversion and energy efficiencies can be achieved under the conditions of Ar = 8.0 L/min, N_2 = 1.0 L/min, and CO_2 = 1.0 L/min than in previous studies.

ACKNOWLEDGMENTS

The authors would like to thank S. Park and K. Kataoka, who were undergraduate students of Osaka Prefecture University, for their help in conducting the experiments. The authors are particularly indebted to Dr. H. J. Kim, principal researcher at Korea Institute of Machinery and Materials, for his support. The work was partially supported by JSPS KAKENHI Grant Number 20K19989 and JP20H02374).

REFERENCES

[1] Mazzoldi A., Hill T., and Colls J.J., 2008, "CO_2 transportation for carbon capture and storage: Sublimation of carbon dioxide from a dry ice bank," Int. J. Greenh. Gas Control., Vol. 2-2, pp. 210–218.

[2] Spencer L.F. and Gallimore A.D., 2011, "Efficiency of CO_2 dissociation in a radio-frequency discharge," Plasma

Chem. Plasma Process., Vol. 31, pp. 79–89.
[3] Morimoto K., Matsumura Y., Iijima T., Wakazono S., Kataoka M., and Yuri M., 2021, "Validation results of 1650ºC class JAC gas turbine at T-point 2 demonstration plant," Mitsubishi Heavy Industries Technical Review, Vol. 58-1, pp. 1–12.
[4] Jwa E., Lee S.B., Lee H.W., and Mok Y.S., 2013, "Plasma-assisted catalytic methanation of CO and CO_2 over Ni-zeolite catalysts," Fuel Process. Technol., Vol. 108, pp. 89–93.
[5] Yamada K., Ogo S., Yamano R., Higo T., and Sekine Y., 2020, Low-temperature conversion of carbon dioxide to methane in electric field," Chem. Lett., Vol. 49-3, pp. 303-306.
[6] Pang R., Teramura K., Morishita M., Asakura H., Hosokawa S., and Tanaka T., 2020, "Enhanced CO evolution for photocatalytic conversion of CO_2 by H_2O over Ca modified Ga_2O_3," Chem. Commun., Vol. 3-137, pp. 1-8.
[7] Jogan K., Mizuno A., Yamamoto T., and Chang J.S., 1993, "The effect of residence time on the CO_2 reduction from combustion flue gases by an AC ferroelectric packed bed reactor," IEEE Trans. Ind. Appl., Vol. 29-5, pp. 876–881.
[8] Wang J.Y., Xia G.G., Huang A., Suib S.L., Hayashi Y., and Matsumoto H., 1999, "CO_2 decomposition using glow discharge plasma," J. Catal., Vol. 185-1, pp. 152–159.
[9] Zheng G, Jiang J., Wu Y., Zhang R., and Hou H., 2003, "The mutual conversion of CO_2 and CO in dielectric barrier discharge (DBD)," Plasma Chem. Plasma Process., Vol. 23, pp. 59–68.
[10] Mori S., Yamamoto A., and Suzuki M., 2006, "Characterization of a capillary plasma reactor for carbon dioxide decomposition," Plasma Sources Sci. Technol., Vol. 15, pp. 609–613.
[11] Horvath G., Skalny J., and Mason N., 2008, "FTIR study of decomposition of carbon dioxide in dc corona discharges," *J. Phys. D,* Vol. 41, 225207.
[12] Paulussen S., Verheyde B., Tu X., De Bie C., Martens T., Petrovic D., Bogaerts A., and Sels B., 2010, "Conversion of carbon dioxide to value-added chemicals in atmospheric pressure dielectric barrier discharge," Plasma Sources Sci. Technol., Vol. 19, 034015.
[13] Nunnally T., Gutsol K., Rabinovich A., Fridman A., Gutsol A., and Kemoun A., 2011, "Dissociation of CO_2 in a low current gliding arc plasmatron," J. Phys. D, Vol. 44-27, 274009.
[14] Yu Q., Kong M., Liu T., Fei J., and Zheng X., 2012, "Characteristics of the decomposition of CO_2 in a dielectric packed–bed plasma reactor," Plasma Chem. Plasma Process., Vol. 32, pp. 153–163.
[15] Wang S., Zhang Y., Liu X., and Wang X.,2012, "Enhancement of CO_2 conversion rate and conversion efficiency by homogeneous discharge," Plasma Chem. Plasma Process., Vol. 32, pp. 979–989.
[16] Ozkan A., Dufour T., Silva T., Britun N., Snyders R., Bogaerts A., and Reniers F., 2016, "The influence of power and frequency on the filamentary behavior of a flowing DBD-application to the splitting of CO_2," Plasma Sources Sci. Technol., Vol. 25, 025013, pp. 1–11.
[17] Ramakers M., Michielsen I., Aerts R., Meynen V., and Bogaerts A., 2015, "Effect of Argon or Helium on the CO_2 conversion in a dielectric barrier discharge," Plasma Process Polym, Vol. 12-8, pp. 755–763.
[18] Xu S., Chansai S., Shao Y., Xu S., Wang Y., Haigh S., Mu Y., Jiao Y., Stere C.E., Chem H., Fan X., and Hardacre C., 2020, "Mechanistic study of non-thermal plasma assisted CO_2 hydrogenation over Ru supported on MgAl layered double hydroxide," Appl. Catal. B, Vol. 268, 118752, pp. 1–12.
[19] Willems G., Hecimovic A., Sgonina K., Carbone E., and Benedikt J., 2020, "Mass spectrometry of neutrals and positive ions in He/CO_2 non-equilibrium atmospheric plasma jet," Plasma Phys. Control. Fusion, Vol. 62, 034005, pp.1–12.
[20] Okubo M., Takahashi K., Kamiya S., and Kuroki T., 2018, "High-efficiency carbon dioxide reduction using nonthermal plasma desorption," IEEE Trans. Ind. Appl., Vol. 54-6, pp. 6422–6429.
[21] Wakimoto H., Yamasaki H., Kuroki T., and Okubo M., 2022, "Effect of argon and helium concentrations on adsorbed CO_2 dissociation using nonthermal plasma flow," Int. J. Plasma Environ. Sci. Technol., 16-1, e01006.
[22] Gherardi N., Gouda G., Gat E., Ricard A., and Massines F., 2000, "Transition from glow silent discharge to micro-discharges in nitrogen," Plasma Sources Sci Technol, Vol. 9-340, pp. 340–346.
[23] Takaki K., Fujiwara T., and Tochikubo F., 2003, "Production of atmospheric-pressure glow discharge," J. Plasma Fusion Res., Vol. 79-10, pp. 1002–1008 (in Japanese).
[24] Kogoma M., 2003, "Generation of atmospheric-pressure glow discharge and its applications," J. Plasma Fusion Res., Vol. 79-10, pp. 1000–1001 (in Japanese).
[25] Tochikubo F., Chiba T., and Watanabe T., 1999, "Structure of low-frequency helium glow discharge at atmospheric pressure between parallel plate dielectric electrodes," Jpn. J. Appl. Phys., Vol. 38, pp. 5244–5250.
[26] Li J., Zhang X. Shen J., Ran T., Chen P., and Yin Y., 2017, "Dissociation of CO_2 by thermal plasma with contracting nozzle quenching," J. CO_2 Util., Vol. 21, pp. 72–76.

Paper No. IWEC2023-05

Proceedings of IWEC2023
The International Workshop of Energy Conversion
March 15-17, 2023, Kyoto, Japan

Controlling post-impact dynamics of ferrofluid droplets with magnetic field

Xiao-Dong Niu[1,2*], Jin-Xiang Zhou[1,2], Hong-Wei Xiao[1,2], Adnan Khan[1,2*], Mu-Feng Chen[3], De-Cai Li[4], Hiroshi Yamaguchi[5]

"[1]Key Laboratory of Intelligent Manufacturing Technology（Shantou University), MOE, 243 Daxue Road, Shantou 515063, Guangdong, China

[2]College of Engineering, Shantou University, 243 Daxue Road, Shantou 515063, Guangdong, China

[3]College of Physics and Electromechanics Engineering, Longyan University, Longyan 364012, China

[4]Department of Mechanical Engineering, Tsinghua University, Beijing, China

[5]Energy Conversion Research Center, Doshisha University, Kyoto 630-0321, Japan"

[*]Corresponding authors' E-mail addresses: 16adnan@stu.edu.cn; xdniu@stu.edu.cn

ABSTRACT

Preventing droplets from splashing after impacting a thin layer or liquid pool is crucial in reducing cross-contamination, the spread of pathogens, and rough surfaces in three dimensional (3D) printing. In this article, we demonstrate that an external magnetic field can be useful to actively control the post-impact dynamics of ferrofluid droplets. A simplified lattice Boltzmann method (SLBM) is applied to simulate the flow field with lower computational cost. For magnetic field, a self-correcting procedure is coupled with SLBM by setting a permanent magnet of desired magnetic field strength at any location of the computational domain. In this article a plashing droplet on a thin layer is studied, and the crown structures is found to be successfully controlled with the help of a permanent magnet.

Keywords: simplified lattice Boltzmann method; self-correcting scheme; droplet splash; non-uniform magnetic field; ferrofluid droplet.

INTRODUCTION

Collisional and post-impact hydrodynamics of a droplet on liquid and solid surfaces have long been studied due to its significance in plenty of applications, including surface coating, spray cooling, inkjet printing, respiratory disease transmission and effective pesticide deposition on plants[1-5]. In a vast majority of biomedical applications, fluids may spread only via splashing phenomenon of impacting droplets[6], with ability to distribute and transport contaminated fluid in controlled environment like labs. It is possible to control the fluid motion that results in a crown formation or rim widening of the droplet, by simply changing the force balance on the striking surface. Although studies on the impacting fluid droplets have produced a vast literature, but research with utilitarian applications is scarce. In this regard, a crucial study is the hydrodynamics of impacting ferrofluid droplets when exposed to a magnetic field.

In the present study, we present a novel idea of controlling the splashing and impacting dynamics of a droplet with the help of a permanent magnet, which are characterized by Maxwell's magnetostatic equations along with Ampere's circuital law and the divergence theorem. To confirm the validity of our idea, we first simulated the droplet spreading phenomenon on a solid surface (also known as static contact angle) and compared our results with analytical predictions. The theme of this study is justified by simulating three different cases of spreading, splashing and impacting droplets, systematically. All of the simulations are carried out with simplified lattice Boltzmann method under non-uniform magnetic. SLBM can simulate multiphase flow problems with less memory and easier direct application of macroscopic boundary conditions.

METHODOLOGY

Flow field and interface

The macroscopic momentum and interface equations can be expressed as:

$$\frac{\partial \rho}{\partial t} + \rho \nabla \cdot \mathrm{u} = 0\,, \tag{1}$$

$$\frac{\partial \rho}{\partial t} + \nabla \cdot (\rho \mathrm{uu}) = -\nabla p + \nabla \cdot \left[\mu \left(\nabla \mathrm{u} + (\nabla \mathrm{u})^T \right) \right] + \mathrm{F}_{total}\,, \tag{2}$$

$$\frac{\partial \phi}{\partial t}+\nabla\cdot(\phi \mathrm{u})=\theta_M \nabla^2 \mu_\phi + q\,, \tag{3}$$

where p, ρ, u and μ denotes the pressure, density, velocity, and viscosity, respectively. The chemical potential is defined as $\mu_\phi = 2\beta\phi(\phi-1)(2\phi-1)-\kappa\nabla^2\phi$, where β and κ can be obtained from the interface thickness ξ and the surface tension σ:

$$\beta = \frac{12\sigma}{\xi}, \kappa = \frac{3\xi\sigma}{2}. \tag{4}$$

F_{total} is the external force which can be expressed as:

$$\mathrm{F}_{total} = \mathrm{F}_s + \mathrm{F}_{mg} + \mathrm{F}_g\,, \tag{5}$$

Here F_s, F_{mg} and F_g are surface force, magnetic force, and gravitational force, respectively, and

$$\mathrm{F}_s = \mu_\phi \nabla\phi\,, \tag{6}$$

$$\mathrm{F}_{mg} = \mu_0(\mathrm{M}\cdot\nabla)\mathrm{H}\,, \tag{7}$$

here μ_0 is the vacuum permeability, ϕ is the order parameter, M is the magnetization and H is the magnetic intensity, respectively.

The last term of Eq. (3) is introduced to correct the mass losses or diffusion and can be written as:

$$q = \begin{cases} \dfrac{1}{\Delta V}\left(\dfrac{\Delta M}{(\rho_L-\rho_G)\Delta t} - \sum_{\Omega_l}\theta_m\nabla^2\mu_\phi dV\right), & 0<\phi<1 \\ 0, & elsewhere \end{cases} \tag{8}$$

where ΔV, ΔM are the interfacial zone volume and initial-to-final step mass difference. ρ_L, ρ_G, Δt are the density of heavier fluid, the density of lighter fluid and the lattice time step, respectively. Moreover, the order parameter ϕ and the density ρ have a linear relationship which can be expressed as:

$$\rho = \rho_G + (\rho_L-\rho_G)\phi\,. \tag{9}$$

Simplified lattice Boltzmann method

To solve the Eq. (1), Eq. (2) and Eq. (3), the simplified Boltzmann method with predictor and corrector steps is employed as

The predictor step:

$$p^* = \sum_\alpha f_\alpha^{eqm}(\mathrm{x}-\mathrm{e}_\alpha\Delta t, t-\Delta t)\,, \tag{10a}$$

$$\rho^*\mathrm{u}^* c_s^2 = \sum_\alpha \mathrm{e}_\alpha f_\alpha^{eq}(\mathrm{x}-\mathrm{e}_\alpha\Delta t, t-\Delta t)\,, \tag{10b}$$

$$\phi^* = \sum_\alpha g_\alpha^{eq}(\mathrm{x}-\mathrm{e}_\alpha\Delta t, t-\Delta t)\,. \tag{10c}$$

The corrector step:

$$p^{n+1} = p^*\,, \tag{11a}$$

$$\begin{aligned}\rho^{n+1}\mathrm{u}^{n+1}c_s^2 = \rho^*\mathrm{u}^*c_s^2 &+ \sum_\alpha \mathrm{e}_\alpha\begin{bmatrix} f_\alpha^-(\mathrm{x}+0.5\mathrm{e}_\alpha\Delta t, t-0.5\Delta t) \\ -f_\alpha^-(\mathrm{x}-0.5\mathrm{e}_\alpha\Delta t, t-0.5\Delta t)\end{bmatrix} \\ -0.5\Delta t\sum_\alpha \mathrm{e}_\alpha &\begin{bmatrix} F_\alpha^-(\mathrm{x}+0.5\mathrm{e}_\alpha\Delta t, t-0.5\Delta t) \\ -F_\alpha^-(\mathrm{x}-0.5\mathrm{e}_\alpha\Delta t, t-0.5\Delta t)\end{bmatrix} + c_s^2(\mathrm{F}_{mg}+\mathrm{F}_s)\Delta t,\end{aligned} \tag{11b}$$

$$\phi^{n+1} = \phi^* + \sum_\alpha(\tau_g-1)\left[g_\alpha^-(\mathrm{x}+0.5\mathrm{e}_\alpha\Delta t, t-0.5\Delta t) - g_\alpha^-(\mathrm{x}-0.5\mathrm{e}_\alpha\Delta t, t-0.5\Delta t)\right]. \tag{11c}$$

And f_α^{eqm}, f_α^-, g_α^- and F_α^- in above equations are defined as:

$$f_\alpha^{eqm}\left(\mathrm{x}-\mathrm{e}_\alpha\Delta t,t-\Delta t\right)=\omega_\alpha p\left(\mathrm{x}-\mathrm{e}_\alpha\Delta t,t-\Delta t\right)+\rho\left(\mathrm{x},t-\Delta t\right)c_s^2\left(\Gamma_\alpha-\omega_\alpha\right), \tag{12}$$

$$\begin{aligned}&f_\alpha^-\left(\mathrm{x}+0.5\mathrm{e}_\alpha\Delta t,t-0.5\Delta t\right)=\left(\tau^f_{\mathrm{x}+0.5\mathrm{e}_\alpha\Delta t,t-0.5\Delta t}-1\right)\\&\times\left[f_\alpha^{eq}\left(\mathrm{x}+\mathrm{e}_\alpha\Delta t,t\right)-f_\alpha^{eq}\left(\mathrm{x},t-\Delta t\right)\right]\end{aligned}, \tag{13}$$

$$\begin{aligned}&f_\alpha^-\left(\mathrm{x}-0.5\mathrm{e}_\alpha\Delta t,t-0.5\Delta t\right)=\left(\tau^f_{\mathrm{x}-0.5\mathrm{e}_\alpha\Delta t,t-0.5\Delta t}-1\right)\\&\times\left[f_\alpha^{eq}\left(\mathrm{x},t\right)-f_\alpha^{eq}\left(\mathrm{x}-\mathrm{e}_\alpha\Delta t,t-\Delta t\right)\right]\end{aligned}, \tag{14}$$

$$g_\alpha^-\left(\mathrm{x}+0.5\mathrm{e}_\alpha\Delta t,t-0.5\Delta t\right)=g_\alpha^{eq}\left(\mathrm{x}+\mathrm{e}_\alpha\Delta t,t\right)-g_\alpha^{eq}\left(\mathrm{x},t-\Delta t\right), \tag{15}$$

$$g_\alpha^-\left(\mathrm{x}-0.5\mathrm{e}_\alpha\Delta t,t-0.5\Delta t\right)=g_\alpha^{eq}\left(\mathrm{x},t\right)-g_\alpha^{eq}\left(\mathrm{x}-\mathrm{e}_\alpha\Delta t,t-\Delta t\right), \tag{16}$$

$$F_\alpha^-=\left(\tau_f-0.5\right)\left(\mathrm{e}_\alpha-\mathrm{u}\right)\cdot\left[\nabla\rho c_s^2\left(\Gamma_\alpha-\omega_\alpha\right)+\left(\mathrm{F}_{mg}+\mathrm{F}_s\right)\Gamma_\alpha\right]. \tag{17}$$

where τ_f is the relaxation parameters for flow field, τ_g is the relaxation parameters for the interface, and $c_s=c/\sqrt{3}$. $f_\alpha^{eq}\left(\mathrm{x},t\right)$, $g_\alpha^{eq}\left(\mathrm{x},t\right)$ are the lattice speed of sound and the equilibrium distribution function which can be written as:

$$f_\alpha^{eq}\left(\mathrm{x},t\right)=\omega_\alpha\left[\rho_0+\rho\left(\frac{\left(\mathrm{e}_\alpha\cdot\mathrm{u}\right)}{c_s^2}+\frac{\left(\mathrm{e}_\alpha\cdot\mathrm{u}\right)^2}{2c_s^4}-\frac{\mathrm{u}^2}{2c_s^2}\right)\right],\alpha=0,1,...,8 \tag{18}$$

$$g_\alpha^{eq}\left(\mathrm{x},t\right)=\begin{cases}\phi-\mu_\phi\theta_M\left(1-\omega_\alpha\right) & \alpha=0\\ 3\omega_\alpha\left(\mu_\phi\theta_M+\phi\mathrm{e}_\alpha\cdot\mathrm{u}\right), & \alpha=1,...,8\end{cases} \tag{19}$$

with

$$F_\alpha=\left(1-\frac{1}{2\tau_f}\right)\frac{\left(\mathrm{e}_\alpha-\mathrm{u}\right)\cdot\delta t}{c_s^2}\cdot\left[\nabla\rho c_s^2\left(\Gamma_\alpha-\omega_\alpha\right)+\left(\mathrm{F}_s+\mathrm{F}_{mg}\right)\Gamma_\alpha\right],\alpha=0,1,...,8 \tag{20}$$

$$\Gamma_\alpha=\omega_\alpha\left(1+\frac{\left(\mathrm{e}_\alpha\cdot\mathrm{u}\right)}{c_s^2}+\frac{\left(\mathrm{e}_\alpha\cdot\mathrm{u}\right)^2}{2c_s^4}-\frac{\mathrm{u}^2}{2c_s^2}\right),\alpha=0,1,...,8 \tag{21}$$

The classical D2Q9 model is used to obtain the discrete velocity, in which the lattice velocity e_α can be defined as:

$$\mathrm{e}_\alpha\begin{cases}(0,0)c & \alpha=0\\ (\pm1,0)c,\ (0,\pm1)c, & \alpha=1,...,4\\ (\pm1,\pm1)c & \alpha=5,...,8\end{cases} \tag{22}$$

with $\omega_0=4/9$, $\omega_{1-4}=1/9$, $\omega_{5-8}=1/36$. $c=\Delta x/\Delta t=1$ is the lattice velocity.

Magnetic field

In this part, to obtain the magnetic force, a self-correcting method is introduced. The Maxwell equation for static magnetic field is defined:

$$\nabla\cdot\mathrm{B}=0, \tag{23}$$

$$\nabla\times\mathrm{H}=0. \tag{24}$$

where B is the magnetic flux density, H is related to magnetic potential ϕ_{mg} through $\mathrm{H}=-\nabla\phi_{mg}$. So, Eq. (24) becomes:

$$\nabla \cdot \left(\mu \nabla \phi_{mg} \right) = 0 \,. \tag{25}$$

Then, a modified self-correcting process is adopted to solve the Eq. (25):
Inside the magnet:

$$\begin{cases} \nabla^2 \phi_{mg}^{k+1} = -\dfrac{1}{\mu_0}\left(1-\dfrac{1}{\omega_B}\right)\nabla \cdot \mathrm{B}^k + \nabla \cdot \mathrm{M} \\ \mathrm{B}^* = -\mu_0 \nabla \phi_{mg}^{k+1} + \mu_0 \mathrm{M} \\ \mathrm{B}^{k+1} = \mathrm{B}^k + \omega_B \left(\mathrm{B}^* - \mathrm{B}^k \right) \end{cases} . \tag{26}$$

Outside the magnet:

$$\begin{cases} \nabla \left(\mu_{mg} \nabla \phi_{mg}^{k+1} \right) = -\left(1-\dfrac{1}{\omega_0}\right)\nabla \cdot \mathrm{B}^k \\ \mathrm{B}^* = -\mu_{mg} \nabla \phi_{mg}^{k+1} \\ \mathrm{B}^{k+1} = \mathrm{B}^k + \omega_B \left(\mathrm{B}^* - \mathrm{B}^k \right) \end{cases} . \tag{27}$$

where ω_B, k are the relaxation parameter and the iteration step, respectively. This iteration will continue until $\mathrm{B}^* - \mathrm{B}^k$ is small enough and the magnetic scalar potential satisfied Eq. (23).

RESULTS AND DISCUSSION

Controlling the crown in splashing droplets on a thin layer

The schematics of the problem are depicted in Figure 1. The whole computational domain is 10D× 10D (D=100 lattice units) with a flow field domain of size 7.5D× 2.5D located at $[\mathrm{D},9\mathrm{D}]\times[5.75\mathrm{D},8.25\mathrm{D}]$ inside it. Initially, the location of the ferrofluid droplet (5D, 5.75D) is tangent to the liquid layer of the thickness of 0.25D and it falls with the non-dimensional reference velocity $U_0 = 0.025$. In this simulation, we keep the Re=500 , $We = 8000$, viscosity ratio $\mu_L / \mu_G = 20$, density ratio $\rho_L / \rho_G = 1250$ and the interface thickness $Cn = 5$. The outer four flow field boundaries are the same as above. For the magnetic field, the magnetic insulation conditions are executed on all boundaries. To facilitate observation of the splashing phenomena, the magnetization $M_0 = 80 e^3 A/m$ is chosen as the magnetic field strength.

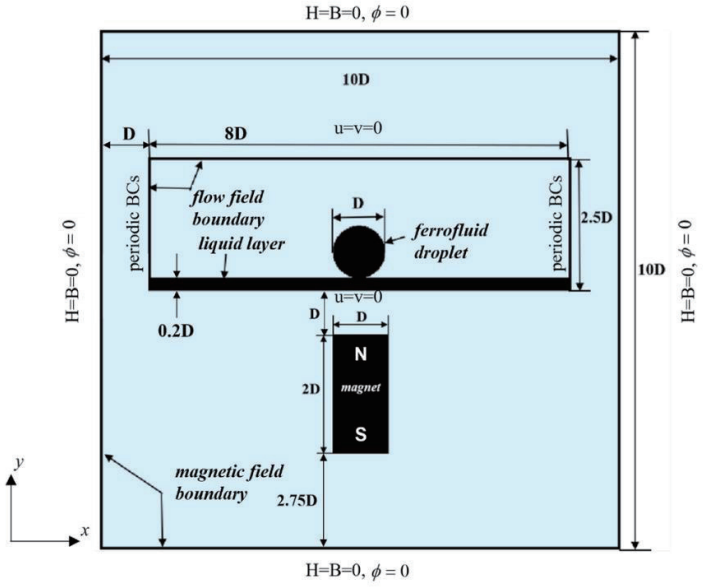

Figure 11. The initial scheme of droplet splashing on a thin layer.

First, we simulate the splashing phenomenon without a magnetic field. Figure 2 shows the evolution of droplet shape upon splashing onto a thin layer of the same fluid without any effect of magnetic field. Initially, ferrofluid droplet falling with reference velocity U_0, impacts the thin layer at time T=0.0. After the impact, the droplet and liquid layer diffuse together, and the kinetic energy gradually converts into surface energy generating a small crown (see Figure 10 at T=0.5). The crown formation at the junction of the droplet and the liquid layer continuously increases due to the rebound and inertial forces. Over time, the height of the crown increases and the distance between its left and right peaks widens, which can be seen in Figure 2 at T=0.5 to T=3.0. A similar phenomenon is reported in[56]. Note that in the later spreading stage, some circumferential instability and fingering of the rim can also be encountered near the maximum spreading diameter, if the falling speed is fast enough. As we are interested in controlling the crown's height, therefore we choose T=3.0 as the ultimate time since, at that point, the crown is completely developed, and further monitoring is unnecessary.

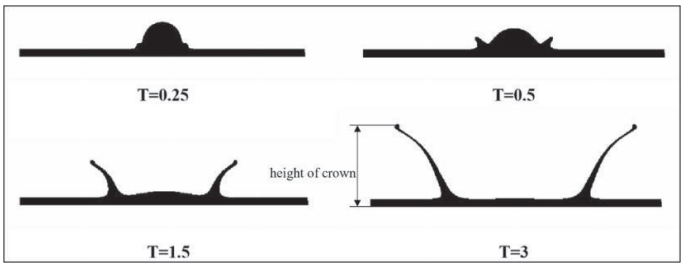

Figure 2. The evolution of splashing ferrofluid droplet on a thin layer without magnetic field.

In the above figure, we have seen that the splashing droplet generates a wide and high crown which is undesirable in many applications. As a primary goal of this study, we try to control and reduce this crown by introducing an external magnetic field. Therefore, we place a magnet of size D × 2D under the solid surface at position $[4.5D,5.5D]\times[2.75D,4.75D]$ in the magnetic field domain. Figure 3 shows the splashing process with a non-uniform magnetic field. One can see that, just like the above case after the droplet splash on a thin layer, it gives rise to a crown shape which gradually grows higher and wider from time T=0.25 to T=1.5, but later as the magnetic force becomes dominance, the crown reduces, and we get a final shape with a very small crown at t=3.0. Although the final shape of the crown with a magnetic field (see Figure 3 at T=3.0) is much smaller than the shape without a magnetic field (see Figure 2 at T=3.0), but if we closely look into the whole evolution process of Figure 3, we see that the crown is always higher and wider unless close to the final shape. The reason behind this unexpected behavior is the presence of magnetic field from the very beginning (i.e., from T=0). It is obvious that if we install a magnet at the onset, the magnetic force will pull the droplet downward towards the magnet and contribute to the kinetic energy by accelerating the droplet's falling velocity. This contribution results in a higher splash and hence fast, wider, and higher crown formation. Therefore, in Figure 3 we can see a clear crown formation even at T=0.25 and T=0.5, which is also higher than the crown in Figure 2 at the same time step. But once the crown grows higher at T=1.5, the magnetic force overcomes inertial force and pulls it back towards the magnet, hence we obtain an improved shape at T=3.0. Moreover, during the downward pull of the crown, the surface tension force also contributes to the magnetic force, and which is strong enough to break the crown against the inertial force leaving a pair of tiny droplets as appeared in Figure 3 at T=3.0. These droplets are negligibly small and have no significant effects on the expected shape.

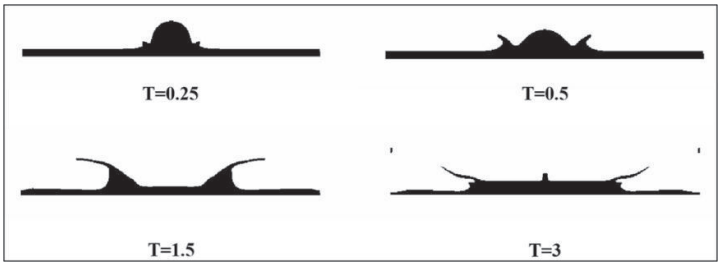

Figure 3. The evolution of splashing ferrofluid droplet on the thin layer with non-uniform magnetic field introduced at T=0.

In the preceding discussion, we have seen that the introduction of a magnetic field from zeroth time step can produce undesirable results in the beginning, and it is anticipated that the outcome can be further improved if the magnetic field is introduced later at a more suitable time step. Therefore, in this part, we place the magnet under the solid surface at time step T=0.75 instead of T=0. Figure

4 displays the evolution process at four different time steps. We can see that at times T=0.25 and T=0.5, the evolution of the crown is smaller compared to Figure 3, and it is similar to Figure 10 (without magnetic field). After the permanent magnet is placed at T=0.75, the crown growth in the existing liquid layer significantly reduces (see Figure 4 at T=1.5), and both the crown height and the spacing of the left and right peaks are lower compared to Figure 13. This illustrates that the impacting velocity and the kinetic energy are smaller when there is no magnetic field in the beginning. Finally, when the magnetic force is dominate, the crown almost disappears at T=3.0. It shows that the crown generation in the splashing phenomenon can be controlled more effectively by the introduction of external the magnetic field at a suitable time step.

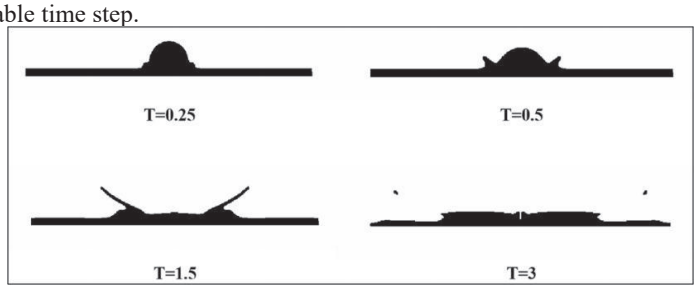

Figure 4. The development of splashing ferrofluid droplet with non-uniform magnetic field introduced at T=0.75

To provide a visual understanding of magnetic pull, we present a vector distribution of magnetic kelvin force in Figure 5(a). To make the force vectors more visible, only the right half of the crown (magnified about 110% and T=1 and $\chi = 0.5$) is shown here. From the figure, one can see that the magnetic force pulls the crown downward towards the magnet. Some of the vectors in the interface are in a tangential direction indicating that the magnetic force competes against the surface tension. Moreover, to demonstrate the effect of magnet field for different magnetic susceptibilities, we also provide a temporal relationship between the maximum kelvin force (magnetic force) at the interface and different magnetic susceptibilities (χ) in Figure 5(b). It should be noted that in two-phase magnetic fluid flows, the magnetic field effects are more prominent in the interface which leads to different shape deformations of a magnetic material [56]. From Figure 5(b), we can see that the maximum kelvin force in the interface increases with the increase in susceptibility. It is also observed that all the curves for different susceptibilities show a similar trend except for $\chi = 2.5$ from T=2.0 to 2.5. The reason behind this sudden jump is the appearance of tiny crowns at the junction point. When the ferrofluid droplet impacts the liquid thin layer, the inertial force and kinetic energy in the crown are much larger than any other part of the droplet. Therefore, the magnetic force that pulls the crown back towards the magnet, will significantly increase unless the tiny crowns merge back into the droplet or thin layer. This abnormal behavior also indicates that for highly susceptible fluids, the magnetic pull becomes too strong and leads to undesirable deformation and crown formation. This behavior can also be controlled by readjusting the magnetic field strength and other related parameters.

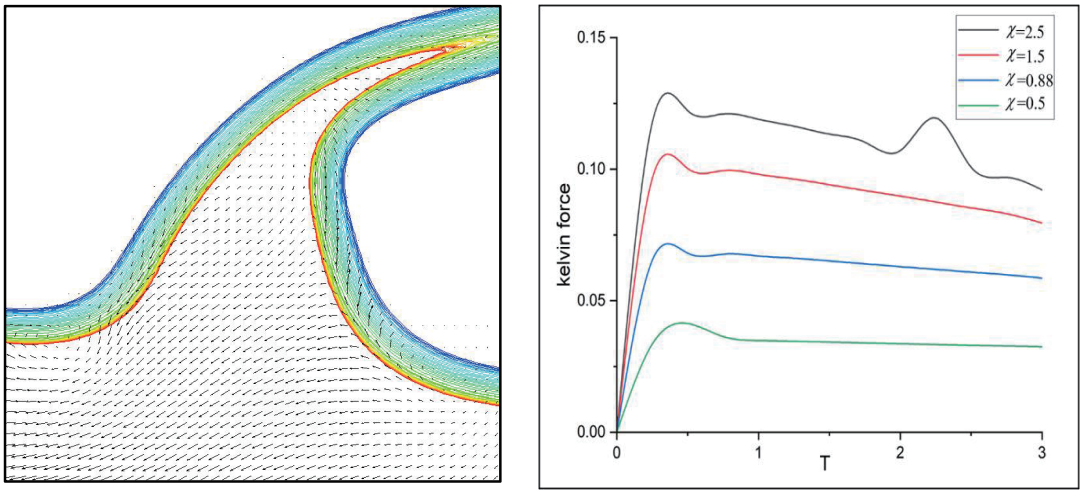

Figure 5: (a)Vector distribution of the kelvin force on the right part of crown at $\chi = 0.5$ and T=1;(b) Temporal relationship

between the maximum kelvin force (magnetic force) at the interface and the different magnetic susceptibilities

Additionally, we study the effect of introducing a magnetic field at various time steps. Figure 7(a) and Figure 7(b) illustrate the temporal evolution of length and height of crown in four distinct scenarios, respectively. Here we define the crown's height as the vertical distance between the crown's peak and the ground, and the crown's length as the horizontal distance between the crown's junction and its peak. From Figure 7(a), we can observe that when a magnetic field is not applied, the length of crown continuously increases during the whole process. In contrast, when a magnetic field is applied, the crown length first grows and then decreases after reaching the peak. Comparing these four cases, we can see that eventually the crown's length will be shorter as the application of magnetic field delays. A similar trend is seen in the evolution of crown's height. However, unlike Figure 7(a), the height of the crown at the final stage for magnetic fields applied at T=0.5 and T=0.75 is almost same, while the length of the crown is longer at T=0.5. What's more, we apply the magnetic field at five different initial time steps including T=0, T=0.5, T=0.75, T=1 and T=1.25 and compute length and height of the crown at the final stage. By comparing these five cases in Table 2, we observed that the best results are obtained for a magnetic field applied at T=0.75. When T < 0.75, the introduction of magnetic field is too early so the droplet falls too fast and the final formation of the crown is very large. Even though at T=0.5 the height of the crown is a little smaller, but the length of the crown is much longer compared to T=0.75, which is unacceptable. On the other hand, when T > 0.75, the insertion of a magnetic field is too late since the droplet has already formed a fully-grown crown. Moreover, the insertion of the magnetic field at that moment will shatter the crown peaks and from two huge secondary droplets separate from the liquid layer.

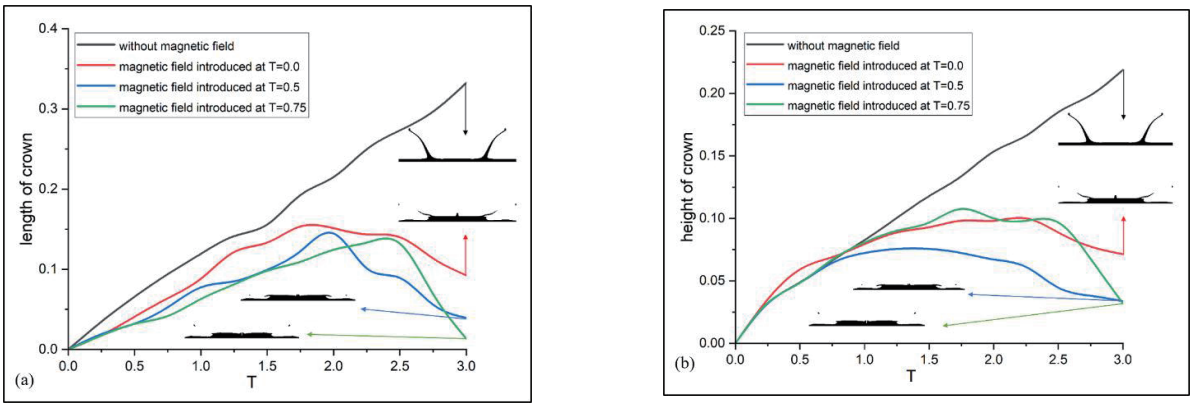

Figure 7. Temporal evolution of (a) length of the crown (b) height of the crown; when magnet is applied at different time steps.

Table 2. The height and length of the crown for five different time steps for the introduction of magnetic field.

	T=0	T=0.5	T=0.75	T=1	T=1.25
Height of crown	0.0713	0.0338	0.0319	shattered crown	shattered crown
Length of crown	0.0924	0.0394	0.0136	-	-

CONCLUSIONS

This article presents a comprehensive analysis and control of post-impact dynamics of splashing ferrofluid droplets under a non-uniform magnetic field. From the results, it is found that the magnetic field can actively control the length and height of crowns appearing on the surface of a thin layer. It is also demonstrated that, if the magnetic field is introduced later at a suitable time instead of the initial time (T=0), the crown control can be significantly enhanced. In all the studys, the phenomena are simulated both with and without a magnetic field, and the comparisons are provided in form of morphology changes.

REFERENCES

[1] Breitenbach J, Roisman I V, Tropea C. From drop impact physics to spray cooling models: a critical review[J]. Experiments in Fluids, 2018, 59(3): 1-21.

[2] Nayak L, Mohanty S, Nayak S K, et al. A review on inkjet printing of nanoparticle inks for flexible electronics[J]. Journal of Materials Chemistry C, 2019, 7(29): 8771-8795.

[3] Qin W, Xue X, Zhang S, et al. Droplet deposition and efficiency of fungicides sprayed with small UAV against wheat powdery mildew[J]. International Journal of Agricultural and Biological Engineering, 2018, 11(2): 27-32.

[4] Rein M. Phenomena of liquid drop impact on solid and liquid surfaces[J]. Fluid dynamics research, 1993, 12(2): 61-93.

[5] Yarin A L. Drop impact dynamics: splashing, spreading, receding, bouncing[J]. Annual review of fluid mechanics, 2006, 38(1): 159-192.
[6] Bourouiba L. The fluid dynamics of disease transmission[J]. Annual Review of Fluid Mechanics, 2021, 53: 473-508.

Proceedings of IWEC2023
The International Workshop of Energy Conversion
March 15-17, 2023, Kyoto, Japan

Paper No. IWEC2023-06

MEDIUM SCALE DISTRIBUTION CHAINS FOR HYDROGEN

P. Nekså [1,2,*], M.Z. Saeed [2], S. Trædal [1], I. Snustad [1], I. Koshelkov [2] and L.D. Jacobsen [2]
[1)] SINTEF Energy Research, Trondheim, Norway
*corresponding author, E-mail: Petter.Neksa@sintef.no
[2)] NTNU, Department of Energy and process engineering, Trondheim, Norway

ABSTRACT

A medium-scale hydrogen distribution chain, 3 tpd, is investigated for distribution in compressed gaseous form or in liquid form. The evaluation is complex and depends on factors like the upstream production and conditioning, the value chain energy efficiency, costs, chain flexibility, end user needs, and safety-related aspects.

The article relates primarily to energy related aspects of a medium scale distribution chain for compressed hydrogen intended for heavy vehicle transport applications. Hydrogen production is assumed based on production by electrolysis from renewable sources. Some initial considerations related to the possible integration of liquid hydrogen in parts of the chain are also made.

A compressed hydrogen value chain involves compression and re-compression in several stages, as well as a possible need for pre-cooling of the hydrogen prior to fuel tank charging. The results show a power demand for compression in the range 4.6-6.2 kWh/kg$_{H2}$ depending on the efficiency of the compression. An additional power demand for refrigeration in the range of 0-0.25 kWh/kg$_{H2}$ will be required depending on end pressure and fueling time limitations. In conclusion, the power demand in the distribution chain may be approximately 10-13 % of the power demand for electrolysis, assumed to be 50 kWh/kg$_{H2}$.

Liquefied distribution might be an alternative. The power demand needed for liquefaction and cryo-pumping may be estimated to about 10 kWh/kg$_{H2}$ based on literature data. Thus, the power demand may be doubled compared to compressed gaseous value chain, but not more than 20 % of the power needed for production.

Cost elements such as for storage tanks and compressors, required energy storage capacity, flexibility of end-use storage, as well as operational costs and safety-related issues may thus be more important factors in design and operation of medium-scale distribution chains for hydrogen if compressed is to be compared to liquified distribution.

INTRODUCTION

Hydrogen is envisioned to be an important energy carrier to decarbonize the energy system. In a "Net zero emissions by 2050" scenario, IEA estimates that the demand only within the transport sector will be about 100 Mt/y of clean hydrogen by 2050 [1], either produced by electrolysis or from fossil sources with CCS.

Locally produced hydrogen will not necessarily be bunkered directly at the production site, and value chains for transport from the production site to distributed refueling stations will be required.

The low density of hydrogen at ambient conditions requires distribution at elevated pressures, e.g. several hundred bar, or in a liquefied state at temperatures around -253 °C.

This article investigates power demand and to some extent cost-related aspects of medium-scale distribution chains, defined to be a transported volume of about 3 tpd of hydrogen. This may correspond to the filling of 1 ferry, 10 - 20 fishing vessels or 85 heavy vehicles per day. The specific power demand and cost-related factors are, however, expected to be comparable, independent of the exact demands at the filling stations.

Such value chains are currently being built in Norway and other countries, see e.g. [13], but there are still gaps in the knowledge related to the actual power demands as well as how these chains should be designed in a cost-effective way.

For a distribution chain based on compressed gaseous hydrogen, most components are available in the market, but the concepts are not yet mature. Even less mature are overall designs of mid-scale distribution chains for gaseous hydrogen and technology concepts for liquified hydrogen.

The intent of the work is to get a better overview and understanding for optimal design of such value chains. The basis for the article has primarily been taken from references [2] and [3], where the main emphasis has been on transport and filling of compressed hydrogen for heavy vehicles application.

VALUE CHAIN DESCRIPTION

A possible value chain from production to cascade filling of a tube trailer is shown in Fig. 1, while Fig. 2 illustrates a possible configuration with cascade filling at the refueling station. The tube trailer with fixed pressure vessels may potentially be replaced with a swappable container-based concept which is transported to the filling station to replace an emptied container or truck trailer.

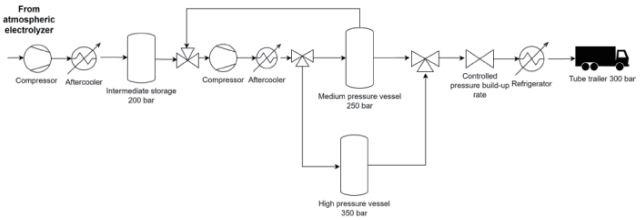

Fig. 1 Flow sheet illustration of the hydrogen production site.

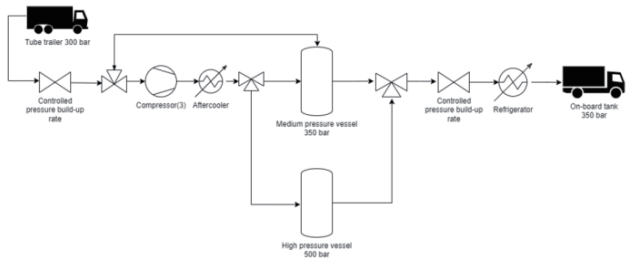

Fig. 2 Flow sheet illustration of the end-user refueling station.

The most likely concept will require cascade pressure storage at both production and refueling sites. This enables fast filling of the tube trailer and the fuel storage tanks for the end-use.

A Compressor is used to refill the MP and HP storage vessels from respectively the intermediate storage for the production site and the tube trailer for the refueling station, unless these storages has been emptied to a pressure level that may accept direct differential pressure transfer.

As illustrated, the hydrogen gas may require refrigeration in order not to exceed the maximum temperature limit of the storage tanks, typically being 65 °C for composite tanks of type IV (to 85 °C for some other types) according to the manufacturer's specifications.

Fueling protocols for light-duty vehicles have been developed by Society of Automotive Engineers (SAE) [4]. The required pre-cooling temperature may be as low as -40 °C, typical for filling to a 350 or 700 bar fuel tank, but this will vary by end pressure, ambient conditions and required filling time. For lower-pressure storage tanks, cold ambient conditions and where longer filling times can be accepted, pre-cooling may not be needed. Operational windows may be investigated by using a dynamic simulation model.

SIMULATION MODELS

Dynamic simulation models were developed and documented by [2] within the Dymola/Modelica environment and utilizing the TIL suite developed by TLK-Thermo GmbH, with thermodynamic data from NIST Refprop. The models enables to investigate the dynamics of the different parts of the value chain, as illustrated in Figure 1 and Figure 2.

Further, a model for multi-stage hydrogen compression was developed in Engineering Equation Solver (EES) by [3].

SOME MODEL ASSUMPTIONS AND RESULTS

As input to the stationary and dynamic simulation model, several assumptions are necessary. The most important assumptions are described in this section.

Storage volumes assumed for the 7 volumes indicated in Figure 1 and Figure 2 are shown in Table 1. It is assumed that the tube trailer is emptied at the refueling station down to a pressure of 20 bar, while the transport pressure is 300 bar. Each trailer can transport a nominal capacity of 958 kg of H_2, meaning that at least three trailers/swappable containers must be delivered from the production site to the end-user refueling station(s) per day.

Table 1 Volume and pressure rating of storge tanks

Storage tank	Pressure rating (bar)	Volume (m^3)
Intermediate (production)	200	500
Medium pressure, MP (production)	250	500
High pressure, HP (production)	350	200
Tube trailer	300	45
Medium pressure, MP (refueling)	350	40
High pressure, MP (refueling)	500	30
End user on-board fuel tank	350	1.6

Thermal conditions in the storage tanks were modelled using data relevant to composite tanks for hydrogen of type IV to obtain realistic heat exchange with the ambient based on data from a vendor, as well as for steel tanks assumed to be used for the intermediate and cascade storage tanks at the production site. Maximum allowed temperature was assumed to be 65 °C.

As input to the dynamic simulation tool a stage efficiency curve for the compressor was used, with a maximum of 55 % at a pressure ratio of 5, as shown in Fig. 3. The curve is arbitrary assumed based on experienced values from oil-free refrigeration compressors since no exact data was found from the compressor vendors. For the relevant capacity compressors in this study, reciprocating labyrinth piston or diaphragm compressors would be typical options, as well as more novel ionic liquid compressors. Intermediate cooling between stages and before charging to the pressure vessels was assumed to be 70 °C.

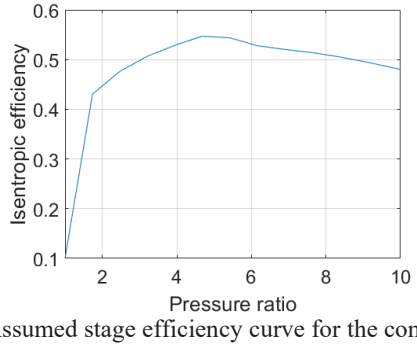

Figure 3 Assumed stage efficiency curve for the compressors in the dynamic simulation model.

Compressor power demand at the production site was also calculated at stationary conditions using EES, assuming a constant stage efficiency of 0.7 and intermediate cooling down to 20 °C, thus representative of a more optimistic scenario. Fig. 4 and Fig. 5 illustrate power demand for compressing from respectively 1 bar and 200 bar, as well as feasible reachable high pressure with a given number of stages for the compressor, indicated by the full lines. Dotted lines indicate unfeasible pressures given a maximum discharge temperature of 180 °C. In practice, the number of required stages may be lower if heat loss from the cylinder is considered.considered The assumed stage isentropic efficiency of 0.7 is deducted from [7], being representative for a medium size reciprocating compressor (190 kg/h) compressing from 30 to 450 bar.

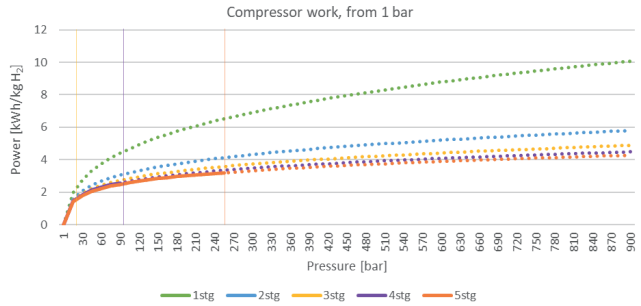

Figure 4 Compressor power demand for hydrogen compression from 1 bar for different number of stages. Full lines indicating reachable pressure assuming a maximum discharge temperature of 180 °C.

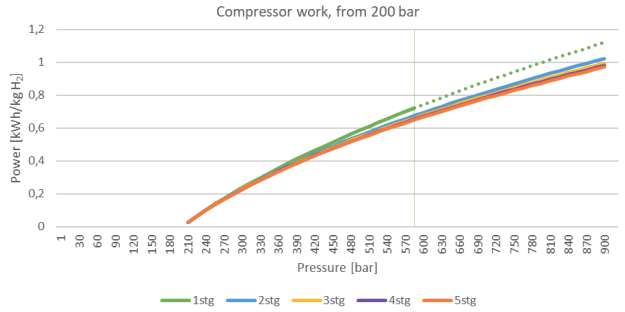

Figure 5 Compressor power demand for hydrogen compression from 200 bar for different number of stages. Full lines indicating reachable pressure assuming a maximum discharge temperature of 180 °C.

In practice, the required power demand also will depend on other factors, such as the compressor station's part load control. Capacity control using high-pressure by-pass is for instance less efficient than speed control, but also more costly.

PRESSURE AND TEMPERATURE CONDITIONS

To investigate the pressure and temperature conditions in the value chain, a dynamic simulation model is required. Important restrictions are also the acceptable temperatures in the storage tanks, typically being maximum 65 °C and minimum -40 °C.

During filling, the heat exchange with the ambient will determine how fast the filling and emptying can be performed and still avoid violating the temperature limitations. Figure 6 illustrates temperature variation in a storage tank assuming adiabatic filling from 20 to 300 bar for different pre-cooling temperatures. As can be observed, pre-cooling to -40 °C is required to avoid reaching the temperature limit of 65 °C. In reality, the filling will not be adiabatic, but the condition will be representative of the fast filling of an end user storage tank. The pre-cooling temperature will also influence the charge filled into the storage tank. Some degree of overpressure may thus be required if end pressure after temperature equalization should be at the nominal level.

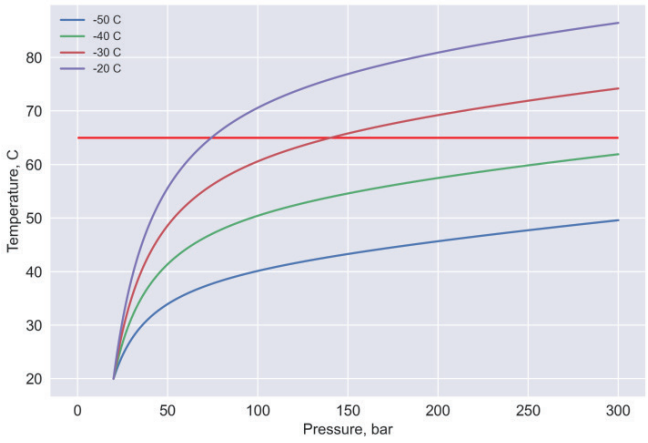

Figure 6 Influence of pre-cooling temperature during adiabatic filling.

When the filling time is long enough, heat exchange with the ambient will play an important role. Figure 7 shows filling at a rate of 1 MPa/min with a pre-cooling temperature of -10 °C at different ambient temperatures. For an ambient temperature of 10 °C, the tank may be filled without violating the maximum temperature if the end pressure is 300 bar.

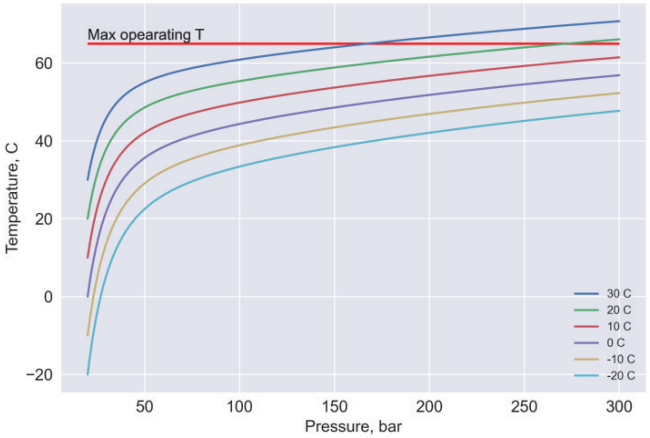

Figure 7 Temperature results for filling at 1 MPa/min and pre-cooling at -10 °C with varying ambient temperature.

The lower temperature limit also restricts the operation of high-pressure storage tanks. Figure 8 illustrates emptying a storage tank from 300 to 80 bar for different pressure decrease rates. As illustrated, emptying at a rate of 0.5 MPa/min can be accepted without reaching the lower temperature limit,

resulting in emptying within 43 min. An ambient temperature of 20 °C is assumed.

In practice, it is possible to design the value chain so that pre-cooling only is required during fast filling of the tube trailers and/or end-user fuel tank filling. If the slow filling is acceptable, e.g. during the night or if a lower storage pressure is accepted, pre-cooling may be avoided.

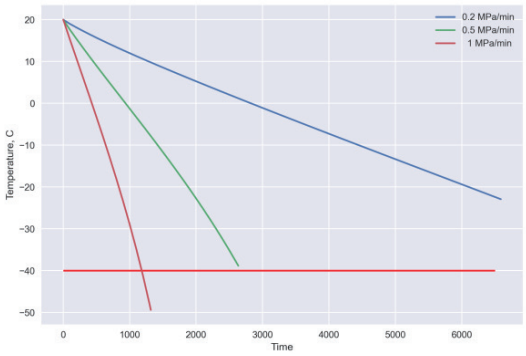

Figure 8 Temperature in storage tank during emptying of the vesselstorage tank from 300 bar to 80 bar for varying pressure decrease rates

In our study, pre-cooling to -40 °C is assumed for both tube trailer filling and for filling to the end-user fuel tank and assumed ambient temperature is 20 °C.

Figure 9 shows the pressure development of tube trailers 1 to 3 when charged from respectively the MP and HP storage tanks at the production site. Starting pressure is assumed to be 80 bar with a pressure ramp rate of 3 MPa/min, resulting in a filling time of about 9 min. The refilled mass is 658 kg, considerably less than the rated capacity of 958 kg. This is due to the assumed starting pressure, indicating that the specified capacity will be highly dependent on the pressure at return.

As may be observed, slight overpressure during filling is required to achieve the transport pressure of 300 bar after temperature equalization with the ambient.

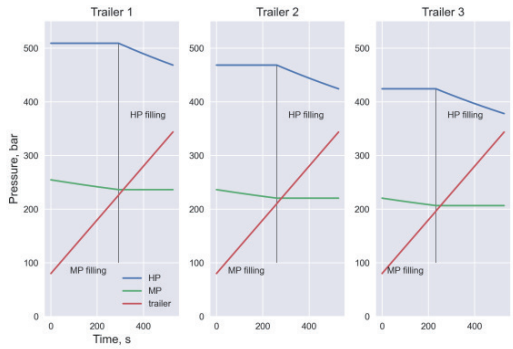

Figure 9 Pressure in storage tanks and trailer during tube trailer filling from 80 bar to 300 bar for three subsequent trailers

Corresponding temperature variations of the hydrogen in the tube trailers and the storage tanks are shown in Figure 10. The results indicate that assumed pre-cooling and pressure drop in the storage vessels are adequate to stay well within operational temperature boundaries at the assumed conditions, even without extra heat inflow from the ambient.

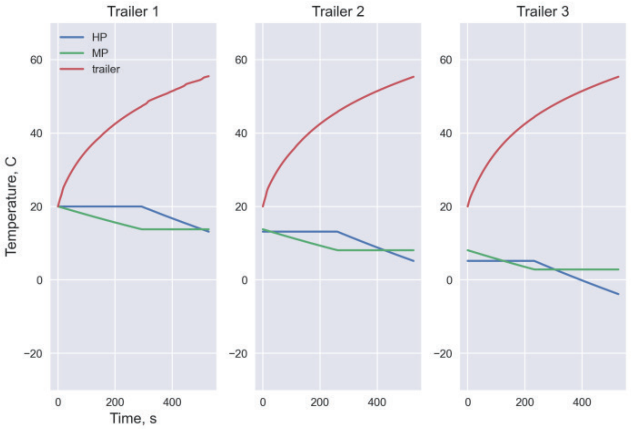

Figure 10 Temperature variations during trailer fillings.

Figure 11 shows the pressure variations of the storage tanks during charging the HP and MP storages from the intermediate storage, see Fig. 1. Hydrogen is first charged by the compressor to fill the MP storage. Charge from the MP storage is then compressed to fill the HP storage from the MP storage. In the last sequence, the MP storage is refilled with the charge from the intermediate storage. A slight pressure reduction in the HP storage may also be observed, resulting from heat dissipation to the ambient.

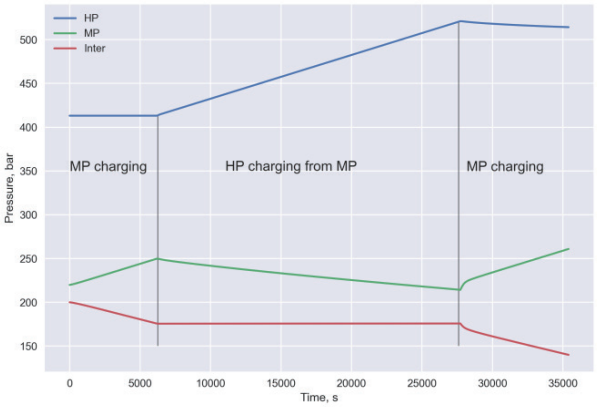

Figure 11 Pressure in intermediate, medium and high pressure storage tank during cascade charging at the production site.

Figure 12 presents corresponding temperature variations at a filling rate of 1.8 Mpa/min, with total charging time of about 10 h. As shown, the temperature variations show only slight deviations from the ambient temperature.

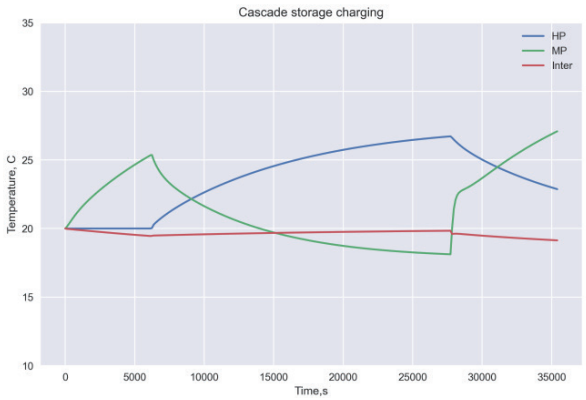

Figure 12 Temperature variations during the cascade charging at the production site.

At the refueling station it is assumed that heavy vehicles are refilled from 20 to 350 bar with a charge of 35.4 kg within 13 min.

Fig. 13 shows the pressure in the tanks of the refueling station and the onboard tank for filling of the two first vehicles after the refueling station have been recharged. The filling results gives only a small decrease of the HP and MP storage pressures. Filling of the onboard tank is done to an over pressure of about 410 bar to reach the nominal pressure of 350 bar after temperature equalization.

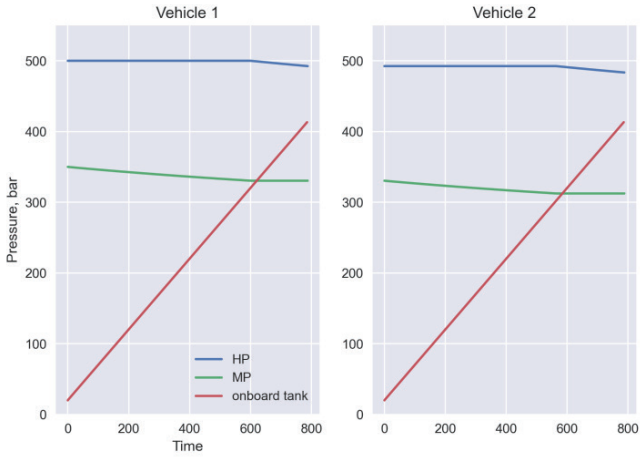

Figure 13 Pressures during end-user refueling for vehicles 1 and 2.

Fig. 14 shows corresponding pressures during filling of vehicles 15 to 18. When the MP storage reaches its lower pressure limit of 80 bar, the last vehicle is filled only from the HP storage. The last tank is refilled only from the HP storage. Further it is indicated refilling of the HP storage by compression from the MP storage during filling of vehicle 15 and 17.

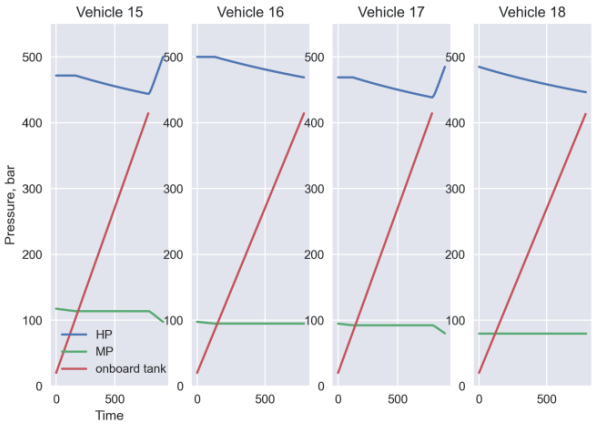

Figure 14 Pressures during end-user refueling for vehicle 15 to 18.

Fig. 15 shows corresponding temperatures variations in the different storage tanks for vehicle 15 to 18. Here it is observed that the assumed scheme of end-user refueling leads to a violation of the operational temperature limit of the MP storage, reaching as low temperature as -84 °C.

If consecutive refueling of 18 trucks is performed, a filling time of around 3 hours is needed. It is then expected that heat gain from the ambient will result in a higher operational temperature, thus avoiding the minimum temperature limitation violation. Alternative strategies may be to use a larger MP storage volume, or to refill the MP storage earlier. This will be case specific and should be investigated for the conditions to be applied for a specific case.

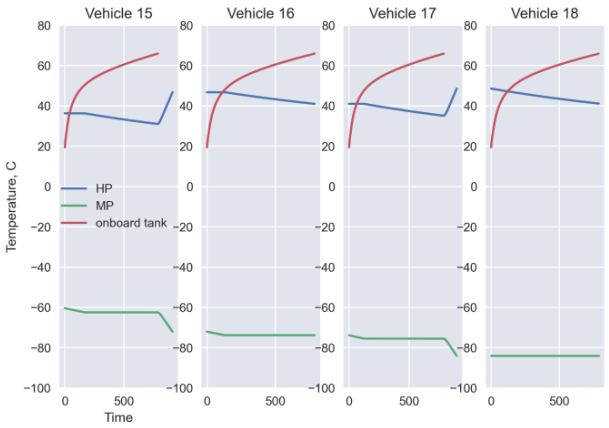

Figure 15 Temperature variations for final filling of vehicles 15 to 18

The cascade charging at the refueling station is assumed to start with all storage tanks at an ambient temperature of 20 °C, after temperature equalization from the conditions displayed in Fig. 15.

Fig. 16 shows the pressure development of the delivery trailer and the MP and HP storage tanks. Charging of the MP tank is partly performed with throttling until the pressure levels are equalized. Further charging is performed using the compressor.

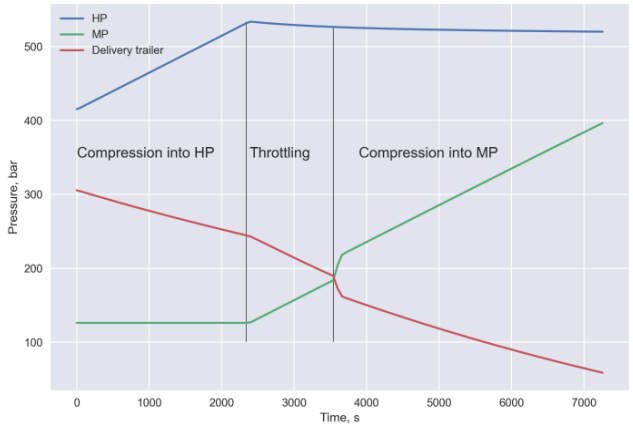

Figure 16 Pressure in storage tanks and delivery trailer during filling of the cascade storage at the refueling station.

Fig. 17 shows the corresponding temperatures of the various tanks. With the assumed charging rate and ambient temperature, the tanks stay well within the operational temperature limits. This may, however, vary depending on the ambient conditions and filling rates for a specific case.

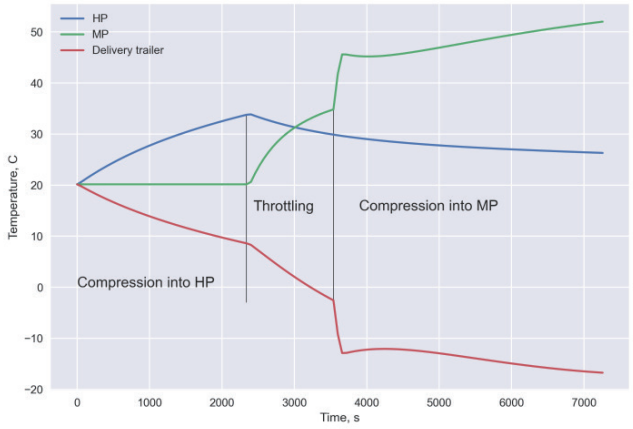

Figure 17 Temperature in storage tanks and delivery trailer during charging of the storage at the refueling station.

POWER DEMAND AT THE PRODUCTION SITE

Hydrogen production by electrolysis is the most power demanding operation in the overall hydrogen value chain, from production to storage in the end-use fuel tank. The demand will vary depending on the efficiency of electrolysis technology used and with the pressure level of production. For production at atmospheric pressure, a ballpark value for the power demand of 50 kWh/kg$_{H2}$ produced can be stated based on vendors' specifications available online, e.g. by [5], for alkaline electrolysers (AEL).

After production, the hydrogen needs to be compressed, see Figure 1. In our case the first compression is to a 200 bar intermediate storage. If hydrogen is produced at ambient pressure, which is the most common for alkaline electrolysers (AEL) [5], the power demand for compression maybe 3-4.6 kWh/kg$_{H2}$ depending on the assumed compressor efficiency. The lower value represents a constant stage isentropic efficiency of 0.7 with intermediate cooling to 20 °C, while the higher representing a lower average stage efficiency compressor of 0.41 according to values displayed in Fig. 3, assuming intermediate cooling to 70 °C. For the purpose of this article, we will use the span in compression power demand.

If the hydrogen is produced at elevated pressures, for which different vendors offers proton exchange membrane electrolysers (PEMEL) producing at 30 bar, the compression to 200 bar intermediate pressure may be reduced to about 1.2 kWh/kg$_{H2}$, when assuming an isentropic stage efficiency of 0.7 with intermediate cooling to 20 °C. Obviously, starting compression at 30 bar would be an advantage from a compressor power demand point of view, but it will be a cost optimization task to find out what is most beneficial, depending on investment cost of the different electrolysers packages, the efficiency of the electrolysers, electricity price, compressor cost, etc.

It is further reasonable to assume that the efficiency of PEMEL will be lower than for AEL to the extent that the reduced power demand for compression will be more than nullified [6], thus AELs producing at atmospheric pressure is assumed here. In the future, this balance may change as high-pressure electrolysers develop.

Further, power for compression is required at the production site for compression from the intermediate pressure to the cascade storage vessels at 250 and 350 bar respectively. Compressed hydrogen from these vessels is used to feed into a tube trailer designed for 300 bar transport pressure. Use of the dynamic model gives an estimation of a power demand for thee compression of 0.71 kWh/kg$_{H2}$.

A power demand of 0.11 kWh/kg$_{H2}$ for cooling of the hydrogen down to -40 °C prior to charging the tube trailer is also required to enable fast filling at an ambient temperature of 20 °C. This power demand corresponds to a COP of the refrigeration plant of 1.94. Use of CO_2 (R744) as refrigerant is a likely alternative for such a refrigeration plant.

POWER DEMAND AT THE REFUELING STATION

In the assumed hydrogen distribution chain, emptying a trailer from 300 bar down to 20 bar and refilling of the HP and MP storages requires a multi-stage compressor at the end-user refueling station, since the nominal MP storage pressure is at 350 bar. Only the initial charging of the medium-pressure storage from 80 bar can be done by direct transfer.

The power demand for compression is estimated to 0.87 kWh/kg$_{H2}$, while an additional power demand for the refrigeration plant to support fast filling with an initial temperature of -40 °C is estimated to be 0.13 kWh/kg$_{H2}$.

The results above correspond well with power demand results calculated by HDSRAM tool developed by the Argonne national laboratory in US [12].

POWER DEMAND SUMMARY

Table 1 summarizes the specific power demands in different parts of the compressed hydrogen value chain.

Table 1 Summary of power demands

Section of chain	Compression kWh/kg$_{H2}$	Cooling kWh/kg$_{H2}$	Sum kWh/kg$_{H2}$
Intermediate storage	3-4.6	0	3-4.6
To cascade storage	0.71	0.11	0.82
At refueling station	0.87	0.13	1.00
Total	**4.56-6.17**	**0.24**	**4.82-6.41**

As shown, the overall power demand varies from 4.8-6.4 kWh/kg$_{H2}$, depending on the assumed compressor stage efficiency. This corresponds to about 10-13 % of the demand for atmospheric production of hydrogen by AEL electrolysis, assumed to be 50 kWh/kg$_{H2}$. Possible extra power demand resulting from the part-load operation of compressors are not considered.

COMPARISON TO DISTRIBUTION OF LIQUID H_2

The compressed gaseous value chain investigated in this paper, starting from atmospheric hydrogen at the production site, to filling of the end-user fuel tanks at 350 bar has a power demand of 4.8 to 6.4 kWh/kg$_{H2}$, depending on the assumed compressor efficiency.

State of the art liquefaction plants with a capacity of 5 tpd use about 10 kWh/kg$_{H2}$ [8], and it is expected that this may be lowered in the future if liquid hydrogen (LH_2) is produced with an energy carrier perspective in mind, demanding a higher energy efficiency of the liquefaction plants.

If compressed storage at end use is demanded, the embedded exergy content of LH_2 at a temperature of -253 °C, can be utilized to greatly reduce the power demand for pressurization, for instance, by performing cryo-pumping of liquid hydrogen, with a subsequent temperature conditioning to the required pre-cooling temperature for fast filling. [9] indicates that the power demand for cryo-pumping at the filling station may be about 1.3 kWh/kg$_{H2}$.

Liquid distribution to the filling station also opens the possibility of storing hydrogen as liquid in the fuel tank of the end-user. The storage capacity will in this case increase around 4 times for the same volume requirement. This will be an advantage for power-demanding transport applications, such as long-haul trucks or maritime vessels. Further, it may reduce the footprint of storage and infrastructure at the refueling station, as well as the number of distribution trucks required.

From the power demand values indicated above, the power demand after production may indicatively increase to the double of that of the compressed gaseous distribution, but still only be about 20 % of the power demand for hydrogen production by electrolysis.

CONCLUSION

Results from this paper show that the power demand of a medium-scale hydrogen distribution chain for compressed gaseous hydrogen is in the range of 4.8 to 6.4 kWh/kg$_{H2}$, being about 10% of the power demand for hydrogen production by electrolysis.

Compressed hydrogen filling, transport and refueling requires relatively complex cascade filling systems both at the production site and at the refueling station(s). Optimization of these systems from an energy- and cost perspective requires detailed dynamic simulation models.

This work only considers the energy aspects of such value chain analysis, but also indicates cost-related aspects such as required storage volumes and compressor demands.

Initial evaluation of a value chain with liquefaction at the production site and distribution of liquid hydrogen to the filling stations indicates that the power consumption after production may double. However, the lesser need for compressors and the flexibility for end-user storage, either as compressed or in liquid state, may lead to a cost-optimal alternative.

Further studies should evaluate the different value chains in more detail, preferably including cost elements in a techno-economical evaluation.

ACKNOWLEDGMENTS

This paper was partly supported by funding from the RCN project ZeroKyst (P.no. 328718) [13] and the RCN centre FME HYDROGENi (P.no 333118) [14]. The authors acknowledge the industry partners in these projects.

REFERENCES

[1] IEA Global Hydrogen Review 2021, International Energy Agency, Website: www.iea.org

[2] Koshelkov, I., 2022, "Evaluation of mid-scale hydrogen distribution chains for compressed hydrogen", Master's thesis in Natural Gas Technology, NTNU, Dept of Energy and Process Engineering, Trondheim, Norway, June 2022

[3] Jacobsen, L.D., 2022, "Evaluation of mid-scale hydrogen distribution chains for hydrogen, Project thesis, NTNU, Dept of Energy and Process Engineering, Trondheim, Norway, december, 2022

[4] SAE J2601, "Fueling Protocols for Light Duty Gaseous Hydrogen of Surface Vehicles", SAE international, May 2020

[5] NEL, 2021, "Nel Hydrogen Electrolysers, The World's Most Efficient and Reliable Electrolysers," 2021. [Online] https://nelhydrogen.com/wp-content/uploads/2020/03/Electrolysers-Brochure-Rev-D.pdf

[6] Berstad, B. et al, 2022, "Liquid hydrogen as prospective energy carrier: A brief review and discussion of underlying assumptions applied in the value chain analysis" J of Renewable and Sustainable Energy Reviews, 154 (2022) 111772, https://doi.org/10.1016/j.rser.2021.111772

[7] Cebolla, O.R., Dolci, F. and Weidner, E.R., "Assessment of hydrogen delivery options", EUR 31199 EN, Publications Office of the European Union, Luxembourg, 2022, ISBN 978-92-76-56421-8, doi:10.2760/869085, JRC130442.

[8] Decker, L., "Liquid hydrogen distribution technology", Presented at the Hyper closing seminar, 11 December 2019, Brussels, https://www.sintef.no/globalassets/project/hyper/presentations-day-2/day2_1105_decker_liquid-hydrogen-distribution-technology_linde.pdf; 2019.

[9] Linde AG, "Tomorrow's fuel today. Linde H_2 refueling technologies", Tomorrows-fuel-today-Linde-H2-refueling-technologies_tcm19-632211.pdf (linde-engineering.com)

[12] Argonne National Laboratory, "Heavy-Duty Vehicle Refueling Cost models (HDRSAM)" Heavy-Duty Refueling Station Analysis Model (anl.gov)
[13] Zerokyst Green Platform project, RCN project no. 328718, https://zerokyst.no/en/forskning/fleksibel-og-konkurransedyktig-hydrogenforsyning/
[14] FME HYDROGENi Research Centre, RCN project no. 333118, https://hydrogeni.no/organisation/

Proceedings of IWEC2023
The International Workshop of Energy Conversion
March 15-17, 2023, Kyoto, Japan

Paper No. IWEC2023-07

RECYCLING OF FISHERIES WASTE

H. kobatak*, S. Tanaka, Y. Suzuki and T. Goto
Doshisha University, Kyotanabe, Japan
*corresponding author, E-mail: hkobatak@mail.doshisha.ac.jp

ABSTRACT

With a part of exception such as, such as scallops or oyster shells, which are utilized for fertilizer, feed, soil conditioner, or fishing ground preparations, most of the shells from aquaculture residue are incinerated as general waste at or above 1000 ℃ in Japan. A huge amount of fuels and cost are required for the incineration. To utilize the products obtained by the processing, such as calcium oxide for heat storage materials, deodorants, or fungicide, lowering the incineration or decomposition temperature is indispensable for cost reduction. As the first approach, the incineration temperature of fisheries waste and incineration kinetics was experimentally investigated. Thermal decomposition temperatures of shells and spines were lower than that of calcite reagent. Instead of the difference of thermal decomposition temperature, the activation energies are scarce difference in the activation energy. This difference could be caused by the microstructures of the shells and spines.

INTRODUCTION

Nowadays, aquaculture is developing worldwide and 40 % of all marine aquaculture products in 2008 were produced through shellfish cultivation [1,2]. The increase in shellfish production causes an increase of fishery waste, which includes culture materials, and the shells of marine organisms has been increased attendant on the development of the aquaculture. Among of the fishery waste, shells make up a high proportion. These fishery wastes are incinerated at temperature above 1000℃. Abolishment of fishery wastes is an environmental and economic strain and a distraction from the sustainable development of the fishery industry. As an example, shells accounted for 46 % of all fishery waste generated in Hokkaido Prefecture in Japan in FY2018; the weight of shells alone as fishery waste amounted to 140 kilotons [3].

Meanwhile, CaO-based materials, which can be obtained through the thermal decomposition of the calcium carbonate, have been attractive thermal energy storage materials due to their high thermal energy density in the reaction of $CaO+CO2 \leftrightarrow CaCO_3$ [5] or $CaO + H_2O \leftrightarrow Ca(OH)_2$ [6]. The main component of the shells is calcium carbonate, so that it is expected to use this thermal energy storage materials. If the Ca-based materials can be obtained at lower temperature in the thermal incinerate temperature, the fishery waste could have potential for the practical use as the thermal storage materials.

This article reports the results of the experimental investigation of the thermal decomposition temperature and its kinetics to evaluate the possibility for lowering thermal decomposition temperature of fish wastes and for developing the lower energy and CO_2 emission technique for the fish waste disposal, and for the use as the thermal storage materials [7, 8].

EXPERIMENTALS

The samples used for the experiments were shells or spines of gastropods (*Volutharpa perryi*), bivalves (*Corbicula japonica*, *Crassostrea gigas*, *Mizuhopecten yessoensis*, *Mytilus galloprovincialis*, *Hiatella orietalis*), barnacles (*Acorm barnacle*), tube worms (*Dexiospira foraminosus*), and sea urchins (*Mesocentrotus nudus*, *Glyptocidaris crenularis*). These samples are fishery wastes that can be obtained relatively easily in the Aomori Prefecture. Among them, shells of *H. orietalis* and *D. foraminosu* are periphyton which has been collected from scallop farming nets. For the comparison, analytical grade calcite (Wako, 99.95%) was also used in the experiment.

The surface deposits on these shells and spines were removed using a wire brush or tweezers, then washed by tap water to obtain a clean specimen. The cleaned samples were crushed in a porcelain mortar, then dried in an oven at 110℃. The dried powder particles were allied by their size using a sieve, then sorted in size in the range between 63 μm and 125 μm.

The powder specimen was put in a container (φ = 5 mm, h = 2.5 mm) and then installed in a DSC (Differential Scanning Calorimetry: Seiko Instrument Inc. DSC6300). The specimen was heated up with the temperature increasing rate of 20℃ min^{-1}. The DSC measurements are conducted in Ar atmosphere (10^5 Pa) with the flow rate of 30 ml min^{-1}. To prevent the generation of dioxin, the thermal decomposition process would be required at temperature above 800 ℃. For this reason, the reaction proportion of the specimen at 830℃ was investigated. In

addition, the reaction completion temperature was investigated for each sample.

In addition, the temperature-increasing rate for each experimental run was changed from 5 K min^{-1} to 40 K min^{-1} for the samples of calcite reagent, *Mizuhopecten yessoensis*, *Crassostrea gigas*, and *Mesocentrotus nudus* to determine the activation energy on the thermal decomposition reaction of calcite. The temperature detected by the DSC was calibrated using the melting point of pure Al and Ag.

RESULT AND DISCUSSION

Figure 1a shows the reaction complete temperature of calcite, shells, sea urchin shells, and spines. The error bar in the figure indicates the standard deviation in the measurement for each sample. Calcite reagent, *M. galloprovincialis* and *A. barnacle shells*, had the highest reaction complete temperature reaching to 880 ± 10℃ and 883 ± 9℃, respectively. Meanwhile, the reaction complete temperatures of *G. crenularis*, *M. nudus*, and *V. perryi* were about 60 K lower than that of calcite reagents. The bivalves have thermal decomposition temperatures ranging between 863 ± 4℃ and 882 ± 2 ℃. *D. foraminosus* completed their thermal decomposition reaction at 870 ± 12℃ . The calculation of the t-test showed that these reaction completion temperatures, except those of *M. galloprovincialis*, *A. barnacle*, and *D. foraminosus*, were statistically and significantly lower than that of Calcite reagent at the $P < 0.01$ level.

Figure 1b shows the reaction proportion of the shells and urchins at 830℃, coupling with that of calcite reagent. The calcite reagents were thermally decomposed only 42% at this temperature, while the shells of *G. crenularis* and *M. nudus* were almost completely decomposed. Shells of *V. perryi* also had the high reaction proportion reaching to 95 % at this temperature. The reaction proportion range of the shells of bivalves at this temperature were between 58 ± 0.5 % and 74.5 ±1.8 %. The reaction proportion of the shells of *D. foraminosus* and *A. barnacles* had lower reaction proportion than these shells and relatively close to that of calcite reagent. From the *t*-test, it was found that the reaction proportion of shells and spines at 830℃ was statistically and significantly higher than that of calcite reagent with the $P < 0.01$ level, while *M. galloprovincialis*, *A. barnacle*, and *D. foraminosus* had closer reaction proportion to the calcite reagent.

According to Ozawa [9], the relationship between the logarithm of the temperature increasing rate, $\ln(\partial T/\partial t)$, and the characteristic temperature, T_{cha}, can be seen in the reaction with the following equation:

$$\ln\left(\frac{dT}{dt}\right) = A - \frac{E_a}{RT_{cha}} \quad (1)$$

Here, E_a denotes the activation energy of the reaction and A denotes the pre-factor, which relates to the collision rate of the molecules, presumably corresponding to the CO_2 gas flux from the calcite in this case. When the reaction-complete temperature, T_{RC}, was employed as the characteristic reaction temperature, T_{cha}, we can obtain the reaction's kinetic parameters from the reaction-complete temperature related to the temperature-increasing rate.

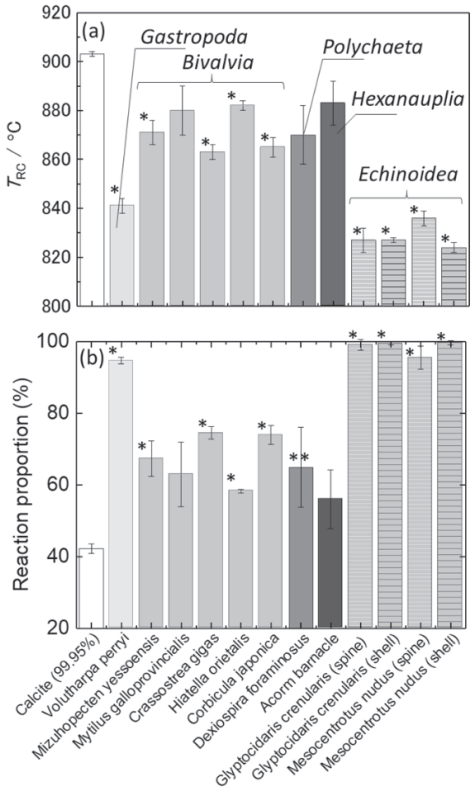

Fig. 1. Comparison of (a) reaction complete temperature and (b) reaction proportion at 830 ℃ for all samples investigated in this research. The error bar in the figure indicates the standard deviation in each measurement. Significant difference between the calcite reagent and the samples are indicated as * ($P < 0.01$), and ** ($P < 0.05$). These figures are referred from the reference [7].

Figure 2 shows the relationship between the inverse number of the thermal decomposition completed temperature, $(1 / T_{RC})$, and the logarithm of the temperature increasing rate, $\log(dT/dt)$. There is a linear relationship between the inverse number of T_{RC} and $\log(dT/dt)$ for calcite reagent, shells of M. yessoensis, and C. gigas, and spines of M. nudus with the sorted grain size from 63 μm to 125 μm (Fig. 2a). When the reaction rate is lower, the reaction continues to a higher temperature, meaning it has a lower $(1 / T)$ value. Therefore, by lowering the reaction rate, the line is shifted to the left. It was found that the reaction rate descends in the following sequence: spines of *M. nudus*, shells of *C. gigas*, and *M. yessoensis*, and calcite reagent.

The effect of size on thermal decomposition kinetics can be evaluated using data from the thermal decomposition reaction of the shells of M. yessoensis (Fig. 2b). As can be seen for the calcite samples with the grain size of from 63 μm to 125 μm, the linear relationship between the inverse number of T_{RC} and dT/dt can be observed for the different grain sizes of *M.*

yessoensis. As grain size increases, the reaction rate lowers in the case of the thermal decomposition process.

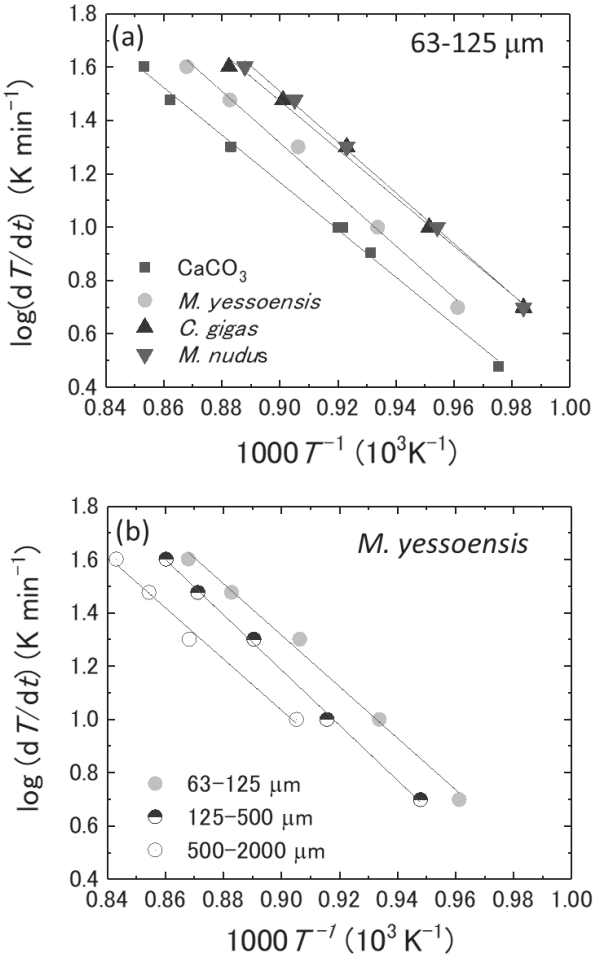

Dig. 2. Logarithmic plot of the relation between logarithm of the temperature increasing rate log (dT / dt) and inverse number of the reaction complete temperature (1 / T) for (a) (■) CaCO3 reagent, (●) M. yessoensis, (▲) C. gigas and (▼) M. nudus with same sample particle size between 63 and 125 μm, and for (b) M. yessoensis with a different sample size of (●) 63-125μm, (◓) 125-500 μm, and (○) 500-2000μm. These figures are referred from the reference [8]. Note that the temperature in these figures used the unit of absolute temperature.

The all the plots in the figure showed the linear relation and these plots are parallel to each other indicated that the activation energy of the thermal decomposition of calcite reagent. This inferred that the rate-limiting process of the thermal decomposition process is the CO_2 gas flux, which emitted from the surface of the sample. These highly reactivity of the shells could be used for the efficient thermal exchange for the heat storage. In addition, this reactivity could be also useful for material recycling using the molten salt electrolysis process [10].

ACKNOWLEDGMENTS

This work was supported by JSPS KAKENHI Grant Numbers Grant-in-Aid for Challenging Research (Pioneering) 20K21854.

REFERENCES

[1] FAO. 2011, Global aquaculture production 1950-2009.
[2] Yao Z, Xia M, Li H, Chen T, Ye Y, Zheng H., 2014, Bivalve shell: Not an Abundant useless waste but a functional and versatile biomaterial, Env. Sci. Tech. 44:2520-2530.
[3] http://www.pref.hokkaido.lg.jp/sr/ssk/30haikibutu.pdf
[4] Shimono I, Kobayashi T., 2002, Thermal decomposition behavior of scallop shell. Report Hokkaido Ind Technol Center 7:56–58.
[5] Obermeier J, Mueller K, Karaginnakis G, Stubos A, Arlt W., 2015 A novel thermochemical energy storage and transportation concept based on concentrated solar irradiation-aided CaO-looping, AIP Conf. Proc. Solar PACES 2015 050033-1-8.
[6] Uchiyama N, Takasu H, Kato Y., 2019, Cyclic durability of calcium carbonate materials for oxide/water thermochemical energy storage, Appl. Therm. Eng. 160:113893-1-6.
[7] Kobatake H, Kirihara S., 2019, Lowering the incineration temperature of fishery waste to optimize the thermal decomposition of shells and spines, Fisheries Science 85:573–579.
[8] Kobatake H, Akahira A, Ioka S, Kirihara S., 2022, Thermal decomposition kinetics of synthesized calcite and fishery wastes such as shell of bivalves, and spines of a sea urchin, Eco-Engineering 34 27-35.
[9] Ozawa T., 1970, Kinetic analysis of derivative curves in thermal analysis, J. Therm. Anal. 2:301-324.
[10] Goto T., 2022, CO_2 utilization by molten salt electrolysis, J. Sur. Fin. Soc. JPN. 73:592-597.

Proceedings of IWEC2023
The International Workshop of Energy Conversion
March 15-17, 2023, Kyoto, Japan

Paper No. IWEC2023-08

REDUCTION IN ENERGY CONSUMPTION IN WATER PURIFICATION TECHNOLOGY WITH WATER

T. Kuwahara*
Department of Mechanical Engineering, Nippon Institute of Techinology, Saitama, Japan
*corresponding author, E-mail: takuya.k@nit.ac.jp

ABSTRACT

Ozone (O_3) is an effective sterilizer, and its range of application has extended to include water purification. Ozone is typically generated from oxygen (O_2) in nonthermal plasma (NTP). However, this process requires the use of an additional gas cylinder or supply device for O_2, thereby entailing increased costs of operation and energy consumption. Air can be used as an alternative to O_2 as a source gas for O_3 production. However, this leads to the generation of nitrogen oxide (NO_x), an air pollutant, during plasma discharge. Hence, it is vital to develop a method for O_3 generation that addresses the challenges of energy costs and emission of air pollutants. The present study therefore proposes an energy-efficient NTP sterilization system. The system is based on electrolysis of water to produce O_2 and hydrogen (H_2). The O_2 produced is used to generate O_3 for sterilization, and H_2 is used in fuel cells to generate electric power. The present study details the characteristics of energy consumption and efficiency in O_3 production, and elucidates the proposed NTP sterilization system. Reduction in energy consumption for O_3 production is achieved with a power recovery rate of more than 11.1% in the present high-efficiency water sterilization system.

INTRODUCTION

Sterilization technologies are widely used in applications across diverse industries such as medical, food processing, and air purification. Conventional methods [1] such as heat treatment comprising the wet heat (autoclave) and dry heat (oven) processes, chemical sterilization such as ethanol immersion, and ultraviolet (UV) [2] and γ-ray sterilizations [3] have been developed. More recently, plasma sterilization technologies have been studied and remarkable developments have been achieved in this field. Plasma sterilization technologies can satisfy the need for rapid and effective sterilization at room temperature. Compared with conventional methods, plasma sterilization technologies provide advantages in various aspects including energy consumption, processing time, area of treatment, and toxicity. One particular advantage is that plasma is easy to handle under conditions of atmospheric pressure. Plasma sterilization techniques are classified according to the types of discharge: dielectric barrier discharge (DBD) [4–6], glow discharge [7–9], corona discharge [10], microwave discharge [11, 12], et cetera. Nonthermal plasma is effective in odor removal [13, 14] and decomposition of chemical substances [15]. The use of nonthermal plasma jet is the recent trend of sterilization [16–19]. The use of plasma sterilization has been extended to water purification too [4, 17, 20–22]. Among the chemical species generated in a plasma-based process, ozone (O_3) is effective for water purification and odor removal; it is second only to fluorine in terms of oxidizability, and also has a relatively short lifetime. The half-life of O_3 in the atmosphere is three days at a temperature of 20 ºC. This decreases with the rise in temperature, falling to 1.5 h at 120 ºC, and 1.5 s at 250 ºC. The half-life of O_3 is even shorter in water: 20 min at 20 ºC, 15 min at 15 ºC, and 8 min at 35 ºC at a pH of 7.0. Thus, the efficiency and duration of water sterilization can be controlled by regulating the temperature of water or its potential of hydrogen (pH). Another significant advantage of using O_3 to purify water is that it prevents the emergence of resistant bacteria. Water is recycled, hence there is a strong need for its purification. Moreover, a large part of the global population does not have access to clean, safe, and potable water. Hence, an advanced water purification technology is of vital importance. Given its benefits, O_3 is favored over other chemicals such as chlorine for use in water purification. Furthermore, the O_3 used in the sterilization process decomposes into non-toxic oxygen (O_2).

Ozone is generated by a nonthermal plasma (NTP) process such as DBD or surface discharge. In this process, O_2 is used as the source gas. An additional O_2 gas cylinder or a supply device such as a pressure swing adsorption (PSA)-based system is required. Production of pure O_2 thus entails additional costs of operations and energy consumption. Alternatively, air is used as the source gas. Generation of O_3 from O_2 in air is a method widely used in commercial applications [23]. Although it addresses the issues of additional operational and energy costs entailed in using pure O_2, the main drawback of this method is

the generation of nitrogen oxide (NO_x) during plasma discharge. Nitrogen oxide is an air pollutant that contributes to acid rain and photochemical smog. Hence, the use of air as a source gas for O_3 generation is not an environmentally friendly solution. An alternative method with low costs of energy consumption and no emission of air pollutants is required.

In view of the application of O_3 in water purification, we propose an energy-efficient NTP-based method for O_3 generation that relies on the electrolysis of water and use of fuel cells [24]. This method of O_3 generation is also investigated for use in water purification. In the present method, O_2 generated in the electrolysis of water is used for NTP-based O_3 generation. Hydrogen (H_2) generated in the electrolysis of water is supplied to fuel cells to generate electric power, thereby reducing the total energy consumption. The proposed method and experimental setup are explained in detail in the sections that follow. In addition, the characteristics of reduction in energy consumed during O_3 generation are investigated, and the findings are presented here. The main purpose is to achieve an efficient way to produce O_3, but the detailed objectives of this study are as follows:

(1) Reduction in energy consumed during O_3 generation using electrolysis of water and fuel cells in an NTP-based process, and

(2) Analysis and evaluation of water sterilization based on the NTP discharge conditions during O_3 generation and O_3 concentration.

PRINCIPLE OF ENERGY RECOVERY AND STERILIZATION

Figure 1 shows the schematic of the proposed energy-efficient NTP-based O_3 generation method using electrolysis of water and fuel cells for water sterilization. The system consists of an electrolysis device, a fuel cell device, a NTP ozonizer, and a sterilization section. First, H_2 and O_2 are generated from water on the cathode and anode of the electrolysis device, respectively, according to reaction (1).

$$2H_2O \rightarrow 2H_2 + O_2. \quad (1)$$

The H_2 generated is supplied to the anode of the fuel cells. The cathode of the fuel cells is exposed to the atmosphere. Oxygen from the atmospheric air is automatically supplied to the fuel cells thorough the cathode. The total energy consumption of the sterilization system can be reduced by recovering the electric power generated by the fuel cells. The O_2 generated by electrolysis of water is supplied to the NTP ozonizer, which produces O_3 by the following reactions:

$$O_2 + e \rightarrow O + O + e, \quad (2)$$

$$O + O_2 \rightarrow O_3 \quad . \quad (3)$$

If N_2 is present in the source gas, NO_x is also generated as a byproduct during plasma discharge by the following reactions:

$$N_2 + e \rightarrow N + N + e, \quad (4)$$

$$N + O_2 \rightarrow NO + O, \quad (5)$$

$$NO + O_3 \rightarrow NO_2 + O_2. \quad (6)$$

Although reactions (4)–(6) also contribute to the sterilization process, NO_x is an air pollutant and, hence, an undesirable byproduct. A simple way to reduce the production of NO_x is to increase the concentration of O_2 and/or minimize the concentration of N_2. High concentration of O_2 provides the added advantage of O_3 formation with less energy consumption in the plasma reaction. The method proposed in the present study can supply extremely high concentration of O_2 to the ozonizer. Thus, the overall system ensures low environmental impact by limiting the emission of air pollutants and reducing energy consumption.

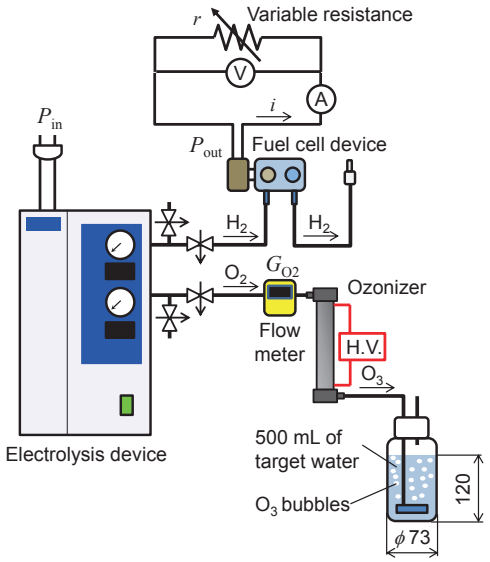

Fig. 1. Schematic of the proposed energy-efficient NTP-based method of O_3 generation, using electrolysis of water and fuel cells, for water sterilization

The O_3 generated is utilized for water sterilization. Ozone is introduced into the water in the form of bubbles. The mechanisms of plasma sterilization have been investigated and reported in the literature [6, 8, 9, 11, 12, 25, 26]. Although some aspects of the mechanisms remain unclear, it is known that microorganisms are sterilized by the physical and chemical reactions in the NTP process. More specifically, it is assumed that the following three processes contribute to sterilization in an NTP-based method [26]: (1) direct destruction of the genetic material of the microorganism by UV irradiation, (2) erosion of the microorganism, atom by atom, through intrinsic photodesorption, and (3) erosion of the microorganism, atom by atom, through chemical etching due to adsorption of the reactive species from the NTP. The physical process takes place directly and involves both the positive and negative ions in the NTP streamer. The chemical process is brought about indirectly by reactive species such as O_3, atomic oxygen, hydroxyl radical (OH radical), etc. In the present case of water sterilization with O_3, the indirect mechanisms are dominant [27–29]. A small quantity of O_3 in water can generate OH radicals that have higher reactivity and oxidizability than other reactive species of oxygen. The OH radical is generated by the self-decomposition of O_3 in water. The process is brought about by reactions (7), (8) [30], (9), and (10) [31]:

$$O_3 + OH^- \rightarrow HO_2^- + O_2 \quad , \qquad (7)$$

$$O_3 + HO_2^- \rightarrow O_3^- + HO_2 \quad , \qquad (8)$$

$$O_3^- + H^+ \leftrightarrow HO_3 \quad , \qquad (9)$$

$$HO_3 \rightarrow OH + O_2 \qquad (10)$$

Due to their high oxidizability, O_3 and the OH radicals oxidize DNA, amino acids, and proteins, thereby damaging the cell membranes and cell walls of the microorganism.

EXPERIMENTAL APPARATUS AND METHODS

Figure 1 shows the proposed sterilization system designed for energy recovery and sterilization. A solid polymer electrolyte (SPE) water electrolysis device (TH-500HO, YMC Co., Ltd.) is installed. It has a production capacity of 500 mL/min of H_2 gas. The electrolysis device can provide extremely high concentrations of H_2 and O_2 gases i.e., greater than 99.999% and 99.9%, respectively. Its electric power consumption, P_{in}, is 250 W. In the first step of the electrolysis, distilled water held in a reservoir in the device is decomposed into H_2 and O_2 gases. The H_2 generated is supplied to the anode of a fuel cell device (H-30, Horizon Fuel Cell Technologies). The cathode of the fuel cell device is exposed to atmospheric air. The fuel cell device consists of proton exchange membrane (PEM) fuel cells, also known as polymer electrolyte (PE) fuel cells. The rated output power is 30 W with an efficiency of 40%. The electric power generated, P_{out}, output direct current, I_{FC}, and voltage, V_{FC}, are measured with a digital multimeter. The fuel cell device is connected to a variable resistor with a load value of r. The O_2 generated in the electrolysis device is supplied to a NTP ozonizer (PA-022, Alita Industries, Inc.). Ozone is produced in the ozonizer by the DBD method. The O_2 source gas flows into a 1-mm gap between concentric cylindrical electrodes with a glass barrier in the NTP ozonizer. The plasma discharge takes place in this gap. The discharge voltage is 5 kV, the discharge current 400 mA, and the frequency 1 kHz. The electric power and current consumed is measured with a wattmeter. The ozonizer has a capacity to produce 500 mg/h of O_3 with a supply of 2.5 L/min of air. The volumetric flow rate of O_2 from the electrolysis device, G_{O2}, i.e., the flow rate of O_2 supplied to the ozonizer, is measured with a flowmeter (SEF-21A, HORIBA STEC Co., Ltd.). The O_3 generated is utilized for sterilization. It is supplied in the form of bubbles to the target water i.e., the polluted water held in a reservoir. The O_3 bubbles are generated through a porous medium (circular plate type; diameter of 40 mm and thickness of 15 mm) set in the water reservoir.

To investigate the reduction in energy consumption in the present method of water sterilization, P_{out}, I_{FC}, and V_{FC} are used as the input data. The characteristics of the electric power generated in the fuel cell device can be evaluated from these relationships. The total electric power consumed in the system, P_{cons}, is calculated as

$$P_{cons} = P_{in} - P_{out}. \qquad (11)$$

The electric power generated P_{out} is the power available for recovery. The O_2 generation efficiency ε_{O2} is determined from P_{cons} and G_{O2} as

$$\varepsilon_{O2} = G_{O2} / P_{cons}. \qquad (12)$$

In addition, the recovery rate of power in O_2 generation, η_{re}, is calculated as

$$\eta_{re} = P_{out} / P_{in}. \qquad (13)$$

It is to be noted that an initial warm-up operation is conducted to allow G_{O2} to stabilize before these measurements are taken or O_3 is generated.

The process of water purification generally comprises filtration, sterilization, and decomposition, and includes odor removal. Filtration can be achieved by using appropriate filters or separation methods. Sterilization and decomposition are the more difficult steps to accomplish in water purification. To investigate the sterilization effect in the present method, an experiment of water sterilization by bubbling O_3 is carried out. The polluted water, which is to be sterilized, is stored in a reservoir with a holding capacity of 500 mL. The growth of bacteria and fungi is investigated. Detection papers (No.3, No.2, No.1, and No.7, Sun Chemical Co., Ltd.) are used to investigate the growth of general bacteria, *Staphylococcus*, coliform bacteria, and mold-yeast, respectively. The sterilization experiments are performed for 1, 3, and 5 min. Each detection paper absorbs 1 mL of target water during sampling, and is placed in an incubator at an appropriate temperature. The number of colonies cultivated is measured in terms of colony forming units per mL (CFU/mL) to evaluate the sterilization effect.

To investigate the decomposition effect, an experiment using a solution of ink in water is performed. The decomposition of chemical substances such as organic solvents is a significant process in water purification. For a visual understanding of the effect of decomposition, a solution of aqueous ink in distilled water is prepared, and O_3 is bubbled into it. The decomposition experiments are performed for 1, 3, 5, 10, 15, and 20 min. The decomposition effect is evaluated based on the transparency of the treated solutions of ink.

RESULTS AND DISCUSSION

Figure 2 shows the relationship between I_{FC} and ε_{O2}. The measured values are plotted along with a characteristic curve in solid line, obtained from the calibration curve of r. In the case without power recovery, that is, at I_{FC} = 0 A, ε_{O2} is 0.09 L/Wh. The value of ε_{O2} with power recovery is 0.10 L/Wh with an O_2 concentration of more than 99.9%. To compare these results with those from a conventional method, a pressure swing adsorption (PSA) device (SOM500B, Sanyo Electronic Industries Co., Ltd.) with an O_2 production capacity of 0.5 L/min and power consumption of 170 W is used as a reference. The PSA method has an ε_{O2} of 0.18 L/Wh with O_2 concentration exceeding 90%. Thus, the value of ε_{O2} in the present method is lower than (56%) that of the PSA method but the concentration of O_2 is higher. This lends the present method an advantage over the conventional method in the aspect of environmental load because the extremely high concentration of O_2 achieved ensures little formation of the air pollutant NO_x and also improves the reaction efficiency of O_3 generation in the NTP reaction.

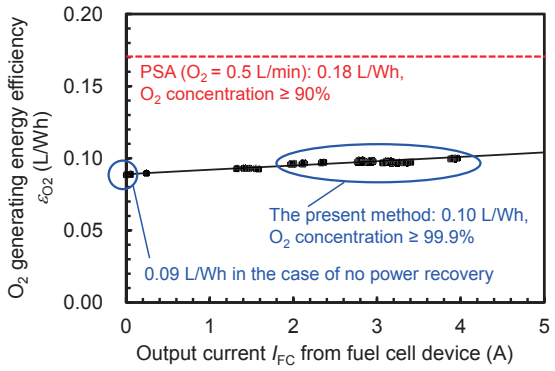

Fig. 2. Relationship between the output current, I_{FC}, and the measured energy efficiency of O_2 generation from the electrolysis device, ε_{O2}

Figure 3 shows the relationship between I_{FC} and η_{re}. The measured values are plotted together with a characteristic curve in solid line, obtained from the calibration curve of r. The maximum power recovery rate $\eta_{re\text{-}max}$ is 11.4% (= 28.6/250×100) at I_{FC} = 3.96 A and P_{out} = 28.6 W. Accounting for the power consumption, P_{NTP}, in the NTP ozonizer, the power recovery rate of the system, η_{reSYS} = P_{out} / P_{SYS} = 28.6/(250+7.5)×100 = 11.1% at P_{NTP} = 7.5 W, as mentioned in the following paragraph. Thus, the characteristic curve agrees well with the measured values. The characteristic curve enables us to estimate η_{re}. In the present system, excess H_2 gas flows out of the fuel cell device, but this can potentially be utilized for power recovery through additional fuel cells, thereby improving both P_{out} and η_{re}. For instance, when I_{FC} reaches 5.5 A, η_{re} of 15% could be achieved.

The characteristics of O_3 generation in the present system are investigated prior to the sterilization stage. The value of P_{NTP} is 7.5 W, the effective electric current is 0.15 A, and voltage is 102 V. The discharge voltage is typically 5 kV, and the discharge frequency is 1 kHz. It is noted that the maximum

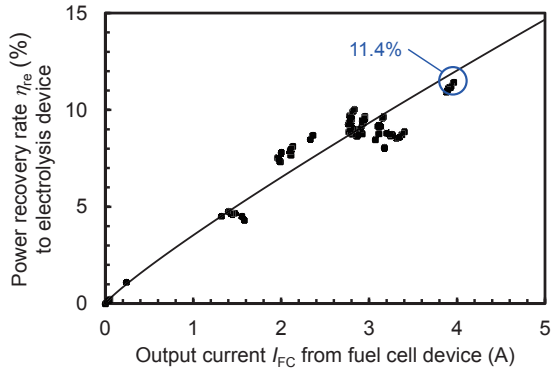

Fig. 3. Relationship between the output current, I_{FC}, and the rate, η_{re}, of power recovery for the electrolysis device during O_2 generation

output power P_{out} of 28.6 W is greater than P_{NTP} and thus fulfils the power requirement of the NTP ozonizer. The flow rate of O_2 supplied from the electrolysis device to the NTP ozonizer is 0.37 L/min. The total electrical power consumed by the system is calculated as P_{SYS} = P_{in} + P_{NTP}. Using an ozone monitor (Model 106-H, UV Absorption type, 2B Technologies, Inc.) for measurement, the concentration of O_3 generated is determined to be 1.78% by volume i.e., 17,800 ppm, which is high at an O_3 temperature of 24.8 ºC and pressure of 101.8 kPa, compared with the most recent plasma method [32]. Ozone at such high concentrations has a potential for strong bactericidal activity. Furthermore, it can be mixed with air, for instance, to yield large volumes for use in sterilization.

In the present experiment, 500 mL of used bathwater serves as the target polluted water. Microorganisms harmful to human health can be classified as virus, bacteria, or fungi. In the present study, the sterilization effect on bacteria and fungi are of interest. Among bacteria, general bacteria, *Staphylococcus*, and coliform bacteria are investigated. **Table 1** shows the classification of the bacteria and fungi that are investigated. A spherical bacterium is classified as a coccus while a rod-shaped one is termed a bacillus. Bacteria can also be classified by their cell wall structure. A bacterium having no outer membrane is classified as Gram-positive because it yields a positive result in the Gram stain test. The cell wall of Gram-positive bacterium consists of a thick peptidoglycan layer. A bacterium having an outer membrane is classified as Gram-negative because it yields a negative result in the Gram strain test. Gram-negative bacterium has a thin peptidoglycan layer for a cell wall. *Staphylococcus* is a Gram-positive coccus. Coliform bacteria are Gram-negative bacilli. *Escherichia coli* (*E. coli*) is an example of a coliform bacterium. *Staphylococcus* and coliform bacterium are facultative anaerobic organisms. Regulations pertaining to water supply in Japan stipulate that less than 100 CFU/mL of general bacteria and no *E. coli* should be detected in the water supplied. The detection papers for general bacteria, *Staphylococcus*, coliform bacteria, and mold-yeast are set in incubators, after sampling of non-sterilized water and water sterilized for 1, 3 and 5 min. Bacteria are cultivated at 36 ºC for 24 h. Fungi are cultivated at 25 ºC for 48 h. The sterilization is performed under the following conditions: P_{SYS} = 257.5 W, P_{out} = 28.6 W i.e., P_{cons} = 228.9 W, η_{re} = 11.4%, and ε_{O2} = 0.10 L/Wh with O_2 concentration ≥ 99.9%.

Table 1. Classification of the bacteria and fungi investigated

		Facultative anaerobic organism	
		Gram-positive bacterium	Gram-negative bacterium
Bacteria	Coccus	*Staphylococcus*	
	Bacillus		Coliform bacteria (*E. coli*, etc)
Fungi		Fungi	

Figure 4 shows the results of sterilization for used bathwater as evaluated by cultivated bacteria and fungi measured in CFU/mL. The values are obtained as an average of six trials. Non-sterilized water i.e., water at time = 0 min has 188 CFU/mL of general bacteria, 1 CFU/mL of *Staphylococcus*, 87 CFU/mL of coliform bacteria, and 1 CFU/mL of mold-yeast. After sterilization for 1 min, the water contains 66 CFU/mL of general bacteria, and 57 CFU/mL of coliform bacteria. No colony of *Staphylococcus* or of mold-yeast is observed on the detection papers. In the case of sterilization for 3 min, the water has 1 CFU/mL of general bacteria, and 2 CFU/mL of coliform bacteria. In the case of sterilization for 5 min, there is 1 CFU/mL of general bacteria on the detection paper. Colonies of coliform bacteria are no longer observed. In summary, sterilization helps reduce the population of general bacteria by 64.9% within 1 min, and by 99.5% within 3 min. The population of coliform bacteria is reduced by 34.5%, 97.7%, and 100% within 1 min, 3 min, and 5 min of sterilization, respectively. *Staphylococcus* and the fungi of mold-yeast are eliminated within 1 min of sterilization. It must be noted, however, that only one colony of each is detected in the non-sterilized water. Thus, the present system can achieve nearly complete sterilization within a minimum of 3 min. Regulations pertaining to water supply in Japan stipulate that less than 100 CFU/mL of general bacteria is permissible in tap water when evaluated by official detection methods. The corresponding value for the present system is provided by the manufacturer of the detection papers, Sun Chemical Co., Ltd. Based on the correlation, the permissible values for general bacteria are 245 CFU/mL, 103 CFU/mL, and 27 CFU/mL at 0 min (i.e., for non-sterilized water), and at 1 min, and 3 min of sterilization, respectively. Thus, the water sterilized for 3 min in the present system meets the regulatory requirements pertaining to general bacteria. Japanese water regulations also mandate the absence of *E. coli* in tap water. Water sterilized in the present system for 5 min satisfies this requirement. Furthermore, a total of 8,580 J

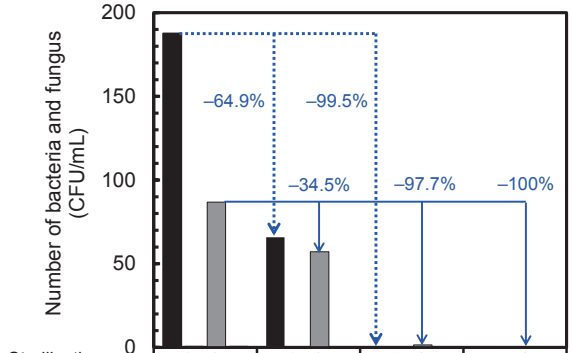

Sterilization	0 min	1 min	3 min	5 min
Bacteria	188	66	1	1
Staphylococcus	1	0	0	0
Coliforms	87	57	2	0
Mold-Yeast	1	0	0	0

Fig. 4. Results of sterilization for used bathwater evaluated by measuring cultivated bacteria and fungi in CFU/mL

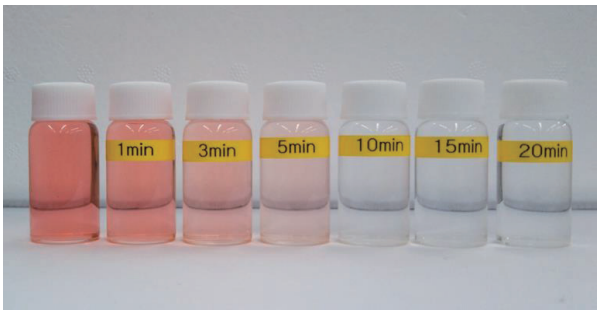

Fig. 5. Photograph of the original solution of ink and the solutions treated by bubbling O_3 for 1, 3, 5 10, 15 and 20 min

(= $P_{out} \times t$ = 28.6×300) of energy can be saved when the present system is used to sterilize water for 5 min (= 300 s).

The decomposition experiments are performed for 1, 3, 5, 10, 15, and 20 min. **Figure 5** shows the images of the original solution of ink in untreated water, and the solutions treated by bubbling O_3 for 1, 3, 5 10, 15, and 20 min. The main components of the water-soluble red ink contains acid red 88 ($C_{20}H_{13}N_2NaO_4S$) (7.0% by mass), glycerol ($C_3H_8O_3$) (50.0%), ethylene glycol ($C_2H_6O_2$) (10.0%), and water (31.2%). The solution of ink is prepared by adding 15 drops of the ink into 1600 mL of water. The solution of ink in untreated water is red, and 500 mL of the solution of ink is used for the decomposition experiments. The method and procedure applied in this case are the same as those followed in the sterilization. The decomposition effect is evaluated by the transparency of the treated solutions, which decolorize with time. It can be seen that bubbling O_3 for 10 min or more removes the color completely. In the present study, the size of O_3 bubbles are several mm, and the same result cannot be obtained in the case of the same size of air-bubbles. Therefore, it appears that the high oxidizability of O_3 and the OH radicals in reactions (7)–(10) contributes to the effective decomposition of chemical substances such as organic solvents.

CONCLUSIONS

The fundamental characteristics of reduction in energy consumption in the proposed NTP-based water sterilization system are investigated, as are the sterilization and decomposition effects. First, the concept and principle of the proposed system in which energy consumption can be reduced with the help of water electrolysis and fuel cells is elucidated. Next, the sterilization system is established. The sterilization system emits no pollutant NO_x. The investigations are performed in the sterilization system and lead us to the following conclusions:

(1) The O_2 generation energy efficiency ε_{O2} of the electrolysis device is 0.10 L/Wh, with O_2 concentration of more than 99.9%. This extremely high concentration of O_2 ensures little production of the pollutant NO_x, which reduces the environmental impact of the system and improves the efficiency of O_3 generation in the NTP reaction.

(2) The rate, $\eta_{re,}$ of power recovered to the electrolysis device in O_2 generation is 11.4%. A characteristic curve is provided to estimate η_{re}. The power recovery rate of the overall system, η_{reSYS} (= P_{out} / P_{SYS}), is 11.1%.

(4) The system can generate and supply O_3 at a high concentration of 1.78% by volume i.e., 17,800 ppm. This high concentration of O_3 has the potential for strong bactericidal activity and/or sterilization in large volumes by mixing with air, for example.

(5) Water sterilized in the present system for at least 5 min satisfies the Japanese regulatory requirements pertaining to permissible levels of general bacteria, *Staphylococcus*, coliform bacteria, and mold-yeast. The population of general bacteria in the target water is reduced by 99.5% with 3 min of sterilization. An energy reduction of 8,580 J is achieved with sterilization for 5 min.

(6) The decomposition experiments demonstrate that bubbling O_3 for 10 min or more removes color completely. Based on these results, it is concluded that decomposition of chemical substances such as organic solvents can be achieved effectively in the present system. Together, the results of the sterilization and decomposition experiments establish that the present system is effective for water purification.

ACKNOWLEDGMENTS

This work was supported by the Japan Society for the Promotion of Science's (JSPS) KAKENHI Grant Number 22K04050.

REFERENCES

[1] Zhao, L., Mei, S., Wang, W., Chu, P. K., Wu, J. and Zhang, Y., 2010, "The role of sterilization in the cytocompatibility of titania nanotubes," Biomaterials, Vol. 31, No. 8, pp. 2055–2063.

[2] Song, K., Mohseni, M. and Taghipour, F., 2016, "Application of ultraviolet light-emitting diodes (UV-LEDs) for water disinfection: A review," Water Research, Vol. 94, pp. 341–349.

[3] Lin, J. J. and Hsu, P. Y., 2011, "Gamma-ray sterilization effects in silica nanoparticles/γ-APTES nanocomposite-based pH-sensitive polysilicon wire sensors," Sensors, Vol. 11, No. 9, pp. 8769–8781.

[4] Zhang, C., Fang, Z., Liu, W., Tian, F. and Bai, M., 2016, "Rapid removal of bacterial endotoxin and natural organic matter in water by dielectric barrier discharge plasma: Efficiency and toxicity assessment, " Journal of Hazardous Materials, Vol. 318, pp. 15–23.

[5] Miao, H. and Yun, G., 2011, "The sterilization of Escherichia coli by dielectric-barrier discharge plasma at atmospheric pressure," Applied Surface Science, Vol. 257, No. 16, pp. 7065–7070.

[6] Choi, J. H., Han, I., Baik, H. K., Lee, M. H., Han, D. W., Park, J. C., Lee, I. S., Song, K. M. and Lim, Y. S., 2006, "Analysis of sterilization effect by pulsed dielectric barrier discharge," Journal of Electrostatics, Vol. 64, No. 1, pp. 17–22.

[7] Akitsu, T., Ohkawa, H., Tsuji, M., Kimura, H. and Kogoma, M., 2005, "Plasma sterilization using glow discharge at atmospheric pressure," Surface & Coatings Technology, Vol. 193, No. 1, pp. 29–34.

[8] Montie, T. C., Kelly-Wintenberg, K. and Roth, J. R., 2000, "An overview of research using the one atmosphere uniform glow discharge plasma (OAUGDP) for sterilization of surfaces and materials," IEEE Transactions on Plasma Science, Vol. 28, No. 1, pp. 41–50.

[9] Laroussi, M., 1996, "Sterilization of contaminated matter with an atmospheric pressure plasma," IEEE Transactions on Plasma Science, Vol. 24, No. 3, pp. 1188–1191.

[10] Kuwahara, T., Kuroki, T., Yoshida, K., Saeki, N. and Okubo, M., 2012, "Development of sterilization device using air nonthermal plasma jet induced by atmospheric pressure corona discharge," Thin Solid Films, Vol. 523, pp. 2–5.

[11] Sato, T., Miyahara, T., Doi, A., Ochiai, S., Urayama, T. and Nakatani, T., 2006, "Sterilization mechanism for Escherichia coli by plasma flow at atmospheric pressure," Applied Physics Letters, Vol. 89, 073902.

[12] Sato, T., Fujioka, K., Ramasamy, R., Urayama, T. and Fujii, S., 2006, "Sterilization efficacy of a coaxial microwave plasma flow at atmospheric pressure," IEEE Transactions on Industry Applications, Vol. 42, No. 2, pp. 399–404.

[13] Hołub, M., Brandenburg, R., Grosch, H., Weinmann, S. and Hansel, B., 2014, "Plasma supported odor removal from waste air in water treatment plants: An industrial case study," Aerosol and Air Quality Research, Vol. 14, No. 3, pp. 697–707.

[14] Kuwahara, T., Okubo, M., Kuroki, T., Kametaka, H. and Yamamoto, T., 2011, "Odor removal characteristics of laminated film-electrode packed-bed nonthermal plasma reactors," Sensors, Vol. 11, No. 6, pp. 5529–5542.

[15] Stratton, G. R., Dai, F., Bellona, C. L., Holsen, T. M., Dickenson, E. R. V. and Thagard, S. M., 2017, "Plasma-based water treatment: Efficient transformation of perfluoroalkyl substances in prepared solutions and contaminated groundwater," Environmental Science and Technology, Vol. 51, No. 3, pp. 1643–1648.

[16] Nikmaram, H., Kanavi, M. R., Ghoranneviss, M., Balagholi, S., Ahmadieh, H., Roshandel, D. and Amini, M., 2018, "Cold atmospheric pressure plasma jet for the treatment of Aspergillus keratitis," Clinical Plasma Medicine, Vol. 9, pp. 14–18.

[17] Ma, S., Kim, K., Huh, J. and Hong, Y., 2017, "Characteristics of microdischarge plasma jet in water and its application to water purification by bacterial inactivation," Separation and Purification Technology, Vol. 188, No. 29, pp. 147–154.

[18] Lin, Z. H., Tobias Tschang, C. Y., Liao, K. C., Su, C. F., Wu, J. S. and Ho, M. T., 2016, "Ar/O2 argon-based round atmospheric-pressure plasma jet on sterilizing bacteria and endospores," IEEE Transactions on Plasma Science, Vol. 44, No. 12, pp. 3140–3147.

[19] Abonti, T. R., Kaku, M., Kojima, S., Sumi, H., Kojima, S., Yamamoto, T., Yashima, Y., Miyahara, H., Okino, A., Kawata, T., Tanne, K. and Tanimoto, K., 2016, "Irradiation effects of low temperature multi gas plasma jet on oral bacteria," Dental Materials Journal, Vol. 35, No. 5, pp. 822–828.

[20] Imai, S., Kumagai, H., Iwata, M., Onodera, M. and Suzuki, M., 2015, "In-water plasma generation on a liquid wall using a compact device and dedicated power supply," IEEE Transactions on Plasma Science, Vol. 43, No. 7, pp. 2166-2173.

[21] Sugai, T., Liu, W., Tokuchi, A., Jiang, W. and Minamitani, Y., 2013, "Influence of a circuit parameter for plasma water treatment by an inductive energy storage circuit using semiconductor opening switch," IEEE Transactions on Plasma Science, Vol. 41, No. 4, pp. 967–974.
[22] Foster, J., Sommers, B. S., Gucker, S. N., Blankson, I. M. and Adamovsky, G., 2012, "Perspectives on the interaction of plasmas with liquid water for water purification," IEEE Transactions on Plasma Science, Vol. 40, No. 5, pp. 1311–1323.
[23] Pavlovich, M. J., Chang, H. W., Sakiyama, Y., Clark, D. S. and Graves, D. B., 2013, "Ozone correlates with antibacterial effects from indirect air dielectric barrier discharge treatment of water," Journal of Physics D: Applied Physics, Vol. 46, No. 14, 145202.
[24] Kuwahara, T., 2018, "Reduction in energy consumption using fuel cells in nonthermal plasma-based water sterilization by bubbling ozone," IEEE Transactions on Industry Applications, Vol. 54, No. 6, pp. 6414–6421.
[25] Liao, X., Liu, D., Xiang, Q., Ahn, J., Chen, S., Ye, X. and Ding, T., 2017, "Inactivation mechanisms of non-thermal plasma on microbes: A review," Food Control, Vol. 75, pp. 83–91.
[26] Moisan, M., Barbeau, J., Moreau, S., Pelletier, J., Tabrizian, M. and Yahia, L. H., 2001, "Low-temperature sterilization using gas plasmas: a review of the experiments and an analysis of the inactivation mechanisms," International Journal of Pharmaceutics, Vol. 226, No. 1, pp. 1–21.
[27] Tamazawa, K., Shintani, H., Tamazawa, Y. and Shimauchi, H., 2015, "Sterilization Effect of Wet Oxygen Plasma in the Bubbling Method," Biocontrol Science, Vol. 20, No. 4, pp. 255–261.
[28] Kitazaki, S., Tanaka, A. and Hayashi, N., 2014, "Sterilization of narrow tube inner surface using discharge plasma, ozone, and UV light irradiation," Vacuum, Vol. 110, pp. 217–220.
[29] Hayashi, N., Guan, W., Tsutsui, S., Tomari, T. and Hanada, Y., 2006, "Sterilization of medical equipment using radicals produced by oxygen/water vapor RF plasma," Japanese Journal of Applied Physics, Vol. 45, No. 10B, pp. 8358–8363.
[30] Tomiyasu, H., Fukutomi, H. and Gordon, G., 1985, "Kinetics and mechanism of ozone decomposition in basic aqueous solution," Inorganic Chemistry, Vol. 24, No. 19, pp. 2962–2966.
[31] Buehler, R. E., Staehelin, J. and Hoigné, J., 1984, "Ozone decomposition in water studied by pulse radiolysis. 1. Perhydroxyl (HO2)/hyperoxide (O2-) and HO3/O3- as intermediates," Journal of Physical Chemistry, Vol. 88, No. 12, pp. 2560–2564.
[32] Ma, S., Kim, K., Huh, J., Lee, S. and Hong, Y., 2018, "Regeneration and purification of water-soluble cutting fluid through ozone treatment using an air dielectric barrier discharge," Separation and Purification Technology, Vol. 199, pp. 289–297.

Proceedings of IWEC2023
The International Workshop of Energy Conversion
March 15-17, 2023, Kyoto, Japan

Paper No. IWEC2023-09

HEAT TRANSPORT CHARACTERISTICS OF A CLOSED TWO PHASE THERMOSYPHON BY WATER WITH AIR MIXED (EFFECT OF THE INTERNAL STRUCTURE)

T. Kitamura, T. Kubota and S. Shuchi*
Department of Mechanical Engineering, Akita Prefectural University, Akita, Japan
*corresponding author, E-mail: shuchi@akita-pu.ac.jp

ABSTRACT

An experimental study was conducted on the change in heat transport characteristics of a cylindrical water two-phase thermosyphon when air is introduced into the interior. In previous studies, it has been shown that the heat transport performance, which is reduced by air entrainment, is slightly recovered when a double-tube structure with an additional circular tube inside is used. This study investigated this phenomenon in detail by conducting experiments under different operating conditions of the thermosyphon (heat input rate, internal air amount, and working fluid level).

As a result of the experiment, it was estimated that the recovery of heat transport performance in a double-tube thermosyphon is due to the circulation of a mixture of air and working fluid inside the thermosyphon. Qualitative trends in the operating conditions under which such circulation occurs were also confirmed.

INTRODUCTION

A two phase closed thermosyphon (TPCT) is a device that transports heat by using gravity to cause vapor to rise and condensate to fall. TPCTs are expected to have a wide range of applications in industry, such as cooling and heat transport devices. Many studies have been conducted on TPCTs, including a detailed study by Imura et al. on heat transfer characteristics using water and ethanol as working fluids [1] and a study by Fukuda et al. on heat transport characteristics including observation of the flow state of the gas-liquid two-phase flow inside [2].

On the other hand, only working fluids such as water or ethanol are usually sealed inside a TPCT, and there are few studies that have examined the effects on heat transport performance when air is mixed inside a TPCT due to some factor such as equipment trouble. Nakazawa [3] investigated the heat transport characteristics of a TPCT when air is mixed inside the TPCT, and reported that the heat transport rate increases when the TPCT has a double-tube structure and air circulates with water vapor inside the device. However, the study did not examine the conditions under which internal circulation occurs in the TPCT. Therefore, the authors decided to investigate the conditions under which circulation occurs inside a double-tube TPCT when air is mixed, and conducted experiments using the following three parameters: (a) heat input rate at the heating section, (b) amount of air inside the TPCT and (c) distance between the working liquid surface of the heating section and the lower end of the inner tube.

EXPERIMENTAL PROCEDURE

Experimental Apparatus

The apparatus used in this study is shown in Fig.1. The apparatus consists of a heating section, an adiabatic section, a cooling section, and a condensate returning section, and has a cooling water circulator consisting of a thermostatic bath, a magnet pump, and a flow meter, as well as measurement equipment as auxiliary equipment. In the experiment, the working fluid becomes vapor in the heating section, rises through the adiabatic section, and condenses in the cooling section. The condensed fluid returns to the heating section through the condensate returning section .

In this study, the working fluid was heated by a stainless steel band heater (150mm length) wrapped around the bottom of the heating section, and the heater output measured by a power meter is used as the heat input rate Q_{in}. Purified water was used as the working fluid. Distance between the working liquid surface of the heating section and the lower end of the inner tube is defined as the L_{dist}, and was changed by 20 mm. In the cooling section, heat was recovered from the working fluid by passing tap water through a spiral-shaped copper tube at a water temperature of 10 °C and a flow rate of 1000 mL/min (the recovered heat is defined as the heat transport rate Q_{out}). The air volume inside the TPCT was set by adjusting the initial pressure inside the device to a specified pressure with a vacuum pump. Thermocouples were installed inside and on the outer wall of the device to measure the temperature of each part. In the experiment, measurements were taken at a sampling interval of 5 seconds, and the arithmetic mean of each measurement during

1200 seconds after the steady state was reached was used as the representative value.

Experimental Conditions

In the experiment, the heat transport performance of a single-tube and two double-tube TPCTs were evaluated. The double-tube TPCT has inner tube with a cross-sectional area ratio k=0.2 and 0.8 between the inner and outer tubes each other. The area ratio k=0.0 is the single tube type. The experimental conditions are shown in Table 1.

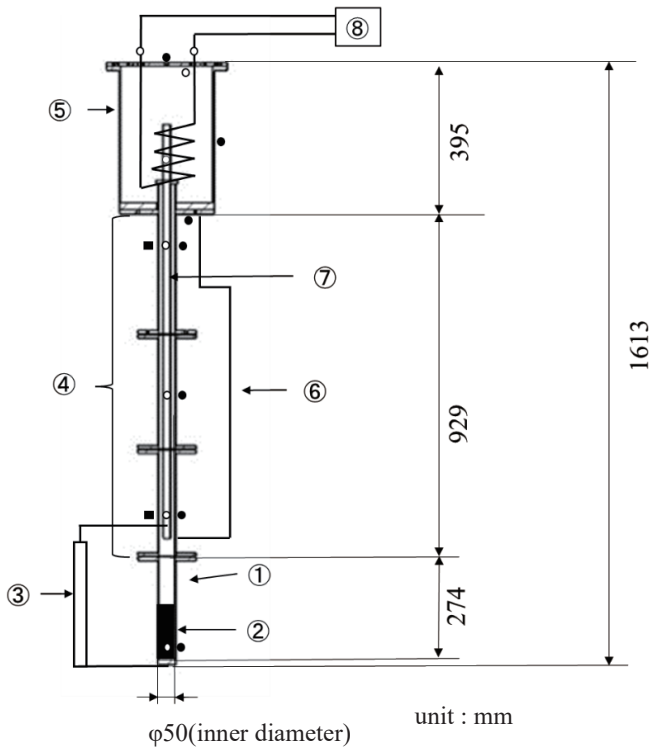

① Heating section ② Heater ③ Water level meter ④ Adiabatic section ⑤Cooling section ⑥Condensate returning section ⑦Inner pipe ⑧Cooling water circulator

Fig. 1 Experimental apparatus.

Table 1 Experimental conditions.

Heat input Q_{in}	300~700 W
Distance bewtween inner tube and water surface L_{dist}	50~ 90 mm
Area ratio k	0.0,0.2,0.8
Initial pressure P_{f}	101.3,81.3 kPa

EXPERIMENTAL RESULTS

Heat Transport rate

Fig.2 shows the relationship between the heat input rate Q_{in} and the heat transport rate Q_{out} for $L_{dist} = 50$ mm, $P_f = 101.3$ kPa, and $k = 0.0, 0.2$ and 0.8, respectively.

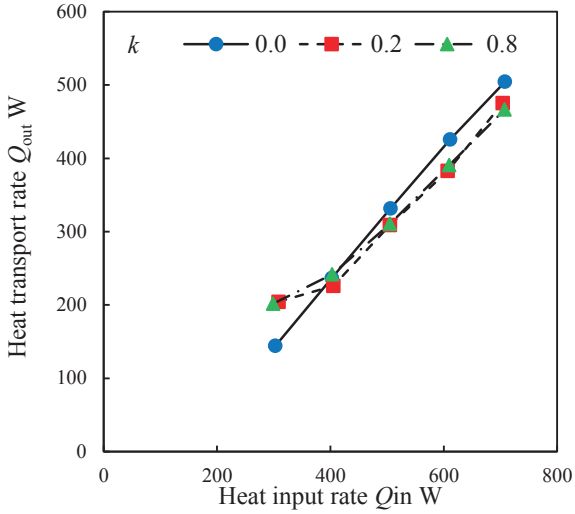

Fig.2 Heat transport rate. ($L_{dist} = 50$mm, $P_f = 101.3$kPa)

Fig. 2 shows that the heat transport rate Q_{out} is almost proportional to the heat input rate Q_{in} when the heat input rate Qin is greater than 400w, regardless of the area factor k.

On the other hand, when comparing the heat transport rate for the same Q_{in} between the single-tube and double-tube cases, the double-tube showed a higher heat transport rate than the single-tube only at 300W, but the single-tube showed a higher heat transport coefficient at 500W and above. In the following, we will take a closer look at how the heat transport rate varies with the heat input rate Q_{in} and the area ratio k.

Temperature distrobution

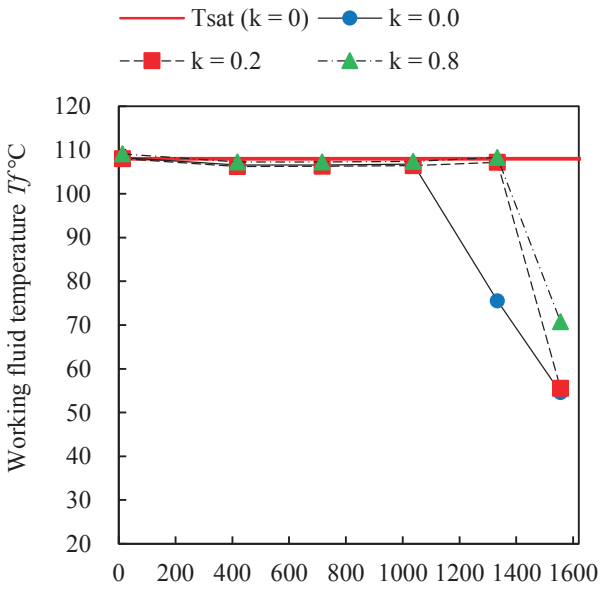

Fig.3 Temperature distribution of the working fluid at the center of the pipes.
($L_{dist} = 50$ mm, $P_f = 101.3$ kPa, $Q_{\text{in}} = 500\ W$)

Fig.3 shows the temperature distribution of the working fluid in the height direction at the center of the tube of the experimental apparatus at Q_{in}=500 W in Fig.2 and the saturated water vapor temperature corresponding to the pressure inside the device.

In Fig.3, it is indicated that the fluid temperature in the adiabatic section ($H = 274 - 1203$mm) is almost constant at any area ratio k and is almost equal to the saturated water vapor temperature corresponding to the measured inner pressure of the device. It can be assumed that the adiabatic section is filled with saturated water vapor under the conditions of $L_{dist} = 50$ mm and $P_f = 101.3$ kPa, regardless of whether it is a single or double-tube. This uniformity of temperature was also observed for other heat input rate of 500 W or more.

Fig.4 shows the temperature distribution inside the device at 300 W, the same as in Fig.3. Fig.4 shows that for a heat input reate Q_{in}=300 W, the temperature in the adiabatic section differs significantly between the single-tube and double-tube cases, with the double-tube case showing a larger temperature drop than the single-tube case and a larger drop for a larger area ratio, k, of the double-tube. Comparing the temperature of the adiabatic section to the saturated water vapor temperature corresponding to the internal pressure (almost unchanged for any k), the single-tube case (k=0) is considered to be close to saturation, while the two types of double-tube cases both show a 10-20°C temperature drop relative to the saturation temperature.

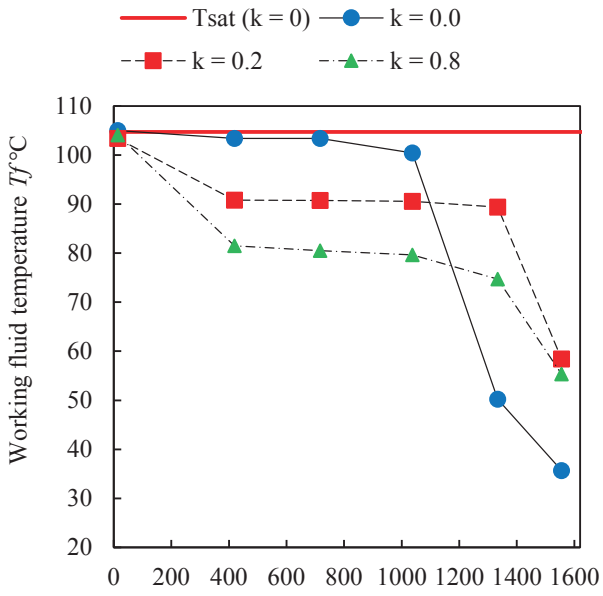

Fig.4 Temperature distribution of working fluid at the center of the pipes.
($L_{dist} = 50$mm, $P_f = 101.3$kPa, $Q_{\text{in}} = 300W$)

On the other hand, the temperatures in the cooling section ($H = 1203 - 1603$mm) were reversed between the single-tube and double-tube cases, with the double-tube cases showing higher temperatures. This is thought to be due to the fact that the tip of the inner tube protrudes into the cooling section in the case of the double-tube, which causes the high-temperature working fluid to blow up from the top of the inner tube to the top of the cooling section.

To examine the state of the fluid in the adiabatic section at a heat input of Q_{in}=300 W, Fig.5 shows the average fluid temperature and internal pressure in the adiabatic section for three area ratios and the saturated vapor pressure curve. Fig.5 shows that the pressure in the adiabatic section is almost the same as the saturated vapor pressure corresponding to the fluid temperature in the case of a single-tube with k=0, while the pressure is higher than the saturated vapor pressure corresponding to the fluid temperature in the cases of double-tube with k=0.2 and 0.8. This indicates that water vapor and air are mixed in the adiabatic section.

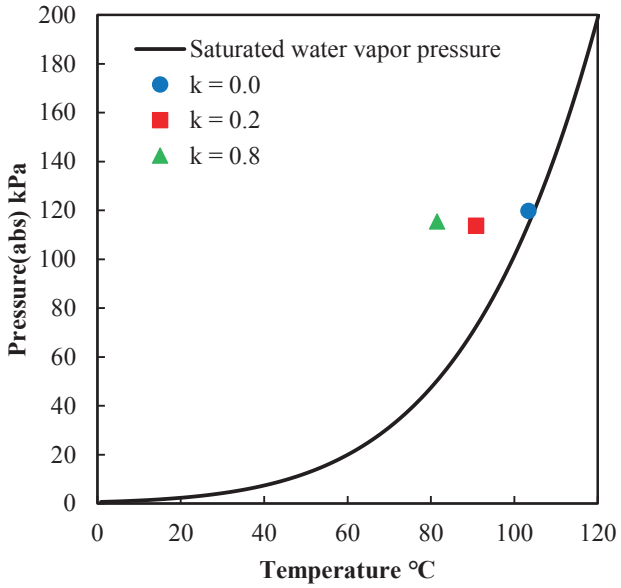

Fig.5 Temperature and pressure of working fluid at adiabatic section.
($L_{dist} = 50$mm, $P_f = 101.3$kPa, $Q_{\text{in}} = 300W$)

In a normal TPCT, only the working fluid is sealed inside, but if air enters the interior for some reason, the air stays in the upper part of the thermosyphon and prevents the movement of water vapor from the heating section, which is thought to reduce the heat transport rate. The heat input $Q_{\text{in}}$of 500 W or more in Fig.2 matches this condition, and Fig.3 shows that the adiabatic section is nearly filled with saturated water vapor, indicating that air inside the device is unevenly distributed in the upper part of the device. On the other hand, when the heat input Q_{in} =300 W, the air mixes with water vapor and circulates inside the device, resulting in the temperature distribution shown in Fig.4. As a result of such circulating flow inside the device, the heat transport rate may have increased in the double-tube cases compared to the single-tube case under the condition of heat input Q_{in} = 300 W.

Effect of the other parameters

Fig.6 shows the heat transport rate for an initial pressure P_f=81.3 kPa inside the TPCT for L_{dist} = 50 mm. In Fig.6, it can be seen that the heat transport rate decreased for all area ratios k compared to the case with the pressure of P_f=101.3 kPa. Lowering the initial pressure means that the amount of air that hinders the movement of water vapor generated in the heating section at the bottom of the TPCT to the cooling section at the top is reduced. Therefore, it was expected that the heat transport rate would increase, but in this experiment, on the contrary, the heat transport rate decreased. The reason for this result is still unknown, and will be verified in future experiments at lower initial pressure.

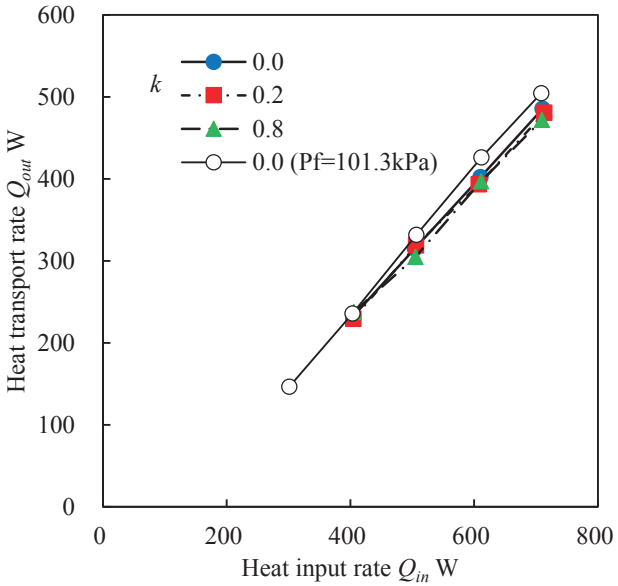

Fig.6 Heat transport rate. (L_{dist} = 50mm, P_f = 81.3kPa)

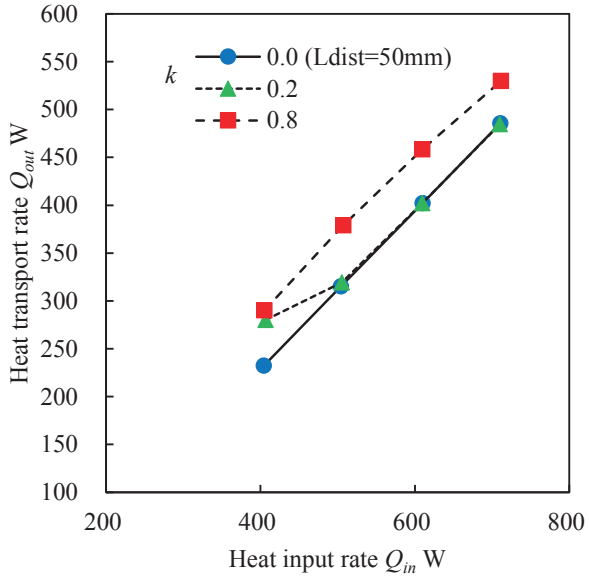

Fig.7 Heat transport rate. (L_{dist} = 90mm, P_f = 81.3kPa)

Fig.7 shows the heat transport rate when the distance between the inner tube and the water surface L_{dist}=90 mm for P_f = 81.3 kPa. Note that the heat transport rate for k =0.0 (single-tube) did not change significantly with L_{dist}, so the one for L_{dist}=50 mm is shown.

Fig.7 shows that for k=0.2, the heat transport rate increased at 400 W, and for k=0.8, it increased for all results from 400 to 700 W, compared to k =0. The pressure and temperature in the adiabatic section under these conditions show similar trends to those shown in Fig.5, and it can be inferred that a mixture of air and water vapor circulates inside the TPCT.

The results obtained so far suggest that the heat transport characteristics of air-entrained TPCT are complicated by the heat input rate ,amount of air anddistance between the working liquid surface and the inner tube and are particularly affected by the presence or absence of circulation flow in the TPCT.

Since there are still many unknown factors that cause such circulating flow, we plan to conduct further investigations over a wider range of operating conditions in the future.

CONCLUSIONS

The effect of a double-tube structure with an inner tube on the heat transport rate of a water two-phase thermosyphon was experimentally investigated assuming that air is mixed inside the vessel. As a result of the experiment, it was assumed that the change in the heat transport rate is caused by the circulating flow of the working fluid only in the case of the double-tube structure. It was also shown that the air amount inside the TPCT and the distance between the lower end of the inner tube and the fluid surface of the working fluid affected the change.

REFERENCES

[1] Imura, H. and Yoshida, M., 1990, “Heat transfer characteristics in a two-phase, double-tube thermosiphon,” Transactions of the Japan Society of Mechanical Engineers. B, Vol.56, No.532, pp. 3816-3820.

[2] Fukuda, K., Hasegawa, O., Kondo, T., Nakagawa, K., Tamura, S. and Okabe, K., 1991, “Heat transfer characteristics of a sealed double-tube two-phase thermosyphon,” Transactions of the Japan Society of Mechanical Engineers. B, Vol.57, No.534, pp. 687-692.

[3] Nakazawa, Y., “Characteristics of Low Temperature Thermosiphon using Double Tube,” 2019, Thesis for Master of Engineering, Doshisha University.

13-23.

PROCEEDINGS OF IWEC2023
THE INTERNATIONAL WORKSHOP OF ENERGY CONVERSION
MARCH 15-17, 2023, KYOTO, JAPAN

Paper No. IWEC2023-10

CENTRIFUGAL CONVECTION IN A BIDISPERSE MEDIUM WITH CHEMICAL REACTION

S. Saravanan,* and S. Vigneshwaran
Centre for Differential Equations and Fluid Dynamics,
Department of Mathematics, Bharathiar University, Coimbatore 641 046, India.
*Corresponding author, E-mail: sshravan@buc.edu.in

ABSTRACT

Centrifugal convection in a fluid saturated bidisperse porous medium is studied in the presence of a reactive solute. The bidispersion arises owing to double porosity of the medium. A two-velocity field model is used to characterize the momentum conservation. A first order chemical reaction is considered to model the underlying reactive kinetics. A linear stability analysis is made to determine the onset of convection. The resulting eigenvalue problem is solved numerically using the compound matrix method. It is found that an increase in the inter-pore momentum transfer parameter and the chemical reaction rate parameter delays the onset of convection. However, it depends on the permeability ratio of the medium and the concentration difference maintained between the medium boundaries.

INTRODUCTION

The research on the effect of bidispersion on fluid saturated porous media has grown in the recent past due to its occurrence in several engineering and geophysical applications [1,2]. A bidisperse porous medium exhibits the usual pores or macropores as well as fissures or cracks of smaller size in the solid matrix leading to what we call as micropores. Studies on thermal convection in bidisperse porous media can be seen in the literature [1-5]. There are also some situations in which convection is induced because of concentration gradients of solute. Double diffusive convection arising as a result of gradients of temperature and solute concentration has a wide range of occurrences in geophysics, oceanography and industrial processes and in particular geothermal energy utilization, migration of solute in water saturated soils and so on to quote a few. One can refer Straughan [6,7] for considering double diffusive convection and inertia in macropores of a bidisperse medium and the ensuing instability.

In most complex flows involving mass transfer, we may have to consider the chemical reaction effect as a consequence of reaction kinetics at the solute-fluid interface. The interaction between the chemical reaction and the already existing diffusion can also induce convection in fluid systems. Chemical reaction effects on the convective flows play an important role in the accumulation of CO_2 in the atmosphere and its storage in brine filled aquifers (see Neufeld *et al*. [8]), chemical processing, solidification, etc. Andres and Cardoso [9] examined the effect of first order chemical reaction on the stability of buoyant boundary layer in a porous medium and it was shown to be completely controlled by a parameter that measures the rates of diffusion and reaction compared to convection. Kim and Choi [10] made a linear stability analysis to predict the onset of instability of a chemically reacting porous layer using first order reaction with an objective to understand CO_2 sequestration in the saline aquifers. Harfash [11] made a stability analysis of a reacting fluid saturated porous medium subject to an external magnetic field and reported that stabilizing effect is observed in the presence of magnetic field and chemical reaction. More interestingly, a careful choice of the pore structure has been shown to upgrade the performance of the catalyst and the efficiency of the reforming process during the reaction. Szczygiel [12] carried out an experimental study to enhance the efficiency of reforming catalyst by optimizing its bidisperse structure. Hence, a detailed study of flow through fractured porous media with chemical reaction effects becomes important. In this direction, one can refer Badday and Harfash [13] who investigated the chemical reaction effects in a fluid saturated bidisperse medium leading to convection.

The interest into studies on the transport phenomena in rotating porous systems stems from fundamental scientific importance and geophysical and engineering applications [14-20]. Centrifugal convection can arise in such systems at high rotation speeds even in the terrestrial environment and has

gained less attention when compared to its gravitational counterpart. Vadasz [14] first made a linear stability analysis to predict the onset of centrifugal convection in a porous medium. Following this, linear as well as nonlinear stability analyses on the same problem was made by including the Brinkman and double diffusion effects [16,17]. Recently, Saravanan and Vigneshwaran [19] predicted the onset of thermal convection in a bidisperse porous medium arising due to alternating directions of centrifugal body force. Centrifugal convection in a fluid saturated bidisperse porous medium has been recently considered by Li *et al* [20] for the purpose of oil production from fractured rocks. Motivated by this, we wish to investigate the effect of chemical reaction on centrifugal convection in a fluid saturated bidisperse medium in this paper. While doing so, the associated reaction kinetics is represented in a simplified manner through a first order chemical reaction.

PROBLEM FORMULATION

A tall vertical fluid saturated bidisperse porous medium of thickness L is considered (Refer Fig. 1 of Saravanan and Vigneshwaran [19] with $x_0^* = 0$). The fluid contains chemically reactive solute with concentrations C_l and C_h $(C_h > C_l)$ maintained at the boundaries $x^* = L/2$ and $x^* = -L/2$ respectively with a uniform concentration gradient β_C. This set up is rotating in zero-gravity environment at a constant rate ω about an axis through its centre lying parallel to the vertical z-axis. We assume the layer to be narrow in the y-direction so that the centrifugal acceleration acts normal to the boundaries. The Coriolis force is assumed to be small and the only inertial effect considered is the centrifugal acceleration. The Boussinesq approximation is used to account for the fluid density variations as a function of concentration of the solute. An averaged solute concentration equation is considered that governs mass transfer within the fluid phase with the first order chemical reaction. A two-velocity field model obeying Darcy's law is considered to take care of momentum exchange between the macro- and micropores.

We use the superscripts f & p to represent the macro- and micropores of the bidisperse porous medium. If we fix the porosity associated with macropores as ϕ and that of micropores as ε, then the volume fractions of the micropores alone and macro- and micropores put together are $\varepsilon(1-\phi)$ and $\phi + \varepsilon(1-\phi)$ respectively. The conservation equations of the flow through the configuration mentioned above are

$$\begin{aligned}
&\nabla \cdot \vec{v}^{f^*} = 0,\\
&\frac{\mu}{K_f}\vec{v}^{f^*} + \zeta\left(\vec{v}^{f^*} - \vec{v}^{p^*}\right) = -\nabla P^{f^*} + \rho\omega^2 x^*\vec{\imath},\\
&\nabla \cdot \vec{v}^{p^*} = 0,\\
&\frac{\mu}{K_p}\vec{v}^{p^*} - \zeta\left(\vec{v}^{f^*} - \vec{v}^{p^*}\right) = -\nabla P^{p^*} + \rho\omega^2 x^*\vec{\imath},\\
&\emptyset_1\frac{\partial C^*}{\partial t^*} + \left(\left(\vec{v}^{f^*} + \vec{v}^{p^*}\right)\cdot\nabla\right)C^* = k_c\nabla^2 C^* - K_1 C^*,
\end{aligned} \tag{1}$$

where the superscript * denotes a dimensional quantity and $\emptyset_1 = \emptyset + \varepsilon(1-\emptyset)$. In the above equations, v is the filtration velocity of the fluid, μ the dynamic viscosity, K the permeability, P the pressure, ρ the fluid density, $\vec{\imath}$ the unit vector in the x-direction, t the time, C the concentration of solute, k_c the salt diffusivity, ζ the inter-pore momentum transfer coefficient and K_1 the chemical reaction rate respectively. The overall salt diffusivity k_c and overall chemical reaction rate K_1 of fluid in the bidisperse porous medium are given by

$$\begin{aligned}
&k_c = \emptyset k_c^f + \varepsilon(1-\emptyset)k_c^p,\\
&K_1 = \emptyset K_1^f + \varepsilon(1-\emptyset)K_1^p.
\end{aligned} \tag{2}$$

The fluid density varies with the solute concentration as

$$\rho(C^*) = \rho_0\left(1 + \alpha_c(C^* - C_0)\right), \tag{3}$$

where the subscript o denotes the state at the reference concentration $(C_h + C_l)/2$ and α_c the solute expansion coefficient.

The governing equations admit the following solution

$$\begin{aligned}
&\vec{v}_b^{f^*} = \vec{v}_b^{p^*} = (0,0,0),\\
&C_b^* = \left(\frac{C_0}{\cosh\left(\frac{LA_1}{2}\right)}\right)\cosh(A_1 x^*) - \left(\frac{C_h - C_l}{2\sinh\left(\frac{LA_1}{2}\right)}\right)\sinh(A_1 x^*),
\end{aligned} \tag{4}$$

where $A_1 = L\sqrt{K_1/k_c}$. Its stability is of interest to us and is investigated by introducing perturbations, denoted through primed quantities, in the form

$$(\vec{v}^r, P^r, C) = (\vec{v}_b^r, P_b^r, C_b) + \left(\vec{v}^{r'}, P^{r'}, C'\right), \tag{5}$$

where $r = f, p$. Then the equations governing perturbations in dimensionless form after introducing the transformations $x = x^*/L$, $C = C^*/(\beta_c L)$, $t = t^* k_c/(L^2\emptyset_1)$, $\vec{v}^r = \vec{v}^{r^*}L/k_c$ and $P^r = P^{r^*}/(\zeta k_c)$ and $\beta_c = (C_h - C_l)/L$ are

$$\begin{aligned}
&\nabla \cdot \vec{v}^f = 0,\\
&\vec{v}^f + \sigma_f(\vec{v}^f - \vec{v}^p) = -\sigma_f\nabla P^f + RcxC\vec{\imath},\\
&\nabla \cdot \vec{v}^p = 0,\\
&\frac{1}{K_r}\vec{v}^p - \sigma_f(\vec{v}^f - \vec{v}^p) = -\sigma_f\nabla P^p + RcxC\vec{\imath},\\
&\frac{\partial C}{\partial t} + \left(\left(\vec{v}^f + \vec{v}^p\right)\cdot\nabla\right)C = g\left(v_x^f + v_x^p\right) + \nabla^2 C - \xi^2 C\ ,
\end{aligned} \tag{6}$$

with

$$g(x,\eta,\xi) = \frac{\xi\cosh(\xi x)}{2\sinh\frac{\xi}{2}} - (1+2\eta)\frac{\xi\sinh(\xi x)}{2\cosh\frac{\xi}{2}}.$$

Here $\sigma_f = \zeta K_f/\mu$ is the inter-pore momentum transfer parameter, $K_r = K_p/K_f$ the permeability ratio, $\xi = A_1 L = \left(\sqrt{K_1/k_c}\right)L$ the chemical reaction rate parameter, $\eta = C_l/(C_h - C_l)$ the inverse concentration difference parameter and $Rc = \rho_0\alpha_c\beta_c\omega^2 L^3 K_f/(k_c\mu)$ the solutal centrifugal Rayleigh number. The above equations are supplemented by

$$v_x^f = v_x^p = C = 0 \qquad \text{on} \qquad x = \pm\frac{1}{2}. \tag{7}$$

STABILITY AND NUMERICAL RESULTS

We restrict the perturbations considered to be small enough so that linear stability analysis can be adopted. Following the normal mode technique, we allow the perturbations to change in the form

$$[v^r, P^r, C] = [v^r(x,z), P^r(x,z), C(x,z)]e^{\sigma t}, \quad (8)$$

where the complex constant σ represents the eigenvalue of each mode. The sign of the real part of σ will then decide stability of the system. Applying the curl operator twice on the momentum equations, exploiting the solenoidal nature of the filtration velocity, retaining the x-component of the resulting equation and assuming $v_x^f(x,z) = U^f(x)e^{ikz}$, $v_x^p(x,z) = U^p(x)e^{ikz}$, $C(x,z) = \Phi(\mathrm{x})e^{ikz}$, one can arrive at the amplitude equations

$$\begin{aligned}
&\left(1+\sigma_f\right)(D^2-k^2)U^f - \sigma_f(D^2-k^2)U^p = -Rck^2x\Phi,\\
&\left(\tfrac{1}{K_r}+\sigma_f\right)(D^2-k^2)U^p - \sigma_f(D^2-k^2)U^f = -Rck^2x\Phi,\\
&(D^2-k^2-\xi^2-\sigma)\Phi = -g(U^f+U^p).
\end{aligned} \quad (9)$$

For convenience, the above equations (9) are rewritten as

$$\begin{aligned}
&(D^2-k^2)U^f = -\left(\tfrac{1+2K_r\sigma_f}{1+\sigma_f+2K_r\sigma_f}\right)Rck^2x\Phi,\\
&(D^2-k^2)U^p = -\left(\tfrac{K_r(1+2\sigma_f)}{1+\sigma_f+2K_r\sigma_f}\right)Rck^2x\Phi,\\
&(D^2-k^2-\xi^2-\sigma)\Phi = -g(U^f+U^p),
\end{aligned} \quad (10)$$

subject to the boundary conditions

$$U^f = U^p = \Phi = 0 \qquad \text{on} \qquad x = \pm\tfrac{1}{2}. \quad (11)$$

We shall now show that exchange of stabilities takes place, by proving the growth rate σ to be real. Combining $(10)_1$ and $(10)_2$ and on using $(10)_3$ in the resulting equation, one can get

$$(D^2-k^2)(D^2-k^2-\xi^2-\sigma)\,\Phi = (e_1+e_2)gRck^2x\Phi, \quad (12)$$

where

$$e_1 = \frac{1+2K_r\sigma_f}{1+\sigma_f+K_r\sigma_f}, \qquad e_2 = \frac{K_r(1+2\sigma_f)}{1+\sigma_f+K_r\sigma_f}.$$

Let Ω denote a typical periodicity cell that ensues in the (y,z) plane and $\|\cdot\|$ denotes the $L^2(\Omega)$ norm. We multiply equation (12) by its complex conjugate Φ^* and integrate it over Ω. This results in

$$\begin{aligned}
&\| D^2\Phi \|^2 + (2k^2+\xi^2+\sigma)\,\| \mathrm{D}\Phi \|^2 = -k^2(k^2+\xi^2+\\
&\sigma)\,\| \Phi \|^2 + (e_1+e_2)\int_\Omega gRck^2x\,\| \Phi \|^2\,\mathrm{d}\Omega,
\end{aligned}$$

on using the boundary conditions. Letting $\sigma = Re(\sigma) + iIm(\sigma)$, vanishing of the imaginary part gives

$$Im(\sigma)[\| \mathrm{D}\Phi \|^2 + k^2\,\| \Phi \|^2] = 0. \quad (13)$$

This implies $Im(\sigma) = 0$ and hence $\sigma \in \mathbb{R}$.

On substituting $\sigma = 0$ in (9) we get the following equations corresponding to neutral linear instability limits:

$$\begin{aligned}
&\left(1+\sigma_f\right)(D^2-k^2)U^f - \sigma_f(D^2-k^2)U^p = -Rck^2x\Phi,\\
&\left(\tfrac{1}{K_r}+\sigma_f\right)(D^2-k^2)U^p - \sigma_f(D^2-k^2)U^f = -Rck^2x\Phi,\\
&(D^2-k^2-\xi^2)\Phi = -g(U^f+U^p).
\end{aligned} \quad (14)$$

Thus (14) and (11) constitute an eigenvalue system of equations for the marginal centrifugal Rayleigh number Rc . We determine the critical Rayleigh number as

$$Rc_{cr} = \min_k Rc(k) \quad (15)$$

and the corresponding k is called the critical wavenumber k_{cr}.

We find an approximate solution of the above optimization problem employing the compound matrix method (see Ng and Reid [21]) which is a generalization of the standard shooting technique. It is a simple and effective method for the numerical treatment of systems of hydrodynamic type which are typical of order four or six. We shall discuss below in detail the general procedure used to solve the eigenvalue problem mentioned earlier.

First the eigenvalue problem is converted into a system of six first order differential equations by defining $\boldsymbol{U} = \left(U^f, U^{f\prime}, U^p, U^{p\prime}, \Phi, \Phi'\right)^T$, where the prime denotes differentiation with respect to x. Since three conditions are specified at the right boundary, we choose three independent solutions of the eigenvalue problem, each satisfying the conditions at the left boundary. We label them as $\boldsymbol{U_1}$, $\boldsymbol{U_2}$ and $\boldsymbol{U_3}$ with $\boldsymbol{U_1} = (0,1,0,0,0,0)^T$, $\boldsymbol{U_2} = (0,0,0,1,0,0)^T$ and $\boldsymbol{U_3} = (0,0,0,0,0,1)^T$ at $x = -1/2$. We then construct the 6×3 solution matrix in which $\boldsymbol{U_1}$, $\boldsymbol{U_2}$ and $\boldsymbol{U_3}$ serve as columns in order. The next step is to define an exhaustive list of possible variables which are the 3×3 minors of the solution matrix. This leads to a total number of $6C_3$ such variables $y_1, y_2, \cdots, y_{20}$. The differential equation for each $y_i (i = 1,2,\ldots,20)$ is then obtained by differentiation which leads to a system of 20 first order differential equations.

The solution matrix has rank 3 by the way of its definition and hence there exists at least one initially non-zero y_i. One can observe by inspection that all y_i are initially zero except y_{15}. Thus, the system of ordinary differential equations has to be integrated numerically from $-1/2$ to $1/2$ with the non-zero initial condition $y_{15}(-1/2) = 1$, for which we used the fourth order Runge-Kutta method. The appropriate final condition that satisfies (11) is found to be $y_6(1/2) = 0$. The eigenvalue Rc is then varied until the final boundary condition is satisfied.

RESULTS AND DISCUSSION

The solutal instability in a chemically reacting fluid saturated bidisperse medium is observed to be controlled by the chemical reaction rate parameter ξ, the inverse concentration difference parameter η, the permeability ratio parameter K_r and the inter-pore momentum transfer parameter σ_f. Typical marginal stability curves for different values of the reaction and bidispersion parameters are shown in Fig. 1. When $\xi \to 0$, the solute is chemically non-reactive and the mass balance equation matches with the energy balance equation of Saravanan and Vigneshwaran [19] and hence the present instability limits match with those of the thermally induced one.

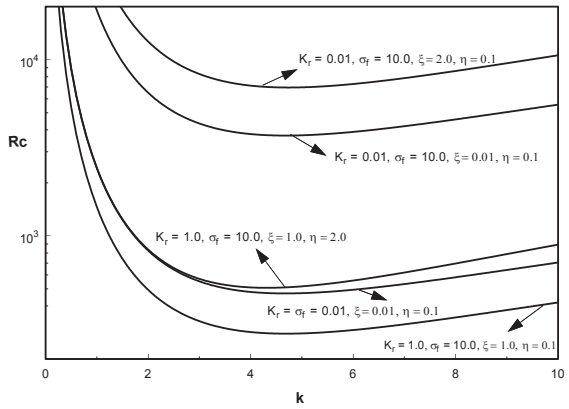

Fig. 1 Marginal stability curves

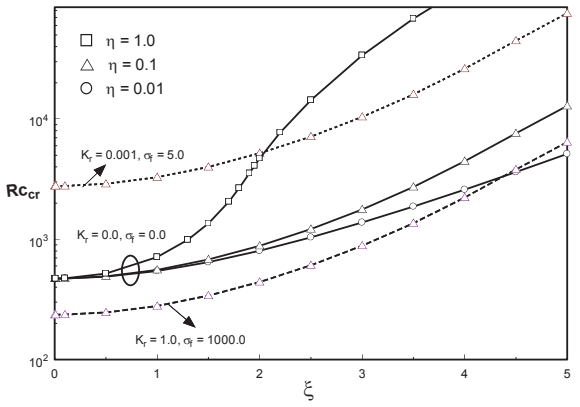

Fig. 2 Rc_{cr} against ξ for different η

Figure 2 displays the effect of ξ on Rc_{cr}. It is clear that an increase in the reaction rate leaves a stabilizing effect to the system resulting in the postponement of the onset of convection. The corresponding k_{cr} is plotted against ξ in Fig. 3. It increases steadily when the concentration difference is high whereas decreases, reaches a minimum and then start to increase forever for higher values of ξ when the concentration difference is low. This minimum k_{cr} might of potential use in relevant centrifugal filtration applications. On the other hand, an increase in the concentration difference across the medium is found to destabilize the system resulting in advancing any instability. It may also be noticed that the instability pattern remains practically invariant against the bidispersion parameters.

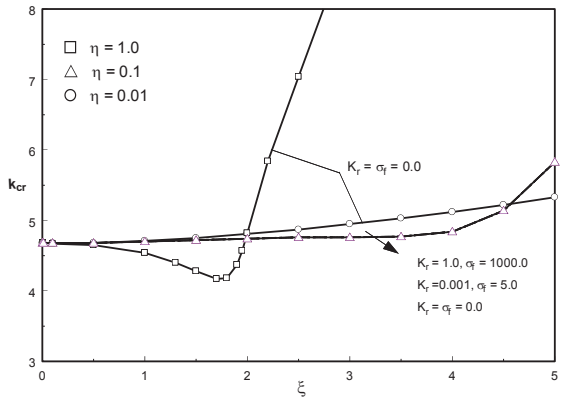

Fig. 3 k_{cr} Vs ξ for parameters considered in Fig. 2

The Rc_{cr} as a function of the permeability ratio K_r fixing $\eta = 2$ is shown in Fig. 4 for different values of σ_f when the solute is non-reacting and reacting. The maximum value of K_r is fixed to be unity on physical grounds. We notice that the onset of convection gets advanced for increasing K_r whereas delayed for increasing σ_f as reported earlier. Other than that, the critical limits of the non-reacting and reacting cases are qualitatively similar and the stabilizing effect of ξ is visible for a wide of σ_f. The corresponding k_{cr} was found to be 4.68 for the non-reactive case and 4.31 for the reactive case. The Rc_{cr} against the inter-pore momentum transfer parameter σ_f for different K_rs is displayed in Fig. 5. The stabilizing effect of σ_f is well observed for its intermediate values only for both the non-reactive and reactive cases. The corresponding k_{cr} was found to be 4.68 for the non-reactive case and 4.82 for the reactive case. It is of interest to note at this stage that k_{cr} remains unaffected by the bidispersion parameters.

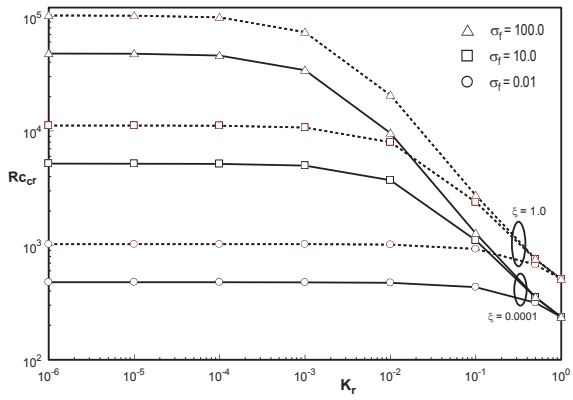

Fig. 4 Rc_{cr} against K_r for different σ_f, ξ when $\eta = 2$

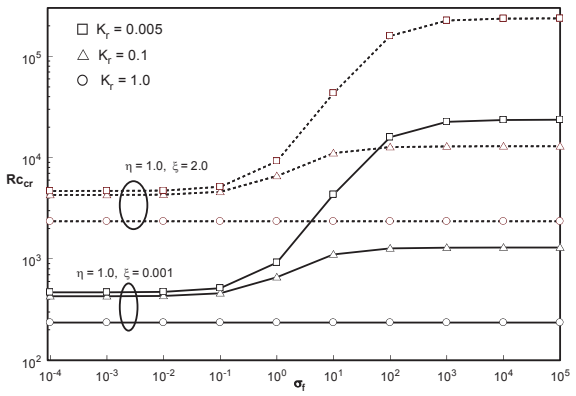

Fig 5 Rc_{cr} against σ_f for different K_r

CONCLUSION

A detailed investigation was carried out to predict centrifugal buoyancy induced solutal instability in a bidisperse porous medium. The reactive nature of the solute was also taken into account. Numerical solution was obtained for the eigenvalue problem resulting via the linear stability analysis. The instability thresholds are found to be affected by the reaction and bidispersion parameters. An increase in the chemical reaction rate and solute concentration difference contribute opposite effects to the system with the former delaying any possible instability. The critical wavenumber is seen to increase against ξ, attaining a local minimum when η takes higher values. The study also reveals that the bidisperse porous medium can be effectively used to suppress convective onset in both non-reactive and reactive cases under consideration.

ACKNOWLEDGMENTS

The authors would like to thank UGC, India for its support through its Special Assistance Programme (SAP) in Differential Equations and Fluid Dynamics. One of the authors (S V) is grateful to UGC for its financial support in the form of Project Fellow under SAP.

REFERENCES

[1] Nield, D.A., Bejan, A., 2017, "Convection in porous media", Springer Science, New York.
[2] Straughan, B., 2017, "Mathematical aspects of multi–porosity continua," Springer Science, New York, 38.
[3] Nield, D. A., and Kuznetsov, A. V., 2006, "The onset of convection in a bidisperse porous medium", Int. J. Heat Mass Transfer, Vol.49, pp.3068-3074.
[4] Straughan, B., 2009, "On the Nield-Kuznetsov theory for convection in bidispersive porous media", Transp. Porous Media, Vol.77, pp.159-168.
[5] Gentile, M., and Straughan, B., 2017, "Bidispersive thermal convection", Int. J. Heat Mass Transfer, Vol.114, pp.837-840.
[6] Straughan, B., 2018, "Bidispersive double diffusive convection", Int. J. Heat Mass Transfer, Vol.126, pp.504-508.
[7] Straughan, B., 2019, "Effect of inertia on double diffusive bidispersive convection", Int. J. Heat Mass Transfer, Vol.129, pp. 389-396.
[8] Neufeld, J. A., Hesse, M. A., Riaz, M., and Hallworth, M. A., 2010, "Convective dissolution of carbon dioxide in saline aquifers", Geophys. Res. Lett., Vol.37p.L22404.
[9] Andres, J. T. H., and Cardoso, S. S. S., 2011, "Onset of convection in a porous medium in the presence of chemical reaction", Phys. Rev. E, Vol.83, p.046312.
[10] Kim, M. C., and Choi, C. K., 2014, "Effect of first-order chemical reaction on gravitational instability in a porous medium", Phys. Rev. E, Vol. 90, p. 053016.
[11] Harfash, A. J., 2015, "Magnetic effect on convection in a porous medium with chemical reaction effect", Transp. Porous Media, Vol.106, pp.163-179.
[12] Szczygiel, J., 2006, "Enhancement of reforming efficiency by optimising the porous structure of reforming catalyst: Theoretical considerations", Fuel, Vol.85, pp.1579-1590.
[13] Badday, A. J., and Harfash, A. J., 2021, "Chemical reaction effect on convection in bidispersive porous medium", Transp. Porous Media, Vol.137, pp.381-397.
[14] Vadasz, P., 1996, "Convection and stability in a rotating porous layer with alternating direction of the centrifugal body force", Int. J. Heat Mass Transfer, Vol.39, pp.1639-1647.
[15] Saravanan, S., and Yamaguchi, H., 2005, "Onset of centrifugal convection in a magnetic fluid saturated porous medium", Phys. Fluids, Vol.17, pp.084105.
[16] Saravanan, S., and Brindha, D., 2010, "Global stability of centrifugal filtration convection", J. Math. Anal. Appl., Vol.367, pp.116-128.
[17] Saravanan, S., and Keerthana, S., 2012, "Effect of double diffusion on centrifugal filtration convection", J. Porous Media, Vol.15, pp.495-500.
[18] Saravanan, S., Brindha, D., and Yamaguchi, H., 2021, "Anisotropic thermomagnetic effects on the universal stability of a diffusive state in porous media", J. Appl. Math. Mech., Vol.101, pp.202000072.
[19] Saravanan, S., and Vigneshwaran, S., 2020, "Centrifugal filtration convection in bidisperse media", Phys. Fluids, Vol.32, pp. 084109.
[20] Li, H., Guo, H., Yang, Z., Ren, H., Meng, L., Lu, H., Xu, H., Sun, Y., Gao, T., and Zhang, H., 2019, "Evaluation of oil production potential in fractured porous media", Phys. Fluids, Vol.31,p.052104.
[21] Ng, B. S., and Reid, W. H., 1985, "The compound matrix method for ordinary differential systems", J. Comput. Phys., Vol.58, pp.209-228.

Proceedings of IWEC2023
The International Workshop of Energy Conversion
March 15-17, 2023, Kyoto, Japan

Paper No. IWEC2023-11

CERN CO_2 PRIMARY COOLING – PROJECT ROADMAP AND FIRST OPERATIONAL UNITS

P. Barroca,* and A. Hafner
Department of Energy and Process Engineering, Norwegian University of Science and Technology (NTNU), Trondheim, Norway
*corresponding author, E-mail: pierre.a.c.barroca@ntnu.no

B. Verlaat and P. Hanf
European Organization for Nuclear Research (CERN), Geneva, Switzerland

ABSTRACT

CERN's two major experiments ATLAS and CMS will undergo the replacement of their entire inner tracker starting in 2026. The new particle detectors to be installed around 100 meters below surface, will be composed of silicon sensors cooled by dedicated CO_2 cooling systems that shall cope with cooling capacity up to 1 MW at -53°C. This work describes what is particular about the design of these systems so the application constraints are respected. Finally, the project's deployment roadmap from the preliminary phases of design studies up to installation of final units is presented together with the experimental feedback from first prototype units already installed and commissioned.

INTRODUCTION

The Large Hadron Collider at CERN has been undergoing major upgrades as part of the High Luminosity Programme (HL-LHC) that plans to increase by a factor of ten the number of events per beam collision with respect to its baseline design [1].

By the end of 2025, the subdetectors located the closest to the LHC particle interaction points (inner detectors) will reach their end-of-life. To cope with the more stringent thermal requirements imposed by the harsh HL-LHC radiation environment and increased need to minimize the amount of mass in the particle tracking region, ATLAS and CMS decided to develop their own modular solution for a reliable and robust cooling system relying solely on CO_2 to cool their inner detectors.

The baseline used for the modular design is described in the technical solution section where the technical challenges particular to this application are described. In the project roadmap section is described system's deployment strategy, the experimental feedback retrieved from testing the first two units built and, finally, a summary of all the learnings to be considered for the final units.

TECHNICAL SOLUTION

The LHC accelerator is located in a 27 km long circular tunnel excavated at a depth of the order of 100 m from the surface. As illustrated in Figure 1, the LHC experiments are built around the accelerator and housed inside large "experimental caverns" while most of ancillaries that are housed in a separate "service cavern" with less restrictive access.

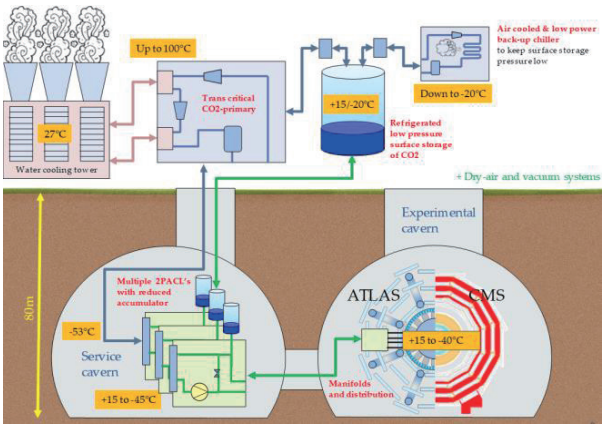

Fig. 1 Overview of ATLAS and CMS cooling system pipeline connections and distribution.

CO_2 evaporative cooling systems based on oil-free mechanically pumped loops have been used successfully for cooling particle detectors since 2008 [2]. It has been adopted since for ATLAS Inner b-Layer (IBL) detector since 2014 [3] and the CMS "Phase-1" Pixel detector since 2016 [4].

The specific CO_2 pumped loop developed for the thermal management of silicon detectors at LHC is commonly referred to as 2PACL [5] and has been the technology adopted by ATLAS and CMS for their future cooling systems.

The 2PACL system will be installed underground in the "services cavern" however, it requires an external system to subcool the liquid CO_2 before pumping it towards the detector and condensate the two-phase CO_2 coming back from the detector. For this, the heat evacuated from the detector must be exchanged with what is called the "primary loop", responsible for rejecting the heat.

Due to space limitations, amount of heat produced and risks of asphyxiation in case of leak, ATLAS and CMS cannot afford installing underground also the primary system. Instead, the system will be installed on surface, inside a dedicated building with all the space and security features needed.

Both experiments decided to go for a CO_2/CO_2 cascade system and the innovative design capable of achieving this ambitious goal is the focus of a research programme launched in common by CERN and NTNU.

Modular CO_2 booster

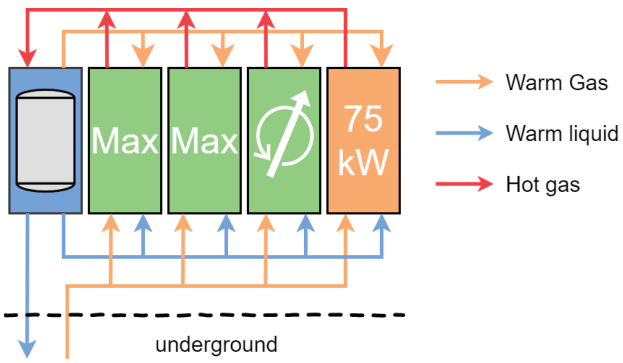

Fig. 2 Illustration of modular scheme adopted for the final system with two modules operating at maximum cooling capacity, one in regulation and one spare module as back-up.

To address the reliability and wide range of cooling capacity required throughout the lifetime of the detector, a modular design for the R744 chillers has been proposed [6]

Inside the dedicated buildings it is foreseen the installation of a group of interconnected CO_2 booster modules as illustrated in Figure 1 with dedicated air gas coolers and a common equipment module with water gas cooler and main liquid receiver.

Each module is designed to cope with the vapour-compressing and heat rejection needs for a given cooling capacity request and will solely operate in case of need. Decoupling the whole unit into independent modules enables the possibility for the maintenance teams to intervene with no risk of perturbing the process.

With a modular scheme, it will be possible to plug the power cabinets of a few compressor slices to a diesel power supply unit, which is quite an advantageous feature in terms of cost and footprint for the whole installation.

Non insulated piping

The R744 liquid supply to the services cavern and the return of evaporated gas to the compressor slices is established via long pipes with no thermal insulation (ambient temperature) leading to a receiver that shall be maintained at pressures higher than conventional R744 applications and to control well the transcritical pressure and temperature at the outlet of the gas cooler so the COP is maximized while sufficient flash gas is produced for pressure control.

Sub-triple point operation

The system is designed to provide cooling underground very close to the triple point saturated temperature of -56°C and with a cooling capacity that may reach up to 1 MW for CMS. Considering the pressure drop along the gas return line, the suction pressure of operation on surface will be at the vicinity of the triple point pressure of 5.2 bara or even below. For that reason, the de-superheating of return line cannot be done via liquid injection due to risk of dry ice. The solution found is to use the CO_2 injected at MT level to desuperheat the return gas via a brazed plate heat exchanger and hence, operate safely the booster system even at below triple-point pressures.

PROJECT'S ROADMAP

The preliminary design studies started around 2018 culminating in a modular CO_2 booster architecture [6]. Given the non-standard design there was need for further research and development. The first studies and evaluation of its inter-operation with a scaled-up version of the second loop CO_2 were launched with the conception of first dual module proof-of concept prototype (System A) and followed by two single module prototypes (System B and C). The second and third unit would learn from first return of experience of System A and used for commissioning the detector parts before transporting them underground.

Fig. 3 System A room two modules installed side by side.

System A

The first prototype (System A) has been installed at CERN since beginning of 2021.
It has been designed with two CO_2 booster modules. Each module equipped with different models of compressors to investigate the performance and reliability of two different manufacturers. The unit has been designed to cope with a maximum cooling capacity of 75 kW for a suction pressure of 6 bara.
Figure 4 illustrates a simplified version of the piping and instrumentation diagram of the system with setpoints corresponding to refrigeration cycle baseline of Figure 5.

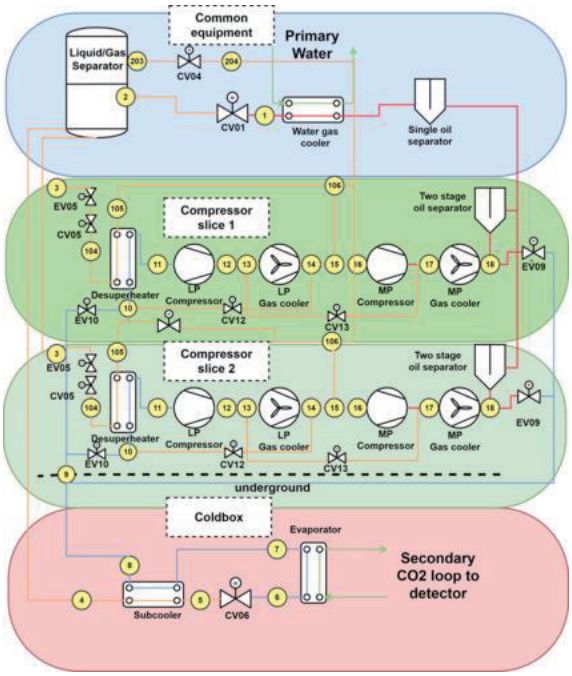

Fig. 4 Simplified piping and instrumentation diagram of System A.

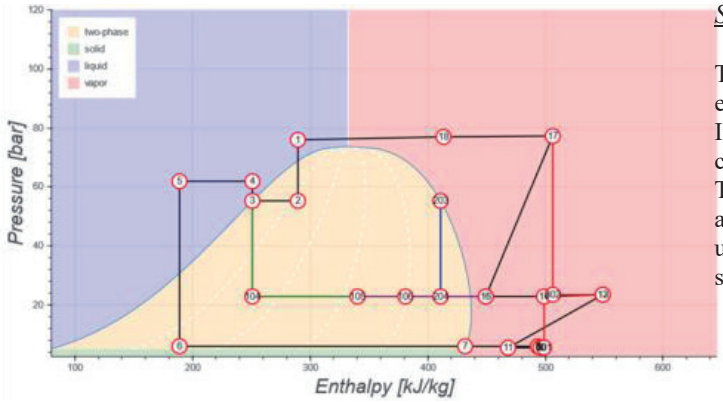

Fig. 5 – Pressure and enthalpy diagram associated to piping and instrumentation diagram of System A.

System B

The second system is the first mature system produced and has been built as a plug and play container so it can easily be relocated. Its design resembles to system A with a three-way valve added to the very last gas cooler and two low pressure (LP) compressors instead of only one.
It presents a cooling capacity around 70 kW at 5.5 bara and its control logic has been improved to get better pressure and super-heating control and to recover more reliably from sudden load changes.
This system has been in use since beginning of 2022 and connected to a surface-to-underground shaft to assess oil separation efficiency and cross check pressure drop measured along the pipeline with expectations.
After conducting every experimental test foreseen, this system will be returned to the ATLAS experiment as a cooling service to commission their systems before installation underground.

Fig. 6 Photo inside System B container with the two low-pressure compressors installed below the medium-pressure compressor.

System C

The third system has just finished its detail design and is expected to be installed at CERN end of first quarter of 2023.
It follows the same design principles as System A with few changes in the sizing and design pressure of equipment.
The performance of this system will be compared to System B and the final learnings will be propagated to the design of final units. Once finished the testing phase, CMS will have the system relocated to their system's commissioning facilities.

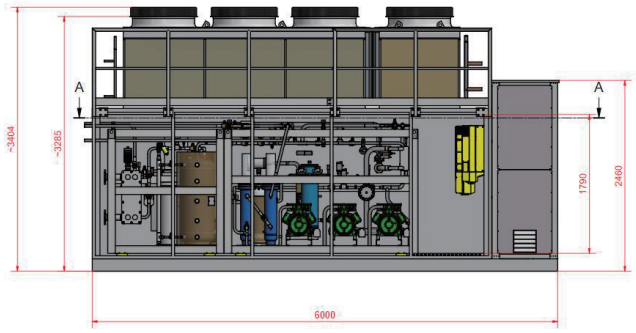

Fig. 7 Preliminary 3D mockup of future System C container with all mechanical and electrical equipment installed.

Final Units

The ATLAS and CMS final systems will be composed of multiple compressor modules operated in parallel and installed in new buildings dedicated to the cooling services installed on surface.

The ATLAS primary system requires a cooling capacity up to 500 kW and will hence be composed of six compressor modules to cover the capacity needs, plus one redundant module – see Figure 8. As the cooling capacity of CMS will top 950 kW, this will be shared between two main collectors that will distribute the flow across one row of six modules and a second row with seven modules. Instead of having all the common equipment shared by every compressor module like the ATLAS design, each row will have dedicated oil separators and gas coolers – see Figure 9. The two module rows will only share a main liquid receiver that with a main supply line connected to the detector underground.

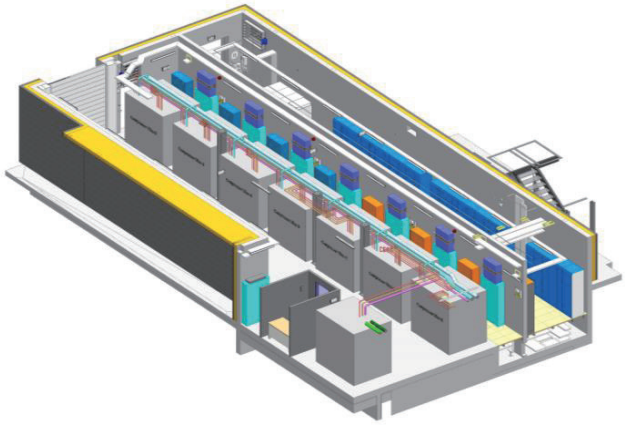

Fig. 8 Future ATLAS machine room for the primary cooling final systems composed of seven compressor modules.

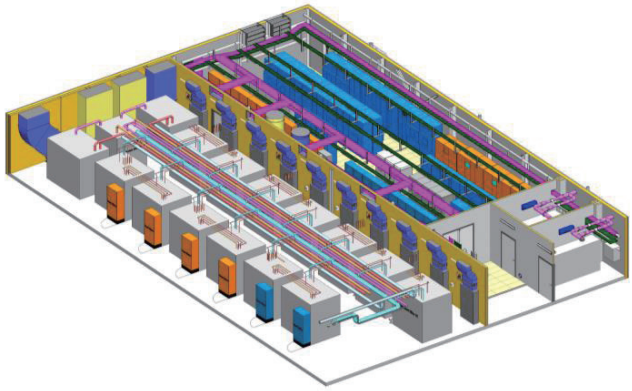

Figure 9 - Future CMS machine room for the primary cooling final systems composed of thirteen compressor modules.

SUMMARY

Learnings and further work

The first proof of concept unit (System A) has been important to validate the system's design and gather the experimental feedback for the design of the following units. On System B a second compressor was added at the low-pressure stage and the control logic as some equipment were changed to resolve some instabilities experienced with the previous unit.

Among the main learnings is the importance for precise control of transcritical pressure and temperature upstream receiver's backpressure valve so the process is kept stable while the temperature of the liquid supply is kept above ambient temperature. The control of liquid injection at the medium pressure level can be particularly tricky during the startup of a compressor module while the desuperheater heat exchanger is still not in thermal equilibrium. As the heat exchanger is designed to operate overflooded, the solution found is to trigger the PID regulation of liquid injection valve only once the heat exchanger is flooded.

Finally, new strategies were adopted in the control logic to avoid abrupt stoppage of the system in case of failure of main sensors and equipment and to keep process stable in case of restart of low-pressure compressors and sudden change of load.

With the final design phase approaching, the management of final units' modular cascade will be of the main importance. For this, a robust dynamic simulation model built with Dymola is currently under work. This simulation model will take the experimental data collected from System B and C for its validation. The goal is to build a digital replica of final units to test different control strategies such that the main requirements in terms of process performance, stability and operation are respected.

REFERENCES

[1] Apollinari, G.; Béjar Alonso, I.; Brüning, O.; Lamont, M.; Rossi, L. High-Luminosity Large Hadron Collider (HL-LHC): Preliminary Design Report; CERN Yellow Reports:

Monographs, CERN: Geneva, 2015. doi:10.5170/CERN-2015-005.
[2] Verlaat, B. et al. CO_2 cooling for the LHCb-VELO Experiment at CERN. Proceedings of 8th IFF/IRR Gustav Lorentzen Conference on Natural Working Fluids, Copenhagen, Denmark, CPD 16-T3-08 2008.
[3] Verlaat, B et al. CO_2 cooling for the LHCb-VELO Experiment at CERN. Proceedings of 8th IFF/IRR Gustav Lorentzen Conference on Natural Working Fluids, Copenhagen, Denmark, CPD 16-T3-08 2008.
[4] Daguin, J. et al. CO_2 cooling for particle detectors: experiences from the CMS and ATLAS detector systems at LHC, and prospects for future upgrades. Proceedings of the 24th IIR International Congress of Refrigeration, Yokohama, Japan, ID:0788 2015.
[5] Colijn, A.; Verlaat, B. Evaporative CO_2 Heat Transfer Measurements for Cooling Systems of Particle Physics Detectors. HEFAT- 2010, 7th International Conference on Heat Transfer, Fluid Mechanics and Thermodynamics, Antalya, Turkey 2010.
[6] Barroca, P.; Hafner, A.; Pardiñas, A.; Verlaat, B.; L., Z.; Hulek,W.; P., P.; Hanf, P.; Battistin, M. Evaporative cooling system with natural refrigerant at -50 °C and 100 m underground. Proceedings of 14th Gustav Lorentzen Conference, Kyoto, Japan, ID:1149 2020.

Proceedings of IWEC2023
The International Workshop of Energy Conversion
March 15-17, 2023, Kyoto, Japan

Paper No. IWEC2023-12

PERFORMANCE IMPROVEMENT STRATEGIES FOR CO_2 BASED EXPERIMENTAL RANKINE CYCLE FOR BETTER SUSTAINABILITY

[1]Serpil Celik-Toker, [1]Onder Kizilkan, [2]Hiroshi Yamaguchi*
[1]Isparta University of Applied Sciences, Faculty of Technology, Department of Mechanical Engineering, 32200, Isparta, Turkey
[2]Doshisha University, Department of Mechanical Engineering, Kyo-Tanabeshi, 610-0321, Kyoto, Japan

*Corresponding author e-mail: onderkizilkan@isparta.edu.tr

ABSTRACT
For the past decades, scientists have focused on research into generating electricity from low-temperature resources like low-grade solar collectors, geothermal energy, and waste heat. Transcritical carbon dioxide (CO_2) Rankine cycle can be used to extract energy from low-temperature heat resources. CO_2 can be directly compressed to supercritical pressures and heated to its supercritical state before expanding to create a better thermal match with the heat resource due to its low critical temperature (31.98 °C) and pressure (7.377 MPa). The perfect temperature-shift matching enables the temperature curves between CO_2 and the heat resource to be almost parallel, thus avoiding pinch point-related constraints and resulting in smaller exergy destruction. In this context, interest in transcritical CO_2 Rankine cycles has been increasing recently to reduce the irreversibility of the heating process. CO_2, which is an environmentally friendly natural fluid, has many special advantages like no ozone depletion and low global warming potential with attractive thermo-physical properties. In this study, energy and exergy analyzes of the solar-based heat recovery transcritical CO_2 Rankine cycle are carried out and compared with the experimental set installed at Doshisha University, Kyoto, Japan. The effects of a regenerator and an energy storage tank are theoretically analyzed for the performance improvement of the transcritical Rankine cycle.

Keywords: PV/T, CO_2, Transcritical CO_2, Hydrogen, PEM Electrolyzer,

INTRODUCTION
Nowadays, a large part of global energy production is supplied from fossil fuels. The use of fossil fuels causes depletion of energy resources, environmental pollution, climate change, and high CO_2 emissions (Li et al., 2016). In this context, electricity generation from low-grade heat resources like renewable energy sources such as solar energy, biomass geothermal energy, and waste heat has been increasing rapidly recently. Because high turbine temperature and pressure cannot be produced in a low-grade heat energy system, the traditional steam Rankine cycle cannot provide high thermal efficiency and is therefore not a viable or economical option (Chen et al., 2006). In contrast, the Organic Rankine Cycle (ORC) is a more suitable alternative for low-grade heat source applications in terms of operating parameters, system dimensions, and thermal performance (Hung et al., 2010). However, in ORC, heat transfer from the weld stream to the working fluid takes place at a constant temperature, causing the pinching problem. The pinching problem causes irreversibility in the cycle, reducing the cycle efficiency (Cayer et al., 2009). High-temperature organic liquids are often flammable and can cause serious safety issues. There are also environmental problems with many organic fluids, especially high Global Warming Potential (GWP) and Ozone Depletion Potential (ODP) (Shu et al., 2017).

Recently, the potential of CO_2-based transcritical Rankine cycles in low-temperature solar energy applications is attracting more interest. The properties of CO_2 can overcome the lack of organic liquids mentioned above. The main advantage of CO_2 as a working fluid is that the pinch point problem that appeared during the heating process of ORC is removed as the heating is in the supercritical area. This situation decreases energy and exergy loss and provides a better temperature match (Baheta et al., 2018). Secondly, CO_2 is natural, non-flammable, non-toxic, environmentally friendly, and non-corrosive. Thanks to these features, it has fewer security problems in case it leaks from the system. In addition, CO_2 is low cost and easily available (Shu et al., 2016). However, the main disadvantage of the transcritical CO_2 Rankine cycle (tCO_2-RC) consisting of an evaporator, turbine, gas cooler, and pump is its low thermal efficiency and low net power output. The first experimental work on the vacuum U tube tCO_2-RC cycle was established in 2004 in Kyoto by a team led by Professor Hiroshi Yamaguchi. Yamaguchi and his team have done many theoretical and experimental studies on the tCO_2-RC. Yamaguchi et al. (2006) calculated the efficiency of the tCO_2-RC between 5-8%. In order to increase the energy efficiency of the tCO_2-RC, a regenerator has been added to the cycle for heat recovery. In addition, since solar energy is an

intermittent renewable energy source, an energy storage tank has been added to the cycle to ensure energy continuity. By adding a regenerator and an energy storage tank to the system, both high thermal efficiency and energy continuity have been achieved.

SYSTEM DESCRIPTION

Figure 1 demonstrates a schematic representation of the experimental tCO_2-RC set up in Kyoto, Japan. The experimental tCO_2-RC consists of a vacuum tube U-tube solar collector, turbine, heat recovery system (HRS), condenser, and circulating pump. The heat required for the tCO_2-RC is supplied from U-tube solar collectors with vacuum tubes. The working fluid, CO_2, heats up and reaches the supercritical phase while passing through the U-tube solar collectors with vacuum tubes. Supercritical CO_2 is sent to the turbine, generating work and then entering the heat recovery system. In the heat recovery system, the temperature of the CO_2 is lowered a little more. The heat energy obtained in the heat recovery system is used in the production of hot water. Then, the CO_2 leaving the heat recovery system enters the condenser and is cooled to the saturated liquid phase. The low-pressure CO_2 in the saturated liquid phase is pressurized with the help of the pump and directed to the solar collector. The U-tube solar collector with the vacuum tube, which acts as a boiler for the tCO_2-RC, is made of 15 collectors, each of which consists of 13 pipes. Figure 2 shows the modified tCO_2-RC. Figures 2a and 2b depict the system in a day and night modes, respectively. The temperature of the CO_2 at the turbine outlet is still high. A regenerator has been added to the system to recover this heat to the system. In addition, since solar energy is intermittent, a heat storage tank has been attached to the system for sustainable energy. During the daytime, energy is stored in the phase change material (PCM) tank from the CO_2 temperature at the turbine outlet. In the night situation, work is produced by taking heat from the PCM tank.

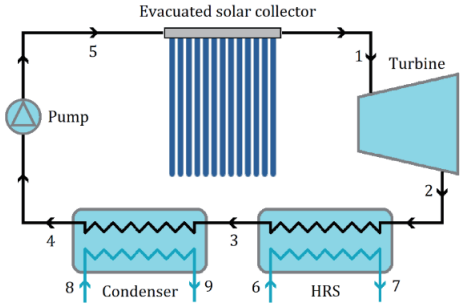

Figure 1. Schematic representation of the experimental tCO_2-RC

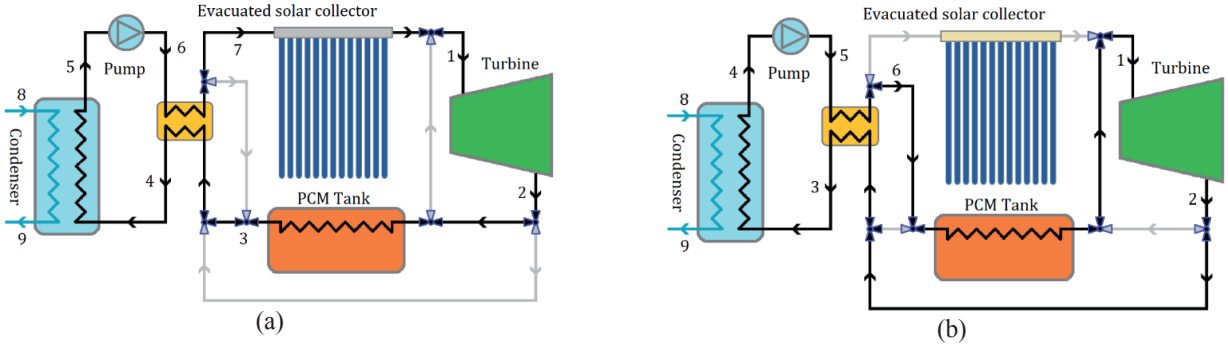

Figure 2. Modified tCO_2-RC a) day mode b) night mode

RESULTS AND DISCUSSIONS

The solar energy-based simple tCO_2-RC installed in Kyoto, Japan, has been modified to recover heat at the turbine outlet, increase the overall energy efficiency of the cycle, and ensure energy sustainability. A generator and a PCM tank are attached to the simple experimental tCO_2-RC. Energy analyzes of tCO_2-RCs with and without regenerator are made, and the systems are compared. In addition, it is calculated how long the energy stored in the PCM tank operates the system in the absence of the sun. Figure 3 displays the time variation of the CO_2 temperature leaving the evacuated U-tube solar collector with and without the regenerator. Higher fluid temperatures are reached in the tCO_2-RC with the regenerator. Figure 4 exhibits the time-dependent variation of the net work produced in the tCO_2-RC with and without the regenerator. As with the collector outlet temperature, the amount of net power generated from the cycle is greater than that of the tCO_2-RC with the regenerator. This is because the temperature of the CO_2 fluid entering the turbine is higher than the tCO_2-RC with the regenerator. The maximum CO_2 temperature is calculated to be 234 °C when the regenerator is employed, while the maximum fluid temperature with the absence of the regenerator is determined as 221 °C.

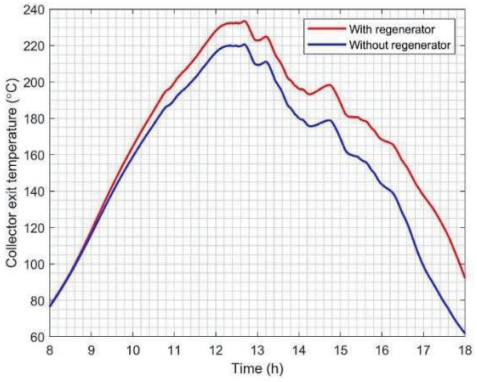

Figure 3. Variation of CO_2 temperature at collector exit

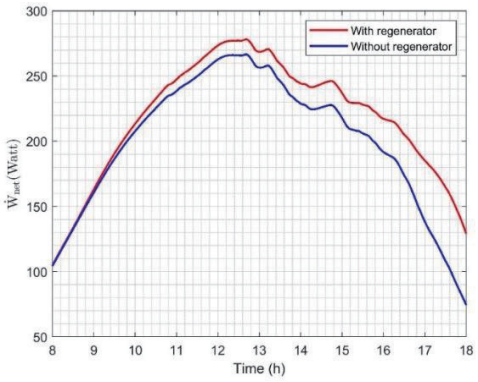

Figure 4. Variation of net power generation

Figure 5 demonstrates the time-dependent energy efficiency variation of the transcritical Rankine cycle with and without the regenerator. As can be seen from Figure 5, the tCO_2-RC with a regenerator is much higher than the tCO_2-RC without a regenerator. Because in the tCO_2-RC with regenerator, the heat of the high-temperature CO_2 at the turbine outlet is recovered to the system. This reduces the heat drawn from the collector and increases the efficiency of the system. While the maximum energy efficiency is 11 % in the case with the regenerator, the maximum energy efficiency is 7 % in the case without the regenerator. In Figure 6, turbine outlet and PCM temperatures are plotted against time. During the analysis carried out by the MATLAB program, the minimum temperature difference between the fluid temperature and the PCM was assumed to be 15 °C in order to maintain a stable heat transfer operation. As can be seen from the figure, the PCM temperature increases with the increase of turbine outlet temperature and reaches phase change temperature at about 10:40 pm, which is 95 °C. After this time, PCM starts to melt, and at about 16:30, the phase change process finishes, and the PCM temperature continues to increase again. However, the energy storage operation finishes after it reaches 99 °C due to the temperature difference between the PCM and the fluid drops below 15°C. It must be noted that there is still some amount of energy to be transferred to the PCM; however, the temperature difference constraint does not allow this. Maybe, at this point, an axillary low-temperature PCM tank can be used in order to sore some more energy; however, this can be a topic of another study. In the current study, it is only aimed to investigate the energy storage possibility of the system.

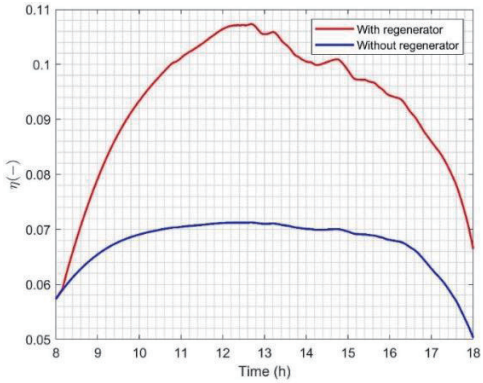

Figure 5. Variation of cycle efficiency

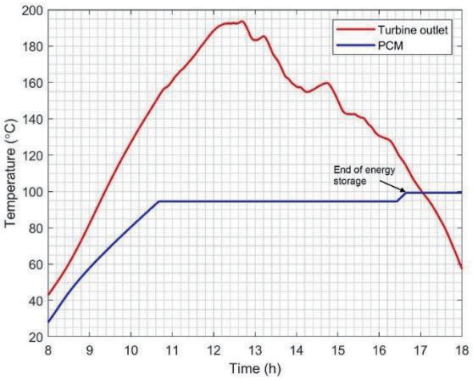

Figure 6. Variation of turbine outlet and PCM temperature

Since the system stops the operation after the sunset, one of the main investigations of the previous study is to extend the operation hours by employing the PCM energy storage. According to the calculations, the stored energy is adequate to run the transcritical power cycle during nighttime. Figure 7 shows the variation of CO_2 and PCM temperatures with time. As can be seen from the figure, after the start of the operation, PCM temperature starts to decrease due to the energy transfer to CO_2. After a couple of minutes, the temperatures remain constant since the PCM reaches to phase change region, and during the phase change process, the CO_2 temperature also remains constant. After 40 minutes, the phase changer process ends, and again the temperatures start to decrease. At about 55 minutes, the operation finishes due to the minimum temperature constraint of the working fluid, which was assumed to be 40 °C. In Figure 8, the variation of net power generation and the efficiency of the transcritical cycle is given. With the same manner as the results of fluid and PCM temperatures explained above, the power generation remains constant during the phase change process and finishes after 55 minutes. As can be seen from the figure, the maximum power generation is calculated to be 120 W, where the maximum efficiency is determined to be 0.068. In order to enhance the power generation duration, some more PCM tanks can be employed. Another option can be employing individual collectors for only storing the solar energy in PCM tanks; thus, energy generation can be extended even to the sunshine hours.

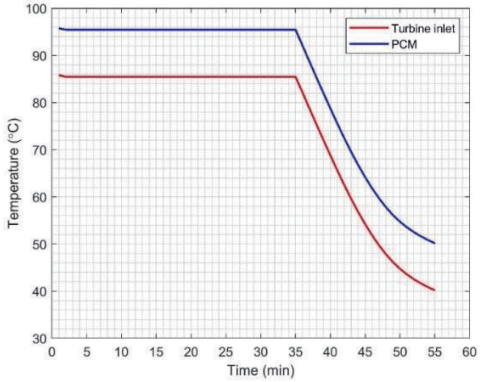

Figure 7. Variation of turbine inlet and PCM temperature in PCM mode

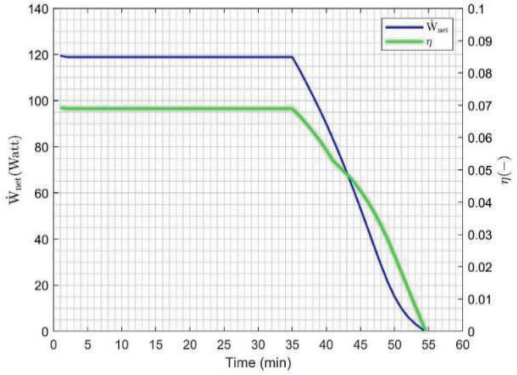

Figure 8. Variation of net power generation and cycle efficiency in PCM mode

To better understand the results of the utilization of the regenerator and the energy storage medium, a comparison is made for the energy generation rate of both systems, as shown in Figure 10. According to the results, the original system is capable of generating an electricity rate of 2817 Wh on a specific day. Besides, with the employment of the regenerator, the energy generation rate increases by about 200 Wh, where total energy generation reaches 3021 Wh. Additionally, after sunset, during the nighttime operation, an energy rate of 136 Wh can be generated using the stored energy by means of the PCM tank. According to the figure, the increment ratio is calculated to be nearly 12 %.

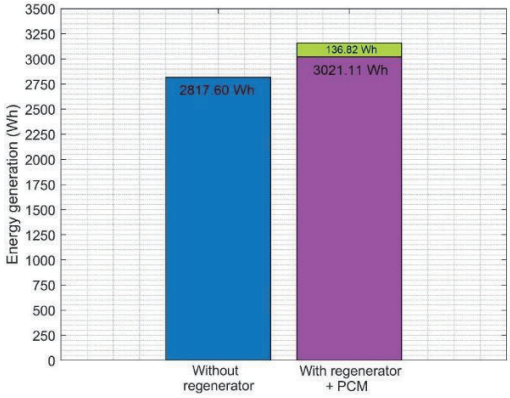

Figure 10. Comparison of daily generated electricity for original and improved cycles

REFERENCES

1. Behata A.T., Hailegiorgis S.M., Oumer A.N., Sulaiman B S.A., 2018. Performance analysis of transcritical carbon dioxide Rankine cycle with regenerator. MATEC Web of Conferences, 225, 05020.
2. Cayer E., Galanis N., Desilets M., Nesreddine H., Roy P., 2009. Analysis of a carbon dioxide transcritical power cycle using a low temperature source. Applied Energy, 86 (7-8), 1055-1063.
3. Hung T.C., Wang S.K., Kuo C.H., Pei B.S., Tsai K.F., 2010. A study of organic working fluids on system efficiency of an ORC using low-grade energy sources. Energy, 35(3), 1403-1411.
4. Li L., Ge YT., Luo X., Tassou, S.A., 2016. Thermodynamic analysis and comparison between CO_2 transcritical power cycles and R245fa organic Rankine cycles for low grade heat to power energy conversion. Applied Thermal Engineering, 106, 1290-1299.
5. Shu G., Shi L., Tian H., Li X., Huang G., Chang L., 2016. An improved CO_2-based transcritical Rankine cycle (CTRC) used for engine waste heat recovery. Applied Energy, 176, 171-182.
6. Shu G., Shi L., Tian H., Deng S., Li X., Chang L., 2017. Configurations selection maps of CO_2-based transcritical Rankine cycle (CTRC) for thermal energy management of engine waste heat. Applied Energy, 186, 423-435.
7. Yamaguchi H., Zhang X.R., Fujima K., Enomoto M., Sawada N., 2006. Solar energy powered Rankine cycle using supercritical CO_2. Applied Thermal Engineering, 26, 2345-2354.

Proceedings of IWEC2023
The International Workshop of Energy Conversion
March 15-17, 2023, Kyoto, Japan

Paper No. IWEC2023-13

TRANSIENT BOUNDARY HEAT TRANSFER ANALYSIS OF A NEAR-CRITICAL EXPERIMENTAL CHAMBER REALIZED BY PIXELATED PHASE-SHIFTING INTERFEROMETRY

Y.Z. ZHANG[1,2], L. Chen[1,2,3]*, Q.X. Wu[1,2], Y. Kanda[4], A. Komiya[4], J.G. Zang[5], Y.P. Huang[5]
1 Institute of Engineering Thermophysics, Chinese Academy of Sciences, Beijing 100190, China
2 University of Chinese Academy of Sciences, Beijing 100049, China
3 Innovation Academy for Light-Duty Gas Turbine, Chinese Academy of Sciences, Beijing 100190, China
4 Institute of Fluid Science, Tohoku University, Sendai 985-8577, Japan
5 CNNC Key Laboratory on Nuclear Reactor Thermal Hydraulics, Nuclear Power Institute of China, Chengdu 610041, China
*Corresponding Email: chenlin2018@iet.cn

ABSTRACT

Supercritical carbon dioxide (CO_2) has been considered to be an ideal working fluid in advanced Brayton cycles. A better understanding of near-critical CO_2 heat transfer mechanism is urgently needed for the condition optimization and efficiency improvement. However, the investigation on the near-critical CO_2, especially near the critical point and pseudo-critical line, has been impeded for the lack of reliable measurement methods.

In this research, near-critical conditions are achieved in a visualization cell (4 mm×7 mm×6 mm), pixelated phase-shifting interferometry method is applied to measure the transient boundary heat transfer behaviors of near-critical CO_2. According to the visualized figures of temperature field and followed quantitative analysis, it was found that when the condition point deviates from the pseudo-critical line (temperature increase from 32 ℃ to 34 ℃ along the isobar), (1) a larger temperature gradient can be produced; (2) high temperature clusters tend to escape from the thermal boundary; (3) the Nusselt number decreases.

INTRODUCTION

More attentions have been attracted to the study of supercritical CO_2 Brayton cycles for the merits of higher cycle efficiency, better equipment compactness and lower purification system requirements compared with that of conventional cycles. [1,2] A wider application area can be seen in nuclear, fossil fuel, waster heat, solar energy, offshore power system, etc. Although CO_2 is considered to possess a higher heat transfer capacity than other gases, which is helpful for the decrease of the size of the heat exchanger, the complex heat transfer mechanism caused by the extraordinary thermal properties in near-critical region brings a great challenge to its feasibility. A clear understanding of near-critical CO_2 heat transfer behaviors is greatly needed.

Although the heat transfer efficiency (the ratio of bulk heating rate to the total heat input) is surprisingly low according to conventional diffusion law in a near-critical region, the so-called Piston Effect (PE) will help enhance the transportation process [3,4]. However, the dramatic change in thermal properties near the critical point brings a great challenge to the system design, fundamental thermal analysis and key parameter measurement.

Hence, under the multi-effects of heat capacity, thermal diffusivity, thermal conductivity, etc., both heat transfer enhancement and deterioration may occur when the pseudo temperature is included by the fluid bulk temperature and the temperature of fluid near the surface in the above-mentioned aerospace applications and energy systems [5,6]. For some heat transfer occasions in high flux conditions, the heat transfer coefficient appears to be lower than expected. Due to the relatively small variation of heat transfer coefficient compared with that of boiling, there is still no precise measurements and prediction methods for such phenomena [7]. In detail, due the steep properties change in supercritical condition the control and measurement of supercritical heat transfer process are very difficult. Accurate and reliable measurements are urgently needed for the clarification of the sensitive and rapid heat transfer mechanism.

In this research, pixelated phase-shifting interferometry method is employed in the investigation of thermal dynamic analysis of transient boundary heat transfer behaviors in near-critical region, the influence of temperature deviation from the pseudo-critical line on the thermal dynamic process is primarily clarified.

METHODOLOGY

Visualization cell

The visualization cell is crucial in the designation of the supercritical fluid experiment system. Two problems should be primarily considered: (1) The sealing of the internal cavity

should be carefully delt to endure the high pressure in supercritical state; (2) transparency should be ensured to decrease the measurement error.

In this research, a visualization cell is carefully designed to achieve the near-critical conditions. This visualization is mainly fabricated with the Al alloy material and connected with bolts. Two thermostat peltier elements are arranged at the upper and bottom surface of the visualization cell to maintain the overall temperature. Inside the cell, one hole is reserved at the upper-right corner of the internal cavity for fluid injection, two thermistors are placed at the upper-left and bottom-left corner to measure the fluid temperature near the upper and bottom surface. With the help of heating peltier element placed beneath the bottom surface of the internal cavity, transient boundary heat transfer progress can be triggered. In addition, in order to enable the optical measurements, two sapphire windows are arranged at the center of the front and back surface. Detailed information can be seen in Fig. 1.

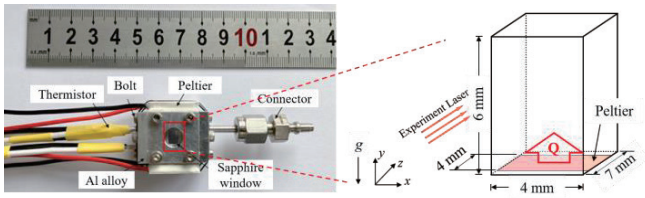

Fig. 1 Picture of the visualization cell and the heat transfer design from button surface.

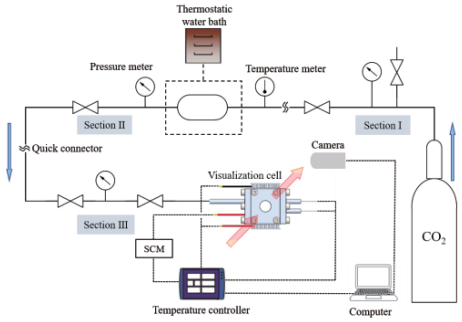

Fig. 2 Schematic diagram of supercritical CO_2 flow control and measurement system.

Measurement system

The aforementioned visualization cell will then be connected to the supercritical CO_2 flow control and measurement system (seen in Fig. 2). This system mainly consists of three sections, the first section starts from the CO_2 cylinder, going through the atmospheric valve and pressure meter, section I ends with a quick connecter to facilitate the convenient operation during experiments. The second section contains a buffer tank, temperature meter and pressure meter. This section is designed to be portable to derive CO_2 from the cylinder and transfer it to the visualization cell. After another quick connecter, the visualization cell is set at the end of the supercritical CO_2 flow control and measurement system. The built-in thermistors and thermostat peltier elements are connected to the temperature controller, according to the internal fluid temperature acquired by built-in thermistors, the thermostat peltier elements can be activated to keep the overall cell temperature at designed conditions.

During the experiment, test beam goes vertically through the visualization cell through two sapphire widows, the variation of refraction rate of internal fluids caused by bottom heating can be recorded in the test beam and obtained by the camera, then transferred to the computer for further procession.

Phase-shifting interferometer system

Fig. 3 gives a clear exhibition of the structure of the Pixelated-Array Masked phase-shifting interferometer used in this research, which originated in the typical design of Mach-Zehnder type. A linearly-polarized He-Ne laser light source is selected to produce a light goes through a neutral density (ND) filter (b), then the polarization angle of the beam was controlled to $\pi/4$ by a half-wave plate (c). A spatial filter (d) consisted of an objective lens and a pinhole (with a diameter of 10 μm) was used to utilize the most stable part of the laser beam. Then the laser beam was collimated to a circular light facula (with a diameter of 20 nm) by a plano-convex lens (e) (f = 150 mm). Then the laser beam was splitted into a test beam and a reference beam, which have a $\pi/2$ polarizing angle difference between each other, through a polarized beam splitter (g). After the test beam goes through the experimental cell (h), it was re-superposed by another polarized beam splitter with the conference beam. After that, the beams were circularly polarized by a quarter-wave plate (i) is and thus the two beams would inter-fere with each other. After redirected and magnified by a plano-convex lens (j) and a concave lens (k), the laser beams were finally recorded by a recording camera (l). And the interferogram information can be transferred to the PC to obtain transient field data.

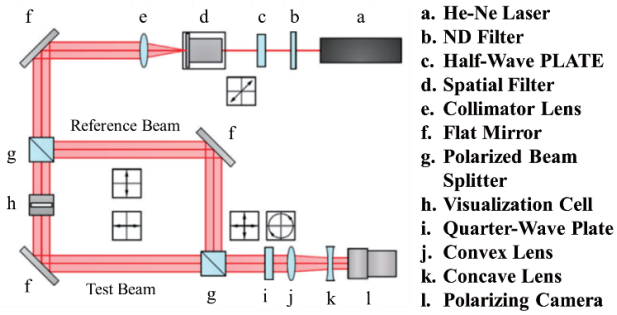

Fig. 3 Schematic of the Pixelated-Array Masked phase-shifting interferometer.

A pixelated-array masked method has been introduced in the capturing of polarized light information during optical measurement. In this study, the 2 × 2 pix-elated-array of optical sensors are mounted in the receive plane of the recording camera. In this design, the camera can capture simultaneous images at four polarizing angles (0, π / 2, π and 3π / 2). Those simultaneous interferogram pictures are calculated to reconstruct the full picture of the transient phenomena during the measurement from four angle data. In the base case analysis in this study, the frame rate was set at 24 fps (full span of 4896 × 4096), while for high-speed measurement it was set up to 500 fps under ROI mode (Region of interest adjustment).

Data extraction procedures

A series of laser diagnostic process has been performed on

the raw figures captured by the camera. Firstly, the phase-difference data is extracted from the raw interferograms, then the obtained phase-difference data will be transferred to density field data. Secondly, considering the relatively small variation in pressure, the temperature can be calculated with constant pressure assumption. Based on the acquired temperature distribution data, the local properties are calculated. Considering the heating developed along the y axis, the cavity is divided into 50 elongated regions along the x axis to embody the heating inhomogeneity in the cavity. More detailed introduction about data extraction procedures can be referred in Zhang et al.'s work[8].

Experimental conditions and parameters

The experimental conditions and parameters can be found in Table 1. Four cases given in Table 1 share two P-T states. These states share a same pressure (7.44 MPa) and differs in temperature (case 1,2: 32℃, case 3,4: 32℃). These parameters are set with the intention of clarify the near-critical CO_2 heat transfer mechanism. Later discussions in this study will be made from those four cases under different heat influx conditions from the bottom of the visualization cell. The influence of condition temperature can be exhibited in the comparison of given cases.

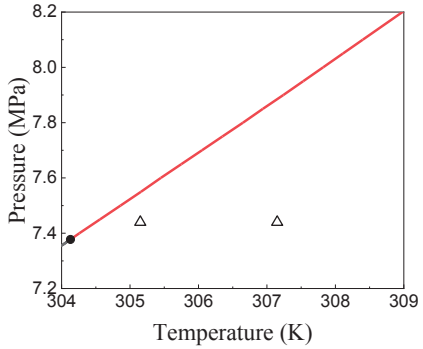

Fig. 4 Condition near-critical CO_2 tests in this research.

Table 1 Summary of experimental conditions. (Calculated using the equation of state proposed by Span and Wagner [9])

Case No.	Pressure /MPa	Temperature /℃	Density /(kg/m^3)	Heat flux /(× 10^4 W/m^2)
1	7.44	32.0	330.14	3.41
2	7.44	32.0	330.14	5.12
3	7.44	34.0	278.02	3.41
4	7.44	34.0	278.02	5.12

RESULTS AND DISCUSSIONS

The detailed temperature distribution is given in fig.5 (p = 7.44 MPa, T = 32.0 ℃) and fig.6 (p = 7.44 MPa, T = 34.0 ℃). For a rough look, there is an obvious difference between two conditions. When the same heat flux is applied to the visualization cell, a larger temperature gradient is produced in case 3 (p = 7.44 MPa, T = 34.0 ℃, q = 3.41 × 10^4 W/m^2) and case 4 (p = 7.44 MPa, T = 34.0 ℃, q = 5.12 × 10^4 W/m^2) compared with that in case 1 (p = 7.44 MPa, T = 32.0 ℃, q = 3.41 × 10^4 W/m^2) and case 2 (p = 7.44 MPa, T = 32.0 ℃, q = 5.12 × 10^4 W/m^2). In detail, even though a wider range of color bar is applied, the measured temperature distributions of near-critical CO_2 in case 3 and case 4 still exhibit larger area of high temperature region. This phenomenon can be generally explained by the different heat capacity in two conditions (18.72 kJ/kg·K in case 1,2 and 6.87 kJ/kg·K in case 3,4).

To be more specific, When the temperature distribution in case 1 is compared with that in case 3, it can be found from the shape of temperature distribution in case 3 (seen in fig.6 (a)) that several high temperature clusters escaped from the thermal boundary, while the border of thermal boundary in case 1 keeps smooth and continuous.

Based on the temperature distribution data, local Nusselt number is calculated, and the heat transfer charactoristic is quantitatively analysed. Here, the local Nusselt number distribution in the visualization cell after different period of heating is given in fig.7 (p = 7.44 MPa, T = 32.0 ℃) and fig. 8 (p = 7.44 MPa, T = 34.0 ℃). In all cases given in this research, the local Nusselt numbers of each location showed a gradual downward trend. In the two set of horizontal comparisons between the local Nusselt number distribution in case 1, 3 and case 2, 4, it can be found that the value of local Nusselt number decreases as the condition temperature increases or input heat flux decreases.

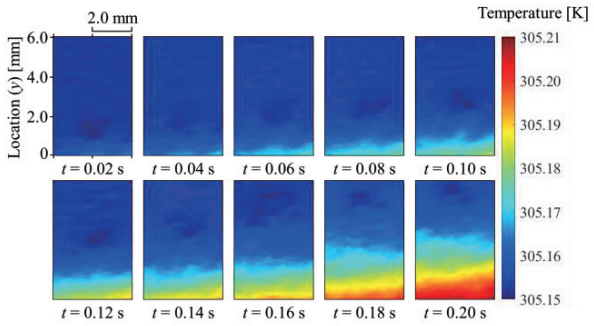

(a) p = 7.44 MPa, T = 32.0 ℃, q = 3.41 × 10^4 W/m^2

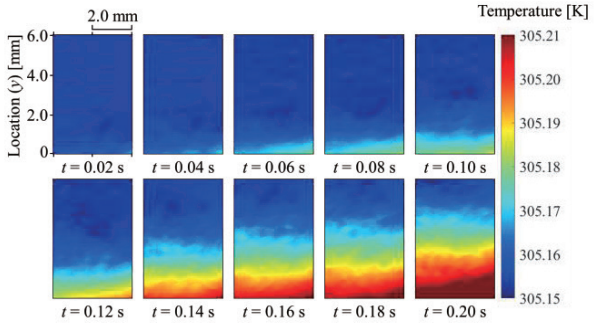

(b) p = 7.44 MPa, T = 32.0 ℃, q = 5.12 × 10^4 W/m^2

Fig. 5 Temperature distributions of near-critical CO_2 fluid under bottom heating. p = 7.44 MPa, T = 32.0 ℃. (a) q = 3.41 × 10^4 W/m^2; (b) q = 5.12 × 10^4 W/m^2.

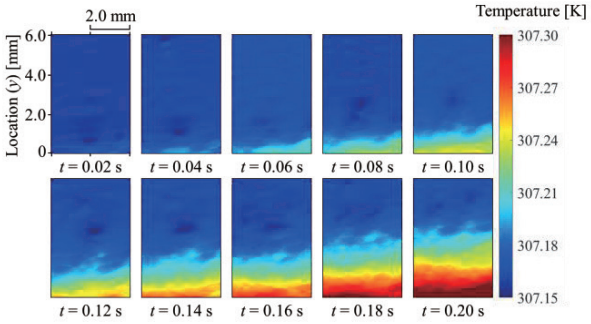

(a) p = 7.44 MPa, T = 34.0 ℃, q = 3.41 × 10^4 W/m^2

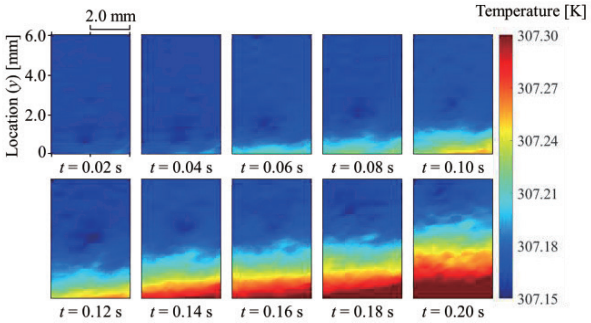

(b) p = 7.44 MPa, T = 34.0 ℃, q = 5.12 × 10^4 W/m^2

Fig. 6 Temperature distributions of near-critical CO_2 fluid under bottom heating. p = 7.44 MPa, T = 34.0 ℃. (a) q = 3.41 × 10^4 W/m^2; (b) q = 5.12 × 10^4 W/m^2.

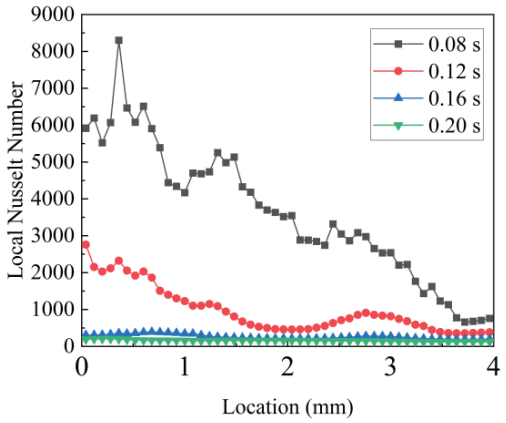

(a) p = 7.44 MPa, T = 32.0 ℃, q = 3.41 × 10^4 W/m^2

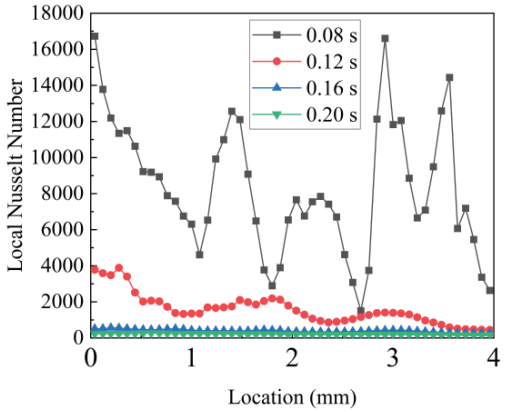

(b) p = 7.44 MPa, T = 32.0 ℃, q = 5.12 × 10^4 W/m^2

Fig. 7 Local Nusselt number of near-critical CO_2 fluid under bottom heating. p = 7.44 MPa, T = 32.0 ℃. (a) q = 3.41 × 10^4 W/m^2; (b) q = 5.12 × 10^4 W/m^2.

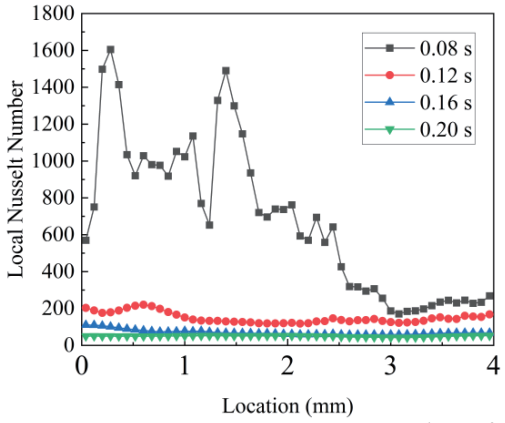

(a) p = 7.44 MPa, T = 34.0 ℃, q = 3.41 × 10^4 W/m^2

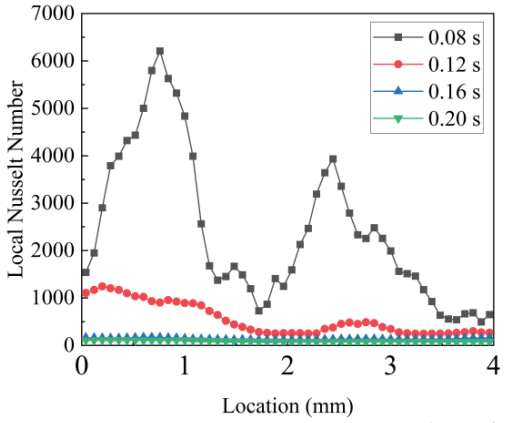

(b) p = 7.44 MPa, T = 34.0 ℃, q = 5.12 × 10^4 W/m^2

Fig. 7 Local Nusselt number of near-critical CO_2 fluid under bottom heating. p = 7.44 MPa, T = 32.0 ℃. (a) q = 3.41 × 10^4 W/m^2; (b) q = 5.12 × 10^4 W/m^2.

CONCLUSIONS

In this research, the transient boundary heat transfer behaviors of near-critical CO_2 are investigated, the influence of temperature deviation from the pseudo-critical line on the thermal dynamic process is primarily clarified. three conclusions are drawn when the condition point deviates from the pseudo-critical line (temperature increase from 32 ℃ to 34 ℃ along the isobar) according to the visualized figures of temperature distribution and followed quantitative analysis: (1) Under the same pressure condition, a larger temperature gradient can be produced in cases with larger distance from pseudo-critical line; (2) The escape of high temperature clusters from the thermal boundary is observed in the condition away from the pseudo-critical line; (3) As the condition temperature increases, the Nusselt number tends to decrease.

ACKNOWLEDGMENTS

This study has been conceptualized by Prof. Lin Chen and executed in Langfang Experimental Center of Institute of Engineering Thermophysics, Chinese Academy of Sciences. This study has been supported by the CAS Project for Young Scientists in Basic Research, grant number YSBR-043, the National Natural Science Foundation of China, grant number 52076207, 51906235 and 51961145201, the Open fund of CNNC Key Laboratory on Nuclear Reactor Thermal Hydraulics, Nuclear Power Institute of China, grant number 2020RETHOF-071801, the Key Research Program of the CAS Innovation Academy for Light-duty Gas Turbine, grant number CXYJJ21-ZD-01 and Start-up Fund of CAS.

REFERENCES

[1] Wu, P., Gao, C., Huang, Y., Zhang, D., Shan, J., 2020, Supercritical CO_2 Brayton cycle design for small modular reactor with a thermodynamic analysis solver, SCI TECHNOL NUCL INS, Vol.2020, pp.1-16.

[2] Chen, L., Iwamoto, Y., 2017, Advanced applications of supercritical fluids in energy systems, IGI Global, Hershey, pp.136-187.

[3] Onuki, A., Hao, H., Ferrell, R.A., 1990, Fast adiabatic equilibration in a single-component fluid near the liquid-vapor critical point, Phys Rev A, Vol.41, pp.2256–2259.

[4] Zappoli, B., Bailly, D., Garrabos, Y., le Neindre, B., Guenoun, P., Beysens, D., 1990, Anomalous heat transport by the piston effect in supercritical fluids under zero gravity, Phys Rev A, Vol.41(4), pp.2264.

[5] Bailly, D. and Zappoli, B., 2000, Hydrodynamic theory of density relaxation in near-critical fluids, Phys Rev E, Vol. 62(2), pp.2353.

[6] Chen, L., Zhang, R., Kanda, Y., Basu, D.N., Komiya, A., Chen, H., 2022, Asymptotic analysis of boundary thermal-wave process near the liquid–gas critical point, Phys. Fluids, Vol. 34(3), pp. 036102.

[7] Chen, L., 2017, Microchannel flow dynamics and heat transfer of near-critical fluid, Springer, Singapore, pp. 6-14.

[8] Zhang, Y., Chen, L., Wu, Q., Yang, D., Kanda, Y., Zang, J., Komiya, A., Huang, Y., 2022, Preliminary measurements of transient boundary heat transfer process under supercritical pressures using pixelated phase-shifting interferometry, Int Commun Heat Mass Transf, Vol. 138, pp. 106396.

[9] Span, R. and Wagner, W., 1996, A new equation of state for carbon dioxide covering the fluid region from the triple-point temperature to 1100 K at pressures up to 800 MPa, *J Phys Chem Ref Data*, Vol. 25, pp. 1509–1596.

Proceedings of IWEC2023
The International Workshop of Energy Conversion
March 15-17, 2023, Kyoto, Japan

Paper No. IWEC2023-14

ONE-STEP REDUCTION PROCESS OF SILICA TO SILICON BY MOLTEN SALT ELECTROLYSIS

Y. Suzuki and S. Tanaka
Organization for Research Initiatives and Development, Doshisha University, Kyoto, Japan

T. Goto*
Department of Science of Environment and Mathematical Modeling Graduate School of Science and Engineering, Kyoto, Japan
*Corresponding author, E-mail: tgoto@mail.doshisha.ac.jp

ABSTRACT

Electrodeposition of silicon from silica in high-temperature melts is one of the promising methods for environmentally friendly and inexpensive process to construct solar power systems. To realize a sustainable resource and energy system for constructing the SDGs society, it is necessary to accumulate fundamental physicochemical properties such as electrochemical behavior and coordination structure of Si ions in high temperature molten salts. In this study, we report the relationship between the Si deposition mechanism from SiO_2 in molten salt and the melt structure by electrochemical methods, high temperature Raman spectroscopy, and quantum chemical calculations based on density functional theory to elucidate the interfacial phenomena between the electrode surface and the molten salt. The addition of Li_2O as an oxide ion source cleaves the Si-O-Si bonds in SiO_2 to form silicon oxyfluoride, resulting in Si electrodeposition, which is confirmed to produce Si films at more than 10 times higher concentration in molten salt. This study suggested the design of the molten salts bath was significant for controlling interfacial phenomena at electrode/molten salts to fabricate high-quality Si layers.

INTRODUCTION

Silicon electrodeposition in molten salts is a key technology for fabricating silicon films, as a material for solar cells, by environmentally friendly and inexpensive processes as well as in-situ resource utilization process. In the electrochemical process, we can obtain Si by one-step reduction process of silica (SiO_2) in high-temperature molten salt. In addition, this process can contribute to the novel utilization of abundant resources on the earth as well as on the Moon and Mars [1, 2]. Especially in the case of resource utilization in space, the feasibility of space exploration will be dramatically enhanced if ISRU can separate the metallic oxide into metal and oxygen from the various metal oxides.

Silicon, which can be obtained from SiO_2 that is abundant in the crust, is the primary material for solar cells due to its inherent semiconducting properties. The traditional terrestrial production method for Si is complicated and expensive. Metallurgical-grade Si is produced by carbon thermal reduction of SiO_2, which is then chlorinated in a fluidized bed. Various chlorinated metal gas species are repeatedly distilled in hundreds of distillation columns to purify the gas to $SiCl_4$ (purification process). The $SiCl_4$ gas is then fed to a pyrolysis reactor where poly-Si is grown around Si rod heaters. Finally, poly-Si is melted in a purified SiO_2 crucible and undergoes a Czochralski process to obtain Si single crystal rods for semiconductor devices. Poor quality silicon that deviates from this inspection or refined silicon is supplied to the Si solar cell industry.

On the other hand, electrochemical processing in molten salt has attracted much attention as a method for reducing SiO_2 to Si [3]. The reaction during the recovery of Si and oxygen gases from SiO_2 in this process is shown below, and a schematic diagram of the reaction principle is shown in Fig. 1.

$$SiO_2 \rightarrow Si(IV) + 2O^{2-} \quad (1)$$

$$Si(IV) + 4e^- \rightarrow Si \quad (2)$$

$$2O^{2-} \rightarrow O_2 + 4e^- \quad (3)$$

The SiO_2 is dissolved in the molten salt according to equation (1), and the silicon ion (Si(IV)) is reduced on the cathode according to equation (2). On the inert anode, the oxygen gas evolution reaction proceeds. In this study, we report the influence of the melt structure of Si ions in the molten salt on the Si deposition process. In particular, we focused on the influence of O^{2-} anions on the dissolution process of SiO_2 and electrodeposition mechanism of Si. The obtained Si was characterized by the surface chemical analyses. The coordination structure of Si ions was analyzed by high temperature Raman spectroscopy and quantum chemical calculations.

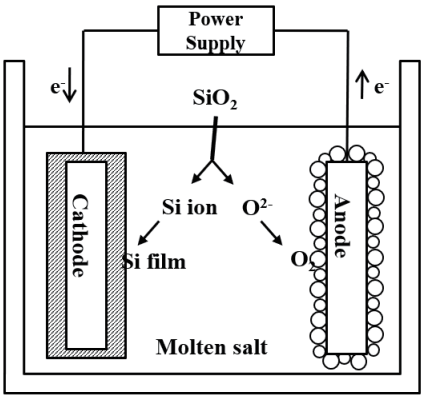

Fig. 1. Principle of the production of Si from silica (SiO_2) by molten salt electrolysis.

EXPERIMENTAL

All high-temperature Raman spectroscopic analyses and electrochemical measurements were performed under an Ar atmosphere. LiF-NaF-KF (46.5:11.5:42.0 mol%) eutectic salt with Li_2O (0.30 mol%) and SiO_2 (5.0 mol%) powder was used as the molten salt in the electrolysis tests. In the electrochemical measurements, an Ag was used as the working electrode, glassy carbon as the counter electrode, and a pseudo-Ni electrode as the reference electrode. The reference electrode potential is the equilibrium potential (K^+/K) between electrodeposited K on the working electrode and K^+ ions in the bath. After electrolysis, the samples were washed and analyzed by XRD, SEM, and EDS. The high-temperature Raman spectroscopy was conducted to investigate the coordination structure of silicon ions. Gaussian 09 (Revision B. 01) software was used for density functional theory-based quantum chemical calculations. The software B3LYP/6-311+G(d) was used for structure optimization calculations and Raman spectra frequencies for various Si ionic structures.

RESULTS AND DISCUSSION

In order to clarify the electrochemical reduction behavior of SiO_2 in molten fluoride, a potentiostatic potential electrolysis was conducted. The morphology of deposited Si was observed by SEM. Fig. 2 shows the results of electrolytic operation under the same conditions using two types of molten salt baths to investigate the effect of the composition of the molten salt on the deposited Si. One is LiF-NaF-KF with 5.0 mol% SiO_2 at 873 K, and the other is Li_2O with 5.0 mol% Li_2O. Li_2O is used as an oxide ion source (O^{2-}). The effect of the anion species O^{2-} was investigated by comparing the results of electrodeposition in these two types of molten salts. On the other hand, when Li_2O was added, Si films with thicknesses ranging from tens to hundreds of μm were obtained, indicating that the addition of O^{2-} to the molten salt increases the deposition rate of Si films under the same electrolysis conditions. XRD analysis revealed peaks that were attributed to polycrystalline Si. The peaks caused by polycrystalline Si were detected in the samples with potentials of 0.2 and 0.3 V. The peaks caused by polycrystalline Si were also detected in the samples with potentials of 0.2 V and 0.3 V, respectively. K-Si alloy was detected in the 0.2 V sample.

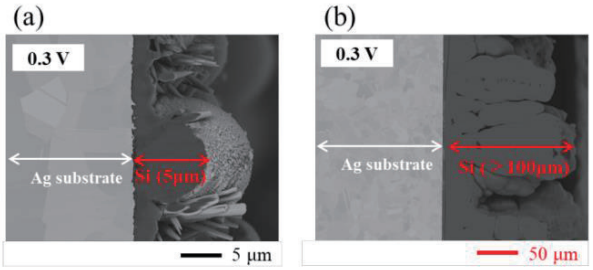

Fig. 2. SEM images of samples after potentiostatic electrolysis at 0.3 V for 3600 s in molten LiF-NaF-KF containing 0.5 mol% SiO_2 (a) without and (b) with 5.0 mol% Li_2O at 873 K.

It was clarified that the addition of Li_2O to the molten salt, i.e., an increase in O^{2-}, enhanced the Si electrodeposition rate. In order to clarify why the addition of O^{2-} causes such a change in electrodeposition behavior, we focused on the dissolution state of Si ions in the molten salt. The authors performed in-situ measurements of the melt structure of Si ions in high-temperature molten salts by using high-temperature Raman spectroscopy and quantum chemical calculations based on DFT (Density Functional Theory).

The coordination structures of various Si ions was simulated by DFT calculations. The melt structure can be classified into two types: one is an Ion-like structure in which the anion species of F- and O^{2-} are coordinated to the cationic Si ion, and the other is an Ion-like structure in which the anion species are coordinated to the Li^+, Na^+, or K^+ cation, and the entire molecule has a non-zero charge. The vibrational calculations were performed after structural optimization to obtain vibrational modes for each ion species. The calculated vibrational frequencies after convergence of self-consistent field calculation confirm that the potential energy surface is the minimum point and that an equilibrium structure has been obtained as a result of the calculation.

The Raman spectroscopy of molten LiF-KF with 5.0 mol% SiO_2 at 873 K was obtained. The obtained Raman spectra were band-separated by the Gauss function. The several Raman bands were assigned by comparison with the calculation results. As a result, the molecular-like SiF_3O-Li structure in the molten LiF-KF-SiO_2 system. In addition, Raman bands [4, 5] due to the $Si_2O_5^{2-}$ structure were also observed around 1100 cm^{-1}.

On the other hand, when the same spectroscopic measurements and melt structure assignments were performed for the molten LiF-KF-SiO_2 system analyze with 5.0 mol% Li_2O, two prominent Raman bands were observed at around 600 cm^{-1} and 970 cm^{-1} . These bands were attributed to the vibrational modes of $SiFO_3^{3-}$ and SiF_3O^-, respectively. However, the Molecular-like structure was not observed in the melt containing Li_2O system, indicating that the coordination structure is clearly different from that of the LiF-KF bath without Li_2O. This result indicates that O^{2-} ions promoted the

formation of the Ion-like structure during the dissolution process of SiO_2. In the Li_2O-free system, the intensity of the Raman band around 1100 cm^{-1} attributed to $Si_2O_5^{2-}$ was relatively low compared to that of the Raman bands at other wavenumbers. This result is consistent with previous results obtained in the LiF-NaF-KF bath [6] , indicating that O^{2-} ions cleave the Si-O-Si bonds in $Si_2O_5^{2-}$ and SiO_2, resulting in the formation of silicon oxyfluorides.

CONCLUSIONS

In this study, the electrochemical and solubility properties of Si ions from SiO_2 were investigated aiming to produce Si by one-step reduction of SiO_2. The effect of O^{2-} ions on the dissolution of SiO_2 and the electrodeposition process of Si in fluoride molten salts revealed a significant increase in the reduction current of Si ions as well as in the film thickness and current efficiency of deposited Si. In the study of the effect of F^- and cation species on the coordination structure of Si ions after dissolution of SiO_2, two Si oxyfluoride structures: Ion-like and Molecular-like exist as interactions between anions (F^-, O^{2-}) and cations (Li^+, Na^+, and K^+) constituting the molten salts and Si ions, respectively, and the Li^+ ion, as the second neighbor atom, was found to interact with Si ions. Furthermore, it was found that the Ion-like structure mainly existed as the O^{2-} content in the bath increased.The molten fluoride system, which can fabricate Si films from SiO2 at low temperatures, has the potential to develop environmentally friendly and sustainable electrolytic systems.

to develop environmentally friendly and sustainable electrolytic sys tems by combining non-consumable oxygen-evolving anodes such as

boron-doped diamond electrodes.2

REFERENCES

[1] M. E. Evans, L. D. Graham, “A Flexible Lunar Architecture for Exploration (FLARE) supporting NASA’s Artemis Program”, Acta Astronautica, 177, 351 (2020).

[2] W.X. Wan, C. Wang, C.L. Li, Y. Wei, “China’s first mission to Mars”, Nature Astronomy, 4, 721 (2020).

[3] Y. Sakanaka, T. Goto, “Electrodeposition of Si film on Ag substrate in molten LiF–NaF–KF directly dissolving SiO_2”, Electrochim. Acta 164 (2015) 139-142.

[4] B. O. Mysen, D. Virgo, C. M. Scare, “Relations between the anionic structure and viscosity of silicate melts—a Raman spectroscopic study”, Am. Mineral., 65 (1980) 690-710.

[5] D. Virgo, B. O. Mysen, T. Kushiro, “Anionic constitution of 1-atmosphere silicate melts: implications for the structure of igneous melts”, Science, 208 (1980) 1371-1373.

[6] Y. Suzuki, Y. Inoue, M. Yokota, T. Goto, “Effects of oxide ions on the electrodeposition process of silicon in molten fluorides”, J. Electrochem. Soc. 166 (2019) D564-D568.

Proceedings of IWEC2023
The International Workshop of Energy Conversion
March 15-17, 2023, Kyoto, Japan

Paper No. IWEC2023-15

PM REMOVAL CHARACTERISTICS IN MAGNETIC FLUID FILTER WITH DIELECTRIC BARRIER DISCHARGE

Y. Asaka* and T. Kuwahara
Department of Mechanical Engineering, Nippon Institute of Technology, Saitama, Japan
*corresponding author, E-mail: 2227001@stu.nit.ac.jp

ABSTRACT

Diesel engines have advantages such as high energy density of fuel, high efficiency, and relatively low CO_2 emission. Therefore, diesel engines are preferred for various applications, such as automobile and ship. Despite the advantages, emission of particulate matters (PMs) from the diesel engines is a grave environmental concern. To address the issue, here, a magnetic fluid filter aided with nonthermal plasma (NTP) for removing diesel particulates without causing any loss in the pressure is proposed . The working principle of the proposed filter and the methodology for evaluating the PM removal efficiency are discussed in the paper. Further, the experimental results including the performance of the proposed filter are analyzed. The feasibility and high efficiency of the filter are evident from the result pollution due to the particulate matter (PMs) like $PM_{2.5}$ is a one of worldwide issues.

INTRODUCTION

Emission of particulate matters (PMs) is usual from fossil fuels-based energy conversion devices. Recently, air pollution due to PMs (especially $PM_{2.5}$) has become a worldwide environmental concern. On-site removal of PMs is an effective solution to the same. Of the various sources of PMs, particulates in the exhaust gas emitted from the combustion of fuel in the combustion engines and boilers are the most critical ones. The main constituents of PMs are carbon soot (C) and sulfur trioxide (SO_3). Further, it is known for a long time that diesel combustion contributes to PMs. However, the advantages of diesel engines such as high energy density of the fuel, high efficiency, and relatively low carbon dioxide (CO_2) emission along with less emission of volatile organic compound (VOC) make them favorable for various applications such as automobiles, ships, electric power generators, and construction machinery. Although diesel particulate filters (DPF) are used at the engine exhaust, it is disadvantageous because of a substantial loss in pressure (due to its honeycomb structure) caused by it. Moreover, the loss in pressure increases with the increase in the collected diesel particulates. For off-site air cleaning, e.g., inside the rooms or buildings, dry-type filters are used. In general, the widely used high-efficiency particulate air filters (HEPA filters) are the most efficient air filters. However, the pressure loss is a problem here as well. Besides, mold and bacteria proofing are needed in this case.

Contrastingly, the collection of PMs using the devices based on electrostatic forces such as electrostatic precipitators (ESPs) is useful for a wide range of sizes of PMs, including nanoparticles. The studies of PM collection technologies using electrostatic forces have been discussed in various reports. Moreover, it is known that the collection efficiency of low-resistive PMs is obstructed by re-entrainment in an ESP [1]. Therefore, ESPs are less effective if used directly to filter out the low-resistive diesel particulates. Although the use of an ESP together with a liquid film has been discussed to prevent the re-entrainment, it is impractical because the liquid should be flowing and its facilitation is necessary. Hence, a PM removal technology with reduced pressure loss and negligible re-entrainment is need of the hour.

Given that, in this paper, a PM removal technique using a magnetic fluid (also known as ferrofluid or ferromagnetic fluid) is proposed [2]. Here, a magnetic fluid suspended on the wall of a flow channel by a magnetic force (exerted by a magnet) acts as a magnetic fluid filter. The surface area of the magnetic fluid can be increased by using the spiking property of the magnetic fluid. When the exhaust gas that contains PMs passes over the magnetic fluid, the PMs are collected on the surface of magnetic fluid without any re-entrainment. Additionally, the PM removal is enhanced by nonthermal plasma (NTP) discharge generated on the spikes of the magnetic fluid. The method can address the issues associated with the liquid film, DPF, and HEPA filter. Moreover, the filter can be mold and bacteria proof owing to ozone (O_3) generated by NTP discharge. The PM removal efficiencies of the proposed magnetic fluid filters (with and without NTP discharge) are evaluated by using the number of PMs in the exhaust before, and after passing through the filter.

PRINCIPLE OF PM REMOVAL IN MAGNETIC FLUID FILTER

A magnetic fluid is a colloidal solution consisting of fine ferro magnetic particles suspended in a solvent with the help of surfactants. The magnetic fluid can be magnetized in the presence of a magnetic field. Magnetite (Fe_3O_4) is commonly used for the ferromagnetic particles. The typical size of ferromagnetic particles is 10 nm. The ferromagnetic particles are coated with the surfactants. In an oil-based magnetic fluid, the hydrophilic end of the surfactant is attached with the surface of a ferromagnetic particle, whereas the hydrophobic end is attached with the oil-based solvent (for instance, kerosene). The surfactant prevents the aggregation of ferro magnetic particles. In a water-based magnetic fluid, a double layer of the surfactants is coated on the ferromagnetic particles. As discussed in the literature, spiking is a unique phenomenon of a magnetic fluid. The spikes are observed along the magnetic field lines. Further, the pattern, density, and length of the spikes can be controlled by controlling the magnetic flux density using a magnet. Moreover, the formation of spikes is an interfacial phenomenon that is observed if the magnetic flux density is higher than a critical magnetic flux density. With increase in the magnetic flux density, the normally flat surface of magnetic fluid shows lumps at higher flux density. The magnetic flux above which the flat surface of magnetic fluid begins to deform is the critical magnetic flux density. Furthermore, spikes can be observed if much higher magnetic flux density is applied. The critical magnetic flux density B_c with the critical magnetization M_c can be obtained from the theoretical studies [3,4] on the interfacial phenomena between the interface of magnetic fluid and air. Accordingly, B_c is given by,

$$B_c = \mu_0 M_c , \tag{1}$$

and the critical magnetization M_c is given by,

$$M_c = \sqrt{\frac{2}{\mu_0}\left(1+\frac{\mu_0}{\mu_{MF}}\right)\sqrt{(\rho_{MF}-\rho_{air})g\alpha}} . \tag{2}$$

Here, μ_0 is the permeability of vacuum, μ_{MF} is the magnetic permeability of magnetic fluid, ρ_{MF} is the density of magnetic fluid, ρ_{air} is the density of air, g is the acceleration due to gravity, and α is the surface tension of the magnetic fluid. For example, the properties of the water-based magnetic fluid (W-40, Ichinen Chemicals Co., Ltd.) are $\mu_0 = 4\pi \times 10^{-7}$ H/m, $\mu_{MF}/\mu_0 = 1.68$, $\rho_{MF} = 1.40 \times 103$ kg/m^3, $\rho_{air} = 1.23$ kg/m^3, and $\alpha = 0.028$ N/m [4]. Accordingly, $M_c = 7.05 \times 103$ A/m and $B_c = 86.6 \times 10^{-4}$ T can be obtained from Eqs. (1) and (2), respectively.

The working principle of magnetic fluid filter is shown in Fig. 1. The exhaust gas (consisting of PMs and other pollutants) flows through the magnetic fluid filter. In the filter, the magnetic fluid is suspended on the wall of the flow channel by a magnet. The formation of spikes and the required field strength to hold the magnetic fluid in its position can be controlled by the intensity and gradient of the magnetic field. The PMs from the exhaust gas are collected on the surface of the magnetic fluid without resulting in any pressure loss. The presence of spikes increases the contact surface for PM removal. Here, the PMs are collected by inertial and gravitational forces. However, the fine particulates such as nanoparticles are collected by Brownian diffusion.

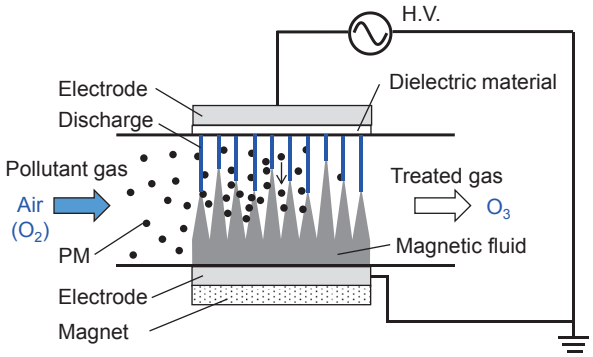

Fig. 1 Schematic of a magnetic fluid filter to remove the diesel particulates.

It is worth to mention here that in the absence of re-entrainment, the collection by electrostatic force is also efficient. Therefore, the magnetic fluid filter aided with NTP discharge in the absence of re-entrainment is expected to more efficiently collect the low-resistive PMs such as diesel particulates (with the help of the electrostatic force and the contact with the liquid interface). NTP discharge from spikes of magnetic fluid and its O_3 production is reported in the literature [5]. The dielectric barrier discharge (DBD) is applied to the spikes of magnetic fluid. The possible methods for the treatment of the collected PMs include replacement of magnetic fluid, oxidation by O_3 injection [6], or oxidation by OH radical and O_3 generated by NTP discharge. The generated OH radical and O_3 can contribute to mold and bacteria proofing [7]. Hence, PMs can be removed from the exhaust gas by using the magnetic fluid filter. In the present paper, the feasibility and fundamental characteristics of a magnetic fluid to remove low-resistive PMs are discussed. The results and analyses presented in the paper can be used to investigate the practical prospects of magnetic fluid as an alternative to DPF.

EXPERIMENTAL SETUP AND METHOD

The present experiments consist of two steps. One is gases sampling of exhaust gas and clean air. The clear air is used for dilution of exhaust gas. Another is experiments for evaluating the PM removal efficiency of the magnetic fluid filer. Before evaluating the PM removal efficiency, a magnetic fluid filter that can generate NTP discharge is designed and the NTP discharge in the magnetic fluid filter is tested. The schematic of the gases sampling method and the system used for evaluating the PM removal efficiency of the magnetic fluid filer is shown in Fig. 2. In the gases sampling, diesel particulates from a diesel-engine power generator (KDE2.0E-60 Hz, KIPOR) are used as low-resistive PMs. A four-stroke direct injection diesel engine (KM170F) and a power generator are integrated. Air-cooling type and single cylinder diesel engine having the speed of rotation 3600 rpm, the cylinder bore of 70 mm, the stroke of 55 mm, and the displacement by volume of 211 mL is used. The rated output power of the power generator is 2.0 kVA. The flow rate of the exhaust gas from the engine is 380 L/min. An electric heater connected with the generator is used as the

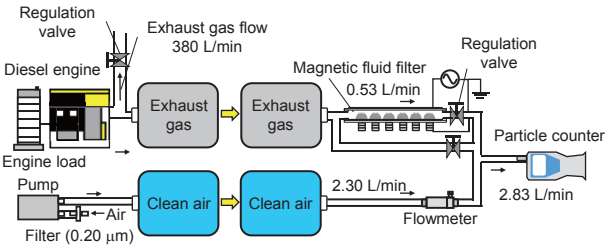

Fig. 2 Schematic of gases sampling method and evaluation system for diesel particulate removal using a magnetic fluid filer.

engine load. In the present experiment, the engine load is 25% (=500 W). In the system, the exhaust gas flows in the main flow channel and is finally emitted to outside atmosphere via a duct. A bypass channel, which is 1/4 in. stainless steel pipe (inner diameter of 4.35 mm, and outer diameter of 6.35 mm), is installed to the main flow channel of the engine exhaust. A part of the exhaust gas from the bypass channel is supplied into a gas sampling bag having a storage of 20 L. In another gas sampling bag, clean air is collected by using a vacuum pump. The clean air is produced by filtering atmospheric air with a membrane filter having pore size of 0.20 μm.

The gases in the sampling bags, i.e., exhaust gas and clean air are used for assessing the proposed magnetic fluid filter as shown in Fig. 2. The sampled exhaust gas flows through the magnetic fluid filter, where diesel particulates are removed. The volumetric flow rate of exhaust gas is set to be 0.53 L/min by a regulation valve. This flow rate of exhaust gas gives the limit of the number of PMs that can be measured by the particle counter. In addition, the flow rate at the intake of the particle counter is fixed. Therefore, this flow rate allows highly accurate measurements by considering the capacity of the particle counter. In this study, two types of filtrations are carried out. One is diesel particulate removal using the magnetic fluid only and another is diesel particulate removal with a magnetic fluid aided with NTP discharge. The water-based magnetic fluid (W-40, Ichinen Chemicals Co., Ltd.) is used in the study. The filtered gas that flows out of the magnetic fluid filter is diluted by the clean air in the sampling bag. The flow rate of the sampled clean air is maintained at 2.30 L/min, which is monitored by a flowmeter. A bypass is installed at the inlet of the magnetic fluid filter. The gas is collected through the bypass route for counting diesel particulates in the unfiltered exhaust gas. The exhaust gas in bypass is diluted by the sampled clean air in the same way the filtered gas is diluted. The diluted (filtered as well as unfiltered) gas flows into the particle counter (HHPC 3+, Beckman Coulter, Inc.). The volumetric flow rate of the gas for particle counter is 2.83 L/min, which is fixed as the specification. The dilution of the exhaust gas is performed because counting capacity of the particle counter is limited. The number of PMs counted by the particle counter is converted to the original number before the dilution. Hence, the numbers of PMs before and after the filtration can be obtained. The number of PMs in the unfiltered exhaust gas (N_{exh}), the number of PMs after the filtration only by a magnetic fluid (N_{MF}), and the number of PMs after the filtration by the magnetic fluid aided with NTP (N_{MFNTP}) are used for calculating the PM removal efficiencies. The PM removal efficiency only by a magnetic fluid (η_{MF}) and the PM removal efficiency by the combination of a magnetic fluid and NTP (η_{MFNTP}) are defined as follows:

$$\eta_{MF} = \frac{N_{exh} - N_{MF}}{N_{exh}}, \tag{3}$$

$$\eta_{MFNTP} = \frac{N_{exh} - N_{MFNTP}}{N_{exh}}. \tag{4}$$

In addition, PM removal efficiency only by NTP effect (η_{NTP}) can be defined as

$$\eta_{NTP} = \frac{N_{MF} - N_{MFNTP}}{N_{MF}}. \tag{5}$$

RESULTS AND DISCUSSION

The schematic of the designed magnetic fluid filter and the image of NTP discharge from the spikes on six lumps of the magnetic fluid are shown in Fig. 3. NTP discharge from the spikes on a single lump of a magnetic fluid has already been reported in the literature [5]. In the present study, simultaneous NTP discharges from the spikes on six lumps of magnetic fluid are achieved to facilitate the PM removal (refer to Fig. 3). The size and shape of the spike is a square bottom (typically 2 mm × 2 mm) having a height of 1.5–2.0 mm. Three sets of permanent magnets (neodymium magnets) generate magnetic flux density of 490 mT on the surface of the magnets. This magnetic flux density is higher than the critical value B_c given by Eq. (1). Therefore, spikes are observed on each lump of the magnetic fluid. The magnetic fluid is placed on the electrodes made of aluminum tape. A 2.0 mm thick glass plate is used as the dielectric substance. It is placed underneath the upper electrode. High alternating voltage is applied to the electrodes

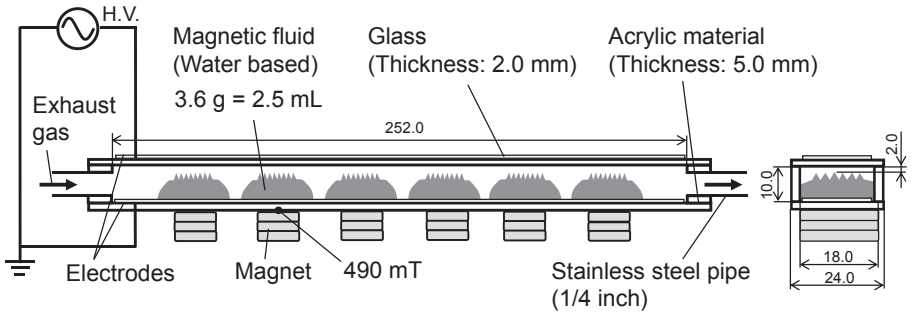

Fig. 3 Schematic of magnetic fluid filter magnetic fluid filter and the image of NTP discharge from magnetic fluid.

by using a high-voltage power supply (LHV-13AC, Logy Electric Co., Ltd.) that has a production capacity of 10 kV at 9 kHz frequency. Input power to the power supply is given by a voltage transformer (MVS520, Yamabishi Denki) such that the voltage of the input power can be regulated. 100 V is considered as the 100% of input voltage. The corresponding NTP discharge is shown in the image. The power consumption is measured by a wattmeter (TAP-TST7, Sanwa Supply Inc.). Here, the occurrence of NTP discharge can be identified by measuring the electric conduction; no electric conduction indicates the absence of discharge. It is observed that, NTP discharge from the spikes of magnetic fluid occurs if the input voltage is higher than 70 V (70% of input voltage). Power amounting to 31 W and 79 W are consumed for 70% and 100% input voltages, respectively.

PM removal efficiencies of proposed design are shown in Fig. 4(a) (η_{MF}) and (b) (η_{MFNTP}). The measurements are taken six times with 70% input voltage. The average numbers of diesel particulates not removed from the sampled exhaust gas are 2.5×10^6 particles/L for diesel particulates having a diameter $d_p > 0.3$ μm, 2.1×10^6 particles/L for $d_p > 0.5$ μm, 1.2×10^6 particles/L for $d_p > 1.0$ μm, 3.3×10^5 particles/L for $d_p > 2.0$ μm, 1.7×10^2 particles/L for $d_p > 5.0$ μm, and 0 (not detected) for $d_p > 10.0$ μm. The corresponding PM removal efficiencies (η_{MF}) are 35% for $d_p > 0.3$ μm, 51% for $d_p > 0.5$ μm, 61% for $d_p > 1.0$ μm, 90% for $d_p > 2.0$ μm, and 100% (complete removal) for $d_p > 5.0$ μm (see Fig. 4(a)). It is observed that η_{MF} is proportional to d_p. It is attributed to the constituents of the velocity of the PMs. In general, the velocity of aerosol due to inertia and gravitational forces is proportional to its diameter, while the velocity due to Brownian diffusion is inversely proportional to its diameter. Therefore, it can be inferred that the inertia and gravitational forces contributes mainly to the PM removal in $d_p > 0.3$ μm. Further, as shown in Fig. 4(b), the PM removal efficiencies after introducing NTP in the magnetic fluid filter (η_{MFNTP}) are 44% for $d_p > 0.3$ μm, 85% for $d_p > 0.5$ μm, 99% for $d_p > 1.0$ μm, and 100% for $d_p > 2.0$ μm. The corresponding effective PM removal efficiencies only by non-thermal plasma (η_{NTP}) are 14% for $d_p > 0.3$ μm, 70% for $d_p > 0.5$ μm, 97% for $d_p > 1.0$ μm, and 100% for $d_p > 2.0$ μm. In the magnetic fluid filter, PMs are charged by NTP discharge. Therefore, the most effective phenomenon of NTP for PM collection is electrostatic force that is effective for a wide range of particle diameters in theory. The efficiency values are sufficiently high for PMs having $d_p > 0.5$ μm. For PMs with $d_p < 0.5$ μm, apparently PMs travel along with the flow of gas because of weak inertial force. Therefore, the probability that PMs get in contact with the spikes or NTP discharge becomes low. Hence, the efficiencies are not high for the particulates having size in this range. The measurements are taken six times with 100% input voltage. As shown in Fig. 4(c), the PM removal efficiencies after introducing NTP in the magnetic fluid filter (η_{MFNTP}) are 40% for $d_p > 0.3$ μm, 72% for $d_p > 0.5$ μm, 98% for $d_p > 1.0$ μm, and 100% for $d_p > 2.0$ μm. The differences in efficiencies between 70% and 100% input voltages are small, or PM removal with 70% input voltage is rather more efficient for $d_p < 1.0$ μm. As a possible reason, because the NTP discharge with 70% input voltage is weak, a spike of the magnetic fluid emits instable NTP streamers. On the other hand, in the case of 100% input voltage, a spike of the magnetic fluid emits a single stable NTP streamer. Therefore, in the case of 70% input voltage, the probability that PMs get in contact with streamers from the spikes becomes higher, and PM

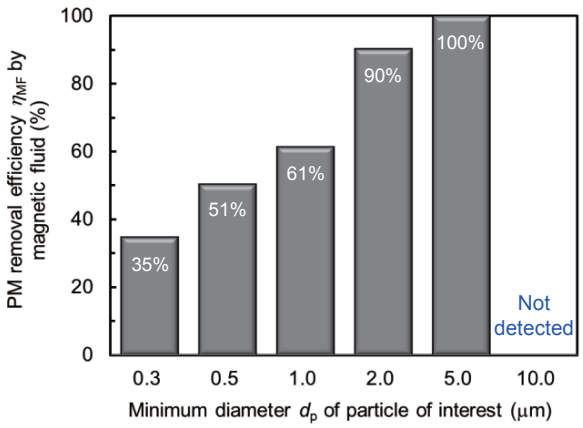

(a)

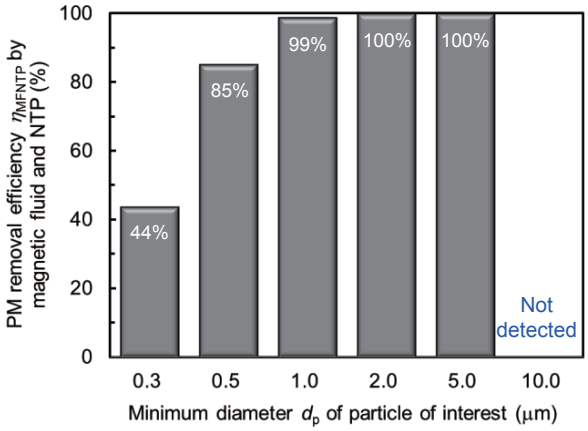

(b)

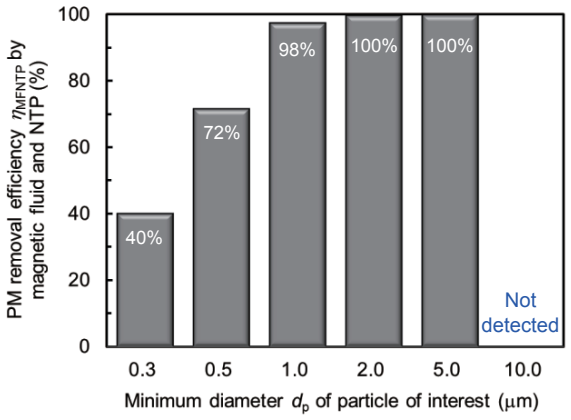

(c)

Fig. 4 PM removal efficiencies (a) only by a magnetic fluid (η_{MF}), and (b) by combination of a magnetic fluid and NTP application (η_{MFNTP}) with 70% input voltage, and (c) by combination of a magnetic fluid and NTP application (η_{MFNTP}) with 100% input voltage.

removal with 70% input voltage is more efficient especially for fine PMs.

As a result, to improve the probability that PMs get in contact with the spikes, the number of spikes and discharge parts of magnetic fluid should be increased. Although it appears that the size and/or shape of the spikes does not make an influence on the efficiency, an increase in the number of spikes of magnetic fluid on applying higher magnetic field could improve the efficiency. In addition, from the viewpoint of PM removal and reduction in energy consumption, PM removal with 70% input voltage is more efficient.

CONCLUSIONS

To summarize, a study is conducted to search for a low-resistive PM removal technology that does not cause a pressure loss. The following conclusions can be drawn from the study:

(1) A magnetic fluid filter is proposed and designed for the removal of PMs. Further, a method for evaluation of PM removal efficiency has been provided.
(2) Simultaneous discharges of NTP from spikes on six lumps of the magnetic fluid are achieved in the magnetic fluid filter. Additionally, NTP discharge conditions are investigated.
(3) The feasibility of low-resistive PM removal using the magnetic fluid filter with high efficiency is confirmed by the experimental results. PM removal efficiencies η_{MFNTP} are 44% for PMs having a diameter $d_p > 0.3$ μm, 85% for $d_p > 0.5$ μm, 99% for $d_p > 1.0$ μm, 100% for $d_p > 2.0$ μm.

Essentially, the fundamental characteristics of PM removal are investigated. The measures to be taken for improving the PM removal efficiency and oxidation of PM with NTP discharge for its practical use are the part of future study.

ACKNOWLEDGMENTS

This work was supported by JSPS KAKENHI Grant-in-Aid for Young Scientists (B) Grant Number 17K18060. The author would like to thank Ms. R. Yanaka, who is an undergraduate student at Nippon Institute of Technology, for the contributions to the experiment.

REFERENCES

[1] Yamamoto. T, Mimura. T, Otsuka. N, Ito. Y, Ehara. Y, Zukeran. A, 2010, “Diesel PM collection for marine and automobile emissions using EHD electrostatic precipitators,” IEEE Trans. Ind. Appl. 46 (4) pp.1606–1612.
[2] Kuwahara. T, 2020, “Fundamental characteristics of low-resistive particulate matter removal using a magnetic fluid and nonthermal plasma,” J. Mag. Mag. Mat. 489, 166161
[3] Cowley. M.D, Rosensweig. R.E, 1967, “The interfacial stability of a ferromagnetic fluid,” J. Fluid Mech. 30 (4) pp.671–688.
[4] Fukuda. Y. Douhara. N, 2005, “Study on interfacial phenomena of magnetic fluids,” JSME Int. J. Ser. B Fluids Therm. Eng. 48 (4) pp.735–742.
[5] Uehara. S, Itoga. T, Nishiyama. H, 2015 “Discharge and flow characteristics using magnetic fluid spikes for air pollution control,” J. Phys. D Appl. Phys. 48 (28) 282001.
[6] Kuwahara. T, Nishii. S, Kuroki. T, Okubo. M, 2013 “Complete regeneration characteristics of diesel particulate filter using ozone injection,” Appl. Energy 111 pp.652–656.
[7] Kuwahara. T, 2018 “Reduction in energy consumption using fuel cells in nonthermal plasma-based water sterilization by bubbling ozone,” IEEE Trans. Ind. Appl. 54 (6) pp.6414–6421.

Proceedings of IWEC2023
The International Workshop of Energy Conversion
March 15-17, 2023, Kyoto, Japan

Paper No. IWEC2023-17

STATUS OF CLEAN COOLING SYSTEMS

Armin HAFNER
Norwegian University of Science and Technology, 7194 Trondheim,
Norway, armin.hafner@ntnu.no

ABSTRACT

Due to the harmful environmental impact of the synthetical refrigerants (CFC, HCFC, HFC), there are fundamental changes ongoing in the refrigeration and heat pump sector. This contributes to the market uptake for refrigeration and heat pumps systems based on natural working fluids with growth rates at different pace in different market segments, while they have always been applied and been available in others. The aim of this article is to present the current state of the market and is only to be seen as snapshot made by end of 2022.

In this article only future proof working fluids/refrigerants are considered, namely substances naturally occurring such as CO_2, different types of hydrocarbons, NH_3, H_2O and air. For each of these refrigerants the possible applications are described depending on temperature range, cooling capacity, type of applications etc. There are new innovative solutions to improve the applicability, energy efficiency and safety.

Fluorinated hydrocarbons are again in the spotlight related to their environmental impact with respect to the TFA pollution of drinking water and being the major source of PFAS[1] pollution also of drinking water and essential foodstuff like mother milk. Therefore, a multi-governmental proposal to ban PFAS across Europe has been submitted to ECHA in February 2023.

INTRODUCTION

The last report for the Technical Options Committee on Refrigeration, Air Conditioning and Heat Pumps of the United Nations Environmental Program was released in 2018. (RTOC-2018). A new RTOC report will be released in early 2023.

As there are many innovations and transitions ongoing / established within the refrigeration, AC and heat pump sector towards the implementation of system applying natural working fluids, this work is summarizing the current status. The status refers to the above-mentioned refrigerants applied in domestic applications, commercial refrigeration, industrial refrigeration and heat pump systems, water and space heating heat pumps, chillers and vehicle air conditioning. Prior the summary part a table summarizes which working fluids are applied within the application sectors mentioned in the RTOC reports.

NATURAL WORKING FLUIDS

To date all the synthetic refrigerants do have harmful environmental impacts, as already stated by Lorentzen 1993 & 1995, Ciconkov 2018, Kauffeld et. al 2021 and lately with the proposal for a restriction of PFAS[2] towards the European Chemical Agency (ECHA) by BAuA (Germany), RIVM (The Nederlands), KEMI (Sweden), NEA (Norway), and DEPA (Denmark).

Therefore, it is advisable for the refrigeration sector to admit this challenge, acknowledge a paradigm shift, and perform the necessary action: All kinds of heating and cooling services currently supplied are possible, and even more energy efficient, when applying natural working fluids. Such a rapid technology shift will not reduce the need for this kind of services and equipment, as seen in some segments, the business growth rates are enormous and even the health and environmental working conditions of the valuable and qualified technical staff can be improved and secured. Therefore, the following subchapters describe in which areas the naturel working fluids currently are applied.

CARBON DIOXIDE, CO_2, R744

CO_2 has a low critical point (31°C). It means that there is no condensation above the critical point, i.e. therefore, systems operate in a transcritical process at gliding heat rejection temperatures. In such a refrigeration cycle, when the temperature before expansion is relatively high, the COP is lower compared with other refrigerants performing in a conventional system configuration. This was the reason that the CO_2 systems were used firstly in regions with cold and moderate climate (Northern Europe), where a subcritical operation mode is dominant. However, during last two decades, the R&D on CO_2 systems contributed to significant improvement of their energy efficiency. The transcritical

[1] Per- and polyfluoroalkyl substances

[2] https://echa.europa.eu/documents/10162/f605d4b5-7c17-7414-8823-b49b9fd43aea

operation can be improved with the following modifications (Hafner, 2015; Ciconkov, 2017): by installing parallel compressor(s); by implementing an internal heat exchanger; by utilizing an external subcooler; by utilizing expansion work with ejectors or other expansion devices, etc.

CO_2 has gained a lot of attention and has become the new norm for domestic hot water heat pumps in Japan and in supermarkets, mainly in Europe, however, getting more and more acceptance in most parts of the world. The technology has developed over the years and currently the 4th generation of supermarket CO_2 units are entering the stage. For the layman, the refrigeration systems build in racks look very identical independently of the various suppliers.

Figure 1: A unit from Advansor, one of the first in the market in 2006

One of the first suppliers of CO_2 racks for mainly centralized refrigeration systems in the market was Linde, now part of Carrier Global. Another early adopter of the technology was ENEX and Advansor, now part of Dover Corporation as well as Epta, Costan, Arneg, etc. Many other suppliers are now suppliers to the market some only suppliers in the region e.g. compact Kältetechnik in Dresden, Germany and others are still growing into new markets e.g. Teko in Germany, SCM Frigo, now part of Beijer Ref, Sweden and Carnot Refrigeration, Canada. The only true global suppliers are probably Carrier and Beijer Ref., however, also Enex, Teko, Epta and Arneg are supplying CO_2 systems out of Europe to both South America and Asia and Australia. The first demonstration projects started about 2004 and in 2021 the number of installed CO_2 units on a global base exceeded 35,000 systems, as shown in Figure 2 from 2020. There is no region on this planet where it is technically impossible to implement a CO_2 refrigeration system. For a single rack, the capacity range for the CO_2 supermarket refrigeration systems is between 10 kW and up to 1000 kW of cooling capacity including both freezing and chilling of foodstuff.

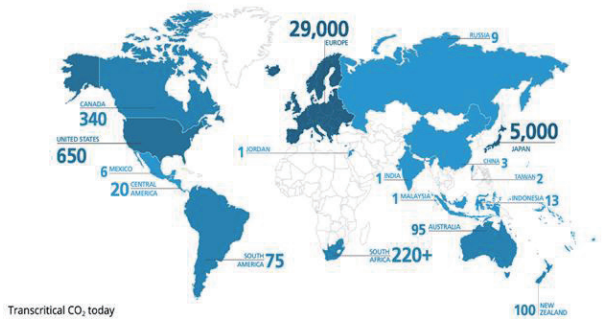

Figure 2: An overview created by Shecco (status middle of 2020)

Carbon dioxide is also used in cascade systems with other natural working fluids, however, mainly in combination with ammonia (NH_3 / R717). Cascade systems are widely used on board ships, warehouses and for industrial refrigeration and heat pump systems located in warm climate regions. The exact number of installed systems globally is not known; however, the total installed cooling capacity is constantly growing. One of the larger systems is phase one for a factory currently built in Russia with a capacity of 89 MW for freezing meat products, in phase two and three even more capacity will be added.

Cascade systems, as shown in Figure 3, have been installed in all parts of the industrialised world and on the inhabited continents. At high ambient temperatures, cascade systems are less sensitive to the ambient temperature compared to the transcritical CO_2 systems and yield a higher energy efficiency. In the cascade system, the ammonia charge is reduced to about 10 % of what was normally used in ammonia systems with similar refrigeration capacities. This part of the charge has been substituted with CO_2, which can be distributed safely within the process plants or building and storage places. In short, it can be said that the two natural refrigerants are applied at the temperature levels where they yield the best energy efficiency, i.e. CO_2 at the low temperature part/heat uptake, NH_3 at the heat rejection circuit.

Figure 3: A packaged cascade system in a plug-and-play type of system

CO_2 is also successfully used in heat pumps as working fluid. One of the new start-up companies working with CO_2 heat pumps is Fenagy, now part of Beijer Ref.

These heat pumps, as shown in Figure 4, has been installed in district heating networks in Denmark. They are especially interesting for markets where the district heating is relatively well developed and where the district heating temperatures (both supply and return) are now reduced to lower levels. The 5th generation of heating networks are predicted to have supply temperatures around 40 °C, and where there are auxiliary solutions in the apartments/houses for heating the domestic hot water to the final temperature.

Figure 4: A Fenagy CO_2 heat pump type H-600. The projected temperature range will be up to 90°C or higher.

Figure 5 shows the simplified system layout of a CO_2 heat pump chiller, develop within the EU funded project MultiPACK and available in the market since 2020. The unit can produce hot water and simultaneously provide chilled water. If heating is not required excess heat can be rejected to the ambient, via an external gascooler.

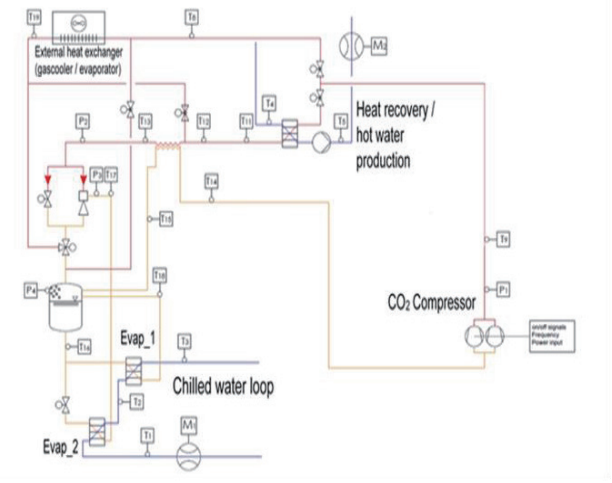

Figure 5: MultiPACK (enex) heat pump chiller unit with ejector supported evaporators.

In case the chilled water loop cannot supply the heat required to produce hot water, ambient air can be the heat source, as the external heat exchanger can also be operated as an evaporator. The innovative concept includes an ejector supported chilled water loop which consists of two evaporators in series to absorb heat from a secondary fluid. The secondary fluid is precooled in Evap_1 which is gravity fed, i.e. liquid refrigerant is supplied from the receiver. The pressure level in the receiver represents the suction pressure of the compressor as well as the corresponding evaporation temperature (Evap_1). The second evaporator (Evap_2) is further reducing the temperature of the secondary loop with a lower evaporation temperature as in Evap_1, as the ejector utilises expansion work to pre-compress all the evaporated CO_2 of Evap_2. The pressure level in the receiver is adapted by the control unit and compressors accordingly to achieve the required supply temperature level for the secondary loop. The ejector capacity is self-adjusting, i.e. at low load conditions and low heat rejection temperatures, mainly Evap_1 is in operation. Compared to traditional chiller units, the suction pressure can be significantly higher and thereby improving the energy efficiency accordingly. This kind of heat pump chiller systems are very applicable for high performance buildings like hotels etc., which do have both heating and cooling demands during a day/week. In case of time-staggered production and demand, appropriate energy storage devices must be implemented on both sides of the heat pump unit.

After decades of R&D by major car manufactures and their suppliers, mobile CO_2 AC systems are standard equipment in Mercedes cars, since 2016. As Volkswagen now develops and introduces new car platforms for their electric cars, even this global car manufacture utilizes CO_2 systems applicable both in summer for cooling the passenger compartment as well during the cold period to enhance the performance when the CO_2 heat pump system is in operation. CO_2 is the most energy efficient, non-flammable refrigerant, which enables to apply the heat pump function to ambient temperatures below -20 °C, and therefore auxiliary electrical heater can be avoided.

During the embargo against Cuba, it was not allowed to export CFC and HCFC to the island. Therefore, in Cuba people were still using CO_2 and hydrocarbon systems installed before WWII. CO_2 as refrigerant was not unknown to Prof. Gustav Lorentzen when the rival took place in the late 1980s; he had worked with CO_2 as refrigerant in his young days. The last reported fishing vessel applying a traditional CO_2 unit registered in a UK harbour was in the 1980's. So even CO_2 has always been used, however, was suppressed to a large extend by the fluorinated hydrocarbons.

AMMONIA - NH_3- R717

Ammonia has been the preferred refrigerant in industrial refrigeration for more than 130 years. Due to some accidents not related to refrigeration in 2013, the suppliers of these applications are forced by different stakeholders to reduce the refrigerant charges in the systems. This has led to new designs and innovations in the packaged Ammonia systems offered to the market.

The low ammonia charge levels can be achieved mostly by using new types of heat exchangers and circuit arrangements

avoiding receivers and pumped systems. The following solutions can be used:

- Dry expansion (DX) evaporators where the refrigerant evaporates in tubes (this requires miscible oil).
- Plate heat exchangers (PHEs) as evaporators and condensers. New types are developed with stainless steel welded modules and nickel brazed PHEs.
- Shell-and-plate heat exchangers are new types of heat exchangers applicable in R717 systems. These are combining the shell-and-tube and PHE arrangement, resulting in a very compact structure able to operate with a small refrigerant charge (see Fig. 6).
- The microchannel type of heat exchanger design is an excellent option for ammonia and CO2 units. New designs in microchannel heat exchangers enable much lower refrigerant charges compared to conventional heat exchangers. Aluminium is very suitable for manufacturing of these types of heat exchangers, compatible with ammonia and allow for a simple recycling after usage.

Low charged R717 chillers, as shown in Figure 6, are offered and installed in many different types of applications e.g., airports, hospitals office buildings but also for chilled- and cold-water production in industrial applications. The shown type is from Sabroe in Denmark, part of Johnson Controls Intl.

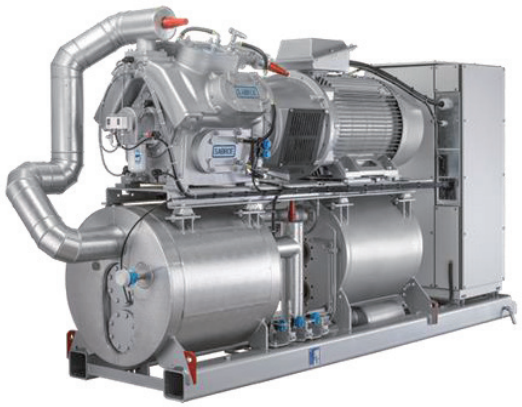

Figure 6: A packaged low charged water cooled NH_3 chiller.

Ammonia systems are used onboard ships, in fish processing factories, meat processing plants, slaughterhouses in general, in chemical and pharmaceutical installations, in breweries and dairies and many other industrial facilities. In the USA alone, it is estimated that more than 9000 sites are applying Ammonia as refrigerant.

Ammonia is also widely used as working fluid in heat pumps up to a supply temperature of about 90 °C. These units are installed in numerous district heating systems in Europe. Ammonia is also used in industrial heating and cooling applications where it performs very well, yields a very high energy efficiency and satisfied end-users.

Ammonia heat pumps for high temperature lifts are normally made in a two-stage design. These systems can be either site- or factory built. The factory-built solutions, as shown in Figure 7, are often delivered with a factory test, so capacity has been tested/verified and the control settings have been checked prior to shipment.

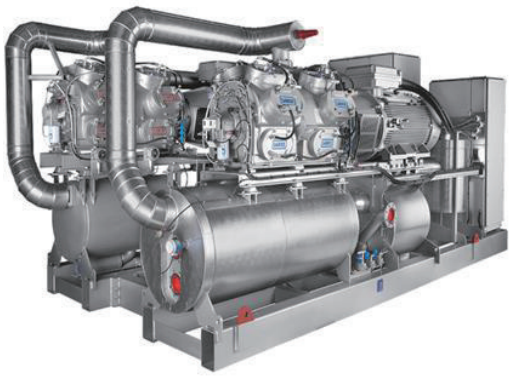

Figure 7: A two stage unit with the front compressor for the low temperature part and the rear compressor for the high temperature part of the heat pump system.

Over the last 20 years, there has been a trend to reduce the charge size in ammonia systems. There has been a lot of talk about low charge systems, and the industry has been lowering the charges significantly in many new installations. This move has come after two major accidents in China and one in West Texas, all three happened in 2013. One of the accidents in China caused about 70 deaths to a large extend because emergency doors had been locked in violation with local law. The second accident in China was a matter about poor welding violating local design rules and performed by a non-qualified welder. The accident in Texas was not even related to refrigeration, it was fertilizer, ammonium nitrate, that exploded causing several deaths and lots of damage. After this accident, the then president of the United States Barack Obama and his administration put a limit of 10,000 pounds (4536 kg) of ammonia in refrigeration systems. Now years later every plant with less than 10,000 pounds has become low charge. There is no real definition of low charge.

The chiller shown in Figure 6 is the lowest charged ammonia chiller in the market, however, the development of new technologies such as direct expansion systems and new microchannels heat exchangers are driving the charges further down. The latest innovations for ammonia systems are the emergence of semi-hermetic compressors for ammonia from several market players. The suppliers are both from Europe but also from China, which can make the competition more intense and drive down the cost for the user of the systems. The main advantage of the semi-hermetic compressors is to avoid the shaft seal, which theoretically can be a risk. However, semi-hermetic design also comes with some disadvantages, mainly related to the motor efficiency or lack of it if the process changes out of the normal operation range envisioned by the designer of the system. The strength of the open type of

compressor is the flexibility of choice of motor. As an example, it is very advantages to be able to isolate the motor and keep the compressor very warm (insulated) if applied in heat pumps to avoid condensation of refrigerant inside the compressor housing. With such a demand for the high temperature side of a heat pump, the motor of a semi-hermetic type of compressor will be a problem and will suffer on the efficiency.

One of the reasons for ammonia being accepted globally as refrigerant is that it is available in all parts of the world and it an inexpensive refrigerant and yields the highest energy efficiency values compared to most other working fluids in most operating conditions. However, during the last years not much effort has been done to further increase the energy efficiency of the vapour compression cycle with ammonia, compared to the effort made with carbon dioxide-based units. This issue is being addressed and some innovation can be expected to emerge in the market targeting a further improvement of the energy efficiency and further reduction of refrigerant charge.

The increased focus on safety around the ammonia plant is also pushing the industry to better education and training of staff to ensure that the systems are designed, installed and maintained in such a way that accidents are prevented in the beat possible way. The Seveso directive has in some countries been used as reference for regulating the use of NH3 in refrigeration, but this is overregulating the issue because the European standard EN-378 (ISO 5149) already cover the safety related to refrigeration systems. When following regulations and standards ammonia applied as a refrigerant is safe. Most accidents happen when ammonia is handled as fertiliser.

HYDROCARBONS

Very often, when hydrocarbons are mentioned as alternative refrigerants, most people think about propane (R290) and in some cases iso-butane (R600a). Propane is often used in heat pumps and in commercial refrigeration and freezer applications. Due to the phase-down of HFCs (Kigali Amendment), R290 is the only viable and future-proof choice for single-split ACs and, furthermore, it is more energy efficient. When following design and operational standards (e.g. EN378), a safe operation can be performed even at higher system charges and capacities for R290 and other flammable working fluids. Several global suppliers manufacture a high number of R290 AC systems annually. Midea made the first Eco-friendly air conditioner certified by Blue Angel in 2018, now also available in Europe, as shown during the Green Cooling Summit 2021.

The standard refrigerant in most domestic refrigerators is iso-butane, in-fact it is estimated that about 95% of all fridges in Europe are now based on this natural working fluid. However, some American style fridges are still supplied to the market based in a fluorinated hydrocarbon.

In plug-in and self-contained units used in smaller shops and supermarkets propane has become mainstream with charges as low as or below 150 g. However, these low levels are not required anymore when the equipment is located inside the sales area, as the volume inside the sales area is sufficiently large. These units have undergone many changes, upgrades and with a water-cooled condenser, the refrigerant charge becomes again comparably low, even for higher cooling capacity units, as required in larger display cabinets. The systems are used in both normal temperature (chilled food) and for low temperature cabinets (frozen food).

For lower temperatures, propene (previously called propylene) or R1270 is used down to -45°C. R1270 is the preferred working fluid in the operation range from -45°C up to -10°C, however, it can be applied even at higher temperature levels. It must be noted that propane yields in a higher energy efficiency above -10°C evaporation temperature and is therefore in many cases preferred for higher operation temperatures. On the commercial side: propane as working fluid requires a larger swept volume at similar cooling capacities compared to propene. Therefore, some manufacturers prefer the propene enabling them to select a smaller and less expensive compressor.

For temperatures down to about -80°C, ethane or R170 is a good and energy efficient working fluid. It is often used in cascade systems with propane on the higher temperature stage and the systems yield a better efficiency than the systems using R23 in cascades with another HFC, which can be seen in Table 1

Table 1 By investigating suppliers of ultralow temperature freezer (-80°C) documentation this will be the result

Manufacture	Refrigerant Type	Volume (liter)	Power cons. (kWh/day)	(Wh/d)/Liter	Relative
Brand 1 cascade	HC	729	7.87	10.8	1.1
Brand 2 cascade	HC	729	7.06	9.7	1.0
Brand 3 cascade	HFC	815	17	20.9	2.2
Brand 4 cascade	HFC	793	17.8	22.4	2.3
Brand 5 Stirling	H_2/C_2H_6	780	6.67	8.6	0.9
Brand 6 auto cascade	HC blend	556	16.3	29,3	3.0
Brand 7 auto cascade	HC blend	300	5.2	17.3	1.8
Brand 8 auto cascade	HC blend	74	5	67.6	7.0

Auto cascade systems are systems containing only one compressor compressing a blend of refrigerants. The refrigerants condense in turns by evaporating another fluid. This concept is applied in both laboratory freezers as reported in Table 1, but also in large industrial systems onboard ships and in petrochemical sites. In the table the information collected for this comparison show that from an energy efficiency point of view auto cascade is not the most efficient solution, however, it has an investment cost advantage.

In special cases where the required temperature needs to be even lower, R1150, ethylene, can be applied. For near absolute zero systems Helium is applied on the lowest stage with nitrogen and methane on the next stage and on the higher stages the above-mentioned gases, all in a multi-cascade construction are applied.

Other hydrocarbon refrigerants are suitable for high temperature heat pumps reaching up to about 250°C. An analysis, Pachai 2021, shows that the way up in temperature is possible by applying butane, pentane and for the very high temperatures heptane is the best choice. That is for the general market, however, optimised blends for different processes and applications with dedicated temperature glide requirements are

possible to generate and utilize. These blends of different hydrocarbons are common working fluids in chemical process plants as well.

The stability of the fluorinated hydrocarbons has been questioned when it comes to high temperature heat pumps. Of other uncertain points can also be the possible lubricants. The currently used lubricants produce soot at about 180°C and coke about 200°C, however, new lubricants are under development and soon ready for the market and these high temperature heat pumps applying hydrocarbons. Also, valves and other components needs to be clarified for operation conditions at such elevated temperatures.

WATER – R718 – H_2O

Water applied as refrigerant is emerging the market for some air-conditioning applications as shown in Figure 8. In addition, high temperature heat pumps are another application area, e.g., when producing steam for process plants by utilizing surplus heat in combination with a cascade heat pump. Water, in comparison to other refrigerants, has a relatively high boiling point at atmospheric pressure, 100°C. At Air Conditioning temperatures, the pressures in the water cycle will be sub-atmospheric and the swept volume in the compressor needs to be relatively large compared to similar systems e.g. based on ammonia. This drawback is reversed when the operation temperatures increase to levels above 100°C or even 200°C. In this temperature regions water becomes a viable and energy efficient solution for high temperature heat pumps. New technology and innovations have demonstrated water is a solution especially for cooling in server environments at higher temperatures levels than normal AC units can be applied for.

Figure 8: The eChiller from Efficient Energy is based on water as the working fluid.

A lot of R&D is ongoing for system applying water as the working fluid in vapour compression systems. It is a cheap and present in most markets in a usable quality. In the current available heat pump cycles the temperatures levels can reach 160°C, which ensures any bacterial activity will stop. In a project in Denmark, the low stage in a heat pump cascade is a water vapor system supplying heat towards the high stage heat pump for the production of district heat for a new part of the city.

With water as the working fluid heat pumps, designed in a conventional vapour compression cycle, will potentially be able to reach temperatures close to 350°C, critical temperature 374°C at 220.9 bar(a), and if used as a transcritical fluid there is no limit, however, the challenge will be to build a compressor for the purpose.

AIR – R729

Atmospheric air can also be used in a special loop to create temperatures from -40 °C and down to about -130 °C but it is possible to reach as low as -160 °C. Such air cycle systems are being used to store frozen tuna at about -60 °C in Japan, where the traditional sushi tuna requires very high-quality tuna flesh. Air cycles are energy efficient compared to traditional vapour compression units at very low temperatures. The need for low temperature storage of some vaccines at -70 °C +/-10 K has triggered a new application area for this kind of system, too.

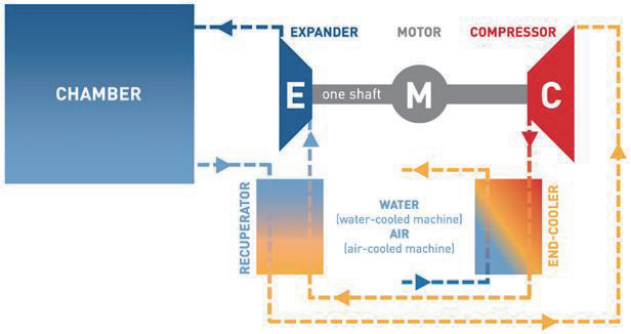

Figure 9: The open air cycle as shown by Mirai Intex

As shown in Figure 9, the compressor and expander are connected to the same motor. Through the connecting shaft, the expander contributes to the driving force to operate the compressor. The air from the refrigerated area enters the compressor. After compression the air temperature is reduces in a cooler and even further reduced in a recuperator before it enters the expander part at high pressure. The air temperature drops significantly as the pressure drops downstream of the expander before entering the refrigerated space/chamber.

The air cycle shown in Figure 9 is often used for storage and process cooling. This cycle is the open type. A closed loop is very common and most used onboard airplanes of any kind and some train AC systems. It is basically the same cycle but here also heating is often needed as most airplanes are flying in high altitudes where the ambient temperature often still is about minus -50 °C. The heat is recovered from both the combustion in the engine and from the passenger cabin. Mayekawa also provides this kind of systems for warehouses storing valuable fish.

STANDARDS AND REGULATIONS

The natural refrigerants have been used for more than 100 years, most known is ammonia but also the hydrocarbons have been used in the petrochemical sector, and there is a lot of knowledge on how to work with and apply theses fluids. The challenges with the barriers in the market today is the influence and market position of the manufacturers of fluorinated hydrocarbons, which virtually have made it impossible to install natural refrigerants in many cases. Based on the real environmental impact of these synthetic fluids, most of them

classified as sources for PFAS, this must end, and the unnecessary barriers must be removed, otherwise the refrigeration sector is not able to deliver solutions supporting the wise proposal for a restriction of PFAS towards ECHA by several environmental agencies of European countries and the strongly emphasized precautionary principle, proposed by latest RTOC / UNEP report.

The standards are now being revised to allow for larger charges of flammable fluids for indoor applications. For chillers located outside, there is no charge limit unless the local fire inspector requires special attention on the installation. The main challenge is the education and training levels regarding the natural refrigerants, which has in many countries been neglected far too long. This is now changing thanks to a strong base of committed trainers in most countries, and due to the fact that also the newly introduce non-natural low GWP working fluids are flammable.

APPLICATION SECTORS AND NATURAL WORKING FLUIDS IN A NUTSHELL

Table 2. Applications and the applied working fluid

	CO_2 (R744)	NH_3 (R717)	HC	H_2O (R718)	Air (R729)
Domestic applications	Domestic hot water heat pumps	-	Refrigerators, AC units (split units) including heat pumps (liquid to liquid, air to liquid, and air to air)	-	-
Commercial refrigeration	Centralized systems, integrated units providing also AC and heating to the building, condensing units and standalone units (for convenience stores) No regional restrictions	As the upper stage of CO_2-NH_3 cascade systems, applied in some stores and warehouses	Self-contained cabinets, water cooled cabinets, refrigeration systems for indirect systems, AC part of the building Safe in operation when following EN378 and other standards	-	-
Industrial refrigeration and heat pump systems,	Freezing applications within food processing from -53° to +5°C, Industrial heat pumps providing high temperature lifts, warehouses and distribution centre cooling and freezing	All kind of freezing, chilling and heat pump applications	ultra-low temperature applications, in process plants, high temperature heat pumps, steam producing heat pumps	Data centre cooling, heat pump applications including high temperature heat pumps	
Water and space heating heat pumps	Domestic hot water heat pumps for hotels and other high performance buildings	Space heating, roof mounted units for distribution centres and warehouses.	Indirect systems providing hot water and space heating		
Chillers	Ejector supported chillers (10kW to 1 MW)	From small capacities to several MW units	From small capacities to several MW units	Large industrial chillers	
Vehicle air conditioning	AC only or reversible system having heat pump function	-	Applied as drop in fluid in Australia. Indirect compact systems	-	Applied in aircrafts and trains

CONCLUSIONS

All temperature levels and most applications can be cooled by applying natural refrigerants. There is no technical barrier to replace currently used synthetical fluorine containing refrigerants with natural working fluids in new systems. It is more about seeing the possibilities than the ghosts when selecting the optimal refrigerant for the project or a product. No single refrigerant can cover all applications; however, the group of natural refrigerants can cover all the applications which can be covered by fluorinated hydrocarbons and even more. None of the fluorinated hydrocarbons can go as low in temperature or as high as the natural refrigerants, they only cover the most profitable markets in the middle temperature range.

The short life HFC blends containing HFO are claimed to be simple and compatible with HFC systems designs, therefore some manufactures are preferring to utilize them. However, as these fluids become flammable when lower GWP values are required, objective information and promotion of natural refrigerants towards end-users are necessary, as they might accept a natural solution when informed about all the risks related to the environmental impact of the fluorinated substances.

With respect to PFAS pollution on earth, the refrigeration sector does have all possibilities to spearhead a complete phase out of HFCs contributing to the PFAS accumulation in our biosphere, without compromising safety, food supply and human comfort.

ACKNOWLEDGEMENTS

The authors gratefully acknowledge the support received from experts in the field, especially from Alexander Cohr Pachai (Global Consultancy ApS).

REFERENCES

Ciconkov R., 2018. Refrigerants: There is still no vision for sustainable solutions, International Journal of Refrigeration 86 (2018), pp. 441–448

Hafner, A., 2017. Integrated CO2 system for refrigeration, air conditioning and sanitary hot water, Ammonia and CO2 Refrigeration Conference, IIR, Ohrid, R. Macedonia.

Kauffeld M., Dudita M., 2021. Environmental impact of HFO refrigerants & alternatives for the future https://www.openaccessgovernment.org/hfo-refrigerants/112698/

Lorentzen G., 1993, Revival of carbon dioxide as a refrigerant. Int. J. of Ref., 17 (5) (1993), pp. 292-301

Lorentzen G., 1995, The use of natural refrigerants: a complete solution to the CFC/HCFC predicament Int. Journal of Refrigeration, 18 (3) (1995), pp. 190-197

Pachai, A., Norman J., Arpagaus C., Hafner A., 2021. Screening of future-proof working fluids for industrial high-temperature heat pumps up to 250 °C. Proceedings of the 9th IIR Conference: Ammonia and CO2 Refrigeration Technologies, Ohrid, 2021

Proceedings of IWEC2023
The International Workshop of Energy Conversion
March 15-17, 2023, Kyoto, Japan

Paper No. IWEC2023-18

RESEARCH HISTORY FOR MAGNETIC FLUID AND CO_2 HEAT PUMP SYSTEM

H. Yamaguchi
Energy Research Center, Department of Mechanical Engineering, Doshisha University, Kyoto, Japan
*corresponding author, E-mail: hyamaguc@mail.doshisha.ac.jp

ABSTRACT

A brief history of magnetic fluid is described from a view point of the present magnetic fluid in thermo-physical science. Magnetic fluid is a suspension with nano-magnetic particles stably dispersed in a carrier liquid. The concept of magnetic fluid appeared in 17 century in history. However, in practice the appearance of practical magnetic fluid, whose particle size is in a order of 10 nm together with the associated technology emerged in 1960's. In order to consider a future trend, various applications of magnetic fluid are viewed with the development of basic theory of continuum mechanics.

The background and recent development of the CO_2 heat pump system are also introduced with a concept of sustainable utilisation for industrial applications. A detailed design feature of the heat pump system is described in order to explain the uniqueness and to provide the functional relation for estimating the performance of the system. Particular attention is focused on a development of CO_2 heat pump system, which can be operated in sustainable development goals.

INTRODUCTION

KIFEE (Kyoto International Forum for Energy and Environment)-10, 2018 was held on board of the ship (MS Finn Marken) between Toromso-Trondheim, Norway. A Norwegian aurora researcher was invited as a guest speaker in the occasion giving a very interesting talk. After the lecture, a CD-ROM titled "The Northern lights; A Magic Experience" was distributed to the participants of the forum. The CD-ROM contained a description of aurora studies in the history. The aurora theory was explained by "Sir Edmond Halley(1656-1742), suggesting aurora can be caused by Magnetic Liquid, which is evaporating from poles in the northern region and moving up the atmosphere along the magnetic line, creating the northern light". Sir Halley probably understood the existence and distribution of the geomagnetic field, and perhaps foreshadowing the later Aurora Oval. Here he explains that the evaporation of magnetic fluid from the earth's surface near the poles causes the aurora's occurrence. It is a wonderful theory that later led to the famous prediction of Halley's Comet. Perhaps Sir Halley's Magnetic Liquid was probably the first magnetic fluid concept ever used in history, if we trace the history of magnetic fluid, magnetic fluid, ferrofluid or magnetic liquid.

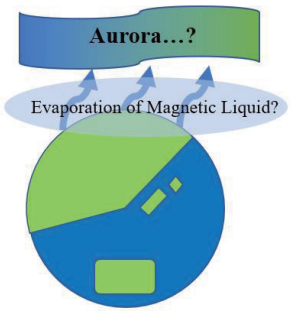

Fig.1 Aurora oval.

Thereafter, aurora research was taken over by Norwegian scientist Kristian Kirkeland. Of interest, he has performed an experiment in which a permanent magnet is placed in a sphere to simulate geomagnetism and reproduce auroras caused by charged particles in his laboratory. For some reason, the history of these natural sciences has been stuck in my mind since the old onboard forum. At the time, I was completely unaware of the work of Sir Halley and Kirklend. I was solely interested in the macroscopic fluid phenomena of magnetic fluid and their relation to torque, for which, I had conducted a research on the hydrodynamic behavior of magnetic fluid on spherical surfaces by applying a magnetic field to the surface of the sphere. [1] Aurora research is a field that deals with charged particles (rarefied gas plasmas), while magnetic fluids we are currently dealing with are liquids. In that sense, although there is a gap between them as the research subject, they can be regarded as the same in the category of magnetohydrodynamics. The future of magnetic fluid research may lie in Sir Halley's ideas regarding the nature of magnetic fluids. Research in the direction of making a liquid magnetic fluid electrically

conductive [2] and furthermore creating a gaseous magnetic fluid is conceivable. We can expect to see the development and unification of Kirland's smart experimental work in thermoelectric conversion[3] and plasma power generation [4] in the field of thermo-fluid physics, as well as in geophysics with the Earth (core) dynamo theory [5]. The smartness of magnetic fluid is that, when magnetic fluid is placed in an magnetic field, it is possible to conduct very inexpensive and small-scale experiments as the behavior of a continuum compared to the large-scale, expensive studies of magnetic plasma and superfluidity under cryogenic conditions, as described above. With a fluid (magnetic fluid) and a magnet, it is easy to conduct a variety of interesting experiments and research, depending on one's ingenuity. A History of Candle" by Mr. Michael Faraday (1791-1867) is well known [6]-[7]. Magnetic fluid is also considered to be a material of education for young researchers. From the creation of realistic magnetic fluids, the history of the development of magnetic materials and dispersants in materials science from a physicochemical perspective must also be mentioned. These are also deeply related to the development of magnetic fluid applications. For example, thermosensitive magnetic fluids [8] have been developed since the early days of magnetic fluid research for energy conversion devices. Along with magnetic particle development, magnetic nano capsules have been used for medical applications. From these viewpoints, it is necessary to take magnetic fluids not from the viewpoint of flow dynamics, but from the viewpoint of smart functional materials. In recent years, magnetic fluids have been used in particle science, drag-deliveries [9], thermo-thermal rapids [10] and, more recently virus testing methods [11].

The background and recent development of the CO_2 heat pump system are also introduced here in this review. A detailed design feature of the heat pump system is described in order to explain the uniqueness and to provide the functional relation for estimating the performance of the heat pump system. The CO_2 refrigeration system with a cyclone separation evaporator, that separates dry ice, utilizes the sublimation heat of the dry ice generated during the expansion process. The system, Fig. 2, proves a sustainable refrigeration system with cold energy storage function compared to that of the conventionally used horizontal evaporator system.

Fig.2 CO_2 Heat Pump System

ALONG THE COURSE OF HISTORY IN MAGNETIC FLUID

As a concept, magnetic fluid does not exist in nature, although it was dated back to the 17th century, and in this sense Sir Halley's hypothesis is incorrect. The magnetic fluid we are currently aware of is an artificial suspension (colloidal suspension) in which ferromagnetic particles of the order of 10 nm are stably dispersed. It appeared in the 1960s in reality. If one examines the historical record consciously, Neuringer and Rosensweig's "Ferrodrodynamics (1964)" [12] was the first to treat magnetic fluid as a new academic concept, a theory of continuum in a magnetic field. It was undoubtedly an influential work in the development of magnetic fluid research in theory, experiment, engineering, and manufacturing in the following years. It is undoubtedly an achievement that had a great influence on the subsequent development of magnetic fluid research. In the following year, Papell obtained a U.S. Patent (1965) of magnetic t by Grinding Methods [13]. Papell's patent was applied for the purpose of preventing sloshing of rocket fuel in space. It is thought that a magnetic fluid already existed at this time for NASA's space program. With the creation of early magnetic fluid and the emergence of the dynamical theory of continuum in magnetic field, the historical development of “Ferrohydrodynamics” separated from "Magnetohydrodynamics" (note: Blums et al. (1986) [14], again discussed as electromagnetic fluids). Shiliomis et al. (1972)[15] and (1974)[16] developed the fluid science theory of suspensions of magnetic particles by introducing the concept of angular momentum as a continuum into the asymmetric part of the stress tensor for Shiliomis' single particle dispersion systems. The theory of fluid science obtained by introducing the concept of angular momentum has undoubtedly made a significant contribution to the subsequent development of not only magnetic fluid research but also the science of electromagnetic particle dispersion systems. In 1985, Rosensweig's famous book Ferrohydrodynamics[17] was published, and magnetic fluids (fluid dynamics of ferromagnetic materials) were established academically. With the advent of magnetic fluids and the establishment of the basic theory, the development of engineering applications has also progressed, particularly in the areas of acceleration sensors and shaft (vacuum) seals. Many ideas for these applications were proposed mainly in the 1980s and 1990s, and many of them have been put into practical use. These results are summarized in Berkorsky et al. (1977) [18], (1993) [19]. Applied techniques are summarized recent application techniques can be traced in the respective references.

The development of magnetic fluids in the 21st century includes, as mentioned above, the improvement of physical properties accompanying application technology, i.e., synthesis of ferromagnetic particles with higher saturation magnetization [20] and ferromagnetic particles [21], formation of mother liquids with high saturation vapor pressure. In applications, effects are focused on development and research of surfactants [22], and development of conductive magnetic fluids with a liquid metal mother liquid [3], as well as the development of magnetic fluids with high vapor pressure in the future. The advances in the production and manufacture of magnetic fluids as a result of their physicochemical results, as well as the

advances in the theory of dynamics based on the internal structure of magnetic fluids, are remarkable in the history of the development of science and technology worldwide. The emergence of magnetic fluids and the progress in theory and application technology are summarized in the proceedings of the International Conference on Magnetic Fluids (ICMF), which began in Udine, Italy in 1977, and in a collection of papers (International Journal of Science). Since the first International Conference was held in Udine, Italy in 1977, the conference has been held every three years in the United States, Brazil, Russia, England, France, Germany, Romania, Slovakia, Japan, India and France. In 2023, Spain is hosting the conference. In Japan, the Magnetic Fluid Research Liaison Group [22] has been organized since 1986 and has been active in research activities every year up to the present, while at the same time publishing the proceedings of the Joint Conference, which traces magnetic fluid research in Japan (Note: The Joint Conference was also held in Taiwan on a regular basis). The study of magnetic fluid is a comprehensive science that includes electromagnetism, fluid physics, continuum mechanics, colloid chemistry, etc., and the field of application is a comprehensive technology that spans a wide range of areas, including magnetic engineering, mechanical engineering, electrical engineering, tribology technology, and medical technology. In addition, the field (magnetic field) applied by treating large particle systems necessitate the treatment of particles in a clustered stracture (note that even in magnetic fluid, the science of single-particle dispersion systems is not sufficient for practical highly concentrated dispersion system, and it is still necessary to treat internal structural changes [23] in a clustered manner).

Many basic and engineering application studies on magnetic fluids have been developed, such as magnetic fluid interfacial phenomena under magnetic field [24]-[26], vacuum deposition [21], specific gravity screening [27]-[28], velocity distribution measurement by the UVP (Ultrasonic Velocity Profile) method [29], material and heat transport [30]. magnetic fluid polishing [31], artificial hearts [32], and hyperthermia [10], among others. Recent publications dealing comprehensively with academic and technical applications along the lines of ferrohydrodynamics mentioned in the introduction include Odenbach [33]-[34], Yamaguchi [35]. There is a very interesting article [36] on the history and future of magnetic fluid. It may be a little obsolete, but from the viewpoint of the development of science and technology, it is a record that should be kept in memory.

"Scientific, Technological and Calfural Aspects of Magnetic Fluids",

- History
- Magnetism is mysterious
- Magnetic fluids hold suientific interest
- Magnetic fluids display other phenomena
- Magnetic fluids yield technological applications
- Magnetic fluids are part of world culture
- What do magnetic fluids promise for the future?

It should be noted that magnetic fluid lends itself to study in developing countries as much of the research can be done cheaply with inexpensive equipment at ambient temperature and the fluids are safe to handle, quoted from ICMF, India.

A typical example of applications is a magnetic fluid speaker [50] for heat dissipation and damping effect. The magnetic fluid is held in place by magnetic force using the magnetic field generated by the voice coil, and the magnetic fluid conducts the Joule heat of the coil to the surrounding parts, cooling the coil and realizing a high quality, loudspeaker. At the same time, the fluid holding force has a centering and damping effect on the pole piece. Other practical applications include specific gravity sorting [27]-[28] and grinding [31] using magnetic buoyancy. There is also an energy conversion technology [30] that adds thermosensitivity to a magnetic fluid so that the fluid is self-driven and transports heat over long distances with only a magnetic field and heat input. This is done by using thermosensitive magnetic particles with a low Curie temperature, such as manganese-zinc ferrite, to take advantage of the magnetic volume force (magnetic pressure) resulting from the difference in spatial average magnetization. On the other hand, in magneto-viscous and electro-viscous fluids, strong chain-like clusters are formed along electromagnetic field [23], so that when a magnetic acts perpendicular to the direction of shear stress of fluid motion, the (apparent) viscosity increases dramatically and a strong magneto-viscous effect is manifested.

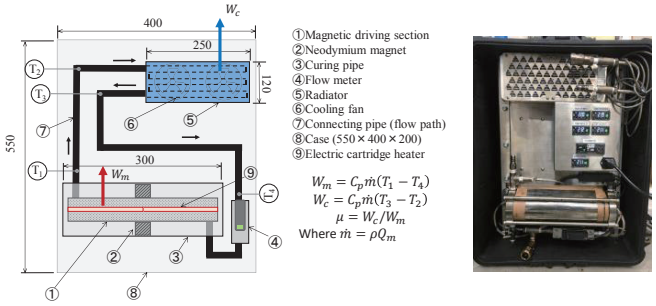

Fig.3 Energy Conversion Technology

CURRENT DEVELOPMENT OF CO_2 HEAT PUMP SYSTEM

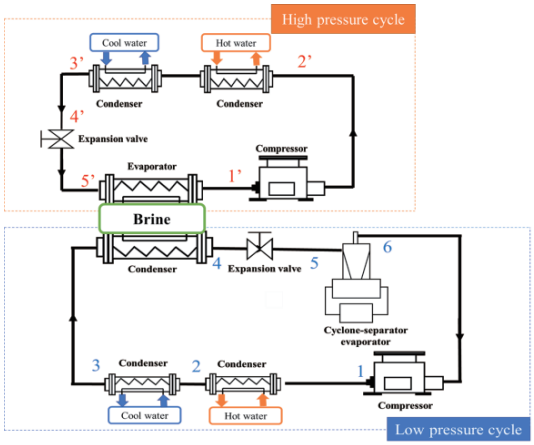

Fig.4 Schematic diagram of the CO_2 cascade system[46]

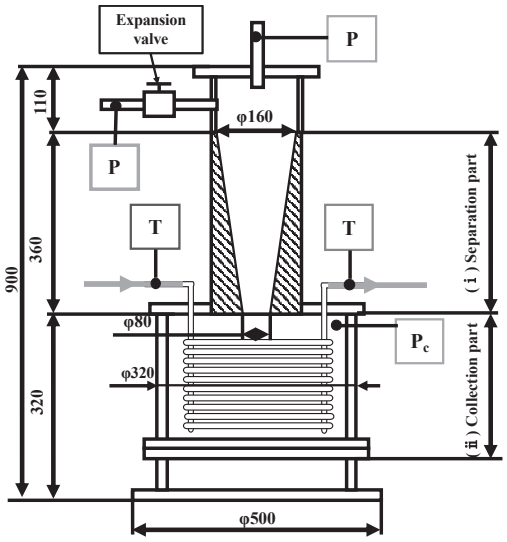

(a)

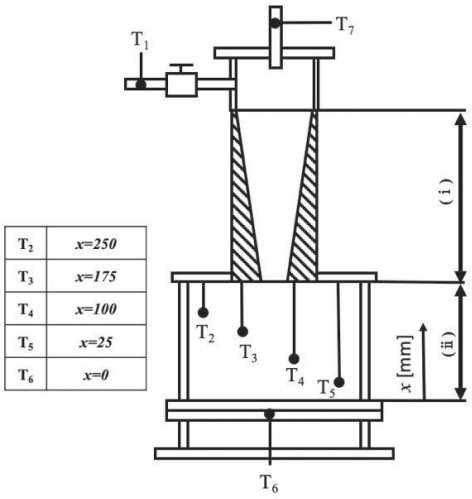

(b)

Fig.5 Schematic of cyclone separator-evaporator[46]

For decades, chlorofluorocarbons (CFCs) and hydrochlorofluorocarbons (HCFCs) were the most popular refrigerants for refrigeration equipment. In recent years, however, the use of these refrigerants has restricted from the viewpoint of environmental protection.In searching environmentally friendly natural refrigerants attention, CO_2 is of particular interest because of its low environmental impact, with an ozone depletion potential (ODP) of zero and a global warming potential of one, as well as its low impact on the human body due to its non-toxic and non-flammable properties [38]-[40].

Due to much demand for ultra-low temperature technology and the environmental impact of refrigerants, CO_2 cascade refrigeration systems have been proposed and studied for practical application [41]-[45]. In these studies, however, cooling performance of about -60℃ was achieved by utilizing sublimation of CO_2 dry-ice, but the aggregation of dry ice in the horizontally installed copper tube evaporator caused thermal resistance. The system has been found to be unstable and its performance degraded, which is a major obstacle to its practical application. A series of studies have been conducted on evaporator geometry to prevent dry ice agglomeration [47]-[49].

A cyclone separator evaporator was introduced instead of a conventional horizontal copper heat-transfer tube evaporator (hereinafter referred to as a horizontal evaporator) to solve the above problems and to improve the performance of the refrigeration system. The cyclone separator evaporator separates and collects dry ice in a CO_2 solid-gas multiphase flow by centrifugal force. In the cyclone separator evaporator, the dry ice is collected at a separate location from the circulation channel, enabling efficient cold heat recovery.

The system, Fig. 4, consists of a two-stage heat pump cycle: a high pressure cycle (HPC) with a high compressor discharge pressure and a low pressure cycle (LPC) with a low compressor discharge pressure. The two cycles that make up the system are the compression process (1–2, 1' –2') and the condensation process (2–3–4 –5, 2' –3' –4'), the expansion process (5–6 or 7, 4' –5'), and evaporation process (6 or 7–1, 5' –1'). The heat transfer of the refrigerant between the cycles is possible by circulating brine antifreeze between the evaporator of the high-pressure side cycle and the third condenser of the low-pressure side cycle.

As shown in Fig. 4, a cyclone separator evaporator was used as the evaporator for the low-pressure side cycle. The cyclone separator evaporator, Fig. 5 (a) and (b) consists of a separator and a collector. The inner wall of the separator has a tapered structure, with the inner diameter decreasing in the vertical downward direction. The collector is equipped with a heater on the bottom surface, and a power meter allows heat input to the cooled material. A coiled copper tube is installed as a heat exchanger to recover cold heat from the collected dry ice. Ethanol flows through the coiled copper tube and exchanges heat with the dry ice in the collection section, enabling the recovery of cold heat. The cyclone separator evaporator has confirmed the high performance of the CO_2 refrigeration system in the ultra-low temperature range operation.

ACKNOWLEDGMENTS

Some part of this review as quoted from a paper [47] of AEM society. Some contents are referred from the original works of HighEFF, Norway and IntER-Cold, Norway.

REFERENCES

[1] H. Yamaguchi and I. Kobori, Spherical Couette flow of a magnetic fluid with inner sphere rotation, *Journal of Magnetism and Magnetic Materials*, Vol. 122, Issue 1-3, pp. 221-223, 1993.

[2] T. Fujita, H.-S. Park, K. Ono, S. Matsuo, K. Okaya and G. Dodbiba, Movement of liquid gallium dispersing low concentration of temperature sensitive magnetic particles

under magnetic field, Journal of Magnetism and Magnetic Materials, Vol. 323, Issue 10, pp. 1207-1210, 2011.
[3] J.W. Schwede, I. Bargatin, D.C. Riley, R.T. Howe, Z.-X. Shen and N.A. Melosh, Photon enhanced thermionic emission (PETE) for solar concentrator systems, *Nature Materials*, Vol. 9, No.9, pp. 762-767, 2010.
[4] P.A. Davidson and A. Thess, *Magnetohydrodynamics*, CISM, Udine, 2002.
[5] P.A. Davidson, *An Introduction to Magnetohydrodynamics*, Cambridge University Press, 2001.
[6] M. Faraday, *Course of six lectures on the chemical history of candle*, Harper & Brothers, New York, 1861.
[7] R.J. Seeger, Michael Faraday and the art of lecturing, *Physics Today*, Vol. 21, No. 8, pp. 30-38, 1968.
[8] R.E. Rosensweig, J.W. Nestor and R.S. Timmins, Ferrohydrodynamic fluids for direct conversion of heat energy, *A.I.Ch.E.-I. Chem. E. Symposium Series,* No.5, pp. 104-118, 1965.
[9] Y. Namiki et al., A novel magnetic crystal-lipid nanostructure for magnetically guided in vivo gene delivery, Nature Nanotechnology, Vol. 4, pp. 598-606, 2009.
[10] M. Suto, Y. Hirota, H. Mamiya, A. Fujita, R. Kasuya, K. Tohji and B. Jeyadevan, Heat dissipation mechanism of magnetite nanoparticles in magnetic fluid hyperthermia, *Journal of Magnetism and Magnetic Materials*, Vol. 321, Issue 10, pp. 1493-1496, 2009.
[11] X. Li, Z.-Q. Dong and P. Yu, Effect of self-assembly on fluorescence in magnetic multiphase flows and its application on the novel detection for COVIC-19, *Physics of Fluids*, Vol. 33, 042004, 2021.
[12] J.L. Neuringer and R.E. Rosensweig, Ferrohydrodynamics, *The Physics of Fluids*, Vol. 7, No. 12, pp. 1927-1937, 1964.
[13] S.S. Papell, Low viscosity magnetic fluid obtained by the colloidal suspension of magnetic particles, U.S. Patent 3,215,572, 1965.
[14] M.E. Blums, Y. Mikhailv and R. Ozols, *Heat and Mass Transfer in MHD Flows*, World Scientific Publishing Co. Pte. Ltd., Singapore, 1986.
[15] M.I. Shliomis, Effective viscosity of magnetic suspensions, *Soviet Physics JETP*, Vol. 34, No. 6, pp. 1291-1294, 1972.
[16] M.I. Shliomis, Magnetic fluids, *Soviet Physics Uspekhi*, Vol. 17, No. 2, pp. 153-169, 1974.
[17] R. Rosensweig, *Ferrohydrodynamics*, Cambridge University Press, 1985.
[18] B. Berkovsky, *Thermomechanics of magnetic fluids: theory and applications*, Hemisphere Pub. Corp., Washington, 1978.
[19] B.M. Berkovsky, V.F. Medvedev and M.S. Krakov, Magnetic fluids: Engineering Applications, Oxford University Press, 1993.
[20] R.E. Ronsesweig, Toward ferrofluids with enhanced magnetization, Journal of Magnetism and Magnetic Materials, Vol. 323, Issue 10, pp. 1191-1197, 2011
[21] I. Nakatani, T. Furubayashi, T. Takahashi and H. Hanaoka, Preparation and magnetic properties of colloidal ferromagnetic metals, *Journal of Magnetism and Magnetic Materials*, Vol. 65, Issue 2-3, pp. 261-264, 1987.
[22] Japan Society of Magnetic Fluid Research HP, http://jsmfr.on.arena.ne.jp/
[23] Y. Iwamoto, S. Kondoh, Y. Ido, H. Yamamoto, H. Nishida, H. Yamasaki, H. Yamaguchi and B. Jeyadevan, Influence of size on anisotropic thermophysical and rheological properties of magnetic suspensions, *International Journal of Applied Electromagnetics and Mechanics*, Vol.58, No.3, pp. 371-385, 2018.
[24] S. Sudo, H. Hashimoto and A. Ikeda, Measurements of the surface tension of a magnetic fluid and interfacial phenomena, *JSME International Journal, Ser. 2, Fluids Engineering, Heat Transfer, Power, Combustion, Thermophysical Properties*, Vol. 32, No.1, pp.47-51, 1989.
[25] Y. Mizuta, Stability analysis on the free surface phenomena of a magnetic fluid for general use, *Journal of Magnetism and Magnetic Materials*, Vol. 323, Issue 10, pp. 1354-1359, 2011.
[26] Y. Ido and M. Sasaki, Three-dimensional lattice Boltzmann simulation of a magnetic fluid drop under magnetic field, *International Journal of Applied Electromagnetics and Mechanics*, Vol. 33, pp. 1671-1676, 2010.
[27] J. Shimoiizaka, K. Nakatsuka, T. Fujita and A. Kounosu, Sink-float separators using permanent magnets and water based magnetic fluid, *IEEE Transactions on Magnetics*, Vol. 16, Issue 2, pp. 368-371, 1980.
[28] T. Fujita and M. Mamiya, Interaction forces between nonmagnetic particles in the magnetized magnetic fluid, *Journal of Magnetism and Magnetic Materials*, Vol. 65, pp. 207-210, 1987.
[29] H. Kikura, Y. Takeda and T. Sawada, Velocity profile measurements of magnetic fluid flow using ultrasonic Doppler method, *Journal of Magnetism and Magnetic Materials*, Vol. 201, Issue 1-3, pp. 276-280, 1999.
[30] Y. Iwamoto, H. Yamaguchi and X.-D. Niu, Magnetically-driven heat transport device using a binary temperature-sensitive magnetic fluid, *Journal of Magnetism and Magnetic Materials*, Vol. 323, Issue 10, pp. 1378-1383, 2011.
[31] N. Umehara, MAGIC polishing, *Journal of Magnetism and Magnetic Materials*, Vol. 252, pp. 341-343, 2002.
[32] Y. Mitamura, S. Arioka, D. Sakota, K. Sekine and M. Azegami, Application of a magnetic fluid seal to rotary blood, *Journal of Physics: Condensed Matter*, Vol. 20, No. 20, 204145, 2008.
[33] S. Odenbach, *Magnetoviscous Effect in Ferrofluids*, Springer, 2002.
[34] S. Odenbach, *Colloidal Magnetic Fluids*, Springer, 2009.
[35] H. Yamaguchi, *Engineering Fluid Mechanics*, Springer, 2008.
[36] R.E. Rosensweig, Keynote address, Seventh International Conference on Magnetic Fluids, Bhavnagar, January 9-14, 1995.
[37] R.E. Rosensweig, Y. Hirota, S. Tsuda and K. Raj, Study on audio speakers containing ferrofluid, Journal of Physics: Condensed Matter, Vol. 20, 204147, 2008.
[38] G. Lorentzen, The Use of Natural Refrigerations: a

Complete Solution to the CFC/HCFC Predicament, *International Journal of Refrigeration*, 1995, Vol.18, No.3, pp190-197.

[39] B. Palm, Hydrocarbons as Refrigerations in Small Heat Pump and Refrigeration systems-A Review, *International Journal of Refrigeration*, 2008, Vol.31, No.4, pp. 552-563.

[40] P. Neksa, CO_2 Heat Pump Systems. *International Journal of Refrigeration*, 2002, Vol.25, No.4, pp. 421-427.

[41] H. Yamaguchi, X.R. Zhang, and K. Fujima, Basic Study on New Cryogenic Refrigeration Using CO_2 Solid-Gas Two Phase Flow, *International Journal of Refrigeration*, 2008, Vol.31, pp. 404-410.

[42] H. Yamaguchi, and X.R. Zhang, "A Novel CO_2 Refrigeration System Achieved by CO_2 Solid-Gas Two-Phase Fluid and Its Basic Study Ion System Performance", *International Journal of Refrigeration*, 2009, No.7, pp. 1683-1693.

[43] H. Yamaguchi, X.D. Niu, K. Sekimoto, and P. Nekså, Investigation of Dry Ice Blockage in an Ultra-Low Temperature Cascade Refrigeration System Using CO_2 as a Working Fluid, *International Journal of Refrigeration*, 2011, Vol.34**,** pp. 466-475.

[44] H. Yamaguchi, Y. Iwamoto, S. Ozaki, and P. Nekså, Experimental Observation of Sedimentation Phenomena of CO_2 Dry Ice in Model Channel, Proceedings of The IIR Gustav Lorentzen Conference on Natural Refrigerants, Hangzhou(2014), ID81.

[45] H. Yamasaki, H. Yamaguchi, O. Kizilkan, T. Kamimura, K. Hattori, and P. Nekså, Experimental Investigation of the Effect of Solid-gas Two-phase Flow in CO_2 Cascade Refrigeration System, *Energy Sources, Part A*: *Recovery, Utilization Environmental Effects*, 2020, DOI: 10.1080/15567036.2020.1767731.

[46] H. Yamaguchi, Y. Ishikawa, H. Yamasaki, T. Kamimura, K. Hattori, P. Neksa, "Investigation on ultra-low temperature CO_2 refrigeration system using cyclone separator-evaporator". The Japan Society of Refrigerating and Air Conditioning Engineers (2022), Vol.2, No.39, pp117-125

[47] H. Yamaguchi, History and Future of Magnetic Fluids, Journal of the Japan Society of Applied Electromagnetics, 2021, Vol. 29, No. 3, pp. 516-520.